COMPUTATIONAL ANALYSIS OF BINARY-FLUID HEAT AND MASS TRANSFER IN FALLING FILMS AND DROPLETS

A Dissertation
Presented to
The Academic Faculty

by

Vishwanath Subramaniam

In Partial Fulfillment
of the Requirements for the Degree
Doctor of Philosophy in the
George W. Woodruff School of Mechanical Engineering

Georgia Institute of Technology
December 2008

COMPUTATIONAL ANALYSIS OF BINARY-FLUID HEAT AND MASS TRANSFER IN FALLING FILMS AND DROPLETS

Approved by:

Dr. Srinivas Garimella,
Committee Chair
George W. Woodruff School of
Mechanical Engineering
Georgia Institute of Technology

Dr. Tim Lieuwen
Daniel Guggenheim School of
Aerospace Engineering
Georgia Institute of Technology

Dr. William Wepfer
George W. Woodruff School of
Mechanical Engineering
Georgia Institute of Technology

Dr. Tom Fuller
School of Chemical and Biomolecular
Engineering
Georgia Institute of Technology

Dr. Sheldon Jeter
George W. Woodruff School of
Mechanical Engineering
Georgia Institute of Technology

Date Approved: November 14, 2008

To my parents ... my first and most influential teachers ...

ACKNOWLEDGEMENTS

Looking back at the wonderful journey that got me here, I realize that there are many people who have helped me tremendously along the way. I would not have got here without their support. Foremost among them is my adviser Dr. Srinivas Garimella, whose constant support played a huge role in the success of this work. He always pushed me to aim higher and guided me achieve those lofty goals. His critical review of my dissertation was instrumental in the document taking its present shape. I would like to thank Jesse Killion, whose work set the stage for this present study. His inputs during the initial stages of model development were invaluable. I would also like to thank my committee members Dr. William Wepfer, Dr. Sheldon Jeter, Dr. Tom Fuller and Dr. Tim Lieuwen for their valuable feedback. Special thanks to Neil Bright, Paul Manno and the excellent maintenance staff of the PACE cluster at Georgia Tech. Their prompt and efficient support of the computer cluster ensured that I was able to run my computations without significant interruptions.

I am grateful to my fellow students of the Sustainable Thermal Systems Laboratory, both past and present, for their help. The students in the group formed a strong support group and were always willing to provide me with advise and/or assistance when I needed it. I would especially like to acknowledge Biswajit Mitra, Ulf Andresen, Akhil Agarwal, Anand Nagavarapu, Ashlie Brown, Brendon Keinath and Alex Raymond for their technical, logistical and moral support on numerous occasions. I would also like to thank the Woodruff School of Mechanical Engineering at Georgia Tech for providing me with the opportunity and infrastructure to conduct this work. I am also thankful to the school to have provided me with the privilege of meeting some of the greatest mechanical engineering minds in the world and learning

from their diverse perspectives.

It would have been impossible for me to get to this position without the love, support and backing from members of my family. Words cannot describe my gratitude towards my parents for all that they have done for me. They sacrificed many of their dreams, so that I could live mine! I consider the lessons that I learnt from them during childhood to be my greatest strength and asset. I will forever be indebted to my uncle Venkatesh and aunt Sasikala for their love and backing of all of my pursuits. They have always treated me like their son and have been there for me in times of need. I am also thankful to Saroj, Ramki, Radhika and Hari in Chicago, and Vyas, Subhashri, Shreya and Hari in Minneapolis for their affection and backing. With their constant care and support, it never felt like I was away from home.

I am sure that I must have missed acknowledging a few people that have contributed significantly to my success. I thank them for their contributions and sincerely apologize from my impertinence. I am extremely fortunate to have such selfless people around me. I could never have got this far without them.

TABLE OF CONTENTS

LIST OF TABLES

LIST OF FIGURES

NOMENCLATURE

A	area.
CFL	Courant Friedriche Lewy Number.
D_{AB}	coefficient of mass diffusivity.
E	energy.
g	gravitational acceleration.
h	enthalpy.
J_i	species mass flux.
k	thermal conductivity.
p	pressure.
q	heat.
R	radius of curvature.
t	time.
v	velocity.
V	volume.
x	Cartesian coordinate x.
y	Cartesian coordinate y.
Y_i	species concentration.

Greek Symbols

α	under-relaxation factor.
δt	time step.
δx	x discretization.
δy	y discretization.
κ	local surface curvature.

μ	dynamic viscosity.
ν	kinematic viscosity.
ϕ	arbitrary scalar.
ρ	density.
σ	surface tension coefficient.
τ	shear stress.

Subscripts

bulk	bulk (average) value of the LiBr solution.
int	liquid-vapor interface.
nb	neighboring cell.

SUMMARY

Vapor absorption systems offer advantages over vapor compression systems for air-conditioning systems in some applications. They use heat as their primary energy input and hence provide opportunities to use solar energy or waste heat to drive these systems. The absorber is the most crucial component of the vapor absorption system and has the largest impact on its performance. Absorber design requires a keen understanding of the underlying heat and mass transfer processes in the absorber. The horizontal tube geometry is by far the most popular absorber geometry, due to the high absorption efficiencies achievable without incurring commensurate pressure drops.

Several models have been proposed in the literature to model the heat and mass transfer during absorption over horizontal tube banks. However all of them make very simplistic assumptions about the flow profiles in the absorber. High speed flow visualization studies in the literature have shown that the flow occurs in the form of droplets and the formation and the detachment of these droplets and their impact on the tube has significant effects on the heat and mass transfer. Most absorption models in the literature neglect these flow modes and assume the solution to flow as a uniform film.

The present study attempts to numerically model the heat and mass transfer in the absorber taking the realistic drop-wise and wavy film flow patterns into consideration. The impact of the fall of these droplets on the tube causes the lithium bromide solution present on the film on the tube to *mix* and present newer regions of the solution for vapor absorption. The impact of the droplets also causes *waves* that propagate axially over the liquid film on the tube. The *mixing effect* and the *waves* caused due

to droplet impact play a very important role in the heat and mass transfer. Results obtained from this study will aid in better understanding of the vapor absorption process, and in the design of more efficient absorbers.

CHAPTER I

INTRODUCTION

1.1 Vapor Absorption Cycle

The vapor absorption cycle is a thermal cycle that uses heat as its primary energy input. It replaces the compressor in the vapor compression system with an absorber and desorber, which together achieve the same result as the compressor, but with heat instead of work as the energy input. The cycle can be used for both heating and cooling. Some of the main advantages of the vapor absorption cycle over the vapor compression cycle are:

- The primary energy input is in the form of heat instead of electricity. This input heat energy could be energy from the burning of fuels, waste heat from other processes, solar energy and many more. This provides an opportunity to couple the vapor absorption system with various novel energy-saving strategies.

- No large moving parts. The absorption system gets rid of the compressor, which is easily the most failure-prone component of the vapor compression system. This leads to a significant reduction in maintenance costs and down-time of the system.

- Vapor absorption systems use environmentally friendly working fluids such as water, ammonia and lithium bromide, instead of chlorofluorocarbons (CFCs) and hydrochlorofluorocarbons (HCFCs) that are frequently used in vapor compression systems. These absorption system working fluids have zero ozone depletion potential (ODP) and global warming potential (GWP).

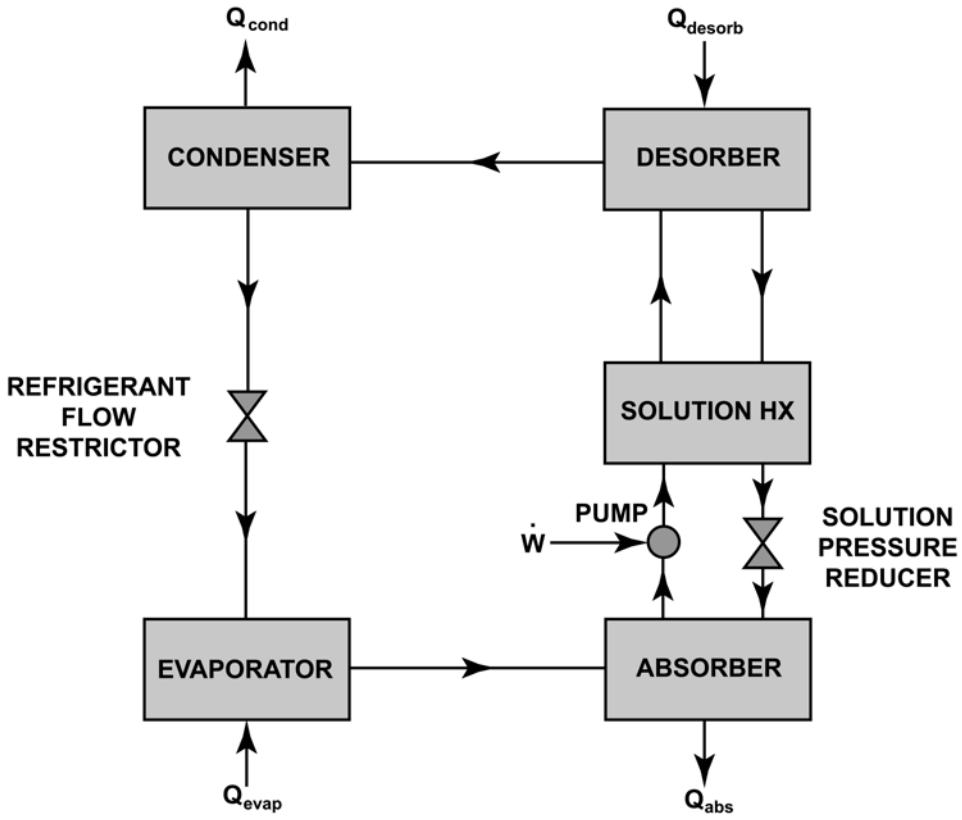

Figure 1.1: Vapor Absorption Cycle

Figure 1.1 shows the schematic of a simple vapor absorption system. Low pressure refrigerant that exits the evaporator in the vapor state is absorbed into a secondary fluid at the same pressure in the absorber. The resulting solution is pumped to a higher pressure by the solution pump. This high pressure solution is heated in the desorber using an external heat input. This heating causes the refrigerant to evolve from the solution. The evolved refrigerant flows to the condenser, where it is condensed with a release of heat. The rest of the refrigerant cycle is similar to that in a vapor compression cycle. The condensed refrigerant flows through a refrigerant flow restrictor, where its pressure is reduced in an isenthalpic process. This low pressure liquid refrigerant evaporates in the evaporator with absorption of heat from the surroundings. The refrigerant then flows from the evaporator to the absorber to complete the cycle.

After the refrigerant is generated from the solution in the desorber, the remaining high concentration solution (concentrations are in % LiBr) is returned to the absorber through a solution pressure reducer that reduces its pressure to that in the absorber. Since the concentrated solution from the desorber is at a temperature higher than that of the solution in the absorber, it is usually passed through a solution heat exchanger, where the heat from this weak solution is used to preheat the desorber inlet.

1.2 Absorption System - Working Fluids

As opposed to the vapor compression system, the vapor absorption system requires two working fluids; a refrigerant, and a fluid to absorb the refrigerant. Some of the desirable characteristics of the working fluid pair are as follows.

- **Affinity:** The two working fluids should have a strong affinity for each other. A high affinity would mean that for the same amount of refrigerant, lesser secondary fluid would be needed in the absorber. This in turn would mean that lesser energy would be wasted in heating and cooling the secondary fluid in the absorber-desorber loop. On the other hand, a high affinity also means that a higher amount of heat per unit mass of refrigerant would be needed in the desorber to separate the absorbed refrigerant from the solution.

- **Relative volatility:** The refrigerant should be much more volatile than the absorbing fluid. This would ensure that when the solution is heated in the desorber, only the refrigerant would escape out to the condenser and all of the absorbing fluid would be retained in the solution.

- **Low freezing point:** The evaporator temperature, which is the lowest possible operating temperature of the system in the cooling mode, is primarily determined by the freezing point of the refrigerant fluid. A lower freezing temperature

would mean that the system could be used as a chiller over a wider range of temperatures and thus be used in a wider variety of applications, including heat pumping for space heating.

- **Operating pressure:** The nominal operating pressures of the working fluids should not be too extreme so as to drive up manufacturing and assembly costs. Operating at very high pressure differences across the cycle could drive up pumping costs and require expensive thick-walled tubes. Very low operating pressures require specialized assembly to prevent influx of non-condensible gases, which drive up costs. Extreme pressures also increase the chances of leaks and refrigerant contamination.

- **Chemical Stability:** Once assembled, absorption systems are expected to operate for extended periods of time without any refrigerant change. During operation, the working fluids are also subjected to a wide range of temperatures and pressures, depending on the operating conditions. The working fluids should be able to perform reliably without chemical breakdown or any drop in performance at these conditions over extended periods.

- **Non-corrosive:** The working fluids should not corrode the pipes and other equipment through which the fluids flow. Mild corrosive tendencies of the fluids could be overcome by using anti-corrosive agents, but severely corrosive fluids should be avoided.

- **Safety:** The working fluids should be safe in terms of toxicity and flammability to be handled by the assemblers and the end users.

- **Transport properties:** The viscosity of the working fluids should be low enough so as to not drive up pumping costs. The thermal and mass diffusivities should be high enough to yield compact systems.

- **Latent heat:** It is desirable that the refrigerant have a high latent heat of vaporization. That would reduce the amount of refrigerant and absorbent required to achieve the desired heating or cooling load.

- **Environmentally benign:** The working fluids should have zero or very low global warming potential and ozone depletion potential. These environmental problems have become a very serious issue in the last few years and refrigerants in particular have been guilty of having caused a sizable fraction of the damage. Thus, it is important that the selected refrigerant comply with and if possible exceed, the current environmental codes.

As engineering problems go, it is almost impossible to find a single working fluid pair that satisfies all of these requirements to the fullest. However two pairs that come very close to satisfying all of these requirements are Ammonia-water and Water-lithium bromide. Some of the pros and cons of these refrigerant pairs are listed below.

1.2.1 Ammonia-Water

Pros

- High affinity for each other

- Low freezing point. The freezing point of ammonia is -77.7℃ and so the system could operate at temperatures as low as -77.7℃.

- High latent heat. The heat of vaporization of ammonia at 500 kPa is 1247.3 kJ/kg [1]. A higher latent heat results in a lower amount of refrigerant being required to achieve the desired cooling or heating load.

Cons

- Low relative volatility. The volatilities of water and ammonia are very close to each other. As a result, when the solution is heated in the desorber, quite a bit of water tends to escape into the condenser with the ammonia. For example, at a desorber temperature and pressure of 150 ℃ and 2.58 MPa, the concentration of the ammonia-water vapor at the desorber outlet is 85.3% by weight of ammonia [2].

- Ammonia is toxic and flammable and safety codes in many countries prohibit the indoor use of ammonia.

- Corrosive. Typically only carbon steel and stainless steel with corrosion inhibitors are usable with ammonia-water mixtures.

1.2.2 Water-Lithium bromide

Pros

- High affinity for each other.

- High relative volatility. Because lithium bromide is a salt, the volatility of the working fluids is significantly different and hence when the fluid is heated in the desorber, typically water is the only fluid that escapes into the condenser.

- High latent heat. The heat of vaporization of water at 1 kPa is 2484.4 kJ/kg [1]. As a result, a relatively small amount of refrigerant is required to achieve the desired heating or cooling loads.

- Not toxic or flammable and hence safer to use than ammonia.

Cons

- Water freezes at 0 °C. The system cannot be used at temperatures lower than 0 °C, which implies that refrigeration and space heating is not possible with such a system.

- Crystallization. Lithium bromide tends to crystallize at higher concentrations. Certain additives could be used this curb this crystallization, although limitations in operating temperatures and concentrations must still be followed.

- Low mass diffusivity. The mass diffusivity of water in lithium bromide is low compared to the diffusivity of ammonia in water. For example, at a typical operating pressure and temperature of 1 kPa and 40 °C, the mass diffusivity of water in lithium bromide is 1.6×10^{-9} m^2/s, while that of ammonia in water at its typical operating pressure and temperature of 500 kPa and 30 °C is more than three times higher at 5.0×10^{-9} m^2/s [3]. The low mass diffusivity decreases the rate of absorption and diffusion of refrigerant and adversely affects system performance.

1.3 Absorber Design

The absorber is the most crucial component of the vapor absorption system because it must accomplish coupled heat and mass transfer with considerable release of heat and reject that heat across small driving temperature differences. Therefore, it has the biggest impact on the performance of the system. The design of the absorber is governed by the heat and mass transfer process during the absorption of the refrigerant into the secondary fluid.

The most popular absorber geometry is the *Falling Film Absorber*. In this, the secondary fluid (e.g., Lithium Bromide solution) falls over a bank of chilled horizontal tubes. The region around the tubes and the film is filled with refrigerant vapor (e.g., water vapor), which is absorbed into the secondary fluid as it falls down the tubes.

A coolant flows through the inside of the horizontal tubes, which is used to cool the lithium bromide solution as it heats up during the absorption process.

The falling film absorber geometry provides excellent heat and mass transfer rates and large surface areas for absorption. The lithium bromide solution flow in the absorber is usually gravity-driven and involves a very small pressure drop.

Various analytical and empirical models have been developed to model the heat and mass transfer process, to aid absorber design. However, these models make very simplistic assumptions about the nature of the flow in an absorber. Most of them assume that the solution flows over the tubes as a uniform laminar film. They also assume that the absorption occurs only when the solution is present as a film around the tube and that the solution flows between the tubes without any heat and mass transfer. Some of these models will be described in the next chapter.

1.4 Present Work

The present study models the absorption of water vapor into lithium bromide solution as it falls over a bank of horizontal cylinders. The actual flow patterns in the absorber are quite complex and the models in the literature do not do justice to the finer nuances of this flow. Surface tension and the resultant droplet formation plays a crucial role in the heat and mass transfer during absorption. The impact of the falling droplet on the tube causes waves and ripples on the solution film, which significantly influences the absorption process. The present model takes these factors into account and attempts to predict the heat and mass transfer based on a numerical simulation of the "actual" flow conditions.

The next chapter (Chapter 2) presents some of the prior work in this area and further elaborates on the need for the present work. Chapter 3 describes the numerical scheme used to model the absorption process. Chapter 4 presents computational

results. Chapter 5 concludes this report and highlights its salient points.

CHAPTER II

LITERATURE REVIEW

2.1 Overview

Heat and mass transfer in absorbers has been studied for a very long time. All the work can be broadly classified into three categories, viz. *Analytical work*, *Experimental work* and *Numerical work*.

Most of the early work in absorption heat and mass transfer was analytical in nature. These involve making simplifying assumptions about the flow and the absorption process and developing mathematical models to predict absorber performance. Very often these studies were done in conjunction with experiments to validate the predicted results.

Due to the dynamic and locally variable nature of the phenomenon, experimental study of the absorption phenomenon presents significant challenges. Experiments typically track the overall heat and mass transferred in the absorber, but fail to account for the local variations in the absorption process. Nevertheless, experiments conducted in conjunction with analytical or numerical work provide valuable insights into the absorption phenomenon. More recently, some experimental studies have included *flow visualization* using high-speed video images of the absorber flow. In addition to the overall heat and mass transfer, such visualization studies also offer some insights into the local variations in the flow in an absorber.

There have been very few numerical studies of the absorption phenomenon. This could be due to the fact that the interfacial heat and mass transfer phenomenon in absorption and the complex flow patterns present very serious numerical modeling challenges. Numerical studies allow for a very detailed study of the absorption

phenomenon at the local level. They also allow for investigation of a wide range of geometries and conditions at a relatively low additional cost. The overall results obtained using numerical methods need to be compared with experiments to ascertain their validity.

2.2 Common Assumptions

There are a few assumptions that are common to almost all of the absorption models in the literature. Before delving into the description of the models, it is instructive to review these assumptions. Additional assumptions, unique to a particular model, are included in the model description. Also, if a model does not make one these assumptions, it is stated in its description. The assumptions are:

- **Vapor Pressure Equilibrium**: The lithium bromide concentration at the interface is such that, the vapor pressure of water in the solution is always equal to the partial pressure of water vapor in the vapor phase.
- **Constant Thermophysical Properties**: In order to simplify the analysis, the properties of the lithium bromide solution and water vapor are usually assumed to be constant.
- **Negligible Streamwise Mass Diffusion and Thermal Conduction**: This assumption is made to simplify the governing equations and is usually a well justified assumption.
- **Negligible Transverse Velocity**: The velocity in the direction perpendicular to the flow and the direction of absorption is neglected.
- **Constant Film Thickness**: The absorption rates are much smaller than the amount of fluid present and hence this is a good assumption.

- **Constant Absorber Pressure**: The pressure in the absorber is assumed to be constant and uniform throughout the volume.

- **Negligible Heat Transfer to Vapor**: It is assumed that the heat of absorption is transferred to the lithium bromide solution in its entirety. This is usually a good assumption, as the liquid-side heat transfer coefficients are much higher than the vapor-side heat transfer coefficients.

2.3 Vapor Absorption on Vertical Walls

Absorption of vapor on a vertical wall was one of the first geometries to be studied and modeled. Inspite of its simplicity, it offers precious insights into the characteristics of the heat and mass transfer process. As a quick and easy approximation, the vertical wall models have been successfully applied to many complex geometries.

Nakoryakov and Grigor'eva [4–11] presented one of the earliest models of the absorption phenomenon on a smooth laminar lithium bromide film falling down an isothermal, impermeable plate. In addition to the common assumptions stated in the previous section, they assumed a uniform velocity across the laminar film. They also neglected the effects of surface tension at the liquid-vapor interface.

The authors provide a Fourier series solution for the concentration and temperature profiles in the lithium bromide solution film. Using these profiles, they derived expressions for the heat and mass transfer rates at the liquid-vapor interface and the heat transfer rate at the wall. They deduced that the heat and mass transfer process is governed by the following four non-dimensional parameters,

- *Lewis Number* $Le = D_{AB}/\alpha$

- *Prandtl Number* $Pr = \nu/\alpha$

- *Reynolds Number* $Re = 4u\delta/\nu$, where δ is the film thickness and

- The dimensionless group $h_a a/C_p$, where h_a is the heat of absorption and a is a dimensional constant

Nakoryakov and Grigor'eva [9] also developed a simpler model using a few further simplifying assumptions. They assumed a linear temperature profile in the lithium bromide solution film and derived the concentration profile based on a boundary layer approximation. Using these assumptions, they derived relations to calculate the temperatures, concentrations and heat and mass fluxes at the wall and the liquid-vapor interface.

A comparison of the simplified model with the Fourier series solution showed that the simpler expressions provides good approximations for the heat and mass transfer rates at points far downstream from the inlet [4]. However, close to the inlet, the absorption rates predicted by the simplified model were much lower than those predicted by the Fourier series solution. To rectify this, the authors developed a model specifically for the inlet region using slightly different assumptions [5, 8].

Kholpanov *et al.* [12] developed an absorption model that takes into account the effect of surface tension and tangential shear stress at the liquid-vapor interface. They developed relations for the concentration and temperature profiles and heat and mass fluxes in the lithium bromide solution film. They assume that the effect of heat and mass transfer at the liquid-vapor interface is restricted to a thin boundary layer close to the interface. Consequently, their model is not valid far downstream, where the boundary layer grows large enough to invalidate the thin layer assumption. They assumed that the velocity profile in the boundary layer is uniform even in the presence of surface tension and shear stress.

Grossman [13, 14] presented a solution for vapor absorption in a constant thickness film falling down a vertical wall. He solved the problem for both isothermal and adiabatic wall boundary conditions. He assumed a fully developed parabolic velocity

profile in the lithium bromide solution film. In the case of the isothermal wall boundary condition, he also assumed that the temperature of the lithium bromide solution is the same as that of the wall. As a result, there is no thermal boundary layer at the wall and the only thermal boundary layer is the one that develops at the liquid-vapor interface and grows inwards towards the wall. He also makes most of the common assumptions enlisted in the previous section.

Grossman presented a Fourier series solution to the heat and mass transfer problem. He demonstrated the calculation of the eigenvalues for both the adiabatic and isothermal wall cases. He also discussed the effect of the number of eigenvalues used on the stability and accuracy of the series solution. He found that a very high number of eigenvalues were required for the series solution to converge near the fluid inlet.

Grossman also presented a *Finite Difference Method* based numerical solution strategy. He encountered difficulties in obtaining a numerical solution near the inlet region due to a discontinuity caused by simultaneously assuming a uniform lithium bromide concentration at the inlet and a vapor pressure equilibrium concentration at the liquid-vapor interface. Hence, he developed a *Similarity Solution* for the inlet region, where the presence of the interface boundary layer is not felt at the wall. He proposed that this similarity solution be used for the inlet region, and the Fourier series solution or the numerical solution be used downstream [15].

Patnaik and Perez-Blanco [16, 17] presented a numerical model for the absorption process in falling films in the presence of roll waves. They assumed a parabolic velocity profile in the film. They also assumed the diffusion to be equimolar in the formulation of the energy balance at the liquid-vapor interface. Based on an image analysis of falling films, they selected a wave frequency of 13 Hz as the dominant frequency for their model. For cases in which prior smooth film-based studies predicted or measured Sherwood numbers between 30 and 80, with their wavy film model, they predicted Sherwood numbers on the order of 300. They attributed this enhancement to the

wave hydrodynamics. They contended that when the components of velocity normal and parallel to the interface were in phase, it led to a significant increase in the mass transfer in the film. Patnaik and Perez-Blanco [18–20] developed a design model for falling-film absorbers using various heat and mass transfer correlations from the literature. They assumed the thermophysical properties of the fluids to be constant, and evaluated them at the average bulk temperature and concentration. They also assumed a linear temperature profile in the solution film and that all the heat of absorption was transferred to the liquid phase. Based on their model they plotted various absorber performance characteristics as a function of the operating conditions.

Barrdahl [21,22] presented an analytical model for the mass transfer in isothermal falling films with periodic waves at high Schmidt numbers. He assumed the film thickness to be much smaller than the characteristic length of the wave. He deduced that the mass transfer process was characterized by the coefficient of mass diffusivity D_{AB}, the mean liquid film thickness δ_o, surface velocity of the liquid at the mean film thickness u_o, wave number ω, the Fourier components of the stream function ψ_α, non-dimensional wave velocity z, Reynolds number Re and the Schmidt number Sc. He found the mass transfer to be significantly higher in the presence of waves, as compared to mass transfer in a smooth falling film. Furthermore, he found the increase in the mass transfer due to the waves to be proportional to the dimensionless parameter $\alpha^2(\omega\delta_o)^{1/2}Re^{1/2}Sc^{1/2}(z+1)^{-3/2}$.

Kawae *et al.* [23] presented a finite difference model for a vertical film with a fully developed parabolic velocity profile and film thickness varying as a function of the absorbed vapor. They also included the effect of change in properties with changing temperature and concentration. They found that the variable properties have very little effect on the final results. They found a 5% difference in the total amount of vapor absorbed calculated using constant and variable properties. They also varied the operating conditions to study their effect on absorption. They found the effect

of absorber pressure, inlet concentration, wall temperature and Lewis number to be straightforward. However, they found that the effect of flow rate and inlet temperature depended on the flow length and that the trend actually reverses after a certain downstream distance.

Brauner *et al.* [24–26] developed a similarity solution for absorption in a vertical falling film near the inlet and a numerical solution for the downstream locations. In the numerical solution, they divided the flow domain into three regions, viz.

- Region of developing thermal and species boundary layers,
- Region in which the thermal boundary layer has reached the wall, but the species boundary layer is still developing and,
- Region in which both the thermal and species boundary layers are fully developed.

van der Wekken and Wassenaar [27] extended the vertical falling film model presented by Grossman [13] by substituting the isothermal and adiabatic walls with a vertical wall that is convectively cooled by a constant temperature cooling fluid. They varied the heat transfer coefficient between the wall and the cooling fluid and studied its effect on absorber performance. They presented the temperature and concentration variations for non-dimensional heat transfer coefficients of 0, 0.1, 1 and ∞. They also plotted the variation in the non-dimensional heat and mass transfer coefficients with parameters such as Lewis number, heat of absorption, and coolant temperature. They found that while the heat and mass transfer coefficients varied significantly with these parameters, the parameters themselves did not vary significantly along the film.

Habib and Wood [28] presented a numerical model that accounts for the momentum transfer that accompanies absorption and its effect on the fluid velocity profiles. They also accounted for pressure gradients in the absorber and interfacial shear between the two phases. They found that the absorption rate was highest just after the

inlet when the effect of the wall temperature is first transmitted to the interface. After the peak, they found that the absorption rates decreases exponentially downstream.

Yang and Wood [29] developed an absorption model for an isothermal vertical wall, in which the solution inlet temperature was not assumed to be equal to the wall temperature. This results in the development of two thermal boundary layers in the flow, one at the liquid-vapor interface and the other at the wall. They presented the variation of the interface and bulk temperatures and concentrations along the flow direction for various film Reynolds numbers. They compared the results from their model with previously conducted experimental work and found good agreement for all but the lowest Reynolds number cases.

Hajji and Worek [30, 31] extended the absorption model in a vertical wall to a *transient* case. They presented results for both an isothermal wall and a constant heat and mass flux wall boundary conditions. They solved the governing equations using Fourier series expansion methods and presented expressions for calculating the eigenvalues. They plotted results for different values of Lewis number and compared their results to experimental data. They found best agreement with experimental data for a Lewis number of 0.015. They also presented the temporal variation of concentration, temperature, and mass and heat fluxes. They suggested that their transient model could be used for steady state absorption calculations by substituting the variable x/u for time (where, x is the downstream distance and u is the velocity along the flow direction).

Ramadane *et al.* [32] introduced a wall-side coolant instead of an adiabatic or isothermal wall in their implicit finite difference model of a laminar falling film. They included the governing equations for the coolant-side heat transfer in their numerical model to accurately predict the coolant-side heat transfer coefficient. They also presented a model in which the coolant-side heat transfer coefficient was calculated using correlations from the literature. They plotted the temperature and concentration in

the film for various downstream positions. They also presented experimentally determined liquid-side interface heat transfer coefficient values for film Reynolds numbers between 15 and 70. The compared the results from their model with the experimental data and found the agreement to be satisfactory. However, they did not quantify the level of agreement or the errors between the two models.

Conlisk [33–38] used the *Laplace Transform* technique to develop a model for absorption in a laminar, vertical falling film, with film thickness varying with the amount of vapor absorbed. He solved the problem for an isothermal wall and with the wall temperature being a function of the downstream position. He systematically varied various problem parameters such as solution flow rate, wall temperature, flow length, etc., and presented the results of these variations. He plotted the temperature and absorption rates at various downstream locations for two different solution flow rates. He also compared his results with experimental data and found the experimentally measured absorption rates to be within $\pm 20\%$ of the values predicted by his model.

Ibrahim and Vinnicombe [39] developed a *hybrid model* that combines the analytical solution proposed by Nakoryakov and Grigor'eva [5, 8] for the inlet and regions close to the liquid-vapor interface, and a finite difference model for the rest of the solution domain. They claim that their model predicts the solution as accurately as the more complex models proposed by Grossman [13] and van der Wekken and Wassenaar [27], but requires less computational resources. They presented the mass transfer coefficients as a function of downstream position, and compared them with those obtained by Grossman [13] and van der Wekken and Wassenaar [27]. They found that except for slight discrepancies, their model agrees very well with the other two, but at a significantly lower computational expense.

Jernqvist and Kockum [40] presented an absorption model for a vertical laminar falling film without many of the simplifying assumptions assumed by the other authors. They used variable fluid properties, developing fluid velocity profiles and film

thickness varying with the amount of vapor absorbed. They presented the concentration profile and film thickness at many downstream locations. They compared their results with experimental data and found several differences between the two results. They concluded that the laminar theory cannot account for all the trends found in the experimental data.

2.4 Vapor Absorption over Horizontal Tubes

Andberg and Vliet [41–45] were among the first to model the heat and mass transfer phenomenon in films falling over horizontal tubes. They used a finite difference formulation, with a coordinate system fit to the shape of the film around the tube. Some of the major assumptions made by them were,

- All the heat and mass transfer occurs when the fluid is over the tube. When the fluid flows between two tubes, it *free-falls* as a *planar jet* and does not contribute to vapor absorption. For the modeled flow rates, though the flow was likely to be *drop-wise* in an actual system, the authors used the planar jet approximation so that they could model the flow as a two-dimensional problem.
- Uniform concentration and temperature profiles in the planar jet.
- In the transition region between the planar jet and the film, the flow is modeled using boundary layer approximations of the Navier Stokes equations. The fluid properties are assumed to be constant in this region.

In the rest of the flow domain, the fluid properties were calculated as functions of temperature and concentration.

The authors presented results for flow over a tube with an outer diameter of 19 mm. Solution inlet temperatures of 46, 39 and 32 °C were used and the tube was cooled with a coolant flowing inside at 30 °C. They reported results for the variations

in the local and bulk values of velocity, temperature and concentration in the fluid. They found that the flow patterns and the concentration profiles were very similar to the classical Nusselt solution. They also found that the overall absorption rate for an inlet temperature of 32℃ inlet temperature was about 80% greater than that for an inlet temperature of 46℃.

Andberg and Vliet [44] also proposed a simpler model to solve the same problem to a reasonable approximation. They used the classical *Nusselt solution* to model the flow and a similarity solution for the concentration profiles. The fluid properties were also assumed to be constant for this simpler model. They compared the results of this simple model with the more elaborate model described earlier, and found that it predicted the bulk concentration variation within an average error of 3% and a maximum error of 10.5%. They also compared their results with those for a commercially available absorber and found an agreement in the predicted bulk concentration change to within 6.6%.

Choudhury *et al.* [46] modeled the absorption heat and mass transfer in laminar films falling over horizontal tubes. The major differences between their model and the model by Andberg and Vliet [45] are that they assumed constant fluid properties and the tube to be isothermal. Also they do not use the boundary layer approximation used by Andberg and Vliet [45]. They too assumed the flow between the tubes to be in the form of free falling jets with no heat and mass transfer. They solved the problem using the finite difference method on a grid fitted around the fluid film on the horizontal tube. As they assumed that the fluid inlet concentration was at vapor pressure equilibrium, absorption in their model did not commence until the fluid had traversed some distance downstream. They also varied various flow parameters such as flow rate, tube diameter etc. and reported the effect of these variations on absorber performance. They found that an optimum absorption rate that depends on the tube diameter occurs at a low solution flow rate.

Lu *et al.* [47] presented a model for absorption in a laminar film over a horizontal tube, with a constant temperature coolant flowing on the inside. They assumed the fluid properties to be constant and used the Dittus-Boelter correlation [48] to calculate the coolant heat transfer coefficient. They also assumed the solution velocity at the top of the tube to be equal to the *free-fall* velocity. The temperature and concentration profiles at the inlet were assumed to be uniform. However, unlike Choudhury *et al.* [46], they did not assume the inlet concentration to be equal to the vapor pressure equilibrium concentration. The authors did not report results from their model. Instead, they presented experimental results for a smooth tube and two spirally grooved tubes, and used these results to empirically calculate two coefficients in their model. They found complete wetting to only occur for the grooved tubes at the highest flow rate corresponding to a Reynolds number of 36. They found the wetting in the smooth tubes to be as low as 40%.

Conlisk and Mao [49] modeled transient film-wise absorption over a horizontal tube. The assumed the tube to be initially coated uniformly with a thin film of the solution. With time, the fluid film around the tube falls due to gravity and also absorbs vapor along the way. They modeled the vapor as a binary mixture, so that the model may also be used for ammonia-water and consider the lithium bromide - water combination to be a special case of the general binary vapor model. They used the classical *Nusselt Solution* to model the fluid flow, but included the effect of change in the film thickness due to the absorption of vapor. They assumed the fluid properties to be constant throughout the flow. They also neglected the effect of surface tension. Similar to Conlisk [33,37] and Brauner *et al.* [24–26], they developed a similarity solution for absorption in which they divided the flow into three regimes based on the development of the thermal and species boundary layers. They presented the results of their calculations for various operating conditions. The found the rate of absorption to be higher at the top of the tube due to the thinning of the liquid film.

They however do add that the absorption at the top of the tube would be affected by droplet impact or jet impingement, which usually occurs at that location.

Min and Choi [50] performed a two-dimensional numerical analysis of the absorption of water vapor into a lithium bromide solution flowing over a horizontal tube. They assumed the flow to occur in the form of a film around the tube. The used a two-step procedure to solve the problem. First, they solved the continuity and momentum equations on an orthogonal grid over the entire domain, to obtain the velocity field and the liquid-vapor interface location. Then they solved the energy and species equations on a new non-orthogonal grid fitted only over the film region of the flow domain. They solved the governing equations using the *SIMPLER* algorithm with the *QUICK* scheme and the *Incomplete Cholesky Conjugate Gradient Method*. They found that contrary to common belief, for $Re < 40$, the stagnation film thickness increased with Reynolds number. They attributed this to the presence of recirculation in the region close to the stagnation point. They also found that this recirculation significantly affects the mass transfer at low flow rates.

Kirby and Perez-Blanco [51] conducted a segmental analysis on a horizontal tube water/lithium bromide absorber. They identified three distinct flow regimes for the flow of lithium bromide solution in the absorber: *falling film regime* around the coolant tube, *droplet formation regime* on the underside of the coolant tubes, and *droplet free fall regime* between the tubes. They predicted the performance of an absorber by calculating the heat and mass transfer separately for each of the flow regimes, using correlations in the literature. The *residence times* of each of the flow regimes was taken into account in the heat and mass transfer calculations. They observed that most of the mass transfer occurred in the drop formation regime, while most of the heat transfer occurred in the falling film regime.

Sultana *et al.* [52] and Wijeysundera *et al.* [53] developed a simple model for the design of horizontal tube absorbers with a counter-flowing coolant. The heat

and mass transfer coefficients required in the model are calculated separately using a numerical model. The model includes the effect of flow between the tubes in the both the *droplet* and *jet/sheet* modes. The local heat and mass transfer coefficients, film thickness, geometry, wetting ratio and some of the exponents in the model were varied and their effects studied. When spatially varying heat and mass transfer coefficients were used, there was found to be good agreement with experimental data. When average heat and mass transfer coefficients calculated from the numerical simulation were used, there was found to be some difference between the observed and predicted temperature and concentration profiles.

Jeong and Garimella [54] developed a flow mechanism-based model for the absorption of water vapor into a lithium bromide solution flowing over a bank of tubes. They analytically solved the two-dimensional governing equations using a differential algebraic solver. They including the effect of incomplete wetting of the tubes by introducing a *wetting ratio* in their model. They found that the wetting ratio played an important role in determining the efficiency of the absorption process. They deduced that the vapor absorption occurred primarily in the film and droplet-formation region of the flow and that the absorption was negligible in the droplets between the tubes. Jeong and Garimella [55] also analyzed the performance of lithium bromide absorbers for different tube diameters, spacing and pass arrangements. They found that smaller diameters provided a significantly better absorber performance than larger diameters.

2.5 Characteristics of Fluid Flow in an Absorber

Killion and Garimella [56–60] studied the actual flow in horizontal tube absorbers in great detail. They used high-speed image visualization in combination with a piecewise spline-fit based edge detection and quantification algorithm to track and study flow of lithium bromide solution. They found that a number of assumptions about

the flow, made in prior absorption models were too simplistic and not in touch with the characteristics of the actual flow. Some of their major observations about the flow are described below.

2.5.1 Droplet formation, detachment and fall

Though most of the prior work in the literature assumed the flow between tubes to be a uniform film, the actual flow is in the form of droplets. Surface tension plays a crucial role in the mechanics of drop formation. As the amount of fluid around the tube increases, instabilities in the film cause the fluid to accumulate around a point on the film. Gravity works against surface tension and tries to increase the drop-size by accumulating more fluid around the point. Eventually, the drop grows big enough to be able to completely overcome the surface tension in the film and detach from the film. As the droplet falls, it tries to take a spherical shape, to minimize the surface tension in the droplet. Immediately after the droplet detaches, the part of the fluid bridge still in contact with the film, is pulled back quickly towards it by the surface tension force. This quick withdrawal of the fluid bridge sometimes causes the generation of a few small *satellite droplets*.

The authors calculated and plotted the variation of surface area and volume in the process of droplet formation, detachment and fall. They suggested that the varying surface areas and velocity fields during the process will have a strong impact on the heat and mass transfer phenomenon that occurs during absorption.

2.5.2 Film waviness

The authors observed that when a droplet falls on a tube, its impact causes waves on the solution film. Similarly, as a droplet detaches from a film, it causes oscillations in the remaining fluid bridge attached to the film, which in turn causes ripples or waves

in the solution film. These waves propagate at high velocities along the axis of the tube. They mentioned that these waves significantly alter the shape of the solution film and the velocity field in it. As a result, they are likely to play an important role in determining the heat and mass transfer characteristics of the film.

Also, the waves formed due to one droplet interact with other waves formed due to neighboring droplets. The nature of these interactions depend of the *phase difference* between the neighboring droplets. These interactions would also affect the heat and mass transfer in the film.

Killion and Garimella [61] also presented a computational model of the behavior of falling films and droplets in horizontal tube banks. The model accounted for the details of droplet formation, impact and film waviness. The authors modeled one 15.9 mm diameter tube with an inter-tube spacing of 15.9 mm. They used a periodic boundary condition at the ends and a symmetry condition at the center of the tube, to minimize the size of the grid. They calculated the surface area and volume of the droplet and compared it with the results from their visualization studies. The initial droplet formation seemed to take a little longer in the computations than that in the experiments. Consequently, there was some discrepancy between the experiments and computations in the calculated values of surface area and volume. This difference was due to the initial quiescent film approximation used in the computations. In the experiments, instead of being at rest, the fluid already possesses some momentum due to the fall from the previous tube in the column. After the initial stages, the flow behavior and the values of the surface area and volume showed a good level of agreement with the visualization data.

2.6 Need for Present Work

The previous sections first reviewed some of the major absorption models for the vertical falling film. Nakoryakov and Grigor'eva [4–11] presented one of the earliest absorption models for smooth laminar films falling over a vertical wall. They provided a Fourier series solution for concentration and temperature profiles. They made a number of simplifying assumptions such as, steady flow, constant film thickness, negligible transverse velocity and mass and thermal transport, and negligible heat transfer to the vapor. Kholpanov *et al.* [12] included the effect of surface tension and tangential shear stress at the interface and developed relations for concentration and temperature profiles and heat and mass fluxes in the film. Grossman [13, 14] improved on the previous models by assuming a fully developed parabolic velocity profile instead of uniform velocity in the film. He presented a Fourier series solution and demonstrated calculation of eigenvalues. Barrdahl [21, 22] presented a mathematical model for mass transfer in isothermal falling films with periodic waves at high Schmidt numbers. He demonstrated the significant increase in mass transfer due to the waves. van der Wekken and Wassenaar [27] extended the vertical falling film model presented by Grossman [13] by using a convectively cooled wall with a constant temperature cooling fluid. He also varied the coolant heat transfer coefficient and studied its effects. Brauner *et al.* [24–26] divided the flow into three distinct regions and proposed different solutions for the three regions. They developed a similarity solution for film near the inlet and a numerical solution for downstream locations. Kawae *et al.* [23] presented a finite difference model for vertical film with parabolic velocity profile and film thickness varying as a function of the absorbed vapor. They also included the effect of the change in properties with changing temperature and concentration. Habib and Wood [28] improved upon the prior models by accounting for the momentum transfer that accompanies absorption. They also considered pressure gradients and interfacial shear. Hajji and Worek [30, 31] extended the vertical wall

absorption model to a transient case. They used Fourier series expansion methods to solve the governing equations. Yang and Wood [29] improved upon prior steady state models by removing the assumption that the inlet temperature was equal to the wall temperature. This resulted in the development of two boundary layers on the film. Ramadane *et al.* [32] presented an implicit finite difference model, which included governing equations for coolant side heat transfer. Conlisk [33–38] improved on prior work by accounting for the variation in the thickness of the film with absorption of vapor. He used the Laplace transform technique to solve the problem. Ibrahim and Vinnicombe [39] proposed a hybrid model that used the model by Nakoryakov and Grigor'eva [5, 8] for the inlet and interface regions, and a finite difference model for rest of the domain. They claimed that their model used less computational resources without any significant loss in accuracy. Patnaik and Perez-Blanco [16, 17] presented one of the first absorption models that dealt with absorption in the presence of waves. They selected a dominant wave frequency of 13 Hz based on image analysis. They found a significant increase in the mass transfer due to the waves. Jernqvist and Kockum [40] presented a model for vertical films without many of the simplifying assumptions in prior work. They used variable fluid properties, developing velocity profiles and film thickness varying with vapor absorption.

In the previous sections, a number of models for absorption on horizontal tubes were also discussed. Andberg and Vliet [41–45] presented one of the pioneering models for absorption over horizontal tubes. They assumed that all heat and mass transfer occurs in the fluid over the tube and that between tubes, the fluid freely falls as a jet with no absorption. Choudhury *et al.* [46] simplified the model of Andberg and Vliet [41–45] by assuming constant fluid properties and an isothermal tube. Kirby and Perez-Blanco [51] separated the flow over a horizontal tube into three flow regimes: falling film, droplet formation and droplet fall. They used separate correlations from the literature for all three regimes and conducted a segmental analysis of the problem.

They found that most of the mass transfer occurred in the droplet formation regime, while most of the heat transfer occurred in the falling film regime. Lu *et al.* [47] presented a model for absorption in a laminar film over a horizontal tube with uniform concentration and temperature profiles at the inlet. Conlisk and Mao [49] modeled transient film-wise absorption, with the vapor as a binary mixture. Hence their model could be used for both $NH_3 - H_2O$ and $H_2O - LiBr$. They assumed the tube to be initially coated with a uniform film. Min and Choi [50] presented a two dimensional computational model, assuming the flow to occur as a film around the tube. They used a two step procedure: an orthogonal grid to solve continuity and momentum equations over the entire domain, and a non-orthogonal grid fitted over the liquid film to solve the energy and species equations. Jeong and Garimella [54] developed a flow mechanism-based absorption model, including the effect of incomplete wetting. They found that vapor absorption primarily occurred in the film and droplet formation regions, and was negligible in the droplets between the tube. Sultana *et al.* [52] and Wijeysundera *et al.* [53] developed a model that included the effect of flow between the tubes in both droplet and jet modes. They used correlations from the literature to calculate heat and mass transfer coefficients required for their model.

Killion and Garimella [56–60] used high-speed flow visualization to study the actual flow that occurs in an absorber. They used a piece-wise spline-fit based edge detection technique to quantify their results. They found that assumptions about the flow made in earlier models were simplistic. Droplet formation, detachment and fall significantly affects the velocity fields and hence heat and mass transfer. Impact of the droplet creates waves on the film that propagate axially along the tube. They suggested that these complex flow patterns would have a profound impact of the absorption phenomenon.

It is seen that though the actual flow patterns in the absorber are quite complex, the absorption models in the literature make simplifying assumptions about the flow.

The effect on heat and mass transfer of the finer details of the flow such as droplet formation and fall and film waviness are ignored in the literature. The present work attempts to bridge this gap, by modeling the heat and mass transfer during absorption taking the complex flow patterns into consideration. The flow, including the droplet and film waviness, along with the heat and mass transfer phenomenon are numerically modeled. The effect of the finer details of the flow field on the absorption process are studied in detail. This would lead to a better understanding of the heat and mass transfer process in the absorber and aid better absorber design. Since the absorber has the greatest impact on the absorption system performance, the present work would also help in the design of more efficient absorption systems, which in turn would result in energy and capital cost savings.

Table 2.1: Vapor absorption on vertical walls

Author	**Type of work**	**Working fluid**	**Details**	**Major findings**
Nakoryakov and Grigor'eva [4–11]	Analytical	Water–Lithium bromide	One of the earliest absorption models for smooth laminar film falling over a vertical wall. Provided a Fourier series solution for concentration and temperature profiles.	Found that heat and mass transfer is governed by 4 dimensionless parameters: Le, Pr, Re and $h_a a/C_p$
Kholpanov *et al.* [12]	Analytical	Water–Lithium bromide	Developed an absorption model that takes surface tension and tangential shear stress at the interface into account. Assumed that heat and mass transfer is restricted to a thin boundary layer close to the interface	Developed relations for concentration and temperature profiles and heat and mass fluxes in the film. Their solution is not valid far downstream as the thin boundary layer assumption does not hold.
Grossman [13, 14]	Analytical, Numerical	Water–Lithium bromide	Assumed a fully developed parabolic velocity profile instead of uniform velocity in the film. Solved the problem for both isothermal and adiabatic wall conditions. Presented a Fourier series solution and demonstrated calculation of eigenvalues. Also developed a finite difference method based numerical solution strategy.	Found that a very high number of eigenvalues were required for the Fourier series solution to converge at fluid inlet. Encountered convergence difficulties with the numerical solution at inlet region. Proposed an alternate similarity solution for the inlet region.

Table 2.1: Vapor absorption on vertical walls

Author	**Type of work**	**Working fluid**	**Details**	**Major findings**
Barrdahl [21, 22]	Analytical	None specifically considered	Presented a model for mass transfer in isothermal falling films with periodic waves at high Schmidt numbers. Assumed film thickness to be much smaller than characteristic length of wave.	Found mass transfer to be significantly higher in the presence of waves. Increase in mass transfer proportional to $\alpha^2(\omega\delta_o)^{1/2}Re^{1/2}Sc^{1/2}(z+1)^{-3/2}$.
van der Wekken and Wassenaar [27]	Analytical	Water–Lithium bromide	Extended the vertical falling film model presented by Grossman [13] by using a convectively cooled wall with a constant temperature cooling fluid. Varied the coolant heat transfer coefficient and studied its effects.	Presented temperature and concentration variation for non-dimensional heat transfer coefficients of 0, 0.1, 1 and ∞. Plotted variation of heat and mass transfer coefficients with Le, heat of absorption and coolant temperature.
Brauner *et al.* [24–26]	Analytical	Water–Lithium bromide	Developed a similarity solution for film near the inlet and numerical solution for downstream locations. Did not assume infinite dilution of the solution film. Divided the flow into 3 distinct regions for the numerical solution	Found that film temperature, concentration and heat and mass fluxes vary significantly when the infinite dilution assumption is removed. The heat transfer coefficient is not significantly affected by infinite dilution assumption.

Table 2.1: Vapor absorption on vertical walls

Author	**Type of work**	**Working fluid**	**Details**	**Major findings**
Kawae *et al.* [23]	Numerical	Water–Lithium bromide	Presented a finite difference model for vertical film with parabolic velocity profile and film thickness varying as a function of the absorbed vapor. Included effect of the change in properties with changing temperature and concentration.	Found that the variable properties only affected the amount of vapor absorbed by about 5%. Also found that the effect of flow rate and inlet temperature reverses its trend after a certain distance downstream.
Habib and Wood [28]	Numerical	Water–Lithium bromide	Accounted for the momentum transfer that accompanies absorption. Also considered pressure gradients and interfacial shear.	Found that the absorption rate was highest just after the inlet when the effect of wall temperature reaches the interface. After the peak, absorption rate decreases exponentially downstream.
Hajji and Worek [30, 31]	Analytical, Experimental	Water–Lithium bromide	Extended the vertical wall absorption model to a transient case. Used Fourier series expansion methods to solve the governing equations.	Found best agreement with experimental data for $Le = 0.015$. Presented temporal variations of concentration, temperature and heat and mass fluxes.
Yang and Wood [29]	Analytical	Water–Lithium bromide	Did not assume the inlet temperature to be equal to the wall temperature. Results in the development of two boundary layers on the film.	Compared their results with experimental data and found good agreement for all but the lowest Re cases.

Table 2.1: Vapor absorption on vertical walls

Author	Type of work	Working fluid	Details	Major findings
Ramadane *et al.* [32]	Numerical, Experimetal	Water-Lithium bromide	Implicit finite difference model, which included governing equations for coolant side heat transfer. Presented experimentally determined liquid-side heat transfer coefficients for Re between 15 and 70.	Compared results from their model with experimental results and found a good degree of agreement.
Conlisk [33–38]	Analytical, Experimental	Water–Lithium bromide	Used Laplace transform technique for falling film with thickness varying with amount of vapor absorbed. Wall temperature was a function of downstream position.	Plotted temperature and absorption rates for downstream locations. ±20% agreement with experimental results.
Ibrahim and Vinnicombe [39]	Analytical, Numerical	Water–Lithium bromide	Hybrid model that combined model by Nakoryakov and Grigor'eva [5,8] for inlet and interface regions, and finite difference model for rest of the domain. Claim that their model uses less computational resources without any significant loss in accuracy.	Presented mass transfer coefficients as function of downstream position. Results agree with more complex models by Grossman [13] and van der Wekken and Wassenaar [27].
Patnaik and Perez-Blanco [16, 17]	Analytical, Numerical	Water–Lithium bromide	Numerical model for falling film in the presence of roll waves. Selected a wave frequency of 13 Hz based on image analysis. Also developed an absorber design model using heat and mass transfer correlations from literature	Obtained a Sh between 30 and 80 for smooth film, while Sh for wavy film was about 300. Attributed enhancement to wave hydrodynamics.

Table 2.1: Vapor absorption on vertical walls

Author	**Type of work**	**Working fluid**	**Details**	**Major findings**
Jernqvist and Kockum [40]	Analytical	Water–Lithium bromide	Model for vertical film without many of the simplifying assumptions in prior work. Variable fluid properties, developing velocity profiles and film thickness varying with vapor absorption.	Presented concentration and temperature profiles. Found several discrepancies between model results and experimental data. Concluded that laminar theory does not completely account for all trends in the phenomenon.

Table 2.2: Vapor absorption on horizontal tubes

Author	**Type of work**	**Working fluid**	**Details**	**Major findings**
Andberg and Vliet [41–45]	Analytical, Numerical	Water–Lithium bromide	Pioneering work in absorption modeling over horizontal tubes. Assumed all heat and mass transfer occurs in the fluid over the tube. Between tubes, the fluid freely falls as a jet with no absorption. Also proposed a simpler model based on the classical Nusselt solution for the flow and a similarity solution for the concentration profiles.	Found that the absorption rate for an inlet temperature of 32 °C was 80% greater than that for an inlet temperature of 46 °C. Also found that their two models differed in predicted value of bulk concentration change by a maximum of 10.5%. Compared results with a commercial absorber and found that their model predicted the bulk concentration change within 6.6%.
Choudhury *et al.* [46]	Numerical	Water–Lithium bromide	Finite difference model. Assumed constant fluid properties and isothermal tube. Neglected absorption when the fluid is between the tubes.	Found that optimum absorption rate depends on tube diameter and occurs at a low solution flow rate. Reported effect of variations of flow rate, tube diameter and other parameters.
Kirby and Perez-Blanco [51]	Analytical	Water–Lithium bromide	Conducted a segmental analysis. Identified three flow regimes: falling film, droplet formation and droplet fall. Used separate correlation from literature for all three regimes.	Found that most of the mass transfer occurred in the droplet formation regime, while most of the heat transfer occurred in the falling film regime.

Table 2.2: Vapor absorption on horizontal tubes

Author	**Type of work**	**Working fluid**	**Details**	**Major findings**
Lu *et al.* [47]	Analytical, Experimental	Water–Lithium bromide	Presented model for absorption in a laminar film over a horizontal tube with constant temperature coolant flowing on the inside. Assumed uniform concentration and temperature profiles at the inlet. Presented experimental results for a smooth tube and two spirally grooved tubes.	Used the experimental results to empirically calculate two coefficients in the model. Observed complete wetting only for the grooved tubes at the highest Re of 36. Found wetting as low as 40% in the smooth tubes.
Conlisk and Mao [49]	Analytical	Ammonia–Water, Water–Lithium bromide	Modeled transient film-wise absorption. Assumed the tube to be initially coated with a uniform film. Modeled vapor as a binary mixture, so the model may be used for both $NH_3 - H_2O$ and $H_2O - LiBr$. Used the classical Nusselt solution to model fluid flow, but accounted for change in film thickness due to absorption. Neglected the effect of surface tension.	Found the rate of absorption to be highest at the top of the tube, due to thinning of the liquid film. In a real case absorption at the top of the tube would be more affected by droplet impact or jet impingement.

Table 2.2: Vapor absorption on horizontal tubes

Author	**Type of work**	**Working fluid**	**Details**	**Major findings**
Min and Choi [50]	Numerical	Water–Lithium bromide	Two dimensional numerical model for absorption over horizontal tube. Assumed flow to occur as a film around the tube. Two step procedure: used an orthogonal grid to solve continuity and momentum equations over the entire domain. Then solved energy and species equation over a non-orthogonal grid fitted over the liquid film.	Found that for $Re < 40$, the stagnation film thickness increases with Reynolds number. Fluid recirculation affects mass transfer at low flow rates.
Jeong and Garimella [54]	Analytical	Water–Lithium bromide	Developed a flow mechanism-based model. Included effect of incomplete wetting.	Found that wetting ratio significantly affected performance. Deduced that vapor absorption primarily occurs in the film and droplet formation regions, and is negligible in the droplets between the tube.

Table 2.2: Vapor absorption on horizontal tubes

Author	**Type of work**	**Working fluid**	**Details**	**Major findings**
Killion and Garimella [56–60]	Experimental	Water–Lithium bromide	Used high-speed visualization to study the actual flow that occurs in an absorber. Used a piece-wise spline-fit based edge detection technique to quantify their results.	Found that assumptions about the flow made in earlier models were simplistic. Droplet formation, detachment and fall significantly affects the velocity fields and hence heat and mass transfer. Impact of the droplet creates waves on the film that propagate axially along the tube. They suggested that these complex flow patterns would have a profound impact on the absorption phenomenon.
Sultana *et al.* [52] and Wijeysundera *et al.* [53]	Analytical	Water–Lithium bromide	Developed a two-part model for design of horizontal tube absorbers with counter-flowing coolant. The heat and mass transfer coefficients were calculated independently using a numerical model. These heat and mass transfer coefficients were used as inputs in an analytical model for absorber design. Includes effect of flow between the tubes in both droplet and jet modes.	Results were compared with experimental data and there was found to be some discrepancy when the heat and mass transfer coefficients from the numerical model were used. Alternately, variable heat and mass transfer coefficients were used with the model, to produce results that agreed better with experimental data.

CHAPTER III

NUMERICAL MODELING

3.1 Challenges in Numerical Modeling

As described in the previous chapter, the flow patterns in a horizontal tube absorber are quite complex. The objective of the numerical model is to model these complex flows and determine their effects on absorption heat and mass transfer. Some of the main features of the model are described below.

3.1.1 Fluid Flow

The fluid flow is primarily governed by the *gravity* and *surface tension* forces. Droplet formation, growth and detachment are determined by a balance between these two forces. Of these, surface tension presents the bigger challenge in modeling due to its discontinuous nature. The effect of surface tension is only felt at the lithium bromide solution - water vapor interface, in the form of a local pressure jump. This discontinuity presents a big hurdle in the development of a stable and accurate numerical model.

3.1.2 Mass Transfer

As it falls over the bank of tubes, the lithium bromide solution absorbs water vapor, causing a decrease in its concentration. This mass transfer process is driven by the equilibrium condition at the solution-vapor interface. The *vapor pressure equilibrium assumption* that has been widely used in the literature, will be used here to determine the solution-vapor interface concentration. According to this assumption, the concentration at the interface instantaneously reaches a value such that, the vapor

pressure of the water in the solution is equal to the pressure of the water vapor surrounding the solution. The difference between this equilibrium concentration and the bulk concentration of the lithium bromide solution acts as the driving potential for the mass transfer.

The correlation by Yuan and Herold [62] is used to calculate the equilibrium concentration. This equilibrium concentration is a function of the temperature and pressure of water vapor and the lithium bromide solution.

3.1.3 Heat Transfer

In the horizontal tube absorber, there are two opposing driving forces for heat transfer. The absorption of water vapor is exothermic and causes a heating of the lithium bromide solution. This heat of absorption depends on the amount of water vapor absorbed and the heat of evaporation of water vapor.

To compensate for the heating due to absorption, and maintain the driving potential for mass transfer, the solution is cooled by passing a coolant through the inside of the horizontal tubes.

3.2 Prior computational models

Killion and Garimella [61] developed a computational model to simulate the flow patterns in a horizontal tube absorber. They found good agreement between the flow patterns simulated by their model and those observed in an actual horizontal tube absorber. The present study borrows some of the aspects of their fluid flow model and extends their work by including the governing heat and mass transfer equations in the model. At this point, it is instructive to recount the salient features of the fluid flow model by Killion and Garimella [61], which lays the groundwork for the present model described in the latter sections.

Killion and Garimella [56–60] first used high-speed flow visualization to study the actual flow patterns in an absorber. They observed that the flow happens in the form of droplets and the formation and fall of these droplets and the resulting film waviness lead to significant local variations in the flow velocities and film thicknesses. They then strived to recreate these flow patterns with a computational model. They chose the commercial CFD package Fluent [63] for their work as it inherently provided all the algorithms required for their work. Fluent also provided the ability to combine the package's algorithms with user-written programs to model problems beyond its inherent abilities. This was done to enable extensions of their model to include heat and mass transfer in the future.

Killion and Garimella [61] assumed the flow to be incompressible, Newtonian and laminar throughout the solution domain due to the low film Reynolds numbers (< 500). They argued that though droplet bifurcation and impact can lead to locally high velocities, they do not generate turbulence in a manner that requires special modeling. They considered both an approximate axisymmetric (2D case, column of spheres) formulation as well as a Cartesian (3D case, horizontal tube bank). They used the VOF technique, first proposed by Hirt and Nichols [64] to model the two-phase flow. They used a finite-volume method to translate the coupled, partial differential equations into algebraic expressions. They integrated the governing continuity and momentum equations over each computational cell and discretized them using a second-order upwind scheme. They linearized the discretized equations and solved them in a segregated, 1st-order implicit manner. They solved the linear system of simultaneous equations for each cell in the domain using a Gauss-Siedel equation solver in combination with an algebraic multi-grid (AMG) method. The algebraic multi-grid method generated coarse level equations using a Galerkin method without actually performing any re-discretization.

Killion and Garimella [61] used pressure correction iteratively, when necessary,

to achieve convergence. They used the Pressure Implicit with Splitting of Operators (PISO) method [65] to relate the solution of the continuity equation to the pressure correction. They used a piecewise-linear-scheme for unstructured grids proposed by Youngs [66] for interface reconstruction. They used a method proposed by Brackbill *et al.* [67] to model the surface tension force. The method converted the pressure rise across the interface due to surface tension into a source term in the momentum equations. In the solution of the momentum equations, Killion and Garimella [61] treated the surface tension source term like a body force similar to gravity. They also used a wall contact angle to adjust the surface normal in the cells near the wall. In most cases, they used a 0° contact angle at the walls, to ensure complete wetting. They implemented the model on fixed quadrilateral (2D) and hexahedral (3D) grids, which were generated using the commercial package Gambit [63].

The present study builds upon the strategies suggested by Killion and Garimella [61] for the solution of the momentum equations. The novelty of the present work is in the extension of their model to include heat and mass transfer. The complex flow patterns associated with droplet formation and fall and film waviness significantly affect the local heat and mass transfer coefficients and temperature and concentration profiles. The study of these variations, and conception of absorber design strategies based on an understanding of the local heat and mass transfer phenomena, is the focus of this study.

3.3 Problem Description

The present chapter discusses the details of the numerical model to be used to model the three dimensional heat and mass transfer phenomenon in the absorption of vapor in a falling film of lithium bromide over a bank of horizontal tubes. In addition, due

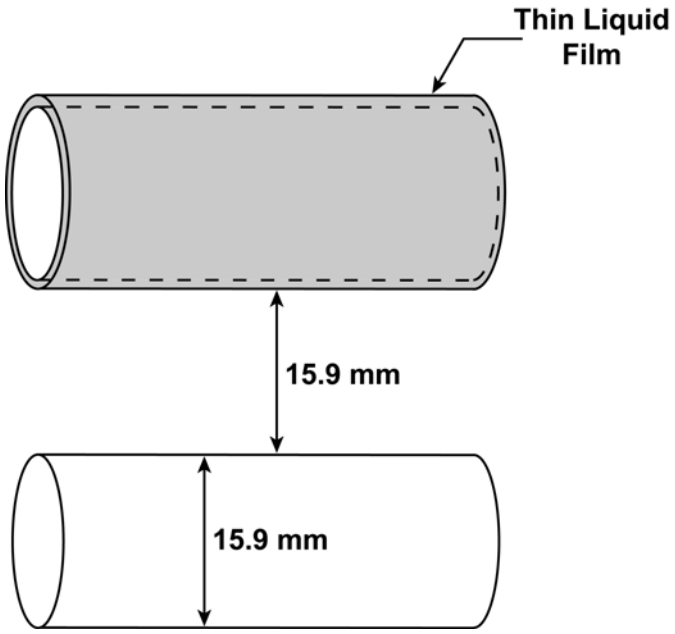

Figure 3.1: Flow geometry of a drop falling around a column of horizontal tubes

to the computational intensity of the three dimensional model, a simpler two dimensional geometry was also used to study the effect of changes in the various operating conditions on absorption.

3.3.1 Column of tubes

The flow conditions for a column of tubes are illustrated in Figure 3.1. The flow geometry consists of a repeated series of tubes with an outer diameter of 15.9 mm placed one above the other, with each tube 15.9 mm apart from the next. In the computational model, this was simulated by modeling a single tube with periodic boundary conditions at both ends. The periodic boundary condition means that all of the fluid that exits the solution domain at the bottom returns from the top with the same conditions. Initially, a very thin film of lithium bromide-water solution is deposited on the tube. This film forms a droplet and then transverses through the column of tubes.

The grid used in the computations is shown in Figure 3.2. Only half the circumference of the tube is modeled and the flow in the other half is assumed to be symmetrical. The grid consists of 1,185,870 hexahedral cells, with a minimum cell size of 0.1 mm.

3.3.2 Column of spheres

The three dimensional geometry presented earlier replicated the actual absorber geometry fairly accurately. However due to the large number of grid cells, it takes a of computational resources and time to solve the model. Hence a simpler two dimensional model was developed for some of the computations. For the two dimensional model, a column of axisymmetric spheres, which present the closest two dimensional approximation to the original geometry, was modeled.

The flow conditions for a column of spheres are illustrated in Figure 3.3. The flow geometry consists of a repeated series of spheres with an outer diameter of 15.9 mm placed one above the other, with each sphere being 15.9 mm apart from the next. In the computational model, this was simulated by modeling a single sphere with periodic boundary conditions at both ends. Initially, a very thin film of lithium bromide- water solution is deposited on the sphere. This film forms a droplet and then transverses through the column of spheres.

The grid used in the two-dimensional computations is shown in Figure 3.4. Only half the circumference of the sphere is modeled and the flow in the other half is assumed to be symmetrical. The grid consists of 19,740 quadrilateral cells, with a minimum cell size of 0.08 mm.

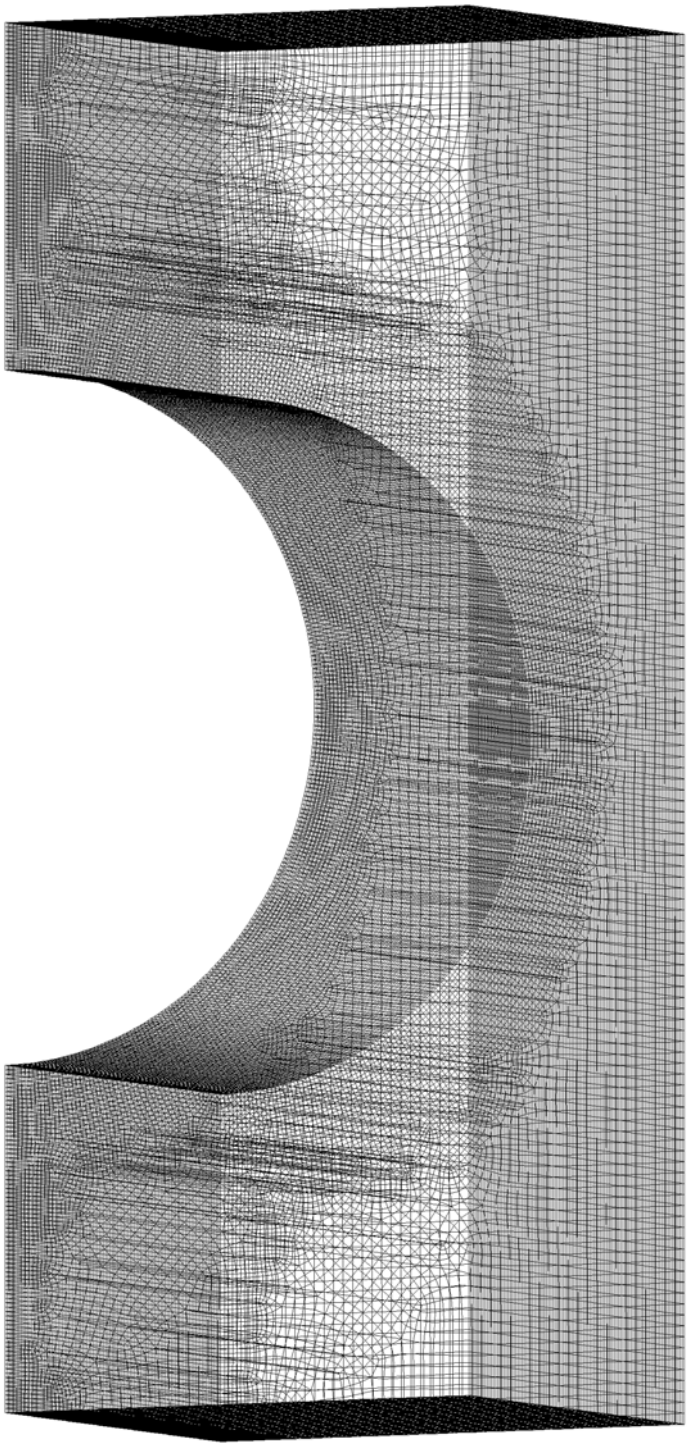

Figure 3.2: Three dimensional grid of a tube

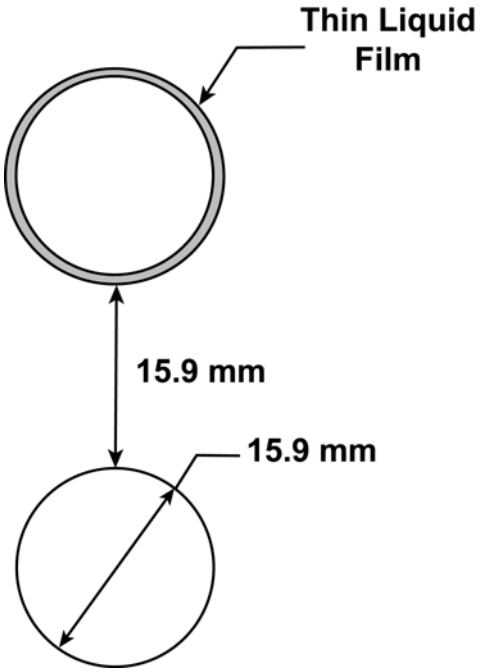

Figure 3.3: Flow geometry of a drop falling through a column of spheres

3.3.3 Heat and mass transfer considerations

For both the flow geometries, the incoming pressure, temperature and concentrations were set based on typical absorber operating conditions. The operating pressure was set at 1 kPa, which corresponds to a water saturation temperature of 7℃. The inlet lithium bromide-water solution temperature was set at 40.5℃ and the inlet concentration was set at 65% by weight of lithium bromide. This temperature, pressure and concentration corresponds to a 17℃ subcooling of the lithium bromide solution. The solution is surrounded by saturated water vapor at 1 kPa. As the lithium bromide solution flows, it absorbs water vapor into the solution, thus reducing its concentration. This absorption process is exothermic, causing a generation of heat, most of which is absorbed by the lithium bromide solution, causing a rise in its temperature. The computational aspects of this heat and mass transfer and its boundary conditions are discussed in the subsequent sections.

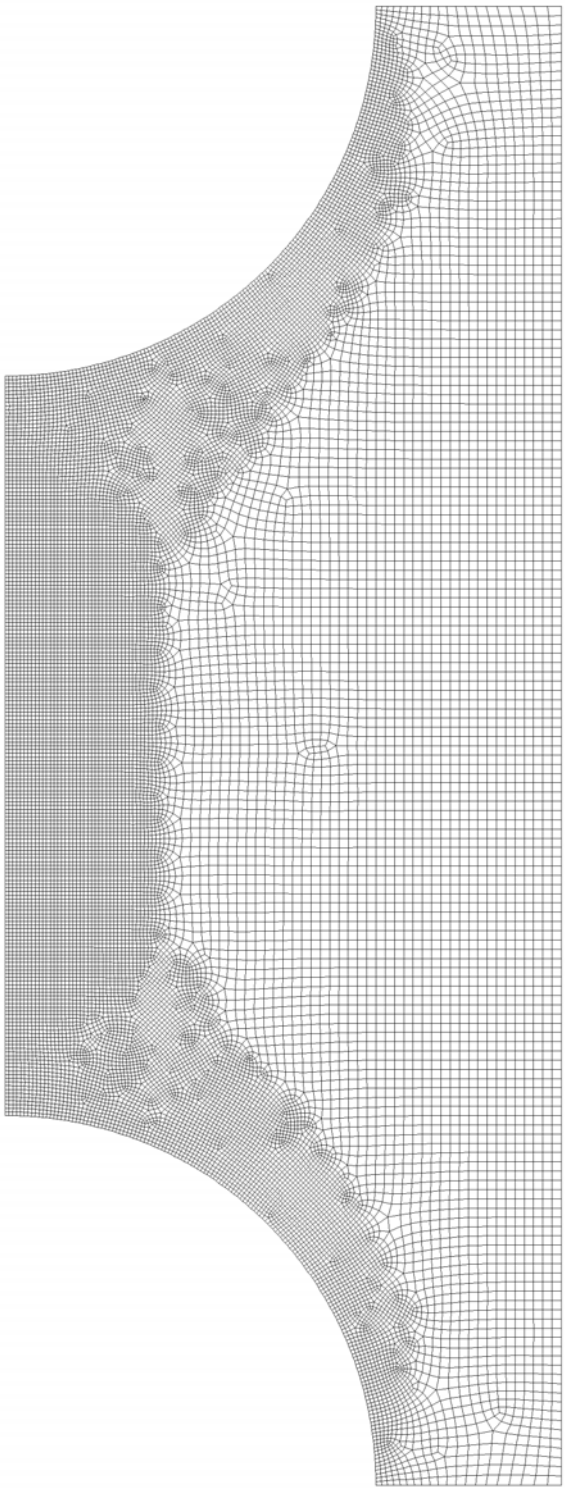

Figure 3.4: Two dimensional grid of a column of spheres

3.4 Governing Equations

The flow is governed by the Navier-Stokes equations. The continuity equation is given by,

$$\frac{\partial \rho}{\partial t} + \nabla \cdot (\rho \vec{v}) = 0 \tag{3.1}$$

The momentum equation is given by,

$$\frac{\partial}{\partial t}(\rho \vec{v}) + \nabla \cdot (\rho \vec{v}\vec{v}) = -\nabla p + \nabla \cdot (\bar{\bar{\tau}}) + \rho \vec{g} + \vec{F} \tag{3.2}$$

where, is the stress tensor $\bar{\bar{\tau}}$ given by,

$$\bar{\bar{\tau}} = \mu \left[(\nabla \vec{v} + \nabla \vec{v}^T) - \frac{2}{3} \nabla \cdot \vec{v} \bar{\bar{I}} \right] \tag{3.3}$$

where $\bar{\bar{I}}$ is a unit tensor.

The energy equation is given by,

$$\frac{\partial}{\partial t}(\rho E) + \nabla \cdot [\vec{v}(\rho E + p)] = \nabla \cdot \left[k_{eff} \nabla T - \sum_j h_j \vec{J}_j \right] + \mu \Phi + q_{gen} \tag{3.4}$$

where, $\mu\Phi$ is the thermal energy due to viscous dissipation, and is given by,

$$\mu \Phi = \mu \left\{ \left(\frac{\partial u}{\partial y} + \frac{\partial v}{\partial x} \right)^2 + 2 \left[\left(\frac{\partial u}{\partial x} \right)^2 + \left(\frac{\partial v}{\partial y} \right)^2 \right] \right\} \tag{3.5}$$

and the species transfer equation is given by,

$$\frac{\partial}{\partial t}(\rho Y_i) + \nabla \cdot (\rho \vec{v} Y_i) = -\nabla \cdot \vec{J}_i + Y_{i,gen} \tag{3.6}$$

where $\vec{J}_i$ is the mass flux, given by,

$$\vec{J}_i = -\rho D_{AB} \vec{\nabla} Y_i \tag{3.7}$$

3.5 The Numerical Algorithm

The segregated solver [68] was used to solve the governing equations. The algorithm used by the segregated solver is illustrated in Figure 3.5. As seen from the figure, the governing equations are solved one after the other in a segregated manner. Usually, several iterations of the solution loop are required for convergence to be obtained. The steps in each iteration are as follows,

1. The fluid properties are calculated at each point based on the value of pressure, temperature and other required state variables at that point. For the first time-step, the properties are calculated based on the initial values of the state variables.

2. The three components of the momentum conservation equations (two components for a two-dimensional case) are solved to obtain a new velocity field. The values of pressure and face mass flux calculated from the previous iteration are used to solve the momentum equations.

3. The velocity field obtained in the previous step may not satisfy the continuity equation. To rectify this, a "Poisson-type" pressure correction equation is solved to obtain corrections to the pressure and velocity fields and the face mass fluxes. This pressure correction equation is derived from the continuity equation and the linearized momentum equations.

4. The energy and species equations are solved using the values of pressure and velocity obtained in the previous steps.

5. The solution is checked for convergence. The entire solution sequence beginning from *step 1* is repeated if convergence is not obtained. If convergence is obtained, the solution is progressed to the next time step.

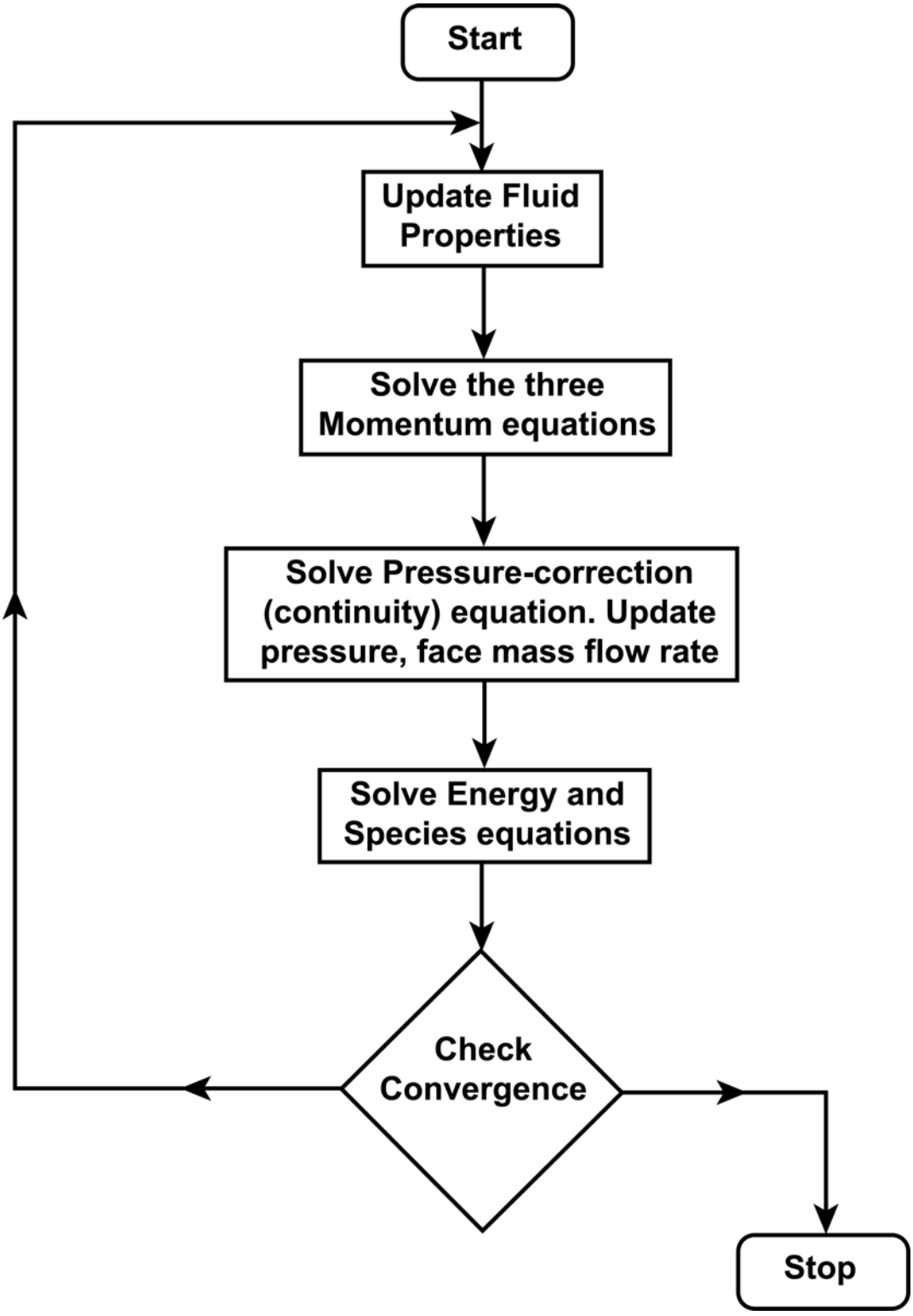

Figure 3.5: The Segregated Solver

3.6 Discretization

Discretization is the process of converting the governing partial differential equations into algebraic equations that can be solved numerically. The method used for discretization strongly affects the accuracy and robustness of the numerical solution.

In the present study, the governing equations are discretized using a control-volume-based technique. The governing equations are first integrated about each control volume to ensure that the conservation equations are automatically satisfied within each control volume. This is illustrated in Equation 3.8, which shows the integration of the conservation equation of a scalar ϕ over an arbitrary control volume V.

$$\oint \rho\phi\,\vec{v}\cdot d\vec{A} = \oint \Gamma_\phi\,\nabla\phi\cdot d\vec{A} + \int_V S_\phi\,dV \tag{3.8}$$

where,

Γ_ϕ is the diffusion coefficient for ϕ

S_ϕ is the rate of generation of ϕ per unit volume

Equation 3.8 is applied to every cell in the computational domain. This integral form is then discretized to obtain Equation 3.9.

$$\sum_f^{N_{faces}} \rho_f\vec{v}_f\phi_f\cdot\vec{A}_f = \sum_f^{N_{faces}} \Gamma_\phi\,(\nabla\phi)_n\cdot\vec{A}_f + S_\phi\,V \tag{3.9}$$

where,

N_{faces} is the number of faces enclosing a cell

ϕ_f is the value of ϕ convected through face f

This discretization is applicable to both structured and unstructured meshes.

3.6.1 Determination of variable values at faces

By default, all variable values were calculated and stored at the cell center. However, as seen from Equation 3.9, the discretization of the governing equation for ϕ required the value of ϕ at the face of the cell. An upwind scheme was used to predict the value of ϕ at the faces, based on the cell center values. A *First Order Upwind Scheme* was used to predict the variable values at the faces. The First Order Upwind Scheme was chosen because of its greater speed and stability as compared to more complex schemes.

The First Order Upwind Scheme assumes that the value of a variable at the cell center represents an average value of the variable throughout the cell. Hence, the value of a variable at the center of the cell just upstream of the face was approximated as the value of the variable at the face.

3.6.2 Evaluation of Derivatives

As seen in Equation 3.9, the gradient $\nabla\phi$ is used to discretize the diffusion and convection terms in the governing equation for ϕ. This gradient $\nabla\phi$ needs to be numerically evaluated in order to solve the equation. In the present study, $\nabla\phi$ is evaluated using the *Green-Gauss Theorem* as follows,

$$\nabla\phi = \frac{1}{V}\sum_{f} \overline{\phi}_f \, \vec{A}_f \tag{3.10}$$

where $\overline{\phi}_f$ is the value of ϕ at the cell face centroid.

The value of $\overline{\phi}_f$ can be evaluated either by a *Cell-Based Derivative Evaluation* or by a *Node-Based Derivative Evaluation*.

In the cell-based derivative evaluation scheme, the value of $\overline{\phi}_f$ is evaluated by taking the average of the values of ϕ at the two neighboring cells.

$$\overline{\phi}_f = \frac{\phi_{cell0} + \phi_{cell1}}{2} \tag{3.11}$$

In the node-based derivative evaluation scheme, the value of $\overline{\phi}_f$ is evaluated by taking an average of the values of ϕ at all nodes on the cell face.

$$\overline{\phi}_f = \frac{1}{N_f} \sum_{n}^{N_f} \overline{\phi}_n \tag{3.12}$$

where N_f is the number of nodes on the face f.

The value of $\overline{\phi}_n$ in Equation 3.12 was calculated using a method suggested by Holmes and Connel [69] and Rauch *et al.* [70]. By this method, $\overline{\phi}_n$ was calculated as a weighted average of the values of ϕ in all the cells surrounding the node.

The node-based derivative evaluation scheme was used in the present study, as it was reported to be more accurate than the cell-based scheme for unstructured meshes [68].

3.6.3 Linearization

An *implicit* linearization strategy is used to linearize the discretized governing equations and obtain a system of equations for each computational cell. The equation used to solve each unknown variable includes both known and unknown variables from neighboring cells.

A linearized form of Equation 3.9 can be written as,

$$a_p \, \phi = \sum_{nb} a_{nb} \, \phi_{nb} + b \tag{3.13}$$

where,

subscript nb refers to neighboring cells

a_P and a_{nb} are linearized coefficients for ϕ and ϕ_{nb}

A similar equation is written for each cell in the computational grid. The equations form a system such that the number of equations equals the number of unknown variables. To obtain the value of a variable, the entire system of equations is solved

simultaneously using the *Gauss-Seidel method*.

3.6.4 Discretization of the Continuity Equation

The integral form of the continuity equation can be written as follows,

$$\oint \rho \, \vec{v} \cdot d\vec{A} \tag{3.14}$$

Similar to the discretization of the scalar equation for ϕ in 3.13, the continuity equation can be discretized as follows,

$$\sum_{f}^{N_{faces}} J_f A_f = 0 \tag{3.15}$$

where, J_f is the mass flux through the face f.

As the velocity values are calculated and stored at the cell-centers, the velocity field needs to be interpolated in order to calculate the face mass flux J_f. In the discretization of the general scalar equation for ϕ in Equation 3.9, a *First Order Interpolation Scheme* was used. However, using this scheme in the interpolation of the velocity field results in an *unphysical checker-boarding* of pressure. Hence a *Momentum Weighted Averaging Scheme* proposed by Rhie and Chow [71] was used to interpolate the velocity field at the faces. In this scheme, velocity is averaged using weighting factors based on the coefficient a_P in Equation 3.18. The equation for the face mass flux can thus be written as,

$$J_f = \hat{J}_f + d_f(p_{cell\,0} - p_{cell\,1}) \tag{3.16}$$

where,

$p_{cell\,0}$ and $p_{cell\,1}$ are the pressures on the two cells on either sides of the face f

$\hat{J}_f$ includes the influence of velocity of $cell\,0$ and $cell\,1$

d_f is a term that depends on the a_P coefficients in the momentum equations for *cell* 0 and *cell* 1

This equation also forms the basis for *Pressure Velocity Coupling*, described in the next section.

3.6.5 Discretization of the Momentum Equation

The previous sections outlined the general discretization strategy. This section describes the special considerations in the discretization of the momentum equations.

Consider the integral form of the steady state momentum equation.

$$\oint \rho \vec{v}\, \vec{v} \cdot d\vec{A} = -\oint p\bar{\bar{I}} \cdot d\vec{A} + \oint \bar{\bar{\tau}} \cdot d\vec{A} + \int_V \vec{F}\, dV \tag{3.17}$$

where,

$\bar{\bar{I}}$ is the identity matrix

$\bar{\bar{\tau}}$ is the stress tensor and

$\vec{F}$ is the external force vector

The momentum equation can be discretized similar to the scalar equation discretized in Equation 3.13 by substituting the ϕ in the equation with velocity u, v and w. The discretized x-momentum equation is shown below.

$$a_P\, u = \sum_{nb} a_{nb} u_{nb} + \sum p_f A \cdot \hat{i} + S \tag{3.18}$$

where p_f is the value of pressure at the face of the cell.

During the course of the computation, the pressure field is calculated and stored at the center of every cell. Hence an *Interpolation Scheme* needs to be used to calculate the pressure p_f at the face.

A very popular pressure interpolation scheme is the one proposed by Rhie and Chow [71], which uses the coefficients of the momentum equations to interpolate the pressure values at the faces. This procedure works well in the absence of sharp gradients in the pressure field between cell centers. In the present problem, due to the presence of multiple phases in the flow and the dominant role of the surface tension forces, sharp gradients in the pressure field are likely. Hence the *Body Force Weighted Interpolation Scheme* was used instead.

The body force weighted interpolation scheme makes the assumption that the normal gradient of the difference between the pressure and the body forces remain constant. This assumption, in combination with separate models to estimate the body forces, is used to calculate the pressure at the faces. This model accounts for the rapid change in pressure at the interface between the two fluids due to the density difference and the surface tension forces.

3.6.6 Pressure Velocity Coupling

As described earlier, the continuity and momentum equations are solved separately in a sequential manner. As a result, the velocities obtained from solving the momentum equations may not necessarily satisfy the continuity equation. To rectify this, the continuity equation is used as an equation for pressure. However pressure does not explicitly appear in the continuity equation for incompressible flow. Hence a pressure velocity coupling scheme is used to artificially introduce pressure into the continuity equation. A description of the most popular and basic pressure velocity coupling algorithm is first given to illustrate the principle. The more complex algorithm that was actually used in the computations is then explained.

3.6.6.1 Semi-Implicit Method for Pressure-Linked Equations (SIMPLE)

The SIMPLE algorithm [72] was one of the earliest pressure velocity coupling techniques, which artificially introduced pressure in the continuity equation for incompressible flow. This was done to ensure that the calculated pressure and velocity fields locally satisfied the momentum and continuity equations.

Consider an arbitrary pressure field p^* across the computational domain. The face fluxes can be obtained from this pressure using an equation similar to Equation 3.16.

$$J_f^* = \hat{J}_f^* + d_f(p_{c0}^* - p_{c1}^*) \tag{3.19}$$

However, this calculated face flux J_f^* would not satisfy the continuity equation. Hence a correction term J_f' is added to J_f^* such that the resultant face flux J_f satisfies the continuity equation.

$$J_f = J_f^* + J_f' \tag{3.20}$$

The SIMPLE algorithm proposes the following equation for J_f'.

$$J_f' = d_f(p_{c0}' - p_{c1}') \tag{3.21}$$

where, p' is the cell pressure correction. Equations 3.20 and 3.21 can be substituted into the discretized continuity equation to obtain the following equation for the pressure correction term p'.

$$a_P\, p' = \sum_{nb} a_{nb}\, p_{nb}' + b \tag{3.22}$$

where b is net flow into a cell, which is given by,

$$b = \sum_{f}^{N_{faces}} J_f^* A_f \tag{3.23}$$

The above equation for pressure correction is very similar to the discretized form of the governing equations and can be solved using the same algorithm used to solve the governing equations. Once a solution for pressure correction p' is obtained, the cell

pressure and face flux are updated using the following equations.

$$p = p^* + \alpha_p p' \tag{3.24}$$

$$J_f = J_f^* + d_f(p'_{c0} - p'_{c1}) \tag{3.25}$$

where α_p is the under-relaxation factor. The corrected pressure field ensures that the continuity and momentum equations are simultaneously satisfied in every cell in the computational domain.

3.6.6.2 SIMPLE Consistent (SIMPLEC)

The SIMPLEC algorithm [73] is a pressure velocity coupling algorithm based on the SIMPLE algorithm. For simple flow conditions, the SIMPLEC algorithm converges faster than the SIMPLE algorithm [68].

SIMPLEC differs from SIMPLE in the calculation of the corrected face flux. Like SIMPLE, the face flux correction equation can be written as,

$$J_f = J_f^* + d_f(p'_{c0} - p'_{c1}) \tag{3.26}$$

However in this case, d_f is calculated as a function of $(\overline{a_P - \sum_{nb} a_{nb}})$

3.6.6.3 Pressure-Implicit with Splitting of Operators (PISO)

The SIMPLE and SIMPLEC schemes use an iterative procedure to calculate the pressure correction. The use of an iterative procedure makes transient calculations computationally expensive, as the pressure correction equation has to be iteratively solved at each time step. Also, the time step and the under-relaxation factors have to be adjusted to get these iterations to converge. The computational expense and convergence considerations offset the advantages gained by solving the governing equations separately. The *PISO* method [65] overcomes the above mentioned deficiencies

of the SIMPLE and SIMPLEC schemes, by getting rid of the need for iterations to solve the pressure correction equation. The *PISO* algorithm was used as the method of choice for pressure velocity coupling in all of the present computations.

Consider the discretized forms of the continuity and momentum equations.

$$\Delta_i \, u_i^{n+1} = 0 \tag{3.27}$$

$$\frac{\rho}{\delta t}\left(u_i^{n+1} - u_i^n\right) = H\left(u_i^{n+1}\right) - \Delta_i \, p^{n+1} + S_i \tag{3.28}$$

The pressure equation can be derived by taking the divergence of Equation 3.28 and substituting it in Equation 3.27. The resultant pressure equation is as follows,

$$\Delta_i^2 \, p^{n+1} = \Delta_i \, H\left(u_i^{n+1}\right) + \Delta_i \, S_i + \frac{\rho}{\delta t}\Delta_i \, u_i^n \tag{3.29}$$

In the PISO scheme, the coupled velocity and pressure equations are solved non-iteratively using a series of predictor-corrector steps. For increased accuracy, the operator H in the momentum equation is split into two operators H' and A_0, where A_0 consists of the diagonal elements in the operator H.

$$H'\left(u_i\right) = H\left(u_i\right) - A_0 u_i \tag{3.30}$$

Also A_0 is moved to the left hand side of the continuity and momentum equations.

The predictor and corrector in the scheme steps are outlined below. The superscripts, $*$, $**$ and $***$ denote intermediate values of variables between time steps n and $n+1$.

Predictor Step

The values of all the variables is known at time step n. The known value of the pressure field p^n at time step n is used in the discretized momentum equation (Equation 3.28) to calculate a new velocity field u_i^*.

$$\left(\frac{\rho}{\delta t} - A_0\right) u_i^* = H'\left(u_i^*\right) - \Delta_i \, p^n + S_i + \frac{\rho}{\delta t} u_i^n \tag{3.31}$$

As u_i^* is the only unknown in Equation 3.31, it can be readily solved using standard numerical techniques.

First Corrector Step

The velocity field u_i^* obtained in the predictor step will not satisfy the continuity equation (Equation 3.27). Hence, in the first corrector step, a new velocity field u_i^{**} and new pressure field p^* are sought, such that the continuity equation is satisfied.

$$\Delta_i \, u_i^{**} = 0 \tag{3.32}$$

First, a new pressure field p^* is obtained using the pressure equation (Equation 3.29 and the velocity field u^* calculated in the predictor step.

$$\Delta_i \left[\left(\frac{\rho}{\delta t} - A_0 \right)^{-1} \Delta_i \right] (p^* - p^n) = \Delta_i u_i^* \tag{3.33}$$

This pressure equation is explicitly solvable, as all the terms on the right hand side at known time steps n and $*$. Having calculated u_i^* and p^*, the new velocity field u_i^{**} is now calculated using an equation obtained by subtracting Equation 3.31 from the momentum equation.

$$\left(\frac{\rho}{\delta t} - A_0 \right) (u_i^{**} - u_i^*) = -\Delta_i (p^* - p^n) \tag{3.34}$$

The above equation can be solved explicitly, as u^{**} is the only unknown quantity in the equation. The new velocity field u_i^{**} satisfies the continuity equation (Equation 3.32.

Second Corrector Step

The second corrector step is similar to the first corrector step. Here, a new velocity field u_i^{***} and a new pressure field p^{**} are sought from the quantities calculated in the previous steps. The explicit equations for pressure and velocity in this step are

as follows,

$$\Delta_i \left[\left(\frac{\rho}{\delta t} - A_0 \right)^{-1} \Delta_i \right] (p^{**} - p^*) = \Delta_i \left[\left(\frac{\rho}{\delta t} - A_0 \right)^{-1} H'(u_i^{**} - u_i^*) \right] \tag{3.35}$$

$$\left(\frac{\rho}{\delta t} - A_0 \right) (u_i^{***} - u_i^{**}) = H'(u_i^{**} - u_i^*) - \Delta_i (p^{**} - p^*) \tag{3.36}$$

Similarly, additional corrector steps may be added to refine the velocity and pressure values. However typically, two corrector steps are quite sufficient to yield satisfactory accuracies.

3.6.7 Temporal Discretization

The earlier sections discussed the discretization of the spatial derivatives. Similarly, the time derivatives in the unsteady governing equations need to be discretized. Temporal discretization is usually less complex than spatial discretization because the governing equations are first order linear partial differential equations with respect to time.

Consider a generic time-dependent equation,

$$\frac{\partial \phi}{\partial t} = F(\phi) \tag{3.37}$$

where, $F(\phi)$ is the result of the evaluation of all the spatial terms.

In the present study, the transient term is discretized using a first order backward difference scheme. This is represented in equation 3.38.

$$\frac{\phi^{n+1} - \phi^n}{\Delta t} = F(\phi) \tag{3.38}$$

The function $F(\phi)$ in Equation 3.38 could either be explicitly evaluated at the current time step or be implicitly evaluated at a future time step. The implicit method was used in the present study and the function $F(\phi)$ is evaluated at the time step $n+1$. This is represented in Equation 3.39.

$$\frac{\phi^{n+1} - \phi^n}{\Delta t} = F(\phi^{n+1}) \tag{3.39}$$

The implicit method was chosen because of its unconditional stability with respect to time step size. However, the drawback of using the implicit method is that the right hand side of Equation 3.38 is not known at the time the equation is solved. Hence the equation needs to be solved iteratively, which requires an additional computational effort.

3.6.8 Under-Relaxation

As the governing equations being solved are non-linear, huge fluctuations in the calculated value of the variables occur quite frequently. To reduce the effect of these fluctuations, the change in the value of the variables is controlled by an under-relaxation factor.

$$\phi = \phi_{old} + \alpha \Delta \phi \tag{3.40}$$

where, α is the *Under-Relaxation Factor*

As seen from Equation 3.40, the under-relaxation factor reduces the effect of fluctuations by reducing the change in the value of a variable in every iteration by an under-relaxation factor.

3.7 The Volume of Fluid (VOF) Model

The Volume of Fluid Model, first proposed by Hirt and Nichols [64] was used in the present study to model the two phase flow. This model is based on the idea of storing in each cell, the data about the volume fraction of every fluid in it. According to Hirt and Nichols, the main challenges in the modeling of free boundaries are;

1. Calculation of gradients at the boundaries,
2. Tracking their change with time and
3. Imposing boundary conditions.

They define a function F such that $F = 1$ is one if the point contains a fluid and $F = 0$ otherwise. In this case, the value of F averaged over a cell would be equal to the volume fraction of fluid in the cell. Thus cells with an F value of one would be filled with fluid, while cells with an F value of zero would be empty cells.

Also, a free boundary cell would have a non-zero value of F and have at least one neighboring cell with a zero value of F. Hirt and Nichols note that the value of F would change most rapidly along a direction perpendicular to the boundary. They use this idea to track the boundary based on the values of F in all cells.

The distribution of F is governed by the following equation,

$$\frac{\partial F}{\partial t} + u\frac{\partial F}{\partial x} + v\frac{\partial F}{\partial y} + S_\alpha = 0 \tag{3.41}$$

where, S_α is the mass source term representing the addition in F due to the absorption of water vapor into the lithium bromide solution.

When water vapor is absorbed into the lithium bromide solution at the interface cells, it causes an increase in the liquid fraction in those cells. The increase in liquid fraction is a function of the amount of water vapor absorbed and the mass of liquid and vapor present in the cell. The amount of mass absorbed at the interface is governed by the Fick's law of diffusion, given by,

$$m_{abs} = A_n \frac{\partial}{\partial n}\left[D_{AB}\rho\frac{\partial Y_i}{\partial n}\right] \tag{3.42}$$

where, A_n is the cell face area in the direction normal to the interface. The derivatives in Equation 3.42 are calculated along the direction normal to the interface. The normal direction of the interface is calculated using the principle that the gradient of liquid fraction would change most rapidly in the direction normal to the interface. The algorithm for calculating the normal derivatives is explained in detail in the section on heat and mass transfer modeling. The source term S_α in Equation 3.41, which is the increase in F due to the mass absorbed, is given by Equation 3.43.

$$S_\alpha = \frac{A_n}{\rho V_{cell}}\frac{\partial}{\partial n}\left[D_{AB}\rho\frac{\partial Y_i}{\partial n}\right] \tag{3.43}$$

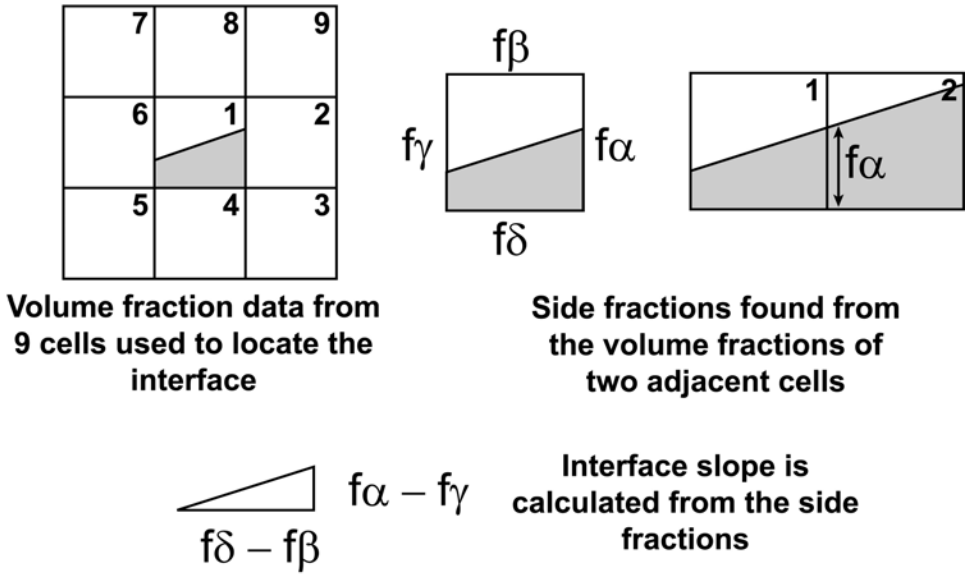

Figure 3.6: Geometric Reconstruction Scheme

Besides the mass of vapor absorbed, S_α also depends on the mass of liquid and vapor present in the cell.

3.7.1 Treatment of the liquid-vapor interface

The *Geometric Reconstruction method* by Youngs [66] was used to track the liquid-vapor interface. In this method, the portion of the interface within a cell is approximated by a straight line. The location and slope of this straight line is determined by the volume fractions in that cell and the volume fractions in the eight cells surrounding it. This is illustrated in Figure 3.6. The interface line is located in such a manner that it divides the cell into two regions in the same ratio as that of the volume fractions in the neighboring cells.

3.7.2 Surface Tension

The *Continuum Surface Force (CSF) model* by Brackbill *et al.* [67] was used to model the effect of surface tension. This method models surface tension as a continuous,

three dimensional function across a fluid interface, as opposed to modeling it as a boundary condition on the interface. This significantly increases the stability and robustness of the numerical model.

At a fluid interface, the surface tension force is balanced by a difference in pressure between the fluids across the interface. In the direction normal to the interface, this boundary condition can be expressed by the following equation,

$$p_1 - p_2 + \sigma\kappa = 2\mu_1\hat{n}_k \left[\frac{\partial u_k}{\partial n}\right]_1 - 2\mu_2\hat{n}_k \left[\frac{\partial u_k}{\partial n}\right]_2 \tag{3.44}$$

The boundary condition in the direction tangential to the interface is given by,

$$\mu_2 \left[\hat{t}_i\frac{\partial u_i}{\partial n} + \hat{n}_k\frac{\partial u_k}{\partial s}\right]_2 - \mu_1 \left[\hat{t}_i\frac{\partial u_i}{\partial n} + \hat{n}_k\frac{\partial u_k}{\partial s}\right]_1 = \frac{\partial\sigma}{\partial s} \tag{3.45}$$

In the above equations,

σ is the fluid surface tension coefficient

p_1, p_2 are the pressures in the two fluids

κ is the local surface curvature = ${R_1}^{-1} + {R_2}^{-1}$, R_1 and R_2 being the radii of curvature of the surface

μ_1 and μ_2 are the viscosities of fluids 1 and 2

$\hat{n}$ is the unit normal vector perpendicular to the interface

$\hat{t}$ is the unit normal vector tangential to the interface

From Equation 3.45 it is seen that a spatial variation of the surface tension coefficient ($\partial\sigma/\partial s$) causes the fluid to flow from the regions of low surface tension to regions of high surface tension.

In the CSF model, Brackbill *et al.* [67] assume a constant surface tension along the interface and thus neglect any tangential flow fields caused by varying surface tension coefficients. In the present case, though the surface tension coefficient varies

slightly with lithium bromide concentration and temperature, the amount variation is very small in the range of conditions. For example, Kulankara and Herold [74] reported that the surface tension coefficient at 60% and 20°C was 0.096 N/m, while that at 53% and 22°C was 0.090 N/m. Hence the constant surface tension coefficient assumption is a reasonable one. Brackbill *et al.* [67] also neglect the effect of viscosity and assume that the surface tension forces are solely balanced by the pressure forces. This reduces Equations 3.44 and 3.45 to

$$p_1 - p_2 = \sigma\kappa \tag{3.46}$$

Most surface tension models use this equation as a boundary condition on the fluid interface, with a step jump in pressure between the two fluids balancing the surface tension forces. However, this form of a discontinuous pressure field leads to severe numerical difficulties for complex interface topologies.

The continuum method used here is illustrated in Figure 3.7. Here, a characteristic function $c(x)$ is used to distinguish between the two fluids. The characteristic function is defined as,

$$c(x) = \begin{cases} c_1 & \text{in fluid 1} \\ c_2 & \text{in fluid 2} \\ c = (c_1 + c_2)/2 & \text{at the interface} \end{cases} \tag{3.47}$$

For the case of incompressible flow, density presents itself as a convenient characteristic function. Now, instead of a step jump, the characteristic function is replaced by the smooth varying function $\tilde{c}(x)$ that varies from c_1 to c_2 over a distance that is of the same order of magnitude as the resolution of the grid. As seen from the contours of constant $\tilde{c}(x)$ in Figure 3.7, the fluid interface is replaced by a smooth transition region where $\tilde{c}(x)$ varies continuously from c_1 to c_2. The effect of surface tension and the resulting pressure jump is now felt on this entire transition region, as opposed to only at the interface.

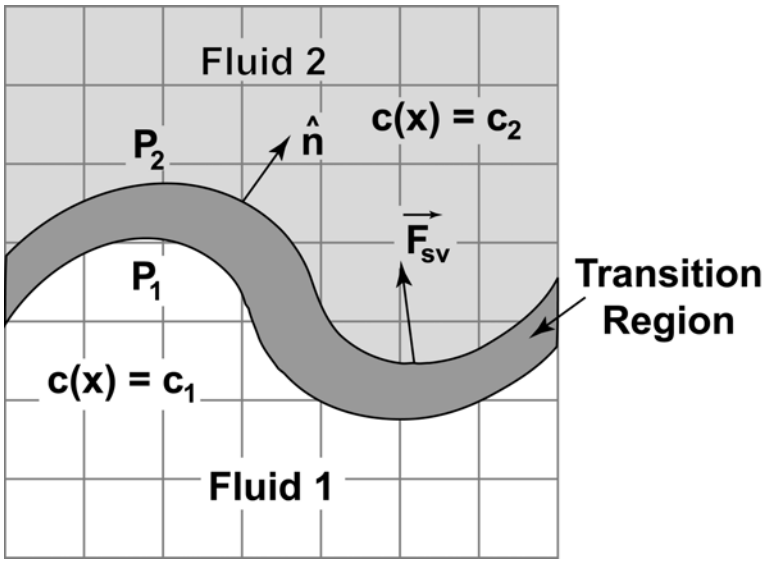

Figure 3.7: The Continuum Surface Model for Modeling Surface Tension

Consider a volume ΔV in the transition region, whose edges are normal to the fluid interface and whose thickness h is the same as the thickness of the transition region. The thickness h is selected to be much smaller that the radius of curvature of the interface. In this volume ΔV, define a volume force term $F_{sv}(x)$ such that in the limit that the thickness h goes to zero, $F_{sv}(x)$ approaches the surface tension force per unit area at the interface.

$$\lim_{h \to 0} \int_{\Delta V} F_{sv}(x)\, dV = \int_{\Delta A} \sigma\, \kappa(x)\, \hat{n}(x)\, dA \tag{3.48}$$

Also the volume force term is defined is such a fashion that it is zero outside the transition region. Using Gauss' theorem, Brackbill et al. [67] have obtained the following expression for the volume force term $F_{sv}(x)$.

$$F_{sv}(x) = \sigma \kappa(x) \frac{\nabla \tilde{c}(x)}{c_2 - c_1} \tag{3.49}$$

To include the effect of surface tension in the governing equation, this volume force term can be simply added as a *source term* to the momentum equation as follows,

$$\rho \frac{Du}{Dt} = -\nabla p + F_{sv} \tag{3.50}$$

3.8 Heat and Mass Transfer Modeling

The mass transfer is governed by the species equation shown in Equation 3.6. This is solved in the liquid phase using the solution method described earlier for the scalar ϕ. A *no flux* boundary condition is used at the solid surfaces. At the liquid-vapor interface, the concentration is determined using the vapor pressure equilibrium assumption. This equilibrium concentration is calculated as a function of the temperatures and pressures of the lithium bromide solution and water vapor, using the correlation by Yuan and Herold [62].

According to Yuan and Herold [62], the lithium bromide solution is in equilibrium with the water vapor when the *chemical potential* of the water in the lithium bromide solution is equal to the chemical potential of the water vapor. This is shown in Equation 3.51

$$\mu_w(x, T, p) = \mu_{vap}(T, p) \tag{3.51}$$

Yuan and Herold [62] provide the following correlation for the calculation of the chemical potential of water in the lithium bromide solution.

$$\begin{aligned} \mu_w(x, T, p) = \; & (A_0 - A_2x^2 - 2A_3x^3 - 0.1A_4x^{1.1}) \\ & +T(B_0 - B_2x^2 - 2B_3x^3 - 0.1B_4x^{1.1}) \\ & +T^2(C_0 - C_2x^2 - 2C_3x^3 - 0.1C_4x^{1.1}) \\ & +T^3(D_0 - D_2x^2 - 0.1D_4x^{1.1}) \\ & +T^4(E_0) + \tfrac{F_0}{T-T_0} \\ & +p(V_0 - V_2x^2 + V_3T - V_5x^2T + V_6T^2) \\ & +\ln(T)(L_0 - L_2x^2 - 2L_3x^3 - 0.1L_4x^{1.1}) \\ & +T\ln(T)(M_0 - M_2x^2 - 2M_3x^3 - 0.1M_4x^{1.1}) \end{aligned} \tag{3.52}$$

The coefficients in Equation 3.52 are shown in Table 3.1.

The chemical potential of water vapor is calculated using the correlation by Ziegler and Trepp [75]. The equation for chemical potential of water vapor is given by the

Table 3.1: Coefficients in Equation 3.52

	$i=0$	$i=1$	$i=2$	$i=3$	$i=4$
A_i	5.506219979E+3	5.213228937E+2	7.774930356	-4.575233382E-2	-5.792935726E+2
B_i	1.452749674E+2	-4.984840771E-1	8.836919180E-2	-4.870995781E-4	-2.905161205
C_i	2.648364473E-2	-2.311041091E-3	7.559736620E-6	-3.763934193E-8	1.176240649E-3
D_i	-8.526516950E-6	1.320154794E-6	2.791995438E-11	NA	-8.511514931E-7
E_i	-3.840447174E-11	2.625469387E-11	NA	NA	NA
F_i	-5.159906276E+1	1.114573398	NA	NA	NA
L_i	-2.183429482E+3	-1.266985094E+2	-2.364551372	1.389414858E-2	1.583405426E+2
M_i	-2.267095847E+1	2.983764494E-1	-1.259393234E-2	6.849632068E-5	2.767986853E-1
V_i, $i=0..4$	1.176741611E-3	-1.002511661E-5	1.695735875E-8	-1.497186905E-6	2.538176345E-8
V_i, $i=5..7$	5.815811591E-11	3.057997846E-9	-5.129589007E-11	NA	NA
T_i	220.0	NA	NA	NA	NA

Table 3.2: Coefficients in Equation 3.53

C_1	2.136131×10^{-2}
C_2	-3.169291×10^{1}
C_3	-4.634611×10^{4}
C_4	0.0
D_1	4.01970
D_2	-5175550×10^{-2}
D_3	1.951939×10^{-2}
h^g_{oR}	60.965058
T_{oR}	5.0705
p_{oR}	3.0000

following equation:

$$\begin{aligned}
\frac{\mu_{vap}}{RT_B} = \; & h^g_{oR} - T_R s^g_{oR} \\
& + \int_{T_{oR}}^{T_R} c^{go}_{pR} dT_R - T_R \int_{T_{oR}}^{T_R} \frac{c^{go}_{pR}}{T_R} dT_R \\
& + T_R \ln(p_R/p_{oR}) \\
& + C_1(p_R - p_{oR}) \\
& + C_2(p_R/T_R^3 - 4p_{oR}/T_{oR}^3 + 3p_{oR}T_R/T_{oR}^4) \\
& + C_3(p_R/T_R^{11} - 12p_{oR}/T_{oR}^{11} + 11p_{oR}T_R/T_{oR}^{12}) \\
& + C_4(p_R^3/T_R^{11} - 12p_{oR}^3/T_{oR}^{11} + 11p_{oR}^3T_R/T_{oR}^{12})/3
\end{aligned} \tag{3.53}$$

where, $c^{go}_{pR} = D_1 + D_2 T_R + D_3 T_R^2$

The coefficients in Equation 3.53 are shown in Table 3.2.

Since the pressure and temperature of water vapor are known, the chemical potential of water vapor can be explicitly calculated using Equation 3.53. Thus the right hand side in equation 3.51 is known. On the left hand side, the temperature and pressure of the lithium bromide solution is known, while the equilibrium concentration is unknown. The equilibrium concentration can be iteratively computed in combination with Equation 3.52. The *Newton Raphson method* was used to iteratively obtain the value of the equilibrium concentration. Having established the methodology to calculate the equilibrium concentration, two different approaches were tried to set the interface at the equilibrium concentration.

The first method tried was a more direct implementation of the interface condition. At every iteration in the computation, the cells on the liquid-vapor interface were spotted using the cell density data. The density of most of the cells in the domain was equal to either the liquid or vapor density, while the interface cells had a density value in between the liquid and vapor densities. Having spotted the interface cells, the equilibrium concentration for the cell was calculated using its pressure and temperature data. After calculating the equilibrium concentration, the value of the concentration in the cell was forcibly changed to the equilibrium value. This procedure was repeated at every iteration in every time step to ensure that the interface concentration was not altered due to the diffusion of species with the neighboring cells on the liquid side.

While the above described method replicates the conditions at the interface very accurately, its solution presents some severe numerical difficulties. Due to the low mass diffusivity of water in lithium bromide solution ($D_{AB} = 1.6 \times 10^{-9}$ m^2/s), most of the water absorbed at the interface stays close to the interface and does not diffuse to the inner regions of the solution. Consequently, there is a sharp concentration gradient on the liquid side of the interface. Also, since the concentration variable is not defined in the vapor phase, the concentration function stops abruptly at the

interface. The sharp gradient on the liquid side near the interface in combination with the discontinuity of the variable at the interface due to it being undefined in the vapor phase, makes convergence of the governing species equations extremely difficult in the interface region.

To help with the convergence, the following alternate algorithm was used. Instead of defining the concentration only over the liquid phase, it was defined over the entire computational domain. In the liquid phase, the concentration variable represented the actual concentration of the solution, while in the vapor phase the variable was defined to be equal to the equilibrium concentration (i.e., it is calculated as a function of temperature and pressure). While this fictional concentration variable has no physical significance in the vapor phase, it helps immensely with the convergence of the solution. This is because this algorithm removes the discontinuity of the concentration variable at the interface. The presence of the sharp concentration gradient on the liquid side near the interface still presented some difficulty, but it was overcome with the present method and the use of fairly small time steps ($\sim 1.0 \times 10^{-6}\ s$).

To implement this method, during every iteration the interface and vapor region cells were identified based on their density data. For all of these cells, the equilibrium concentration was calculated as a function of its temperature and pressure. The concentration variable in the cell was then forcibly changed to the equilibrium value. While this method presents significant advantages over the earlier method with respect to convergence, the disadvantage is that it requires a greater amount of computational effort. Instead of calculating the equilibrium concentration for just the interface cells, the calculation is now conducted for the interface and the entire vapor domain.

The energy equation shown in Equation 3.4 is solved for both the liquid and vapor phases using the algorithm described earlier for ϕ. A *constant temperature* boundary condition is used at the solid surfaces. The solid wall temperature is set at a value

lower than the lithium bromide solution, so as to provide the cooling required to sustain absorption.

The absorption of water vapor by the lithium bromide solution is an exothermic process. The specific heat of absorption for this reaction is assumed to be equal to the heat of vaporization of water vapor at that pressure. The amount of heat generated is calculated at the liquid-vapor interface, as a function of the rate of absorption and the specific heat of absorption. This is shown in equation 3.54.

$$q_{gen} = \frac{\partial}{\partial n}\left[D_{AB}\,\rho\,h_a\frac{\partial Y_i}{\partial n}\right] \tag{3.54}$$

Using the Gauss Theorem, Equation 3.54 is modified to a volumetric heat source term, as shown in Equation 3.55.

$$q_{gen} = D_{AB}\,\rho\,h_a\frac{\partial Y_i}{\partial n}\frac{\nabla\rho\cdot\rho}{[\rho]\langle\rho\rangle} \tag{3.55}$$

where, $[\rho] = \rho_{LiBr} - \rho_{vapor}$ and $\langle\rho\rangle = \frac{1}{2}(\rho_{LiBr} + \rho_{vapor})$. All the gradients in Equation 3.55 are calculated in the *normal direction*.

In the regions near the liquid-vapor interface, the cell density gradually changes from the liquid density to the vapor density. The rate of this change is maximum in the direction normal to the interface. This principle is used to find the normal direction at the interface. The normal direction is the direction in which the density gradient is maximum.

At every iteration, the density gradients in the x, y and z directions ($\partial\rho/\partial x, \partial\rho/\partial y$, $\partial\rho/\partial z$), are calculated and stored at each cell in the computational domain. Using these three components of the density gradient, the gradient in any direction can be calculated as,

$$\frac{\partial\rho}{\partial r} = \frac{\partial\rho}{\partial x}\sin\theta\cos\phi + \frac{\partial\rho}{\partial y}\sin\theta\sin\phi + \frac{\partial\rho}{\partial z}\cos\theta \tag{3.56}$$

where, θ and ϕ are the zenith and azimuth angles in spherical coordinates.

The zenith and azimuth angles are varied from 0 to π and 0 to 2π respectively, and the values that produce the maximum value of the density gradient ($\partial\rho/\partial r$) are

found. These values of the angles (θ_n and ϕ_n) correspond to the direction normal to the interface and the density gradient corresponds to the normal density gradient ($\partial\rho/\partial n$). Having found the normal direction, the normal gradient of any quantity α can now be calculated using the following equation:

$$\frac{\partial \alpha}{\partial n} = \frac{\partial \alpha}{\partial x}\sin\theta_n \cos\phi_n + \frac{\partial \alpha}{\partial y}\sin\theta_n \sin\phi_n + \frac{\partial \alpha}{\partial z}\cos\theta_n \tag{3.57}$$

The normal gradients in Equation 3.54 are calculated using the above described methodology. The heat of absorption thus calculated is added as a *heat generation* term in the governing energy equation (Equation 3.4).

The absorption of water vapor into the lithium bromide solution is also a transfer of mass from the vapor phase to the liquid phase. The rate of mass transfer can be calculated using Equation 3.58.

$$m_{tran} = \frac{\partial}{\partial n}\left[D_{AB}\,\rho\,\frac{\partial Y_i}{\partial n}\right] \tag{3.58}$$

Similar to the heat generation term, Equation 3.58 is modified using the Gauss Theorem.

$$m_{tran} = D_{AB}\,\rho \frac{\partial Y_i}{\partial n}\frac{\nabla\rho\cdot\rho}{[\rho]\langle\rho\rangle} \tag{3.59}$$

This mass transport term is added as a *mass source* term in the continuity equation for the liquid phase. Also, the same term is added as a *mass sink* term in the continuity equation for the vapor phase.

The momentum of the vapor as it is being absorbed into the lithium bromide solution is assumed to be negligible. Consequently, no momentum source or sink terms are added to the momentum conservation equations for the liquid and vapor phases.

The numerical model was implemented in *C*, in conjunction with the commercial software package *Fluent* [63]. The following algorithms present in Fluent were used:

- The Gauss Seidel based numerical equation solver.

- Solution of the momentum equation.
- Calculation of the surface tension forces.
- Various plotting tools, including plotting of the concentration and temperature contours and velocity vectors.

The following algorithms were written in C to supplement the functionality provided by Fluent, and solve the vapor absorption problem in its entirety:

- The species equation solver, including the fictitious concentration field in the vapor phase
- Calculation of the equilibrium concentration as a function of the temperature and pressure of the lithium bromide solution and water vapor.
- Tracking the shape and location of the interface and implementing the equilibrium concentration conditions at the interface.
- Solution of the energy equation, including calculation and implementation of the heat of absorption at the interface.
- Tracking the transfer of mass due to absorption and accounting for it in the mass conversation equations.
- The more advanced post processing algorithms, including calculation of heat and mass transfer coefficients and plotting of temperature and concentration profiles at various axial and circumferential locations.

The codes present in Fluent and the ones written in C, were compiled together on the *GCC* compiler. Once compiled, all of the codes (except the post processing codes) were executed synchronously during every iteration. The results from the computations were stored in a file at periodic intervals. The post processing operations

Table 3.3: Operating conditions for the baseline case

Operating parameter	**Value**
Film initial concentration	65% by wt of LiBr
Film initial temperature	40.5℃
Tube wall temperature	30℃
Tube diameter	15.9 mm
Tube pitch	15.9 mm

including plotting of the concentration and temperature distributions, calculation of the heat and mass transfer coefficients, etc., were conducted on the stored data after the conclusion of the iterations.

3.9 Initial conditions

Similar to the work by Conlisk and Mao [49] and Killion and Garimella [61], the computations were started with a thin, uniform film around the tube. This film was generated by running the simulations with a velocity inlet boundary condition at the tube wall for a flow time of 0.01 s. After the flow time of 0.01 s, the boundary condition at the wall was changed to a stationary, solid wall and the actual computations were commenced. With time, due to gravity, the liquid in the film collects at a point, forms a droplet, and starts the flow. The velocity and size of the falling droplet depends on the thickness of the initial film. The concentration and temperature of the initial film were set based on the desired initial conditions for the flow. The initial conditions for the baseline case are shown in Table 3.3. The initial temperature, pressure and concentration of the lithium bromide solution correspond to a subcooling of 17℃.

In the two dimensional case, the fluid automatically accumulated at the bottom of the sphere, resulting in droplet formation at that point. However, for the three dimensional geometry with a uniform film, the droplet is just as likely to form at

any axial location on the bottom of the tube. To avoid that and ensure that the droplet forms at the center of the tube, the film thickness was perturbed such that the thickness was slightly higher at the center. The initial film thickness as made to vary sinusoidally from 0.53 mm at the center of the tube, to 0.20 mm at the tube end. This draws a greater amount of fluid at the center, resulting in droplet formation at that point. One motivation for having the droplet form at the center was to be able to study the effect of droplet impact and waves to the maximum possible extent on both sides of the tube. Another motivation was that due to the symmetrical nature of the flow, this allows us to model only half the droplet and specify a symmetry condition at the center of the tube.

3.10 Boundary conditions

The boundary conditions used in the computations are summarized in Table 3.4. A *no slip* velocity boundary condition, *no mass flux* species boundary condition, and a *constant temperature* boundary condition are specified at the tube wall. The constant wall temperature lower that the lithium bromide solution temperature replicates the presence of coolant inside the tube in a real absorber. The coolant provides the cooling required to compensate for the heating due to the absorption process.

The flow is assumed to be symmetrical on both sides of the axial center of the tube. The droplet is forced to form at the center of the tube and only half of the droplet is modeled, while the other half is replicated by symmetry. The flow is also assumed to be symmetric about the diameter of the tube in line with the direction of fluid flow. The velocity, temperature and concentration gradients are assumed to be zero at the domain boundaries on the sides.

A symmetry boundary condition was applied at the ends of the tube. This is the equivalent of having duplicate droplets falling on either side, in sync with the

Table 3.4: Boundary conditions for the baseline case

Boundary	**Velocity**	**Concentration**	**Temperature**
Tube wall	No slip	No mass flux	Constant temperature 30℃
Tube center along the length	Symmetry	Symmetry	Symmetry
Tube end along the length	Symmetry	Symmetry	Symmetry
Tube diameter in the direction of flow	Symmetry	Symmetry	Symmetry
Domain boundaries on the sides	Free stream	No mass flux	No heat flux
Domain boundaries on the top and bottom	Periodic	Periodic	Periodic

droplet of interest. The waves generated due to these duplicate droplets on the sides perfectly mirror the wave generated due to the main droplet. Since the length of tube modeled was chosen based on the most dangerous wavelength for droplet formation, having another droplet at the mirrored location represents the actual flow situation accurately for adjacent droplets falling in phase. However, in practice, the neighboring droplets will not fall in perfect unison, but a little out of sync. As a result, the waves from the two droplets may not interact at the center and with the same velocity, as was assumed in this case. But the synchronous neighboring droplet assumption was made in the interest of computational efficiency.

At the top and bottom boundaries of the domain, the flow is assumed to be *periodic*. That is, any fluid that leaves the bottom of the domain in one time step is reintroduced from the top for the next time step at the exact same velocity, temperature and concentration conditions that it left the bottom. This is illustrated in Figure 3.8, where a series of frames of the concentration profiles of a droplet are shown. In frame b in the figure, the droplet has reached the bottom boundary of the computational domain. As seen subsequently in frames d and e, due to the periodic

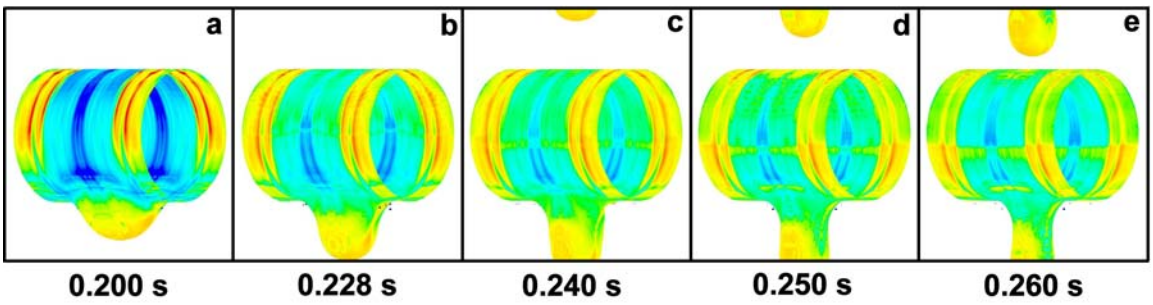

Figure 3.8: Periodic boundary condition

boundary condition, the droplet reenters the domain from the top, with the same concentration, temperature and velocity with which it left from the bottom. The use of such a periodic condition allows us to model the progression of the flow over a long time duration over successive tubes in a bank beyond the formation and fall of the first droplet, within a reasonably sized grid.

3.11 Numerical Stability Analysis

Numerical instability of an algorithm refers to its tendency to develop large oscillations and thus fail to converge. In certain cases, such instability could also cause the algorithm to converge to incorrect results. To prevent such instability, certain stability conditions need to be satisfied. In transient computations, the stability conditions generally place a limit on the largest time step that could be used to solve the problem.

3.11.1 Stability Condition for Interface Tracking

The volume of fluid algorithm requires that the fluid not move more than one cell in one time step [64]. This is because the volume of fluid algorithm only balances fluxes between adjacent cells. This condition can be mathematically represented as follows,

$$\delta t_{vof} < min \left\{ \frac{\delta x_i}{|u_{i,j}|}, \frac{\delta y_j}{|v_{i,j}|} \right\} \tag{3.60}$$

In all the computations conducted here, the u velocity is the larger velocity and hence the time step is determined by its magnitude.

Typically this condition is further strengthened as follows,

$$\delta t_{vof} < CFL \times \frac{\delta x_i}{|u_{i,j}|} \tag{3.61}$$

where, CFL is the Courant Friedrichs Lewy Number (also known as Courant Number). This is a ratio of the dimensionless temporal discretization to spatial discretization. A CFL number of 0.25 was used in all the present computations.

To address this stability criterion, the code was designed to automatically modify the time step for the volume of fluid calculation if it is greater than the maximum allowed value. For a certain case, if the prescribed time step were greater than the allowed value, the code would automatically reduce it to the maximum allowed value. If this modified time step size was not taken into account, (i.e. if the flow time was calculated as the number of time steps multiplied by the original input time step) it would make the flow seem slower than it actually was. In such a case, the time step size would be a function of the grid size and smaller grid sizes would use smaller time steps, making the flow seem slower for finer grids. As will be seen later, this stability criterion plays a crucial role in the behavior of the solution with different grids.

For the sake of completeness, the other stability conditions are listed. As seen later, these stability conditions are much weaker than the condition for interface tracking.

3.11.2 Stability Condition for Momentum Diffusion

This condition ensures that the momentum does not diffuse through more than one cell at a time. This condition is mathematically represented as,

$$\delta t_{mom} < \frac{1}{2\nu} \frac{\delta {x_i}^2 \cdot \delta {y_j}^2}{\delta {x_i}^2 + \delta {y_j}^2} \tag{3.62}$$

where ν is the kinematic viscosity.

3.11.3 Stability Condition for Surface Tension

The condition for the surface tension forces is as follows [67]. This condition ensures that the time step is small enough to resolve the propagation of capillary waves.

$$\delta t_{surf} < \left[\frac{(\rho_1 + \rho_2)(\Delta x)^3}{4\pi\sigma} \right]^{\frac{1}{2}} \tag{3.63}$$

3.11.4 Sample Calculations

To obtain a conservative estimate of the maximum allowable time step, the velocity u in Equation 3.61 was estimated as follows,

$$u = \sqrt{2gh} \tag{3.64}$$

where, h is the height through which the droplet falls.

The calculation results are summarized in Table 3.5

This concludes the description of the numerical model used in the present study. The next chapter presents results obtained using this model.

Table 3.5: Maximum time step prescribed by the stability criteria

Case	**Velocity u (m/s)**	$\mathbf{dt_{vof}}$ **(s)**	$\mathbf{dt_{mom}}$ **(s)**	$\mathbf{dt_{surf}}$ **(s)**
3.2 mm Capillary	0.54	2.21×10^{-5}	1.24×10^{-4}	4.58×10^{-4}
5.0 mm Capillary over a flat plate	0.63	3.19×10^{-5}	3.45×10^{-4}	7.64×10^{-4}
Column of 15.9 mm diameter sphere (coarse grid)	0.56	4.48×10^{-5}	5.39×10^{-4}	9.55×10^{-4}
Column of 15.9 mm diameter sphere (medium grid)	0.56	3.58×10^{-5}	3.45×10^{-4}	7.64×10^{-4}
Column of 15.9 mm diameter sphere (fine grid)	0.56	2.87×10^{-5}	2.21×10^{-4}	6.11×10^{-4}

CHAPTER IV

RESULTS AND DISCUSSION

4.1 Introduction

The present chapter describes the results of the various computations conducted in this study. Some of the results presented include the flow patterns, the concentration and temperature variations in the solution, and the variation in the heat and mass transfer coefficients. The main focus of the discussion is on the effect of the flow on the heat and mass transfer characteristics, and its effect on absorber performance.

The chapter starts with a description of the baseline case, computed on a three dimensional grid. This is followed by a description of a case with a different tube diameter and pitch. The motivation behind the study of this particular case is to observe the effect of the absorber geometry on its performance. After that, operating conditions of the absorber are varied and their effect on performance is presented. The parameters varied include, inlet solution concentration, inlet solution temperature, inlet solution flow rate and coolant temperature. Due to the resource-intensive nature of the calculations on the three dimensional grid, the absorber operating parameter variations were conducted on a smaller two dimensional grid. For comparison, the baseline calculation was also repeated on a two dimensional grid. The chapter concludes with a grid independence study to document the accuracy of the presented computational results.

Most of the computations were conducted in parallel on a Sun Fire X2200 M2 server with four 64 bit AMD Opteron processors and 4 GB RAM, running Red Hat Linux. Some of the more resource intensive computations were run on a Sun Fire V40z server with eight 64 bit AMD Opteron processors and 16 GB RAM, also running

Table 4.1: Operating conditions for the baseline case

Operating parameter	**Value**
Solution inlet concentration	65% by wt of LiBr
Solution inlet temperature	40.5℃ (17℃ subcooled)
Tube wall temperature	30℃
Tube diameter	15.9 mm
Tube pitch	15.9 mm
LiBr mass flux	0.0086 kg/ms

Red Hat Linux.

4.2 Three dimensional baseline case

Table 4.1 shows the geometry and operating conditions for the baseline case. These conditions were selected based on the operating conditions of a typical lithium bromide absorber. The pressure, temperature and concentration correspond to a subcooling of 17℃ of the lithium bromide solution. The calculation was started by initially creating a thin lithium bromide film around the tube and letting the solution in the film accumulate and fall in the form of a droplet. The concentration and temperature of the lithium bromide solution in the film were the same as the inlet conditions specified in Table 4.1.

The Reynolds number for a film-wise flow around a tube is defined as $4u\delta/\nu$, where δ is the thickness of the film. The film thickness is different at different points on the tube and hence so is the Reynolds number. These local Reynolds numbers are integrated over the entire tube to calculate the average Reynolds number. Also, it is to be noted that such a Reynolds number cannot be defined for the droplet region, as droplet Reynolds numbers are defined very differently. However, in this case the flow is characterized by the film Reynolds number as a majority of the heat and mass transfer, which is the focus of this study, occurs on the film. Also, since the fluid

velocity gradually increases with time, the Reynolds number also increases. Within the time interval computed, the average Reynolds number was found to be always less than 110.

As shown in Figure 3.2, only one tube (actually half a tube with assumed symmetry) is modeled in the computational domain. When the lithium bromide solution falls over the tube and reaches the end of the computational domain, it is reintroduced at the top of the domain, at the exact same velocity, temperature and concentration (at the exit of the domain). This is known as the *periodic boundary condition*. This condition ensures the continuation of the flow over an extended period of time, while still confining the computations to a reasonably sized grid. The condition effectively simulates a *column of tubes* instead of just one. This is because when the lithium bromide solution reenters the domain from the top, after having exited from the bottom, the tube in the grid is now equivalent to the next tube in the column.

4.2.1 Flow pattern

Figure 4.1 shows the fluid flow pattern and the droplet shape as it falls down the column of tubes. It is to be noted that the frames presented in Figure 4.1 are not at equal time differences. Instead, time steps at which the flow patterns display features of interest have been carefully selected and presented. The two main forces acting on the fluid are *gravity* and *surface tension*. The gravitational force acts in the downward direction and causes the solution to accumulate at the bottom of the tube. This results in the formation of the droplet. This is shown in Figure 4.1 at times 0.150 s and 0.200 s. The surface tension force opposes the gravitational force and tries to hold the droplet from falling off the tube. The balance between these two forces drives the droplet formation. Gravity causes more and more fluid to accumulate in the droplet, leading to an increase in its size. As the droplet size increases and

gravity starts to become more dominant than surface tension, more of the fluid starts to move towards the lower regions of the droplet. This causes a thinning of the droplet at regions close to the tube surface, akin to a *neck*. This is seen at time step 0.264 s in Figure 4.1. Eventually, the droplet grows in size and the gravitational force on it increases to a point where the droplet can detach from the tube and fall off.

Depending on the lithium bromide solution flow rate and the tube geometry, the droplet may or may not detach before it hits the next tube. In the present case, as seen from time step 0.270 s in Figure 4.1, the droplet reaches the next tube before it detaches completely from the previous one. The impact of the droplet on the tube causes a *ripple* or *wave* in the solution film on the tube. This is seen at time steps 0.275 s, 0.284 s and 0.305 s in Figure 4.1. As will be seen later, this wave and its propagation along the tube plays a crucial role in heat and mass transfer.

With time the *neck* region of the droplet (also called *liquid bridge*) gets thinner and thinner and eventually the droplet detaches. This is seen in time steps 0.305 s, 0.337 s and 0.339 s. When the droplet detaches, the gravitational force on the part of the droplet still in contact with the tube suddenly decreases, while the surface tension force does not change significantly. This sudden force imbalance causes the part of the liquid bridge still in contact with the tube to quickly retract towards the tube after droplet detachment. This is seen at time step 0.339 s in Figure 4.1. This force imbalance and resulting retraction causes oscillations in the liquid attached to the lower portion of the tube. These oscillations are transmitted to the solution film present on the lower portions of the tube, creating some *ripples* in them. Though not as dominant as the waves created by droplet impact, these ripples created by the retraction of the liquid bridge also have a significant impact on the heat and mass transfer.

In some cases, the droplet breakup and liquid bridge oscillations result in the creation of a few small droplets, called *satellite droplets*. These satellite droplets

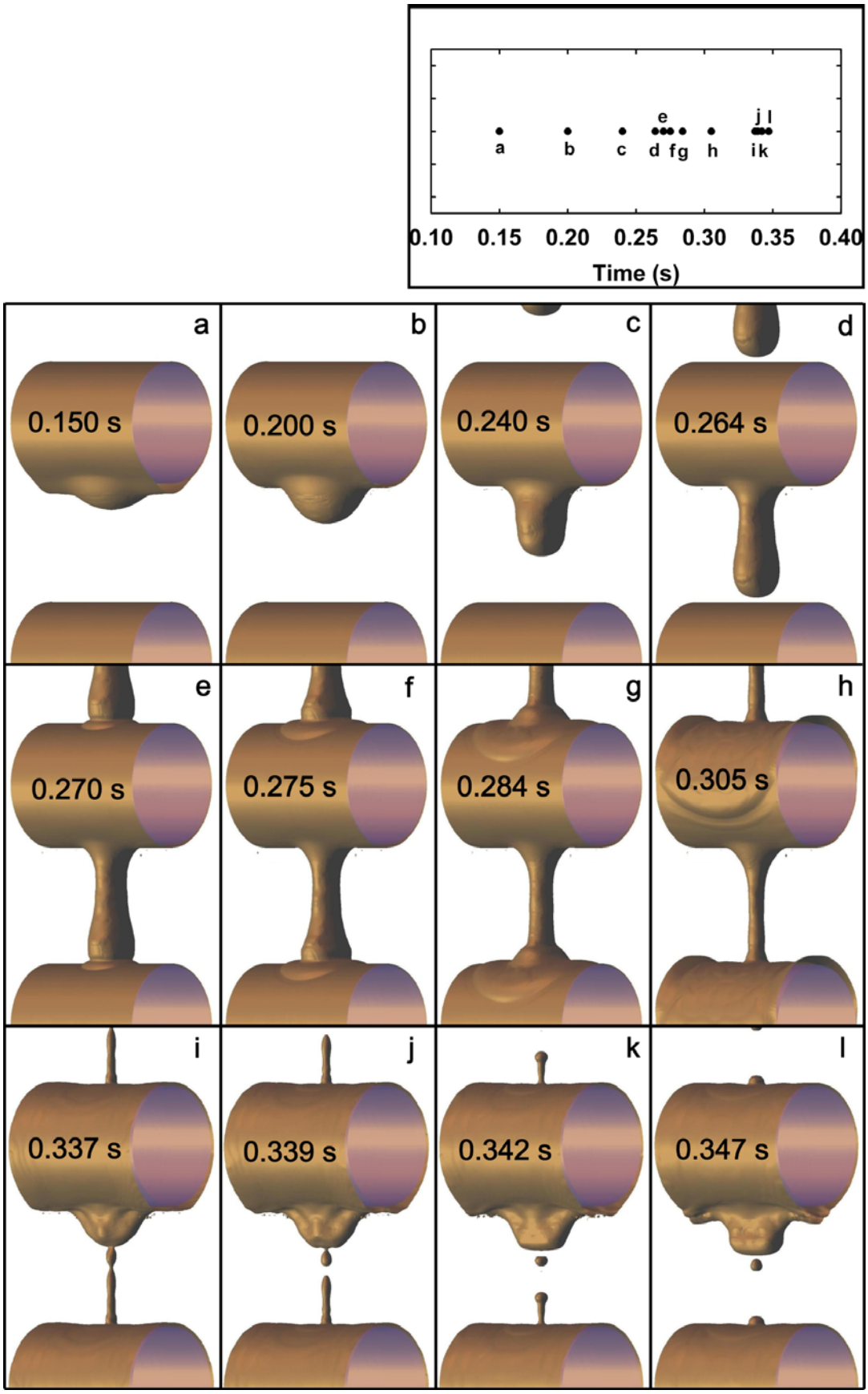

Figure 4.1: Droplet flow over a column of tubes

are seen at time steps 0.339 s, 0.342 s and 0.347 s in Figure 4.1. These satellite droplets increase the surface area available for heat and mass transfer and thus have a significant effect on the absorption phenomenon. In computations were conducted up to a flow time of 0.347 s. During this time the lithium bromide solution passed through three tubes in the column.

Figure 4.2 shows the variation of the interfacial surface area available for heat and mass transfer in the lithium bromide solution. The surface area is calculated by summing the individual faces of the cells that comprise the liquid-vapor interface. This is shown in Equation 4.1.

$$A = \int dA = \sum_{i=1}^{n} |A_i| \tag{4.1}$$

The cells on the interface are detected by tracking the density of the fluid within the cell. It is seen that the surface area is lowest when the lithium bromide solution is present as a film around the tube. Slowly, as the droplet begins to form, the available surface area increases. The available surface area is maximum at 0.265 s, just before the droplet touches the next tube. The surface area available for heat and mass transfer at 0.265 s is 328.4 mm^2. After the droplet hits the next tube, the total surface area begins to decrease as the lithium bromide solution travels as a film over the tube. The available surface area hits a *local minima* at 0.323 s with an area of 301.5 mm^2. Again, as the solution starts accumulating and the next droplet starts to form, the available surface area starts increasing. The satellite droplets also contribute to an increase in the available surface area.

4.2.2 Concentration distribution

Figure 4.3 shows the local changes in the lithium bromide concentration as it falls down the column of tubes. As shown in the accompanying scale, the local concentrations are represented by varying colors, with red denoting the highest concentration

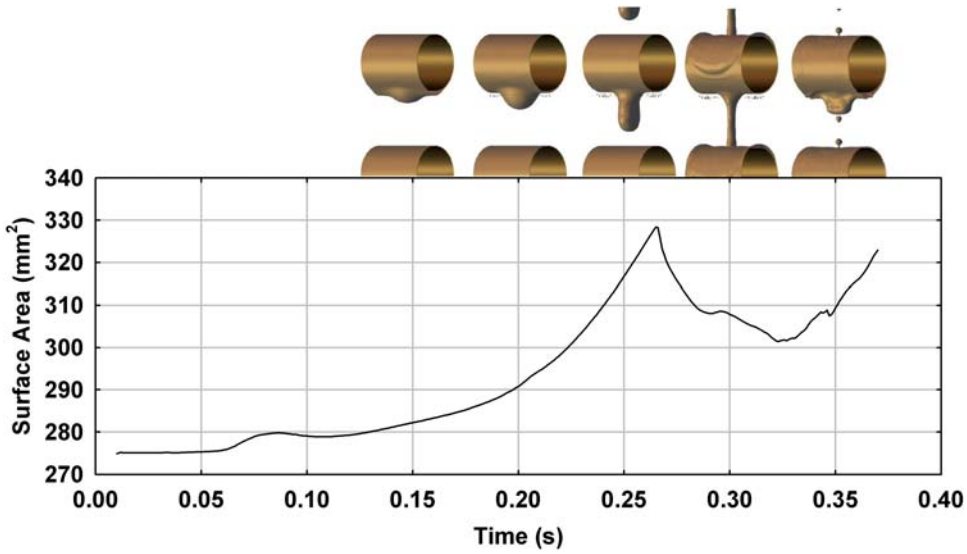

Figure 4.2: Surface area variation in flow over a column of tubes

at 65% and blue denoting the lowest concentration at 55%. Concentrations in between these limits are denoted in a decreasing order by different shades orange, yellow and green respectively. All concentrations are represented as a percentage weight of lithium bromide in the solution. The average concentration of the lithium bromide solution at each of the time steps is also printed over the tube. In a flow time of 0.347 s, the lithium bromide solution travel over three tubes in the column.

As the lithium bromide solution falls, it absorbs water vapor, causing a decrease in its concentration. The absorption happens at the liquid-vapor interface and as a result, the concentration is lowest at the interface. Also the absorption of water vapor being an exothermic process causes a rise in the temperature of the solution. In order to sustain the absorption, the solution needs to be cooled by the coolant flowing on the inside of the tube. As a result of this, the vapor absorption rates are higher in the interfaces close to the tube, as compared to interfaces on the droplet, which are not in good thermal contact with the coolant in the tube.

Initially the lithium bromide solution is present as a film around the tube at a uniform concentration of 65%. When the droplet starts forming, the concentration of the solution in the droplet decreases at a slower rate as compared to that of the

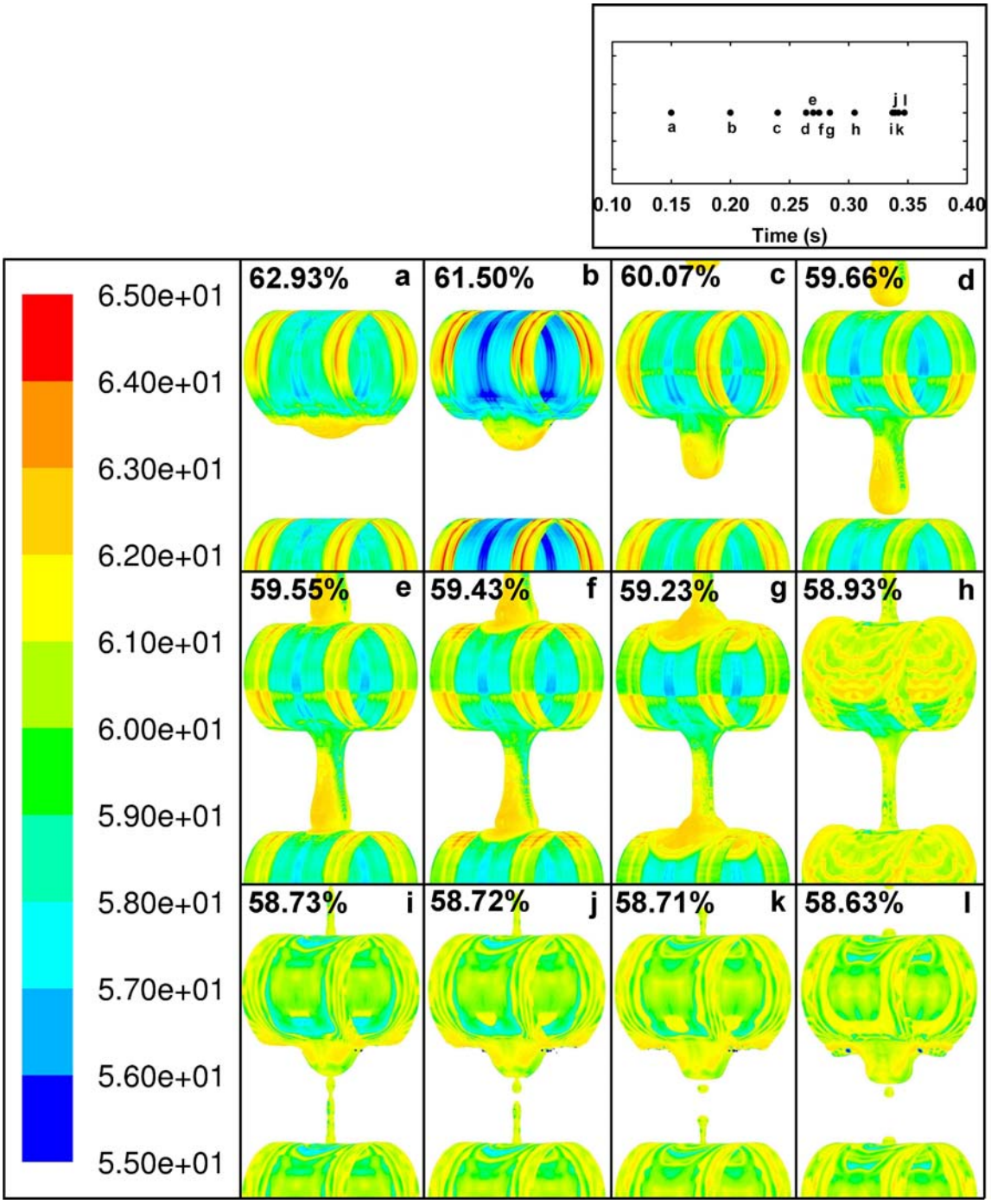

Figure 4.3: LiBr concentration profiles in a droplet falling over a column of tubes

solution in the film over the tube. This is seen in the first frame (average concentration 62.93%), where most of the film over the tube is green or blue in color, while most on the solution in the droplet is yellow or orange in color. This is because the solution in the film, being closer to the coolant tube, is cooled more effectively than the solution in the droplet. This cooling compensates for the heating of the solution during the exothermic absorption process and helps sustain a higher absorption rate on the film. The higher absorption rate results in lower concentrations.

It is seen that during the droplet formation stages (average concentration 62.93%, 61.50%, 60.07% and 59.66%), the solution in the parts of the film immediately above the droplet has a lower concentration than those in parts of the film away from droplet formation. Due to the fluid accumulation in the droplet, the fluid velocity on the film is higher in the regions above the droplet than in regions away from it. Also the thickness of the liquid film in this region is lower due to the accumulation of fluid in the droplet. The higher velocities and lower film thicknesses result in higher mass transfer coefficients, which lead to a greater amount of absorption of water vapor, which in turn result in lower concentrations in these regions.

As explained earlier, the absorption of water vapor happens at the surface of the lithium bromide solution. Due to the low mass diffusivity of water in lithium bromide ($D_{AB} = 1.6 \times 10^{-9}$ m^2/s), the water vapor is not transported efficiently to the interior of the solution, but stays near the interface. This reduces the difference between the interface concentration and the equilibrium concentration, which is the driving potential for the mass transfer. This causes a gradual decrease in the vapor absorption rate. When the droplet falls on the tube, the impact of the droplet mixes the lithium bromide solution in the film, forming a more uniform concentration distribution in it. This is seen in Figure 4.3 in the frames with average concentrations 59.55%, 59.43%, 59.23% and 58.93%. Before the droplet impacts the film (average

concentration 59.66%), the surface of the film on the tube is at a very low concentration (blue and green color), while the interior of the film is at a high concentration. However, due to the low concentration layer on the surface, this high concentration interior cannot absorb any water vapor. When the droplet falls on the tube, the impact of the fall mixes the fluid in the film, causing a more uniform concentration distribution in the film. This mixing causes a higher concentration at the surface of the film (orange, yellow and green colors) as seen in Figure 4.3 in the frames with average concentration 59.23% and 58.93%. This *mixing effect* significantly increases the overall mass transfer rates by presenting newer surfaces of the lithium bromide solution to the vapor for absorption, thus acting as a very important catalyst in the absorption phenomenon.

The impact of the droplet causes *waves* on the film on the tube. These waves propagate axially on the tube away from the point of droplet impact. As the waves travel, they mix the fluid in the film, bringing high concentration solution from the bottom of the film to the surface. This is seen in the frames with concentrations 58.73%, 58.72%, 58.71% and 58.63%. The waves also increase the local fluid velocities, which in turn increase the local heat and mass transfer coefficients. This will be studied in one of the later sections.

Over a flow time of 0.36 s, the average concentration of the lithium bromide solution decreases from 65.0% to 58.6% over the course of fall of the solution over three tubes. This concentration change is higher than those found in many actual absorbers, where a similar concentration change occurs during the fall of the solution over ten or more tubes. The relatively high concentration change in the present case is due to the mass flow rate of the solution being lower than that in conventional absorbers. The typical mass flow rate per unit tube length in absorbers is about 0.020 kg/ms [55], while that in the present case is 0.0086 kg/ms.

4.2.3 Temperature distribution

Figure 4.4 shows the variation in the temperature of the lithium bromide solution as it falls through the tubes. The different temperatures are denoted by the variation in the colors, with red denoting the hottest temperature at 40.5℃ and blue denoting the coldest temperature at 30℃. Temperatures in between these two extremes are denoted, in the order of decreasing temperatures by various shades of orange, yellow and green, respectively. Also, the average temperature of the lithium bromide solution at that time step is printed over the tube in each frame.

Since the absorption process is exothermic, it causes an increase in the temperature of the solution at the liquid-vapor interface. To compensate for this heating, the lithium bromide solution is cooled by a coolant flowing inside the tubes. The solution in the film over the tube is usually low in temperature as it is cooled very effectively by the coolant inside the tube. The solution in the droplet, being farther away from the coolant, is not cooled very effectively and hence is higher in temperature. This is seen in Figure 4.4, where most of the solution in the film over the tube is marked in blue, while most of the solution in the droplet is marked in green or yellow. This is especially true initially for the frames at average temperatures, 35.12℃, 34.90℃, 34.68℃, 34.56℃ and 34.52℃. At later times, the fall and impact of the droplet alters the temperature distribution, and the difference between the temperatures in the film and droplet regions begin to decrease.

Initially, the flow starts off with all the lithium bromide solution as a thin film over the tube at a uniform temperature of 40.5℃. As the simulation proceeds, this film very quickly cools due to the coolant in the tube at 30℃. As the droplet starts forming, the fluid in the droplet starts rising to warmer temperatures than the film around the tube due to absorption without commensurate heat transfer. This is seen in Figure 4.4 in the frames with average temperatures 35.12℃, 34.90℃, 34.68℃ and 34.56℃.

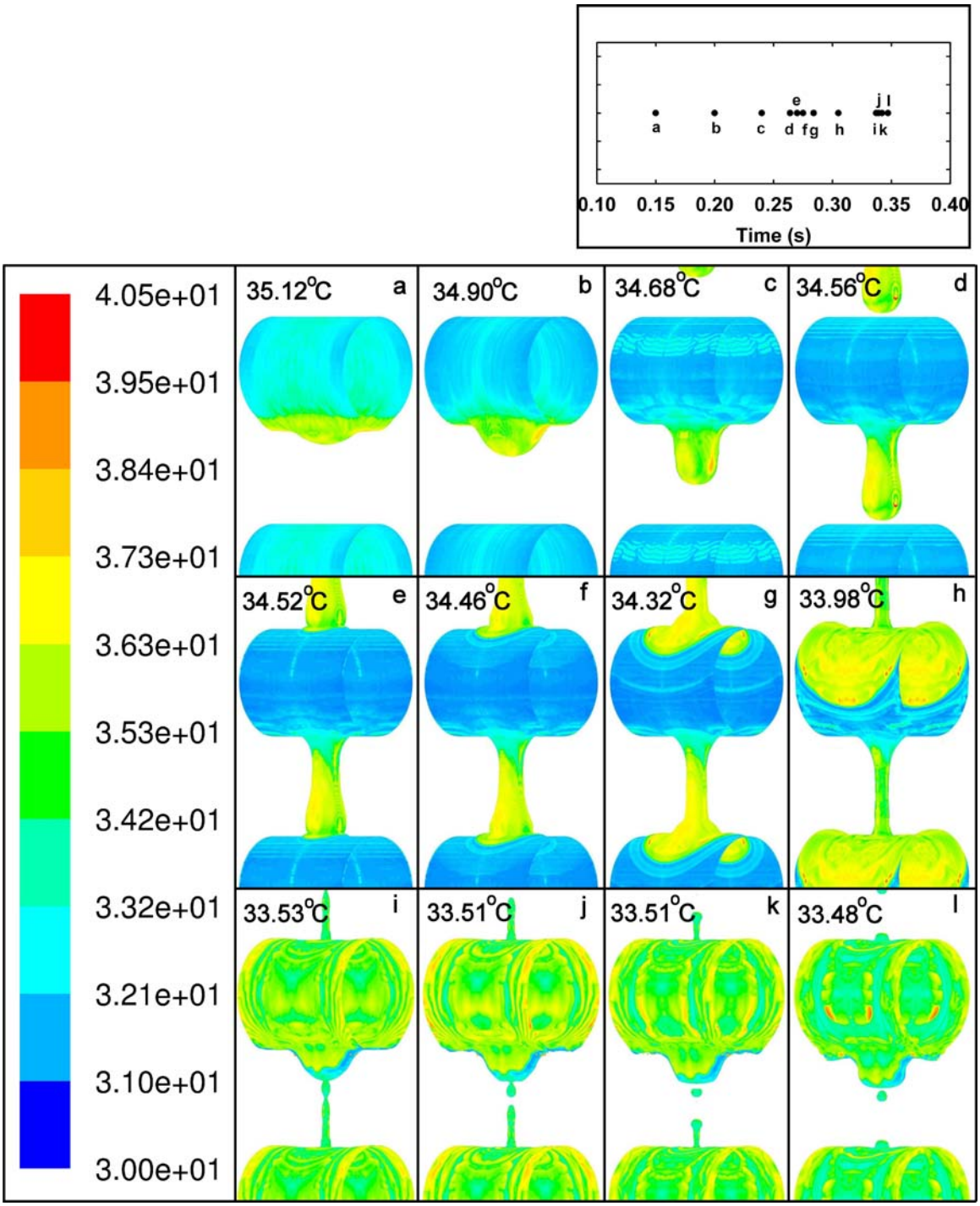

Figure 4.4: LiBr temperature profiles in a droplet falling over a column of tubes

When the droplet falls on the next tube, as with the concentration distribution, the impact of the droplet causes a *mixing effect* of the temperature distribution. This is seen in Figure 4.4 in the frames with average temperatures 34.52℃, 34.46℃, 34.32℃ and 33.98℃. Before the droplet impact, the lithium bromide solution in the film is cooled (marked in blue color), while the solution in the droplet is much warmer (marked in yellow and green colors). The warm temperature solution has a much lower potential for absorption of water vapor. When the droplet impacts on the tube, the fluid in the droplet region mixes with the fluid in the film forming a more even temperature distribution throughout the solution. This is noticeable in Figure 4.4 in the frames with average temperatures 33.53℃and 33.51℃, where almost the entire lithium bromide solution is close to the average temperature at that time step, and is marked in green. This *mixing effect* is very beneficial to the absorption phenomenon and is one of the biggest advantages of a drop-wise inter-tube flow regime.

4.2.4 Velocity distribution

Figure 4.5 shows the distribution of velocity in the lithium bromide solution. The velocity is represented by a series of arrows, where the direction of the arrow denotes the direction of the velocity vector, while the length of the arrow is proportional to the magnitude of the velocity at that point.

Initially, the lithium bromide solution is present around the tube as a stationary film. This film is gradually accelerated downwards due to gravity. Thus the average velocity of the fluid keeps increasing with time. This is seen in Figure 4.5, where the length of the arrows progressively increases with time.

When the droplet falls on the tube, the impact of the fall causes the fluid to be dispersed in all directions in the form of waves. This is seen in Figure 4.5 at time steps 0.275 s, 0.284 s and 0.305 s, where the fluid velocity at the point of impact is seen to

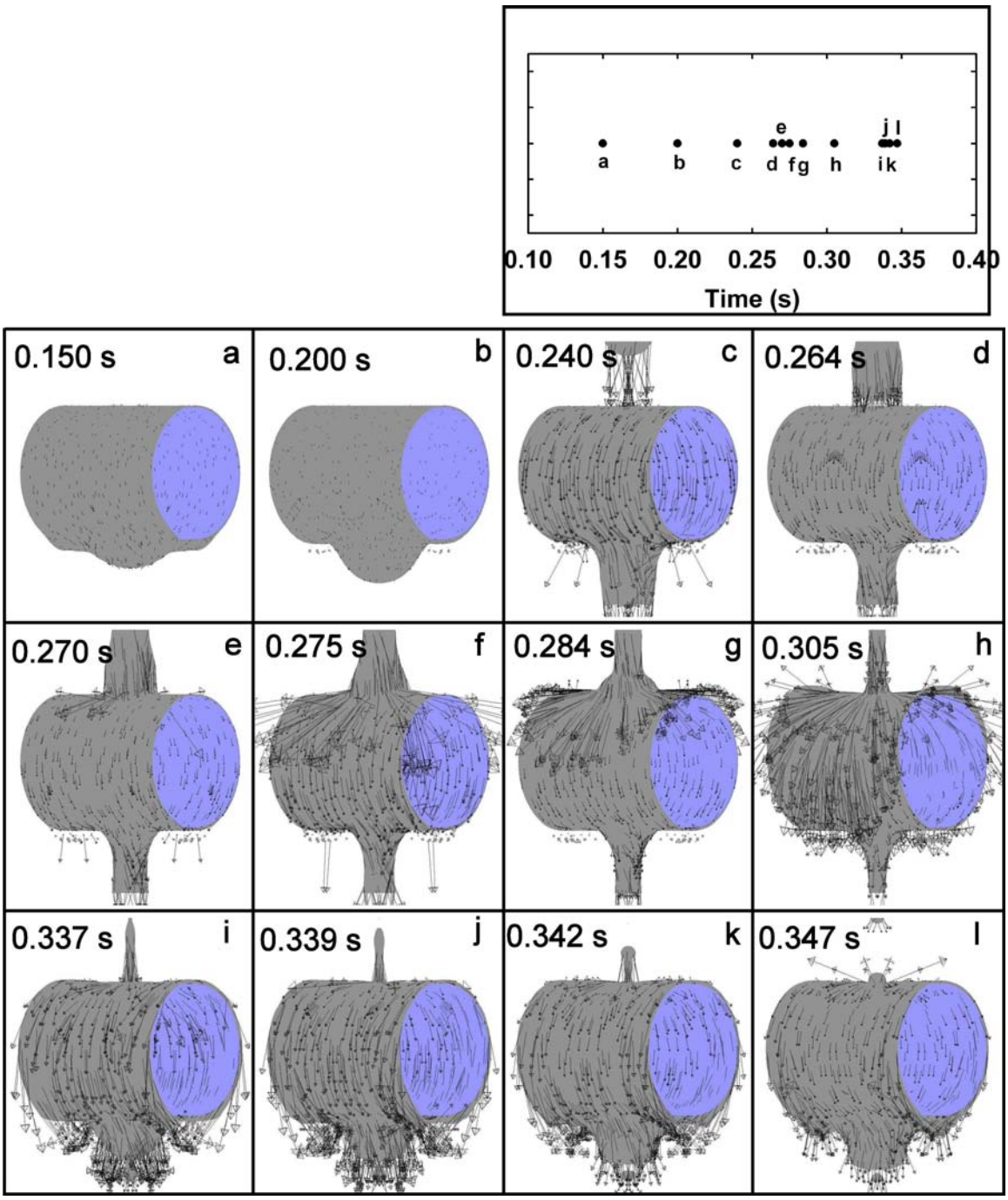

Figure 4.5: Velocity vectors in flow over a column of tubes

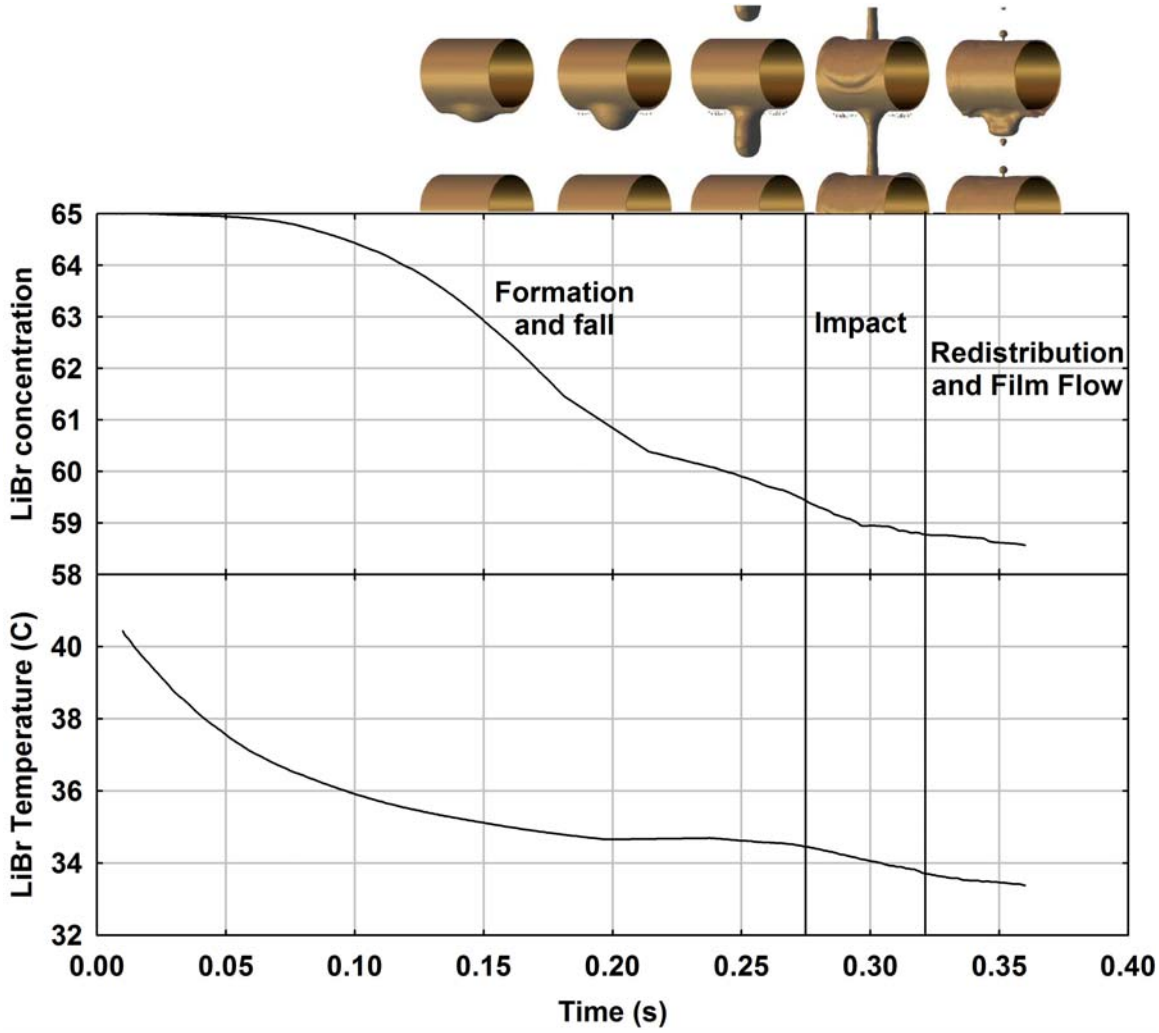

Figure 4.6: Temporal variation of bulk LiBr concentration and temperature

the spread in all directions at high magnitudes. The formation and propagation of these waves have a significant impact on the heat and mass transfer processes.

4.2.5 Bulk concentration and temperature variation

Figure 4.6 shows the temporal variation of the average concentration and temperature of the lithium bromide solution. The flow patterns at the respective times are shown above the plot.

The bulk concentrations and temperature are calculated by averaging the concentration and temperature over all the lithium bromide solution present in the computational domain. This is shown in Equations 4.2 and 4.3.

$$Y_{i,bulk} = \frac{1}{M_{LiBr}} \sum_{j=1}^{n} m_{LiBr,j} Y_{i,j} \tag{4.2}$$

$$T_{bulk} = \frac{1}{M_{LiBr}} \sum_{j=1}^{n} m_{LiBr,j} T_{j} \tag{4.3}$$

As shown in Figure 3.2, the computational domain consists of one tube and a half diameter space above and below the tube.

Initially, the lithium bromide solution is present at a uniform concentration of 65%. As the droplet falls, it absorbs water vapor, causing a decrease in its concentration. The absorption is driven by the difference between the concentration of lithium bromide solution at the interface and the vapor pressure equilibrium concentration. The vapor pressure equilibrium concentration is a function of the lithium bromide solution temperature at the interface. This variation of the equilibrium concentration with the lithium bromide solution temperature is shown in Figure 4.7. The equilibrium concentration decreases with decrease in the lithium bromide solution temperature.

Initially the lithium bromide solution is at a temperature of 40.5 ℃. At this temperature, the equilibrium concentration is 57.35%. Due to proximity to the coolant, the lithium bromide solution in the film rapidly cools to close to 30 ℃. This is seen in Figure 4.6 in the plot on temperature variation, where the temperature decreases at a rapid rate initially. At 30 ℃, the equilibrium concentration is 51.20%. Initially when the solution is warmer (40.5 ℃), the rate of mass transfer process is relatively slow due the high equilibrium concentration, and hence low driving concentration difference. Initially, when the lithium bromide solution is at a temperature of 40.5 ℃ and a bulk concentration of 65%, the average driving concentration difference is 7.65%. However, as the temperature drops, the equilibrium concentration decreases and the

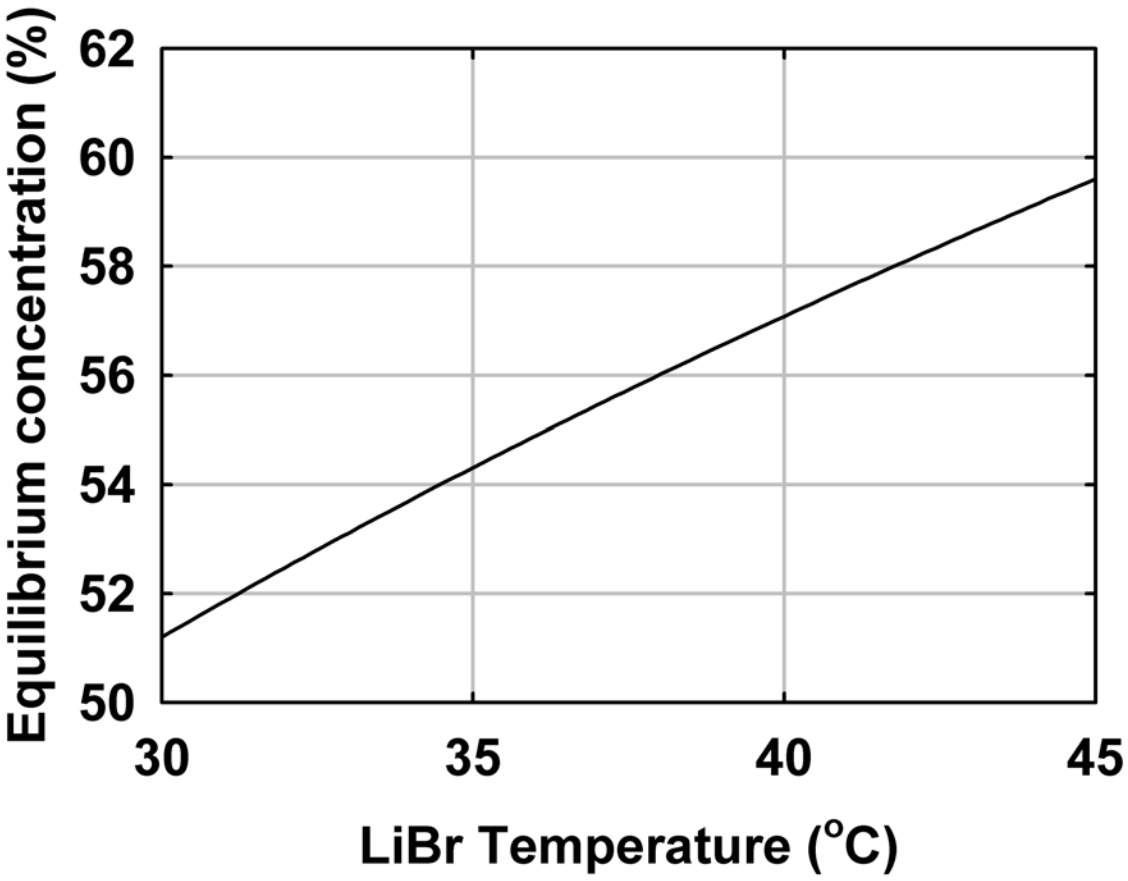

Figure 4.7: Variation of the vapor pressure equilibrium concentration with LiBr temperature

large driving concentration difference results in a higher rate of mass transfer. At 0.05 s, when the temperature of solution in the film falls close to 30℃, and the bulk concentration is 64.94%, the average driving concentration difference is 13.74%. This is seen in Figure 4.6 in the plot of concentration change, where the concentration initially decreases slowly and then starts decreasing rapidly once the solution cools down.

Since the absorption process is exothermic, the mass transfer is accompanied by generation of heat in the lithium bromide solution. After the initial sharp drop in temperature, the increased absorption and the accompanied heat generation causes a decrease in the rate of temperature drop. This decreased rate of cooling is also accompanied by a slight decrease in the rate of absorption. This is seen in Figure 4.6 from about 0.10 s to about 0.27 s, where both the concentration and temperature curves gradually level out after the sharp initial drops.

At about 0.27 s, the droplet hits the next tube and forms a film around the second tube. The impact of the droplet and the associated *waves* and *mixing effect* cause an increase in the heat and mass transfer coefficients. This leads to an increase in the rate of cooling of the lithium bromide solution, as seen in Figure 4.6. The increased rate of cooling also causes an increase in the rate of absorption of water vapor, as seen from the plot on concentration change. Once the effect of the droplet impact phases out, the concentration and temperature curves level out once again, as seen in Figure 4.6 at about 0.30 s. When the next droplet hits the tube, the rate of concentration and temperature changes increase and the entire cycle is repeated again.

4.2.6 Heat and Mass Transfer Coefficients

Figures 4.8, 4.9, 4.10, 4.11 and 4.12 present the local heat and mass transfer coefficients, temperatures and concentrations at various points on the tube at times 0.264 s,

0.275 s, 0.284 s, 0.305 s and 0.337 s, respectively. The state of the flow at each time step is shown in the picture below the plot. The heat and mass transfer coefficients are calculated at eleven axial locations on the tube, marked on the x-axis in the plot. The distances on the x-axis are measured from the center of the tube or the point of droplet formation. Thus, 0 mm denotes the tube center, while 10 mm denotes a point close to the edge of the tube shown in the figure. For each axial location, the heat and mass transfer coefficients are calculated at five points along the tube circumference. These are labeled as 0°, 45°, 90°, 135° and 180° in the plots.

The local heat transfer coefficient at a point on the liquid-vapor interface is defined as the ratio of the normal local heat flux at that point and the difference between the local lithium bromide solution temperature at the interface and the bulk solution temperature. The bulk solution temperature is calculated by averaging the temperature of the lithium bromide solution over the entire computational domain. This is shown in Equation 4.4.

$$h = \frac{q''_n}{T_{int} - T_{bulk}} \tag{4.4}$$

The local mass transfer coefficient at any point on the interface is defined as the ratio of the normal local mass flux at that point and the difference between the local interface concentration and the bulk lithium bromide solution concentration. The bulk solution concentration is calculated by averaging the concentration of the lithium bromide solution over the entire computational domain. This is shown in Equation 4.5.

$$h_m = \frac{J_{i,n}}{Y_{i,bulk} - Y_{i,int}} \tag{4.5}$$

The fluxes q''_n and $J_{i,n}$ are calculated in the direction normal to the liquid-vapor interface. The normal direction is calculated using the principle that the density gradient is maximum in the direction normal to the interface.

Figure 4.8 presents the local heat and mass transfer coefficients, temperatures and concentrations at 0.264 s. As shown in the picture of the flow attached to the plot, at

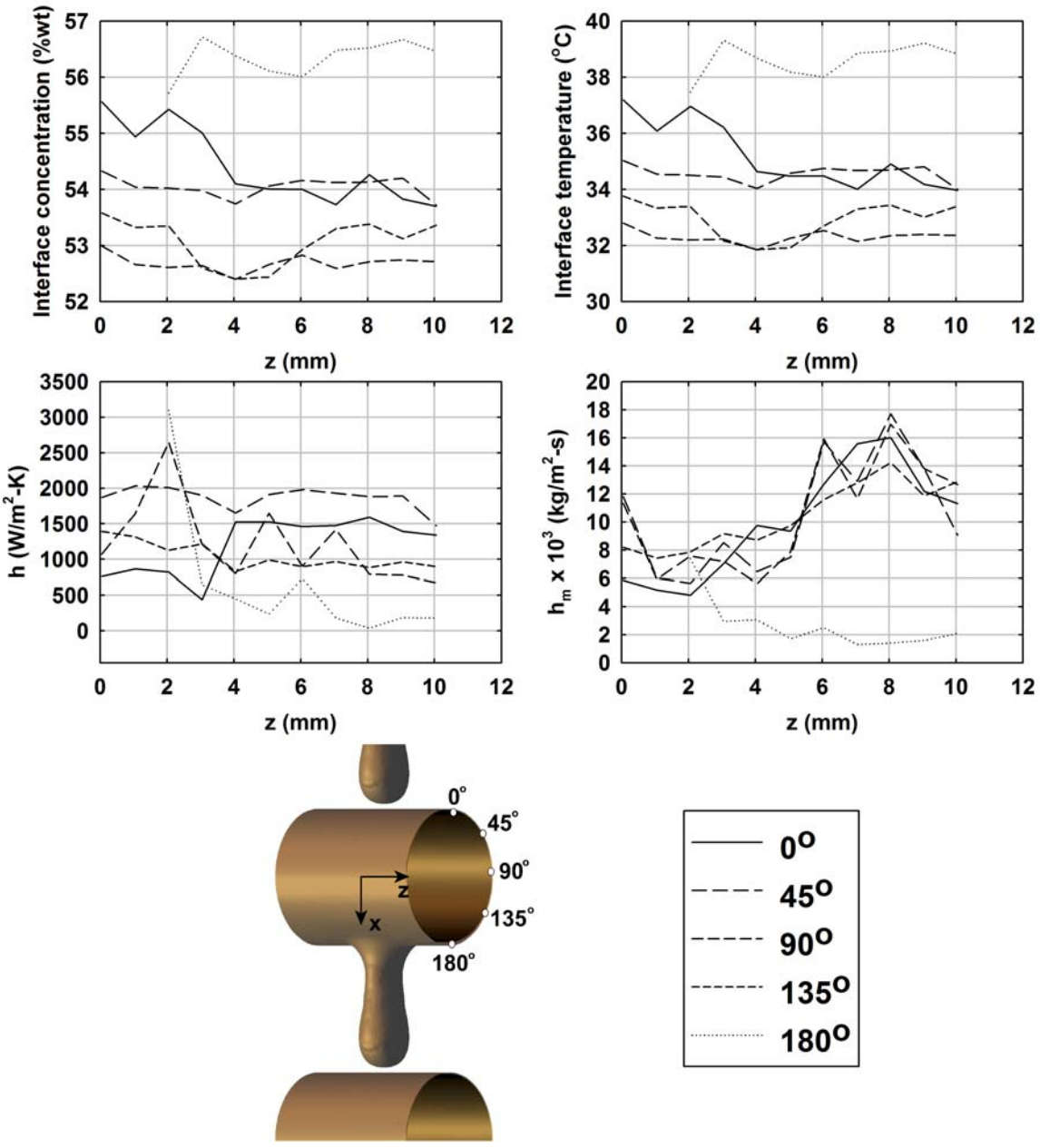

Figure 4.8: Local heat and mass transfer coefficients at 0.264 s

this time step, the droplet has formed and is close to hitting the next tube. At this time step, the lithium bromide solution is between the first two tubes in the column. The droplet is rapidly growing by drawing fluid away from the film over the tube. As a result of this flow of fluid towards the droplet, the lithium bromide film is thickest at the base of the tube (180°). Due to the higher film thickness, the fluid in these regions is not cooled effectively by the coolant, leading to a rise in the temperature of the lithium bromide solution. For example, at a distance of 3 mm from the center of the tube, the temperature at 180° is 39.31 ℃, while the temperatures at 0°, 45°, 90° and 135° are, 36.21 ℃, 34.44 ℃, 32.23 ℃ and 32.17 ℃, respectively. Similarly, at a distance of 8 mm from the center of the tube, the temperature at 180° is 38.94 ℃, while the temperatures at 0°, 45°, 90° and 135° are, 34.90 ℃, 34.69 ℃, 32.35 ℃ and 33.43 ℃, respectively.

As the interface concentration is a strong function of the interface temperature, its variation is very similar to the temperature variation. The concentration is high at points with a high temperature, while it is low at points with a low temperature. Due to the higher film thickness, the temperature is high at 180°. Consequently, the concentration is higher at 180°. For example, at a distance of 3 mm from the center of the tube, the concentration at 180° is 56.72%, while the concentrations at 0°, 45°, 90° and 135° are, 55.01%, 53.98%, 52.64% and 52.60%, respectively. Similarly, at a distance of 8 mm from the center of the tube, the concentration at 180° is 56.52%, while the concentrations at 0°, 45°, 90° and 135° are, 54.26%, 54.13%, 52.71% and 53.38%, respectively.

The large film thickness also results in lower heat and mass transfer coefficients at 180° than at other points along the circumference of the tube. This is seen in Figure 4.8, where the heat and mass transfer coefficients corresponding to 180° are lower than the others. At a distance of 5 mm from the center of the tube, the heat transfer coefficient at 180° is 237 W/m^2-K, while the heat transfer coefficients at 0°,

45°, 90° and 135° are, 1529 W/m^2-K, 1910 W/m^2-K, 1647 W/m^2-K and 989 W/m^2-K, respectively. Also, at a distance of 5 mm from the center of the tube, the mass transfer coefficient at 180° is 1.71×10^{-3} kg/m^2-s while the mass transfer coefficients at 0°, 45°, 90° and 135° are, 9.34×10^{-3} kg/m^2-s, 7.49×10^{-3} kg/m^2-s, 7.86×10^{-3} kg/m^2-s and 9.73×10^{-3} kg/m^2-s, respectively.

Figure 4.9 presents the local heat and mass transfer coefficients, temperatures and concentrations at 0.275 s. At this time step, the droplet has just hit the next tube and a wave has been created due to the impact of the droplet. The impact of the droplet causes a *mixing* of the lithium bromide film over the tube. This causes the higher concentration fluid from below the surface to rise up to the surface. As a result, the surface concentration increases at the region of impact. This is seen in Figure 4.9, where the concentrations at 0° are higher than any at other point on the circumference. For example, at an axial distance of 5 mm, the concentration at 0° is 56.05%, while the concentration at 45°, 90°, 135° and 180° are 53.65%, 52.55%, 52.73% and 55.34%, respectively. The mixing effect at 0° is only felt up to an axial distance of 5 mm from the tube center, as the wave due to droplet impact has only propagated to 5 mm at this time. Hence, the interface concentration drops sharply beyond 5 mm. At 0°, the interface concentration at 5 mm is 56.05%, while that at 6 mm is 56.05%.

This *mixing effect* is also seen in the temperature field, where the temperature at 0° is higher than that at other locations on the circumference. For example, at 5 mm, the temperature at 0° is 38.07 ℃ while the temperature at 45°, 90°, 135° and 180° are 33.88 ℃, 32.08 ℃, 32.38 ℃ and 36.79 ℃, respectively. Since, the mixing effect at 0° is only felt up to an axial distance of 5 mm, the interface temperature drops sharply beyond 5 mm. At 0°, the interface temperature at 5 mm is 38.07 ℃, while that at 6 mm is 32.62 ℃. The temperature is also high at 180° due to the high film thickness and the resulting poor thermal contact with the coolant. As seen from the figure, the

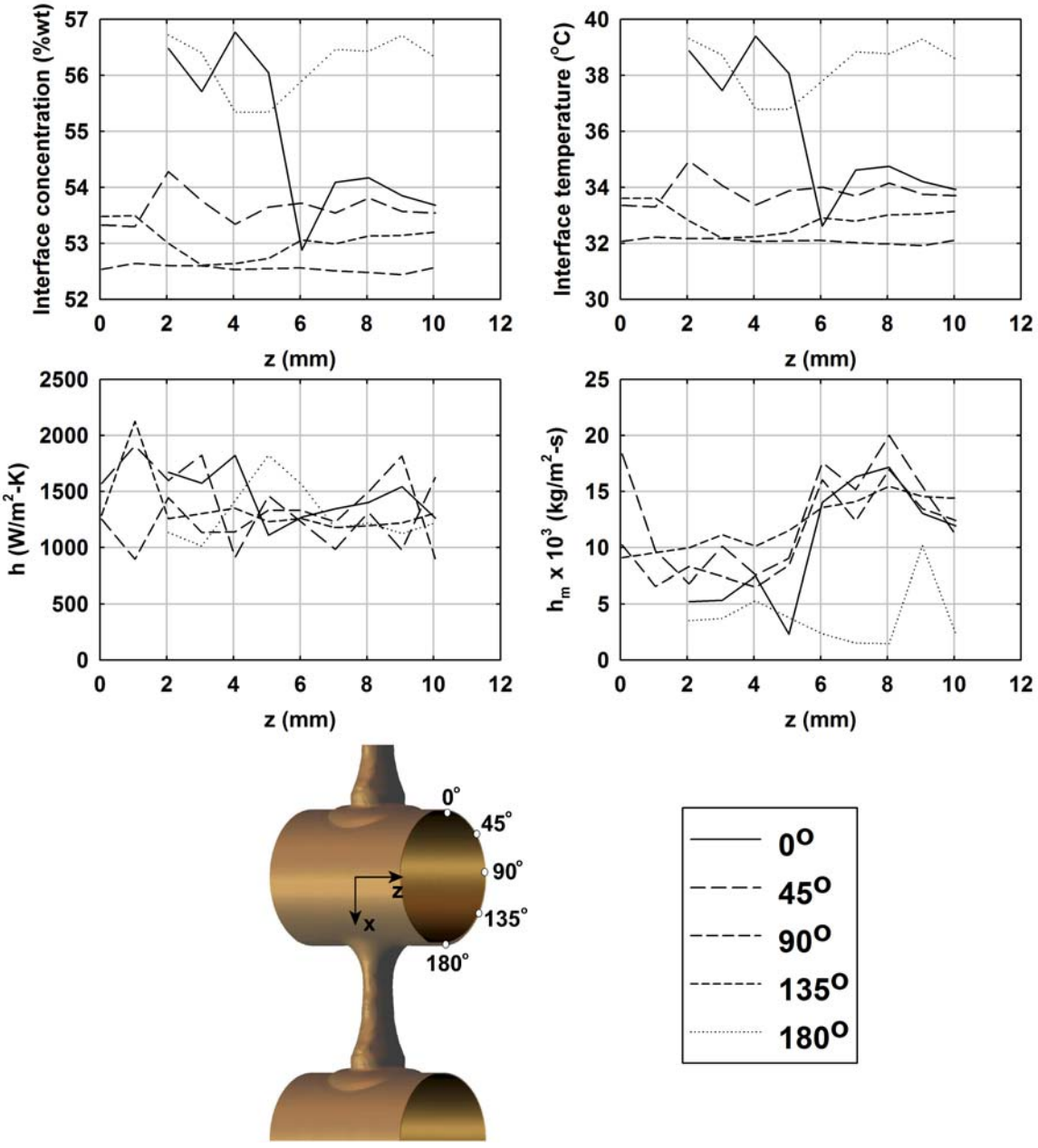

Figure 4.9: Local heat and mass transfer coefficients at 0.275 s

mixing does not have a significant effect on the heat and mass transfer coefficients. Instead, the effect increases the rate of absorption by increasing the difference between the concentration at the surface of the fluid and the equilibrium concentration. The mass transfer coefficient is lower at 180° as compared to the other locations, due to the higher film thickness. Also due to droplet impact at 0° and the drawing of fluid towards the fluid at 45°, 90° and 135°, the film thickness is higher closer to the center of the tube. Beyond 5 mm, the film thickness decreases, causing an increase in the mass transfer coefficients. For example, the mass transfer coefficients at 0°, 45°, 90° and 135° at an axial distance of 4 mm are, 7.5×10^{-3} kg/m^2-s, 7.6×10^{-3} kg/m^2-s, 6.5×10^{-3} kg/m^2-s and 10.1×10^{-3} kg/m^2-s, respectively, while those at an axial distance of 6 mm are, 14.0×10^{-3} kg/m^2-s, 17.6×10^{-3} kg/m^2-s, 16.1×10^{-3} kg/m^2-s and 13.6×10^{-3} kg/m^2-s, respectively . However, the higher film thickness does not seem to have a very significant impact on the heat transfer coefficient. This is because the thermal transport properties of the lithium bromide solution are much better than the mass transport properties.

Figure 4.10 presents the heat and mass transfer coefficients, temperatures and concentrations on the surface of the lithium bromide film at 0.284 s. The state of the flow at this time step is shown in the adjoining picture. The wave that was generated at the previously plotted time step (Figure 4.9) has propagated a little. The propagating wave front causes an increase in the heat and mass transfer coefficients. At the 45° angle, the wave front is at the 8 mm axial location at this time, causing a local increase in heat and mass transfer coefficients. At the 45° locations, the mass transfer coefficient at 8 mm is 19.7×10^{-3} kg/m^2-s, while the mass transfer coefficients at 7 mm and 9 mm are, 14.6×10^{-3} kg/m^2-s and 15.1×10^{-3} kg/m^2-s, respectively.

The peak of the heat transfer coefficient seems to lag behind the mass transfer coefficient peak. At 45°, while the maximum mass transfer coefficient was observed at 8 mm, the maximum heat transfer coefficient was observed at 6 mm. While the mass

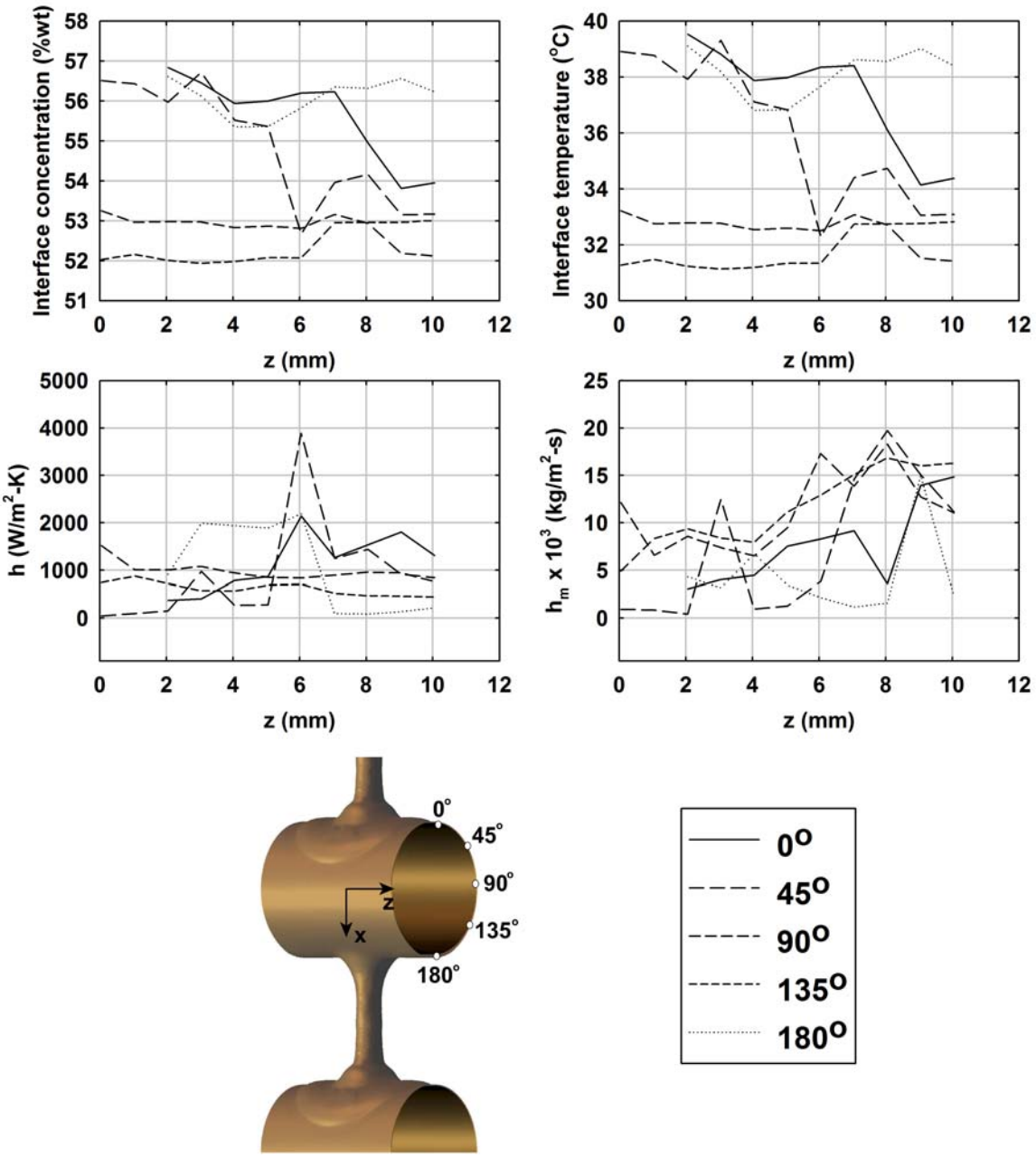

Figure 4.10: Local heat and mass transfer coefficients at 0.284 s

transfer happens primarily at the liquid-vapor interface, the heat transfer is greater closer to the tube. As a result, fluid velocities underneath the surface of the film will have a greater impact on the heat transfer than they do on the mass transfer. Due to the viscous forces, the wave propagates at a lower velocity underneath the surface as compared to the wave on the surface. As a result of this, the peak of the heat transfer coefficient lags the peak of the mass transfer coefficient. At 45°, the heat transfer coefficient at 6 mm is 3889 W/m^2-K, while the heat transfer coefficients at 5 mm and 7 mm are, 279 W/m^2-K and 1248 W/m^2-K, respectively.

The propagation of the wave also mixes the concentration distribution in the lithium bromide solution, and brings to the surface the high concentration solution from underneath. As a result, the surface concentrations are higher at 0° and 45°, where the wave has passed through, as compared to 90°, where the wave is yet to reach. For example, at an axial position of 4 mm, the concentrations at 0° and 45° are 55.94% and 55.52% respectively, while the concentration at 90° is lower at 52.83%. Due to a higher film thickness and poorer thermal contact with the coolant, the interface temperature temperature is higher at 180°, as compared to the other locations. Since the interface concentration is a function of the interface temperature, it is also relatively high at 180°.

Figure 4.11 shows the heat and mass transfer coefficients, concentration and temperature at 0.305 s. As shown in the figure, at this time the wave formed due to droplet impact has propagated to the lower half of the tube. The position of the wave front is around the 135° mark on the tube. This causes an increase in the mass transfer coefficient at 135°. As seen in Figure 4.11, the mass transfer coefficient at the axial location of 3 mm is 16.10×10^{-3} kg/m^2-s at 135°, while the mass transfer coefficients at 0°, 45°, 90° and 180° are, 4.97×10^{-3} kg/m^2-s, 7.35×10^{-3} kg/m^2-s, 3.54×10^{-3} kg/m^2-s and 3.35×10^{-3} kg/m^2-s, respectively. Though the mass transfer coefficient increased at the wave front, there was found to be no significant increase

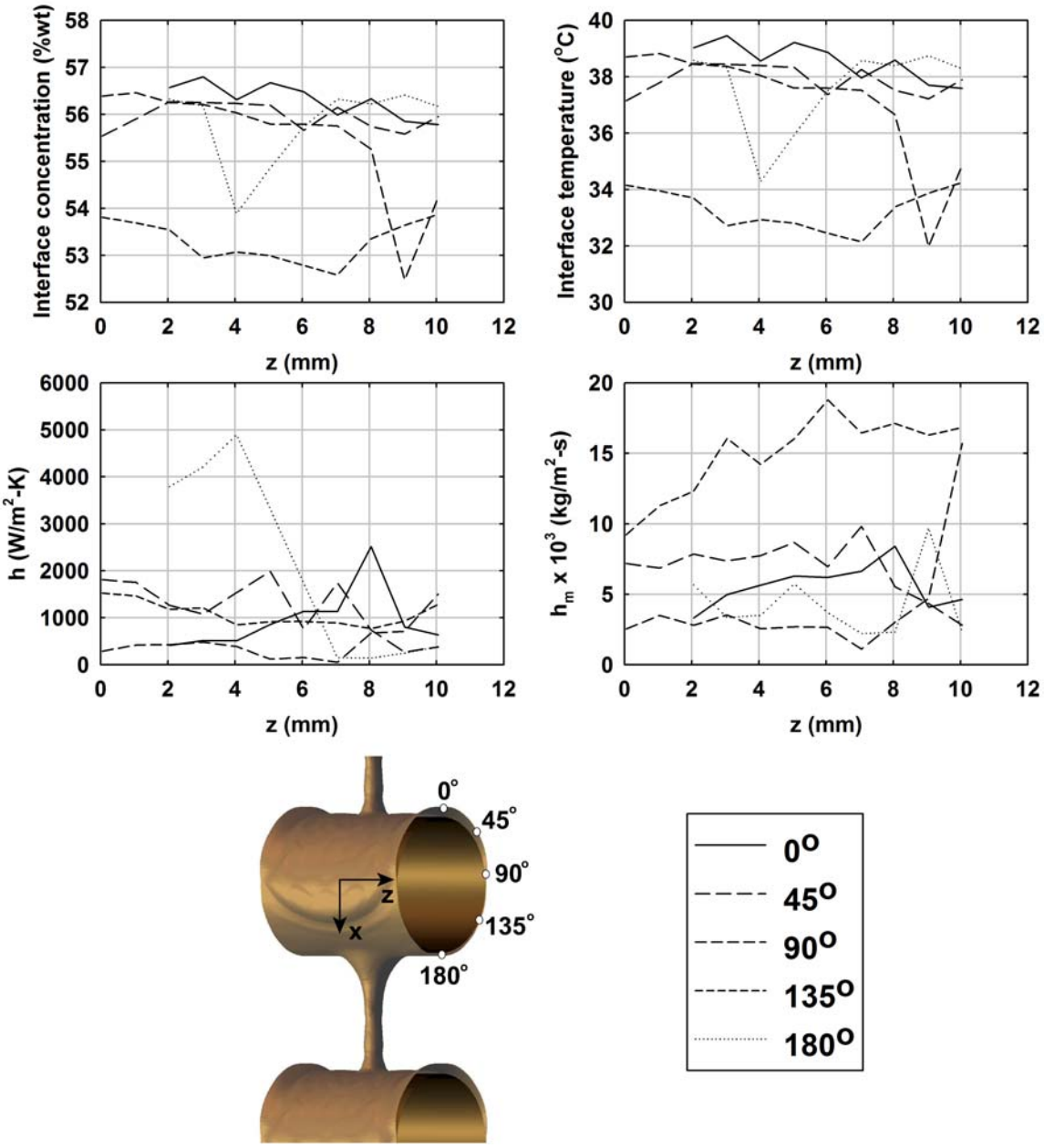

Figure 4.11: Local heat and mass transfer coefficients at 0.305 s

in the heat transfer coefficient due to the wave front. As mentioned earlier, this could be because the heat transfer is primarily governed by the conditions close to the tube under the surface, as opposed to conditions at the liquid surface.

The heat transfer coefficient is seen to be high at 180° near the point of droplet formation. For example, at an axial distance of 2 mm, the heat transfer coefficient at 180° is 3790 W/m^2-K, while the heat transfer coefficients at 0°, 45°, 90° and 135° are, 416 W/m^2-K, 1264 W/m^2-K, 426 W/m^2-K and 1176 W/m^2-K, respectively. The high heat transfer coefficient near the regions of droplet formation is due to the high local velocities at these points. The high velocity is a result of the lithium bromide solution being drawn from these points by the falling liquid bridge. This high heat transfer coefficient is in spite of the film thickness being high at 2 mm at 180°. The film thickness at 2 mm at 180° is 3.25 mm, while that at 10 mm is 0.54 mm. This is because the local velocity at 2 mm at 180° is 0.10 m/s, while that at 10 mm is 0.03 m/s.

The wave front and its resulting mixing causes the low temperature solution from the bottom of the film to be moved closer to the surface. As a result the temperature of the lithium bromide solution is lower at 135° than other locations on the circumference. For example, at an axial distance of 3 mm, the temperature at 135° is 32.72 ℃, while the temperatures at 0°, 45°, 90° and 180° are, 39.46 ℃, 38.44 ℃, 38.37 ℃ and 38.32 ℃, respectively. Since the interface concentration is a function of the interface temperature, the concentration is also low at 135°, as compared to other locations. At an axial distance of 3 mm, the interface concentration at 135° is 52.94%, while those at 0°, 45°, 90° and 180° are, 56.80%, 56.25%, 56.21% and 56.18%, respectively.

Figure 4.12 presents the concentrations, temperatures and heat and mass transfer coefficients at 0.337 s. At this time step, the *liquid bridge* is about to detach from the upper tube, accompanied with the formation of a *satellite droplet*. By this time step, the impact of the droplet and the subsequently generated waves have mixed the

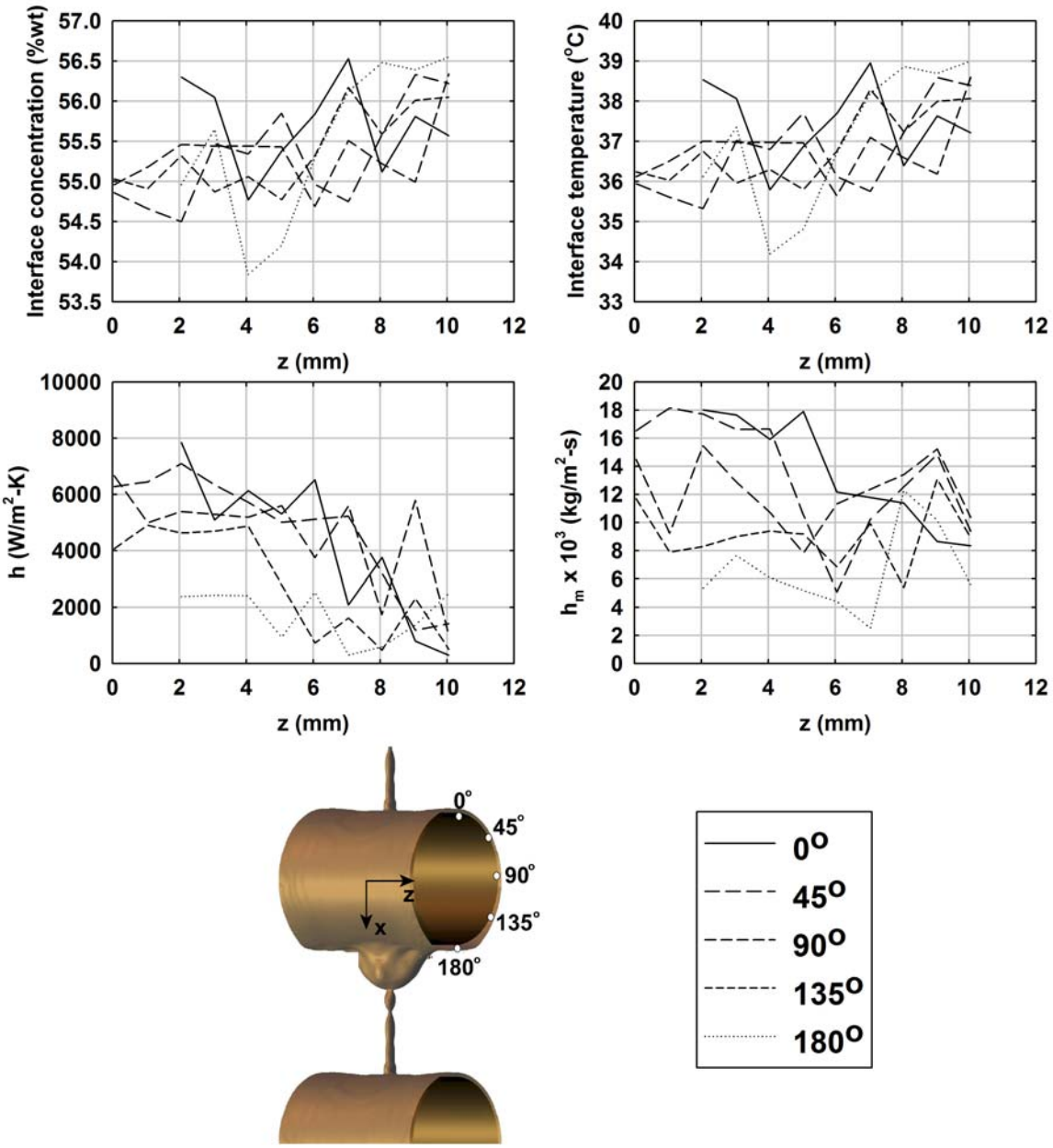

Figure 4.12: Local heat and mass transfer coefficients at 0.337 s

lithium bromide solution very well. The surface concentrations are higher towards the end of the tube as compared to closer to the center. For example, at 135°, the concentrations at axial locations 3 mm, 6 mm, and 9 mm are, 54.87%, 55.32% and 56.01%, respectively. This increase in concentration towards the ends of the tube is due to the fact that the waves generated due to droplet impact have passed through the end regions more recently than the center regions of the tube. These waves mix the film and bring the high concentration solution from under the surface closer to the surface, where the mass transfer process occurs. The lithium bromide solution at the surface near the center of the tube has had enough time since the passing of the wave to absorb water vapor, causing a decrease in its surface concentration.

Similar to the interface concentration, the temperature also slightly increases towards the end of the tube. This is also due to the fact that the waves have passed through the end regions of the tube more recently. For example, at 135°, the interface temperatures at axial locations 3 mm, 6 mm and 9 mm are, 35.96 ℃, 36.75 ℃ and 38.00 ℃, respectively.

The film around the tube is slightly thicker towards the ends than near the center of the tube. This is due to the waves formed due to droplet impact having passed through those regions more recently. Due to the higher thickness, the heat and mass transfer coefficients are slightly lower towards the ends of the tube than near the center. For example, at 45°,the heat transfer coefficients at the axial locations of 2 mm, 4 mm and 6 mm are, 7087 W/m^2-K, 5721 W/m^2-K and 5110 W/m^2-K. Similarly, at 45°, the mass transfer coefficients at 2 mm, 4 mm and 6 mm are, 17.7×10^{-3} kg/m^2-s, 16.6×10^{-3} kg/m^2-s and 5.1×10^{-3} kg/m^2-s.

4.2.7 Film concentration and temperature profiles

Figures 4.13, 4.14, 4.15, 4.16 and 4.17 present the concentration and temperature profiles in the lithium bromide solution film on the tube at times 0.264 s, 0.275 s, 0.284 s, 0.305 s and 0.337 s, respectively. The x-axis of these plots represents a non-dimensional distance from the tube surface, which is obtained by dividing the distance from the tube by the film thickness at that point. This is shown in Equation 4.6

$$\overline{y} = \frac{y}{\delta} \tag{4.6}$$

where,

$\overline{y}$ is the non-dimensional distance from the tube surface,

y is the dimensional distance form the tube surface, and

δ is the film thickness.

The non-dimensional concentration at a point is obtained by dividing the difference in the concentration at that point and the bulk concentration, by the difference between the initial concentration and the bulk concentration. This is shown in Equation 4.7

$$\overline{Y_i} = \frac{Y_i - Y_{i,bulk}}{Y_{i,ini} - Y_{i,bulk}} \tag{4.7}$$

This dimensionless concentration represents the change in the local concentration at that point as compared to the change in the bulk concentration of the entire solution.

Similarly, the non-dimensional temperature at a point is obtained by dividing the difference in the temperature at that point and the bulk temperature, by the difference between the initial temperature and the bulk temperature. This is shown in Equation 4.8

$$\overline{T} = \frac{T - T_{bulk}}{T_{ini} - T_{bulk}} \tag{4.8}$$

The dimensionless temperature represents the change in the local temperature at that point as compared to the change in the bulk temperature of the lithium bromide solution.

The concentration and temperature profiles are plotted at five locations along the tube circumference. These are labeled as 0°, 45°, 90°, 135° and 180° in the plots. Within each angular location, the profiles are plotted for eleven axial locations on the tube. Each set of plots correspond to a particular angular location, while each of the lines within the plot correspond to an axial location within the angular location. The axial distances are measured from the center of the tube or the point of droplet formation. Thus 0 mm denotes the tube center, while 10 mm denotes a point close to the edge of the tube shown in the figure.

Figure 4.13 shows the concentration and temperature profiles at 0.264 s. At this time, the lithium bromide solution in the film has accumulated at a point to form a droplet and the droplet has grown to such a size that it is close to hitting the next tube.

It is seen in Figure 4.13 that for most points on the tube, the concentration is highest close to the surface of the tube and then decreases away from the surface, towards the liquid-vapor interface. This is because the lithium bromide solution at the interface absorbs water vapor from the vapor phase, causing a decrease in its concentration. Due to the poor mass diffusivity of water vapor in lithium bromide ($D_{AB} = 1.6 \times 10^{-9}$ m^2/s), most of the water vapor does not transport towards the inner regions of the film, but remains near the surface.

However, at points close to the center of the tube, the concentration is almost uniform. In fact for certain cases, it is low near the tube surface and increases slightly towards the liquid-vapor interface. This is because, when the droplet forms at the center of the tube, it draws lithium bromide solution from the film around the tube, towards the droplet. This displacement of liquid near the droplet formation

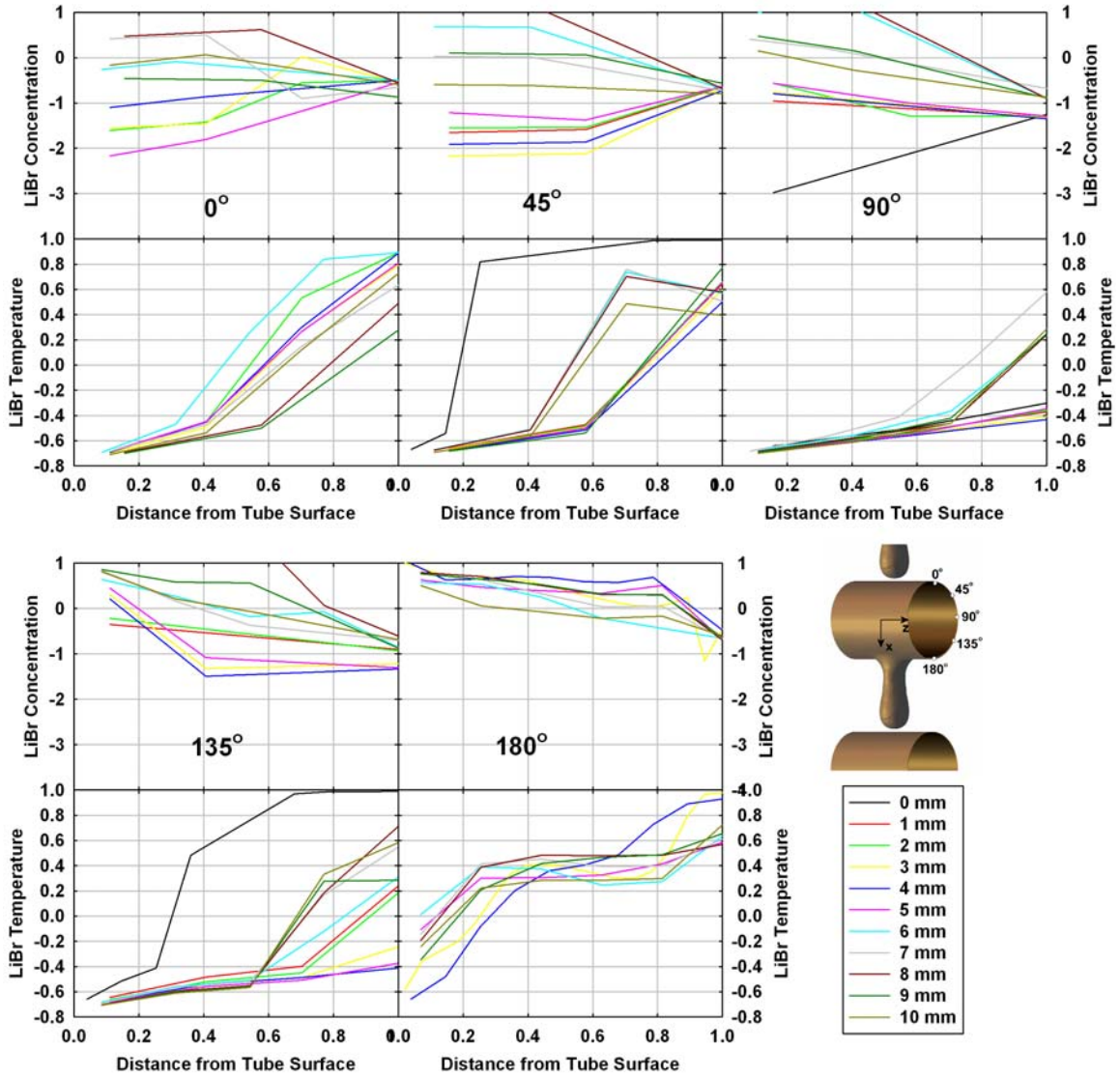

Figure 4.13: Concentration and temperature profiles at 0.264 s

site draws away fluid near the liquid-vapor interface and presents newer liquid surfaces for absorption. This mixes the concentration profiles, creating a more uniform concentration profile at these points.

It is also seen in Figure 4.13 that the temperature is lowest close to the surface of the tube and highest close to the liquid-vapor interface. The absorption that happens close to the liquid-vapor interface is an exothermic process, causing a rise in the temperature of the solution close to the surface. To compensate for this rise in temperature, the lithium bromide solution is cooled by a coolant flowing through the inside of the tube. Due to the cooling provided by this coolant, the lithium bromide solution close to the tube surface is at a lower temperature.

Typically, the thickness of the lithium bromide solution film over the tube was very small (between 0.1 mm and 1.0 mm). Due to computational limitations there were usually very few grid cells (< 10) in the thin film region. Because of this limitation, the slopes in the profile plots may not be very accurate. For instance, lithium bromide solution possesses much better thermal transport properties ($k = 0.6$ W/mK than mass transport properties ($D_{AB} = 1.6 \times 10^{-9}$ m^2/s). As a result, the concentration gradients close to the interface are steeper than the temperature gradients. However, due to insufficient nodes in the film region, the difference in the gradients is not very perceptible. At 180°, i.e. at the bottom of the tube, the film is thicker due to the accumulation of liquid from the rest of the film, due to gravity. Due to the larger thickness, there are a greater number of nodes within the film at 180°, compared to other locations. As a result, the profile shapes are more accurate at 180°. Here it is seen that the concentration profile has a steep gradient close to the interface, while the temperature has a much shallower gradient, due to better transport properties. Similarly, due to droplet formation, the film is thicker at the center of the tube (0 mm), resulting in a more accurate representation of the profile at this point. It is seen in Figure 4.13 that the 0 mm line (black color) sticks out from the other lines

for 45° and 135° due to this difference in thickness.

There are two thermal boundary layers and one concentration boundary layer within the film. The concentration boundary layer, which is formed due to the absorption of water vapor into the solution film, starts at the liquid-vapor interface and grows inwards towards the tube. Due to the poor mass transport properties of the lithium bromide solution, the rate of growth of the concentration boundary layer due to diffusion alone is very low. In Figure 4.13, the concentration boundary layer can be seen at 180°. At the other locations, the concentration boundary layer is disturbed due to the flow fields caused by droplet formation. This was explained in the previous paragraphs. There is a thermal boundary layer formed near the tube wall due to the cooling provided by the coolant in the tube. This boundary layer starts at the tube wall and grows outwards towards the liquid-vapor interface. There is another thermal boundary layer formed close to the interface due to the exothermic nature of the vapor absorption process. This boundary layer starts at the liquid-vapor interface and grows inwards towards the tube wall. The two boundary layers can be observed in Figure 4.13 in the temperature profiles at 180°. It is seen that there is sharp temperature gradient near the tube wall due to the wall boundary layer, a relatively flat region, and then another sharp gradient due to the interface boundary layer. It is seen that the wall boundary layer is the more dominant boundary layer, with the higher heat fluxes and sharper gradients. This is due to the low rate of absorption and the high temperature difference between the lithium bromide solution and the coolant. The thermal boundary layers at the other angular locations are disturbed due to the velocity flow fields caused by droplet formation.

Figure 4.14 presents the concentration and temperature profiles at 0.275 s. At this time, the droplet has hit the lower tube and a wave generated due to the impact of the droplet has just started propagating over the tube. The impact of the droplet hitting the tube mixes the solution in the film, creating a more uniform concentration

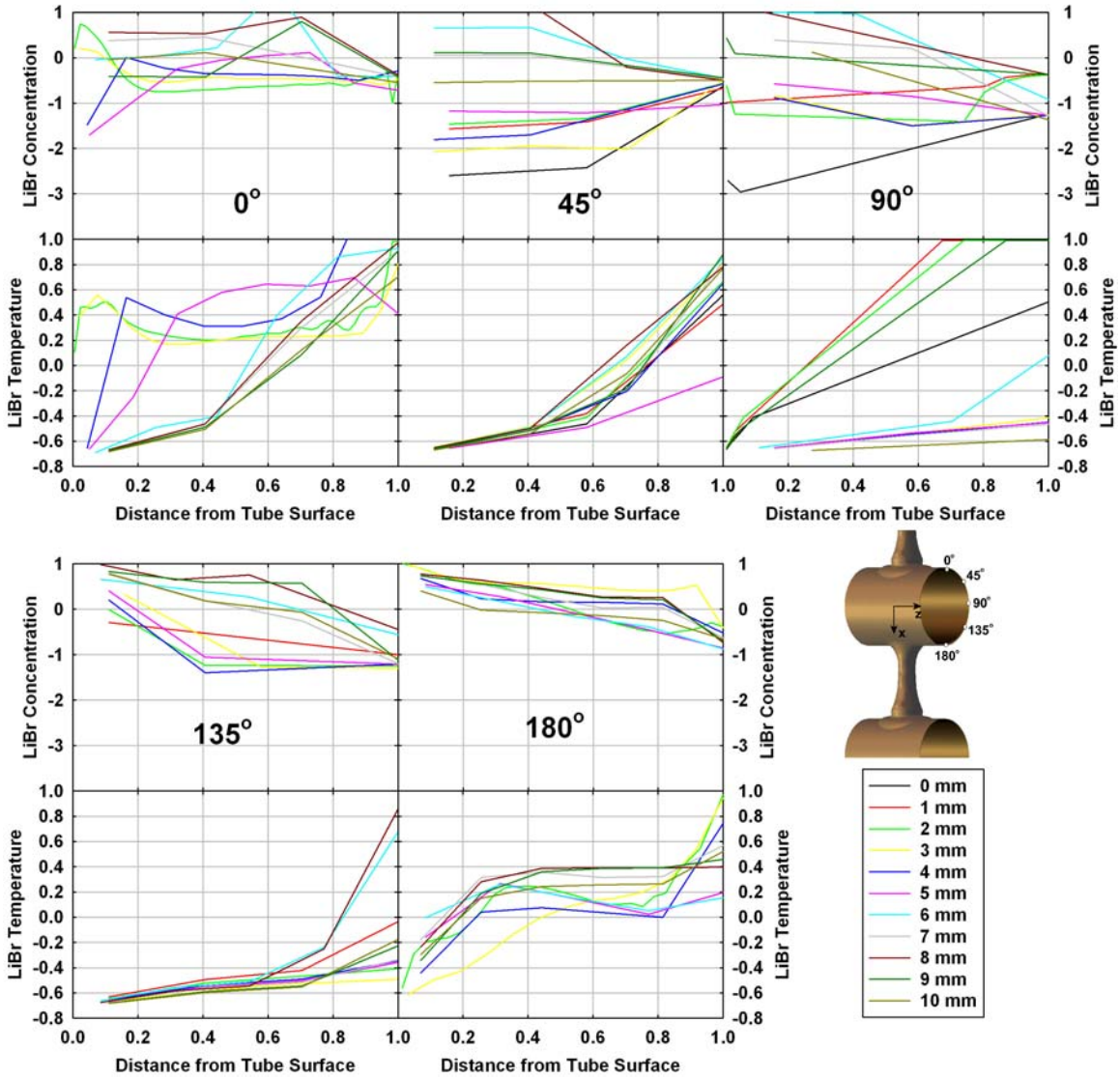

Figure 4.14: Concentration and temperature profiles at 0.275 s

profile. This is seen at 0°, where the effect of the droplet impact is felt up to about 6 mm from the point of impact of the droplet. At 0°, the concentration profiles for 0 mm to 6 mm show a much flatter gradient as compared to the concentration profiles in other regions of the tube. The film is very thick at 2 mm and 3 mm at 0°, due to the droplet and so these profile lines have significantly higher number of grid points in them. The nature of these lines is not significantly different, but their concentration and temperature profile exhibit a few local wave-like fluctuations due to the velocity fields associated with the droplet. Similarly, the film thickness is higher at 2 mm and 3 mm at 180°, resulting in the profile lines at those axial locations exhibiting a few minor variations due to the flow fields associated with droplet formation.

The mixing effect of the droplet impact is also felt on the temperature profiles. As seen in the temperature profiles for 0°, the temperature profiles are flatter in the region close to the droplet impact, due to this mixing. As in the previous time step, the profiles at 180° present a more truer picture of the actual profiles, due to the higher film thickness resulting in the presence of more nodes within the film in this region.

As seen at 45°, 90° and 135° in Figure 4.14, the temperature profile rises steeply towards the surface of the film due to vapor absorption. Due to the variable rate of absorption, the rate of rise of the temperature profile is different at different axial locations. The rates of absorption are higher towards the center of the tube due to the higher fluid velocities associated with the drawing of the fluid away from the film towards the droplet during droplet formation.

Figure 4.15 shows the concentration and temperature profiles at 0.284 s. At this time step, the wave generated due to the droplet impact has progressed a little further, to about the 45° line on the tube. The *mixing effect* is now felt on the concentration profiles at 0° and 45°. As seen in Figure 4.15, the concentration profiles at these location are flat, as the droplet impact and the subsequent waves bring to the surface,

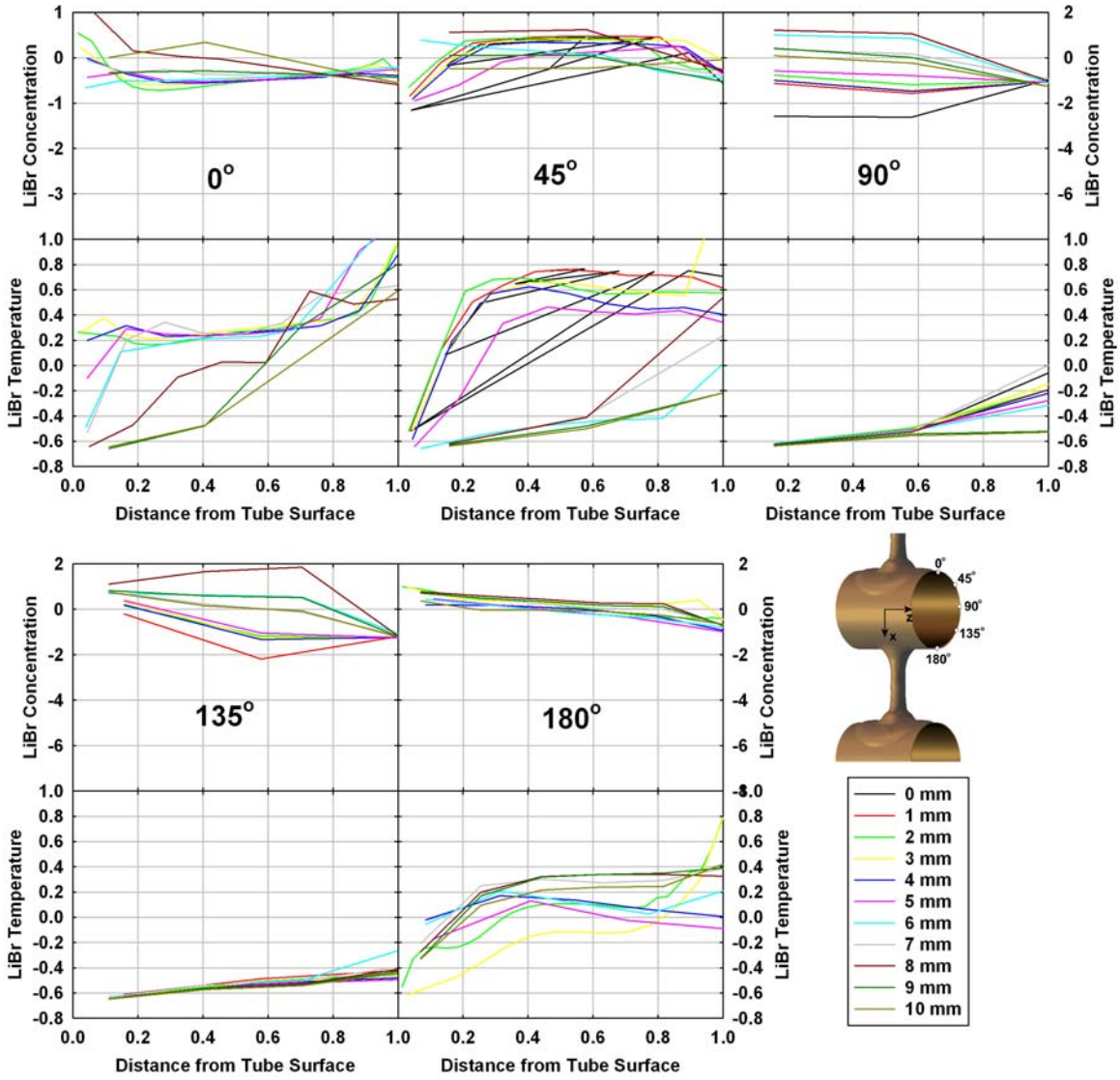

Figure 4.15: Concentration and temperature profiles at 0.284 s

the high concentration solution from underneath the surface. The *mixing effect* is also seen in the temperature profiles, where the profiles at 0° and 45° exhibit a lot more fluctuations than at the other locations, due to the local velocity fields created by droplet impact and subsequent film waviness.

The profiles at 90°, 135° and 180° do not show much change from the previous time step, as the effect of the droplet impact has not yet reached these locations. As before, the profiles at 180°, provide a more accurate representation of the actual concentration and temperature profiles.

Figure 4.16 presents the concentration and temperature profiles in the film at 0.305 s. At this time step, the wave generated due to the impact of the droplet has propagated much further all the way to about the 90° mark. The *mixing effect* is now felt at 0°, 45° and 90°. It is seen that the concentration profiles at these locations are flatter than the profiles at 135° and 180°, where the effect of the droplet impact is not yet felt.

The *mixing effect* is also seen in the temperature profiles at 0°, 45° and 90°. At these locations the temperature gradients are seen to be less steeper than the regions where the wave is yet to propagate, viz. at 135° and 180°. Also, as in the previous time steps, due to the higher film thickness, the profiles at 180° are more accurately portrayed than the other locations.

As explained earlier, there are two thermal boundary layers on the liquid film, one close to the wall due to the coolant, and the other at the interface due to the exothermic absorption. These boundary layers are seen at 180° in Figure 4.16, where there are steep increases in the temperatures at wall and at the interface and a relatively even temperature profile in between. Similarly, the steep rise due to vapor absorption is seen at 135° at the interface. However, the boundary layer near the wall at 135° was not captured due to the lack of sufficient grid points close to the wall in the thin film. As similar boundary layer development is also seen at 45°, though the

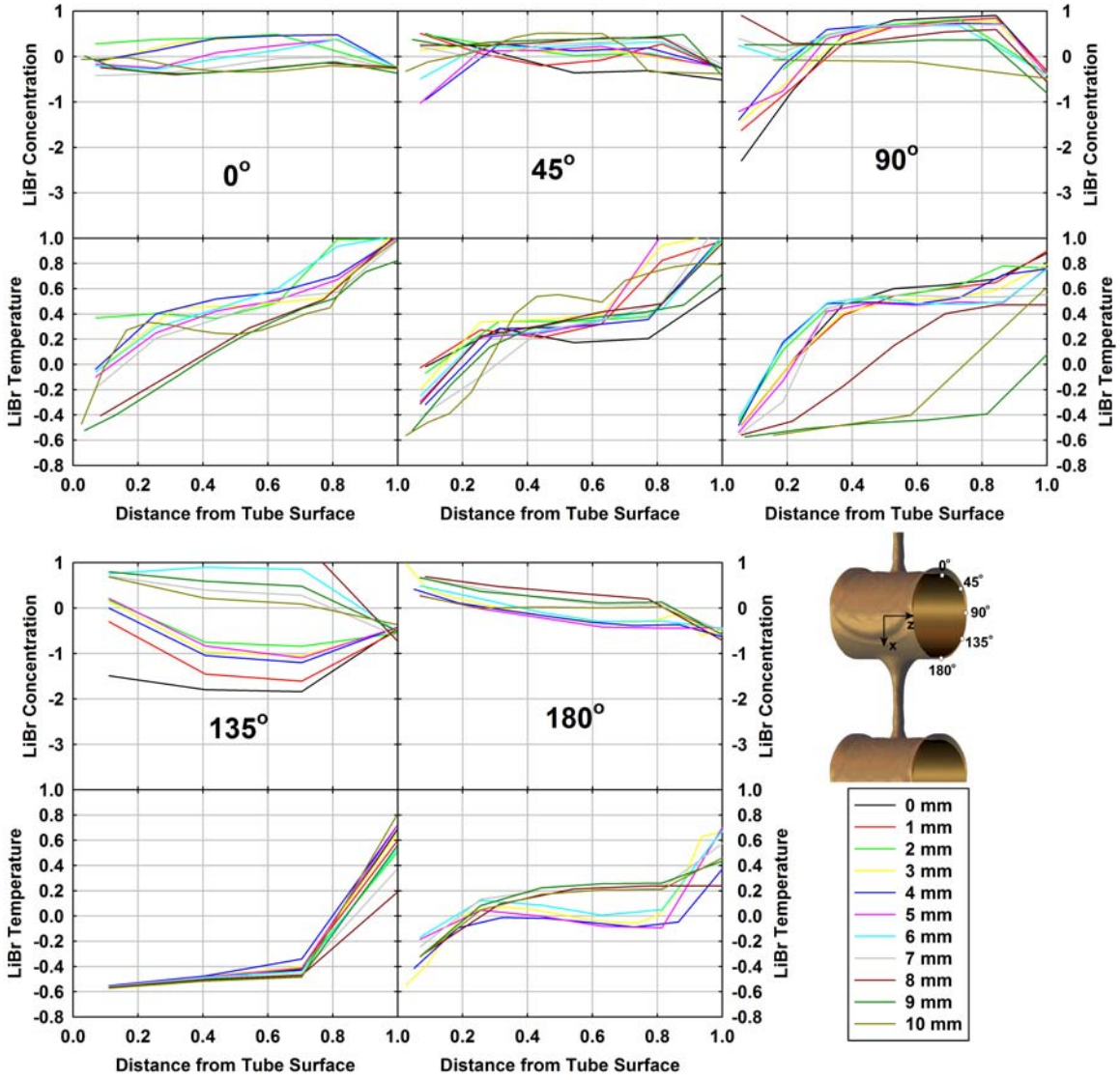

Figure 4.16: Concentration and temperature profiles at 0.305 s

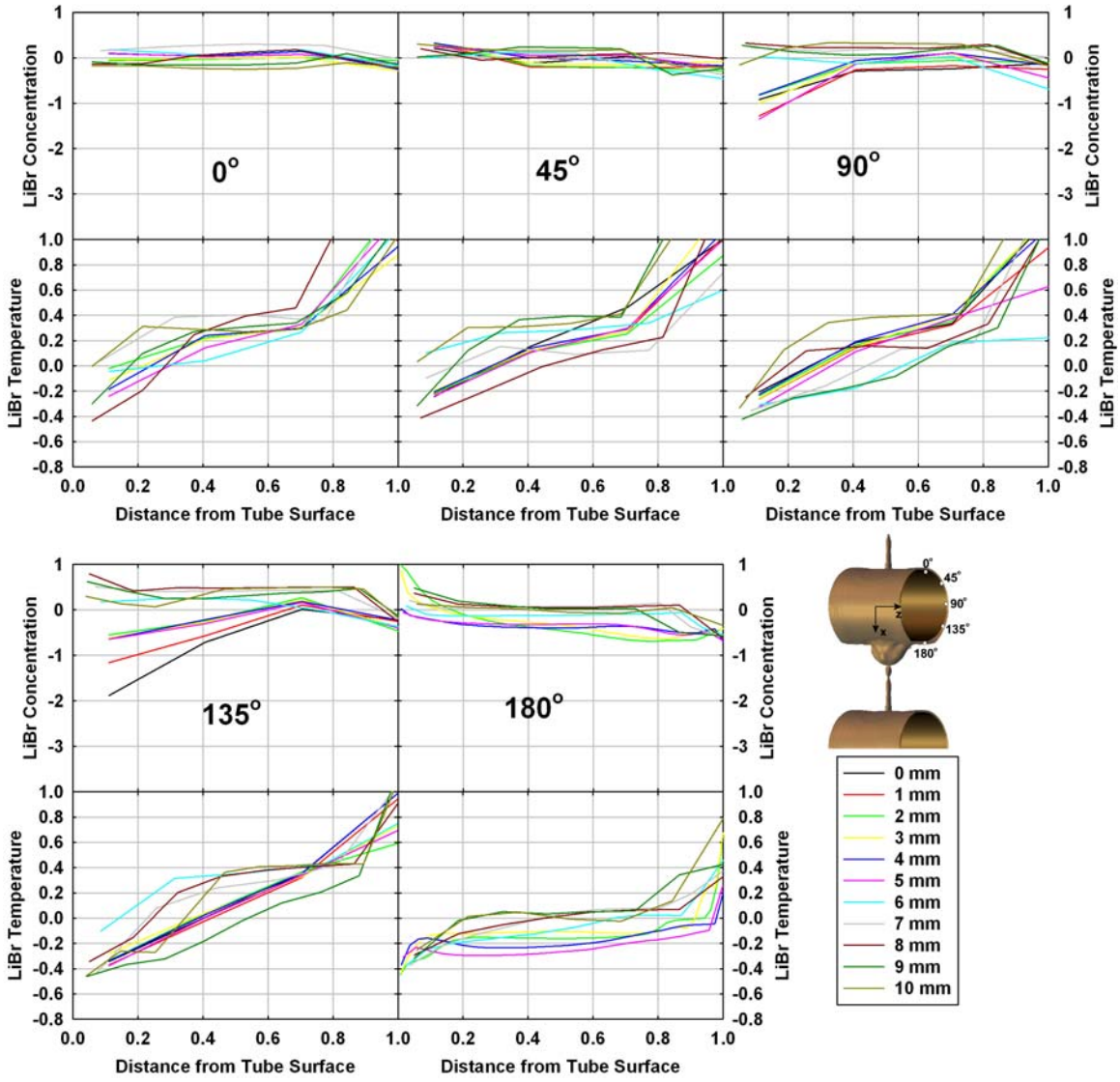

Figure 4.17: Concentration and temperature profiles at 0.337 s

profiles are quite disturbed due to the recent passage of the wave through that region. The temperature profile at 90° is highly mixed due to the very recent passage of the wave. A thermal boundary layer near the interface is disturbed and a majority of the fluid is at a higher temperature. The region near the tube wall has a sharp gradient due to the coolant.

Figure 4.17 shows the concentration and temperature profiles at 0.337 s. At this time step, the wave generated due to droplet impact has propagated throughout the tube. The liquid bridge formed by the falling droplet between the two tubes is about

to break, accompanied by the formation of a *satellite droplet*.

As seen from Figure 4.17, the *mixing effect* of the wave is now seen most at all the angular locations. The concentration profiles at all the location are flat due to the mixing associated with droplet impact and wave propagation. As with the concentration profiles, the mixing effect is also seen in the temperature profiles, where the temperature gradients are seen to be less sharp due to the mixing.

This concludes the discussion on the baseline case. It was seen that the flow exhibits some very interesting patterns such as, droplet formation, detachment, fall and impact and the resulting waves and their propagation. These flow patterns have a significant impact on the heat and mass transfer process. The local heat and mass transfer coefficients were seen to increase with the increased local velocity due to the wave. The impact of the droplet mixes the concentration profiles and exposes newer surfaces of the film for mass transfer.

The average Reynolds number for the case was always less than 110. The average solution flux was 0.0086 kg/ms. The average heat transfer coefficient for this case was found to be 1500 W/m^2-K, while the average mass transfer coefficient was found to be 4.67×10^{-3} kg/m^2-s. The average Nusselt number (based on the tube diameter) for the flow was 39.8, while the average Sherwood number was 29.2. The average absorption flux on the film was 6.65×10^{-4} kg/m^2-s, while that on the droplet was 1.78×10^{-4} kg/m^2-s. The droplet accounted for 4.4% of the total absorption in the lithium bromide solution.

In the following sections, a number of the absorber operating conditions will be varied and their effects studied at a local level.

Table 4.2: Operating conditions for the 6.35 mm diameter tube case

Operating parameter	**Baseline case**	**Present case**
Solution inlet concentration	65% by wt of LiBr	65% by wt of LiBr
Solution inlet temperature	40.5 ℃	40.5 ℃
Tube wall temperature	30 ℃	30 ℃
Tube diameter	*15.9 mm*	*6.35 mm*
Tube pitch	*15.9 mm*	*5.12 mm*
LiBr mass flux	*0.0086 kg/ms*	*0.011 kg/ms*

4.3 Different tube geometry

After having studied the local characteristics of the flow for the baseline case, the effect of a change in the tube geometry was studied. The baseline case consisted of a column of tubes of diameter 15.9 mm, spaced 15.9 mm apart. In the present case, the flow on a column of 6.35 mm diameter tubes, spaced 5.12 mm apart is investigated. These dimensions were obtained from the work by Jeong and Garimella [55]. Table 4.2 summarizes the operating conditions for this case. In the range of time computed, the average Reynolds number in this case was found to be always less than 470. The average mass flux in this case was 0.011 kg/ms.

4.3.1 Flow pattern

Figure 4.18 presents the flow patterns for this geometry at nine different time steps. As in the previous case, the two main forces acting on the fluid are *gravity* and *surface tension*. The gravitational force acts in the downward direction and causes the solution to accumulate at the bottom of the tube. This results in the formation of the droplet. This is shown in Figure 4.18 at 0.050 s. The surface tension force opposes the gravitational force and tries to hold the droplet from falling off the tube. The balance between these two forces drives the droplet formation. Gravity causes more and more fluid to accumulate in the droplet, leading to an increase in its size.

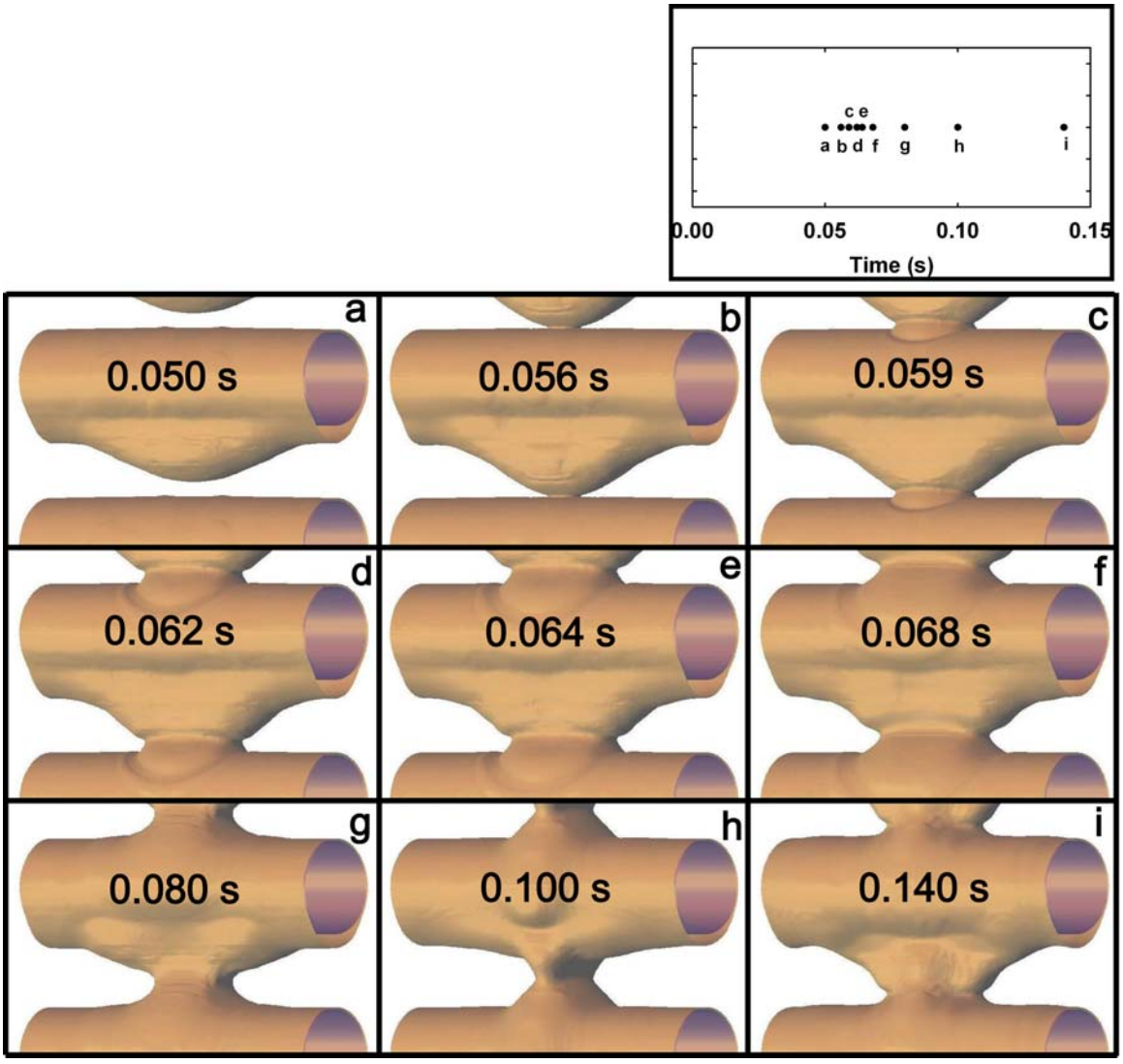

Figure 4.18: Fluid flow pattern with a 6.35 mm diameter tube

Due to the smaller tube size in the present case, the flow starts off with a thicker film than the baseline case. The baseline case starts off with a 0.35 mm film, while the present case starts with a 0.70 mm film. Due to the thicker film and the shorter inter-tube distance, the droplet hits the next tube before it fully attains the typical droplet shape. As seen in the frame at 0.056 s, the droplet hits the next tube before the formation of a *neck* region and breaking off from the previous tube. As seen from the subsequent time steps, due to the smaller geometry, the droplet never completely breaks off from the previous tube. The flow between the two tubes occurs through a liquid bridge, whose thickness varies with the local liquid flow rate.

When the droplet hits the next tube, the impact of the droplet causes a *ripple* or *wave* on the solution film on the tube. This is seen at time steps 0.062 s, 0.064 s and 0.068 s in Figure 4.18. Unlike the baseline case, in the present case the wave generated due to the droplet impact does not seem to propagate axially all the way to the end of the tube. The wave seems to die down after about 6 mm from the center of the tube (0.080 s). This difference in the behavior of the wave is due to the following reasons:

- Due to lower inter-tube distance (5.12 mm as opposed to 15.9 mm), the droplet impacts the tube with lower momentum than the baseline case.
- The thicker film in the present case damps the wave more than the thinner film in the baseline case.
- As the liquid bridge does not break in the present case, a significant portion of the fluid in the falling droplet is drawn towards the bridge rather than propagate axially with the wave.

As will be seen later, the wave and its propagation along the tube plays a crucial role in heat and mass transfer.

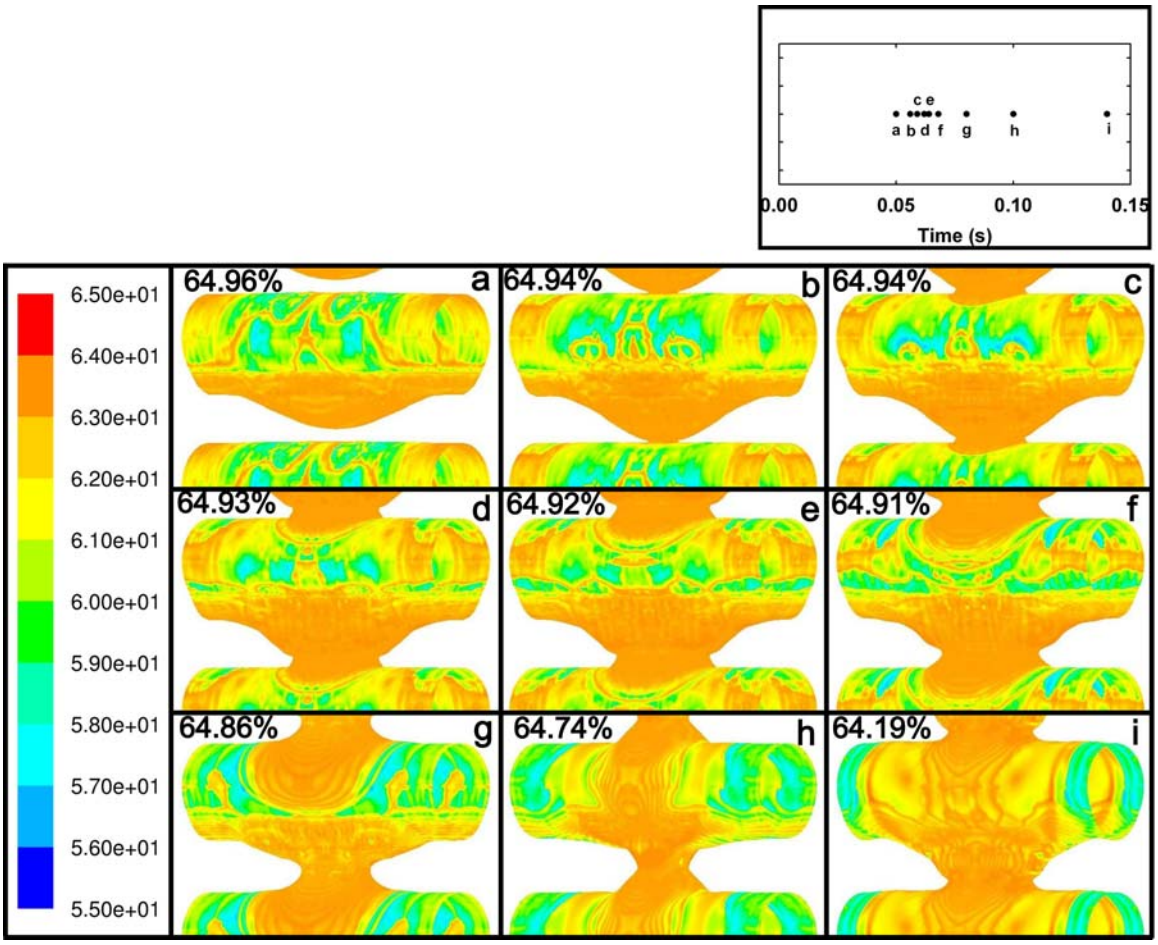

Figure 4.19: Concentration variation within the LiBr solution for flow over a 6.35 mm diameter tube

4.3.2 Concentration distribution

Figure 4.19 shows the local changes in the lithium bromide concentration as it falls down the column of tubes. As shown in the accompanying scale, the local concentrations are represented by varying colors, with red denoting the highest concentration at 65% and blue denoting the lowest concentration at 55%. Concentrations in between these limits are denoted in a decreasing order by different shades orange, yellow and green respectively. All concentrations are represented as a percentage weight of lithium bromide in the solution. The average concentration of the lithium bromide solution at each of the time steps is also printed in the frame.

As the lithium bromide solution falls, it absorbs water vapor, causing a decrease

in its concentration. The absorption happens at the liquid-vapor interface and as a result, the concentration is lowest at the interface. Also the absorption of water vapor being an exothermic process causes a rise in the temperature of the solution. In order to sustain the absorption, the solution needs to be cooled by the coolant flowing on the inside of the tube. As a result of this, the vapor absorption rates are higher in the interfaces close to the tube, as compared to interfaces on the droplet, which are in poor thermal contact with the coolant in the tube.

Initially, the lithium bromide solution is present as a film around the tube at a uniform concentration of 65%. When the droplet starts forming, the concentration of the solution in the droplet decreases at a slower rate as compared to the solution in the film over the tube. This is seen in the first frame (average concentration 64.96%), where most of the film over the tube is green or blue in color, while most of the solution in the droplet is yellow or orange in color. This is because the solution in the film, being closer to the coolant tube, is cooled more effectively than the solution in the droplet. This cooling compensates for the heating of the solution during the exothermic absorption process and helps sustain a higher absorption rate on the film. The higher absorption rate results in more vapor being absorbed on the film, resulting in lower concentrations.

As explained earlier, the absorption of water vapor happens at the surface of the lithium bromide solution. Due to the low mass diffusivity of water in lithium bromide ($D_{AB} = 1.6 \times 10^{-9}$ m^2/s), the water vapor is not transported efficiently to the interior of the solution, but stays near the interface. This reduces the difference between the interface concentration and the equilibrium concentration, which is the driving potential for the mass transfer. This causes a gradual decrease in the vapor absorption rate. When the droplet falls on the tube, the impact of the droplet mixes the lithium bromide solution in the film forming a more uniform concentration distribution in it. This is seen in Figure 4.19 in the frames with average concentrations 64.93%,

64.92%, 64.91% and 64.86%. Before the droplet impacts the film (average concentration 64.94%), the surface of the film on the tube is at a very low concentration (blue and green color), while the interior of the film is at a high concentration. However due to the low concentration layer on the surface, this high concentration interior cannot absorb any water vapor. When the droplet falls on the tube, the impact of the fall mixes the fluid in the film, causing a more uniform concentration distribution in the film. This mixing causes a higher concentration at the surface of the film (orange, yellow and green colors) as seen in Figure 4.19 in the frames with average concentration 64.91% and 64.86%. Unlike the baseline case, the waves generated due to the droplet impact do not propagate axially all the way to the end of the tube. Hence the mixing effect due to the droplet impact also does not occur in the regions near the end of the tube. This is seen in the frames with average concentrations 64.86% and 64.74%, where the effect of mixing is only felt up to a distance of about 6 mm from the center of the tube. In the frame with average concentration 64.19%, the mixing effect is seen to occur up to about 8 mm away from the tube center. However, the mixing effect was never seen to propagate all the way to the end of the tube. The *mixing effect* significantly increases the overall mass transfer rates by presenting newer surfaces of the lithium bromide solution to the vapor for absorption, thus acting as a very important catalyst for the absorption phenomenon.

Unlike the baseline case, in the present case, due to the small geometry and high flow rate, the droplet never detaches from the previous tube. After the impact of the first droplet, a *liquid bridge* is created between the two tubes and a continuous flow of the lithium bromide solution occurs through the bridge. As a result, after the impact of the first droplet, no further droplet impact occurs. Consequently there is no significant *mixing effect* or *wave generation* after the first droplet. This absence of the mixing affect plays a detrimental role in the absorption process. The average absorption mass flux in this case was 2.44×10^{-4} kg/m^2-s, while that in the baseline

case was 5.94×10^{-4} kg/m^2-s.

4.3.3 Temperature distribution

Figure 4.20 shows the variation in the temperature of the lithium bromide solution as it falls through the tubes. The different temperatures are denoted by the variation in the colors, with red denoting the hottest temperature at 40.5 ℃ and blue denoting the coldest temperature at 30 ℃. Temperatures between these two extremes are denoted, in the order of decreasing temperatures, by various shades of orange, yellow and green, respectively. Also, the average temperature of the lithium bromide solution at that time step is printed in each frame.

Since the absorption process is exothermic, it causes an increase in the temperature of the solution at the liquid-vapor interface. To compensate for this heating, the lithium bromide solution is cooled by a coolant flowing inside the tubes. The solution in the film over the tube is usually low in temperature as it is cooled very effectively by the coolant inside the tube. The solution in the droplet, being farther away from the coolant, is not cooled very effectively and hence is warmer. This is seen in Figure 4.20 where, most of the solution in the film over the tube is marked in yellow or green, while most of the solution in the droplet is marked in orange.

Initially, the flow starts off with all the lithium bromide solution as a thin film over the tube at a uniform temperature of 40.5 ℃. As the droplet starts forming, the fluid in the droplet is at a warmer temperature than the film around the tube. The film around the tube cools better than the droplet due to better thermal contact with the coolant in the tube at 30 ℃. This is seen in Figure 4.20 in the frames with average temperatures 39.20 ℃, 39.04 ℃ and 38.96 ℃, where the solution in the droplet is shaded in orange, while the solution in the film over the tube is marked in yellow and green.

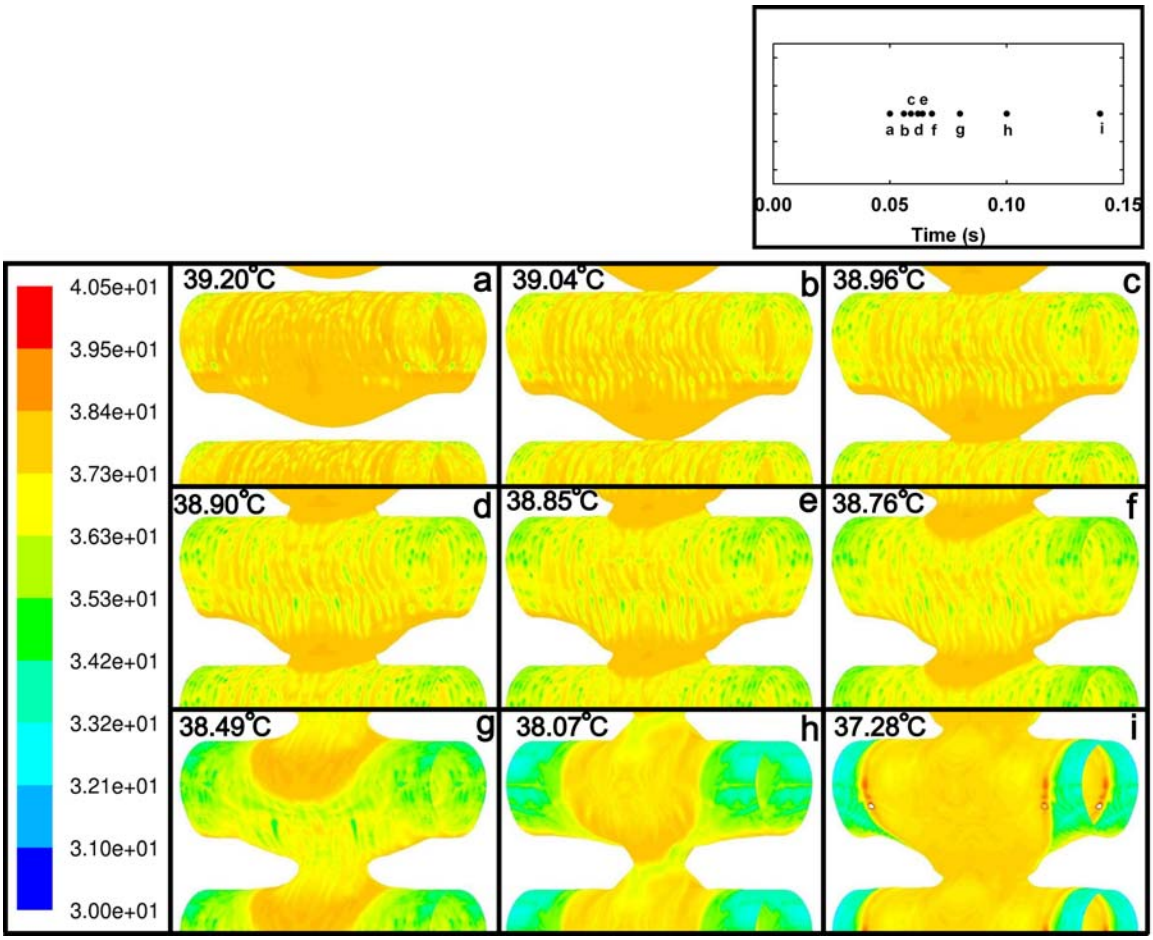

Figure 4.20: Temperature variation within the LiBr solution for flow over a 6.35 mm diameter tube

When the droplet falls on the next tube, as with the concentration distribution, the impact of the droplet has a *mixing effect* on the temperature distribution. This is seen in Figure 4.20 in the frames with average temperatures 38.85℃, 38.76℃, 38.49℃ and 38.07℃. Before the droplet impact, the lithium bromide solution in the film is cooled (marked in yellow and green colors), while the solution in the droplet is much warmer (marked in orange color). The warm temperature solution has a much lower potential for absorption of water vapor. When the droplet impacts on the tube, the fluid in the droplet region mixes with the fluid in the film forming a more even temperature distribution throughout the solution. This is noticeable in Figure 4.20 in the frame with average temperature 38.07℃, where a significant portion of the lithium bromide solution is close to the average temperature at that time step, and is marked in orange. However, as discussed earlier, the mixing effect only occurs up to about 6 mm from the center of the tube. Beyond 6 mm from the center, the film is still unmixed. This is seen in the frames with average temperatures 38.49℃ and 38.07℃. The temperature in this unmixed region is low due to a low film thickness and the resulting good thermal contact with the coolant. This *mixing effect* is very beneficial to the absorption phenomenon and is one of the biggest advantages of a drop-wise flow regime.

As mentioned earlier, in the present case, due to the small geometry and high flow rate, the droplet never detaches from the previous tube. After the impact of the first droplet, a *liquid bridge* is created between the two tubes and a continuous flow of the lithium bromide solution occurs through the bridge. As a result, after the impact of the first droplet, no further droplet impact occurs. Consequently there is no significant *mixing effect* after the first droplet.

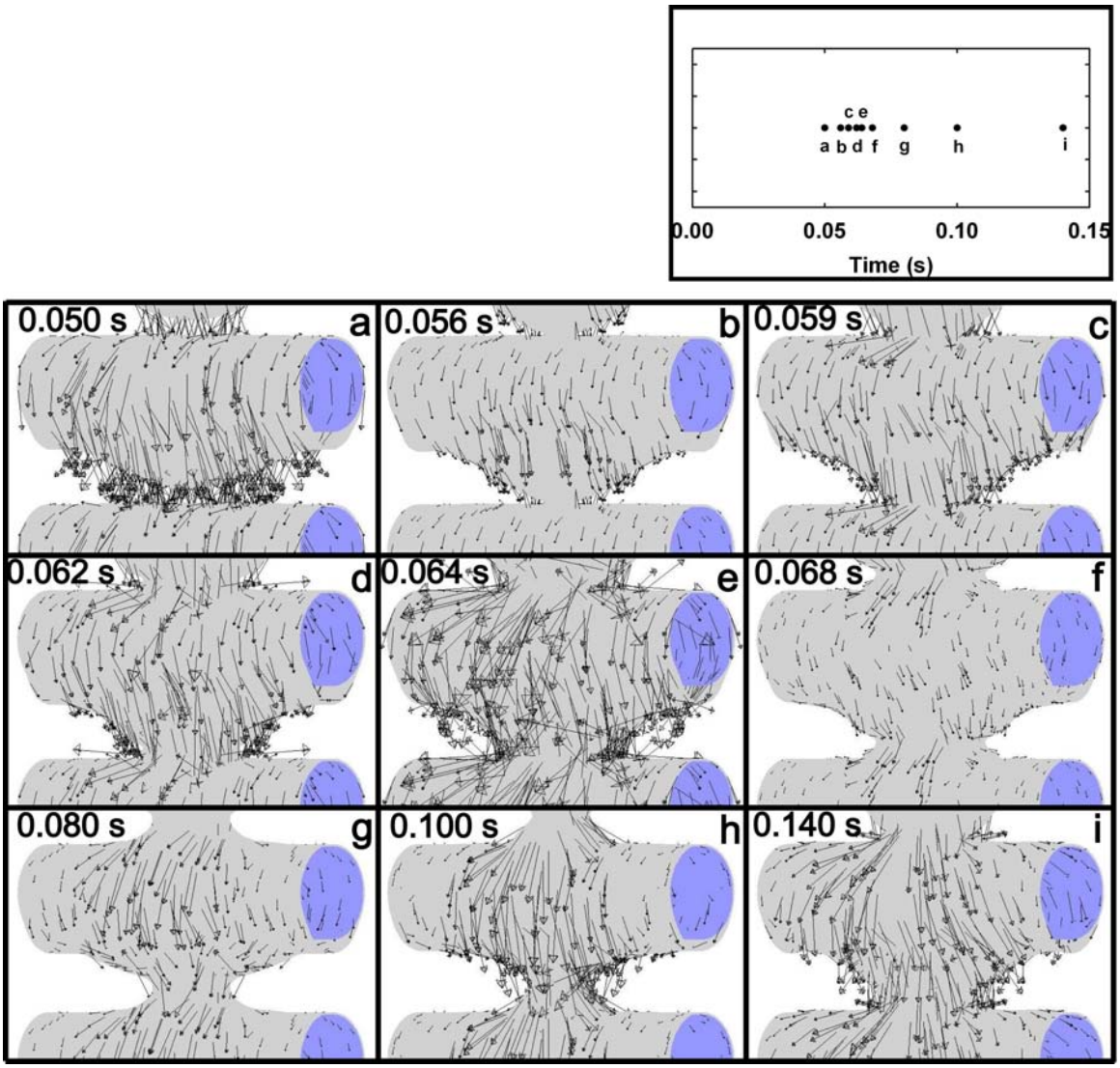

Figure 4.21: Velocity vectors for a 6.35 mm diameter tube

4.3.4 Velocity distribution

Figure 4.21 shows the distribution of velocity in the lithium bromide solution. The velocity is represented by a series of arrows, where the direction of the arrows denotes the direction of the velocity vector, while the length of the arrow is proportional to the magnitude of the velocity at that point.

Initially, the lithium bromide solution is present around the tube as a stationary film of thickness greater than that in the baseline case. Due to the thicker film, the outer regions of the film do not experience much of the retarding viscous force from

the tube. As a result, the outer layers of the film fall down very quickly due to gravity. This is seen in Figure 4.21 at 0.050 s. Once the fluid in the outer layer falls from the tube and accumulates at the bottom of the tube, the thickness of the film on the tube decreases. This thinner film is more affected by he retarding viscous forces near the tube wall. As a result, the velocity of the outer layers of the film decreases. This is seen in Figure 4.21 at time step 0.056 s, where the velocity vectors are shorter than those at 0.050 s. Similarly at 0.068 s, when a bulk of the fluid is between the tube resulting in a very thin film on the tube, the velocity of the fluid on the outer layers of the film on the tube is quite low. Such a variation in the velocities due to the change in the film thickness was not seen in the baseline case as the film thickness was much lower in that case and the fluid in the outer regions of the film always experienced the viscous forces from the tube wall. Also, as seen in Figure 4.21, the fluid velocity near the tube center is higher than that near the ends due to a higher film thickness.

When the droplet falls on the tube, the impact of the fall causes the fluid to be dispersed in all directions in the form of waves. This is seen in Figure 4.21 at time steps 0.062 s and 0.064 s, where, the fluid velocity at the point of impact is seen to the spread in all direction at high magnitudes. The formation and propagation of these waves have a significant impact on the heat and mass transfer processes.

4.3.5 Bulk concentration and temperature variation

Figure 4.22 shows the temporal variation of the average concentration and temperature of the lithium bromide solution. The flow patterns at the respective times are shown above the plot. The concentration and temperature variations are compared with those for the baseline case, which are represented by a dashed line in Figure 4.22.

Initially, the lithium bromide solution is present at a uniform concentration of

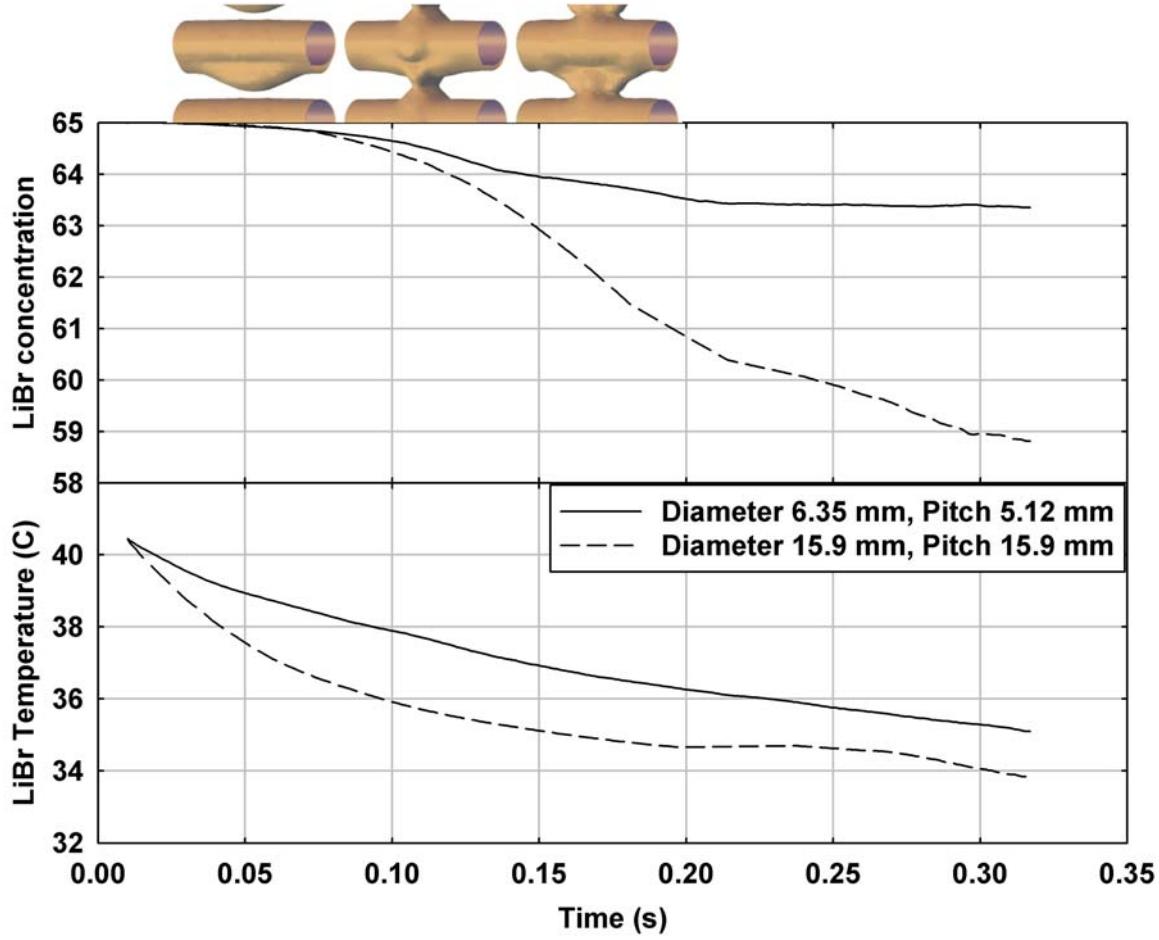

Figure 4.22: Bulk concentration and temperature for flow over a 6.35 mm diameter tube

65%. As the droplet falls, it absorbs water vapor, causing a decrease in its concentration. The absorption is driven by the difference between the concentration of lithium bromide solution at the interface and the vapor pressure equilibrium concentration. The vapor pressure equilibrium concentration is a function of the lithium bromide solution temperature at the interface. This variation of the equilibrium concentration with the lithium bromide solution temperature was shown in Figure 4.7. The equilibrium concentration decreases with a decrease in the lithium bromide solution temperature.

Initially the lithium bromides solution is at a temperature of 40.5 °C. At this temperature, the equilibrium concentration is 57.35%. Due to proximity to the coolant, the lithium bromide solution in the film rapidly cools to close to 30 °C. This is seen in Figure 4.22 in the plot on temperature variation, where the temperature decreases at a rapid rate initially. At 30 °C, the equilibrium concentration is 51.20%. Initially when the solution is warmer (40.5 °C), the rate of the mass transfer process is relatively slow due the high equilibrium concentration, and hence low driving concentration difference. However, as the temperature drops, the equilibrium concentration decreases and the high driving concentration difference results in a higher rate of mass transfer. This is seen in Figure 4.22 in the plot on concentration change, where the concentration initially decreases slowly and then starts decreasing rapidly once the solution cools down. As the film thickness is greater in the present case as compared to the baseline case, the lithium bromide solution is cooled less efficiently by the coolant. Due to this, the vapor absorption rate is initially lower in the present geometry, as compared to the previous case. This is seen in Figure 4.22, where the concentration corresponding to the baseline case (dashed line) falls faster than the present case (solid line).

Since the absorption process is exothermic, the mass transfer is accompanied by generation of heat in the lithium bromide solution. After the initial sharp drop in

temperature, the increased absorption and the accompanied heat generation causes a decrease in the rate of temperature drop. This decreased rate of cooling is also accompanied by a slight decrease in the rate of absorption. This is seen in Figure 4.22 at about 0.14 s, where both the concentration and temperature curves gradually level out after the sharp initial drops.

Due to the smaller diameter and tube spacing, and the higher film thickness, there is not a very pronounced droplet breakup and fall in the present case. After the first droplet hits the tube, the flow of the lithium bromide solution occurs through a steady liquid bridge between the two tubes. As a result, there is no droplet impact and subsequent *wave generation* after the first droplet. Consequently the *mixing effect*, which mixes the concentration profiles on the film and present newer surfaces of the liquid for absorption, is absent in the present case. Due to the lack of this extremely beneficial effect, the absorption rate in the present case drops significantly with time. This is seen in Figure 4.22, where in the absence of mixing there is barely any absorption in the present case beyond 0.20 s, while absorption continues to occur in the baseline case.

The surface area of the tube in the present case is 253.4 mm^2, while that for the baseline case in 524.5 mm^2. However, in a given absorber volume, a lot more of the smaller tubes could be accommodated, as compared to the baseline tubes. Thus the amount of mass transfer area per unit absorber volume could actually be higher for the smaller tube case. As was mentioned earlier, the reason for the poorer performance of the smaller tube geometry is the lack of drop-wise flow and the resultant mixing. The flow occurs as a continuous liquid bridge instead of droplets due to the low inter-tube spacing and the high initial film thickness. If the tube spacing were increased from the present value to provide enough space for droplet formation and if the initial film thickness were reduced so that there is not enough fluid present to form the continuous liquid bridge to the next tube, drop-wise flow might occur. In

such a case, due to the mixing effect of the drop-wise flow the smaller tube geometry could perform as well or better than the baseline case.

4.3.6 Heat and mass transfer coefficients

Figure 4.23 presents the local heat and mass transfer coefficients, temperatures and concentrations at 0.068 s. As shown in the picture of the flow attached to the plot, at this time step the droplet has hit the next tube and a *liquid bridge* has been formed. Some waves generated by the impact of the first droplet are still present on the film. The heat and mass transfer coefficients are calculated at thirteen axial locations on the tube, marked on the x-axis in the plot. The distances on the x-axis are measured from the center of the tube or the point of droplet formation. Thus 0 mm denotes the tube center, while 12 mm denotes a point close to the edge of the tube shown in the figure. For each axial location, the heat and mass transfer coefficients are calculated at five points along the tube circumference. These are labeled as 0°, 45°, 90°, 135° and 180° in the plots.

The lithium bromide film is thickest at the base of the tube (180°). Due to the higher film thickness, the fluid in these regions is not cooled effectively by the coolant, leading to a rise in the temperature of the lithium bromide solution. For example, at a distance of 7 mm from the center of the tube, the temperature at 180° is 40.46℃, while the temperatures at 0°, 45°, 90° and 135° are, 38.74℃, 38.18℃, 38.29℃ and 38.76℃, respectively. Similarly, at a distance of 10 mm from the center of the tube, the temperature at 180° is 40.49℃, while the temperatures at 0°, 45°, 90° and 135° are, 37.41℃, 37.75℃, 37.69℃ and 37.91℃, respectively. Also, the film thickness is highest at the center of the tube and decreases gradually towards the ends, due to the presence of the liquid bridge at the center. The higher film thickness results in poorer thermal contact at the center and hence the temperature gradually decreases from the

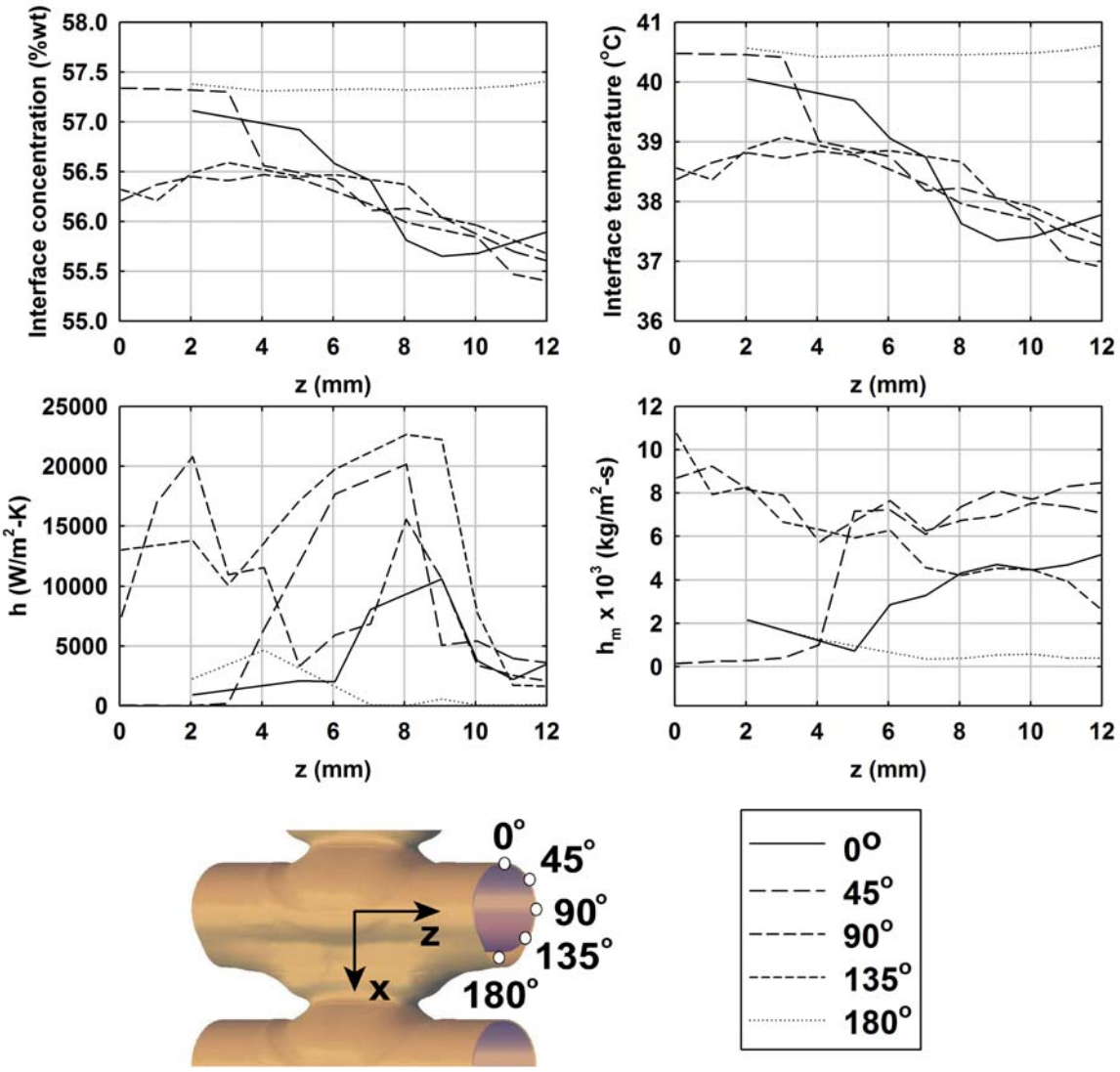

Figure 4.23: Local heat and mass transfer coefficients for flow over a 6.35 mm diameter tube

center towards the ends. This is seen in the interface temperature plots in Figure 4.23. For example, at 45° the temperatures progressively decrease from 40.48℃ at 0 mm, to 40.41℃ at 3 mm, 38.75℃ at 6 mm, 38.06℃ at 9 mm and 37.25℃ at 12 mm.

The interface concentration is a function of the interface temperature and hence follows a similar pattern. The interface concentration is higher at 180°, as compared to the other locations, due to a large film thickness. For example, at a distance of 7 mm from the center of the tube, the interface concentration at 180° is 57.33%, while the interface concentrations at 0°, 45°, 90° and 135° are, 56.41%, 56.11%, 56.17% and 56.42%, respectively. Also, similar to the temperature distribution, the interface concentration is highest at the center of the tube and gradually decreases towards the ends. For example, at 45°, the interface concentration gradually decreases from 57.34% at 0 mm, to 57.30% at 3 mm, 56.42% at 6 mm, 56.04% at 9 mm and 55.60% at 12 mm.

The large film thickness also results in lower heat and mass transfer coefficients at 180° than at other points along the circumference of the tube. This is seen in Figure 4.23, where the heat and mass transfer coefficients corresponding to 180° are lower than the others. At a distance of 7 mm from the center of the tube, the heat transfer coefficient at 180° is 74 W/m^2-K while the heat transfer coefficients at 0°, 45°, 90° and 135° are, 8066 W/m^2-K, 18896 W/m^2-K, 6854 W/m^2-K and 21191 W/m^2-K, respectively. Also, at a distance of 7 mm from the center of the tube, the mass transfer coefficient at 180° is 0.35×10^{-3} kg/m^2-s while the mass transfer coefficients at 0°, 45°, 90° and 135° are, 3.29×10^{-3} kg/m^2-s, 6.08×10^{-3} kg/m^2-s, 6.25×10^{-3} kg/m^2-s and 4.58×10^{-3} kg/m^2-s, respectively.

The wave generated due to the droplet impact increases the local fluid velocities on the film, as it propagates over the tube. These increases in local velocities cause an increase in the local heat and mass transfer coefficients. At 0°, the wave front is at about 9 mm from the center of the tube, resulting in high heat and mass transfer

coefficients around that region. The heat and mass transfer coefficients at 5 mm are 2078 W/m^2-K and 0.73×10^{-3} kg/m^2-s, while those at 9 mm are 10608 W/m^2-K and 4.72×10^{-3} kg/m^2-s, respectively. The heat and mass transfer coefficients are also high at 6 mm, 7 mm and 8 mm due to the high local velocities caused by the recent passage of the wavefront through those points. At 45°, the wavefront is at about 7 mm, resulting in high heat and mass transfer coefficients in that region. The heat and mass transfer coefficients at 4 mm are 6370 W/m^2-K and 1.01×10^{-3} kg/m^2-s, while those at 7 mm are 18896 W/m^2-K and 6.08×10^{-3} kg/m^2-s, respectively. At 90°, the wavefront is at about 2 mm from the center resulting in high heat and mass transfer coefficients in that region. The heat and mass transfer coefficients at 4 mm are 11569 W/m^2-K and 5.75×10^{-3} kg/m^2-s, while those at 2 mm are 20789 W/m^2-K and 8.16×10^{-3} kg/m^2-s, respectively. At this time step, the wavefront has not yet reached 135°, and hence does not affect the heat and mass transfer coefficients in those regions.

The heat and mass transfer coefficients along 135° are affected by the flow field generated due to the drawing to fluid towards the liquid bridge. This is particularly high close to the center of the tube, resulting in higher local velocities and higher heat and mass transfer coefficients. For example, for 135°, the heat and mass transfer coefficients at 0 mm are 13039 W/m^2-K and 10.80×10^{-3} kg/m^2-s, while those at 3 mm are 10089 W/m^2-K and 6.65×10^{-3} kg/m^2-s, respectively. Also, at 0°, 45° and 90°, the mass transfer coefficients are high towards the end of the tube due to small film thickness at these points caused by fluid being drawn away from these regions towards the liquid bridge.

4.3.7 Film concentration and temperature profiles

Figure 4.24 presents the concentration and temperature profiles in the lithium bromide solution film on the tube at 0.068 s. At this time, the droplet formed due to accumulation of the lithium bromide solution has hit the next tube, but has not detached from the previous one. There is a continuous liquid bridge connecting the two tubes. The x-axis on the plots contains a non-dimensional distance from the tube surface, which is obtained by dividing the distance from the tube by the film thickness at that point. The non-dimensional concentration at a point is obtained by dividing the difference in the concentration at that point and the bulk concentration, by the difference between the initial concentration and the bulk concentration. Similarly, the non-dimensional temperature at a point is obtained by dividing the difference in the temperature at that point and the bulk temperature, by the difference between the initial temperature and the bulk temperature.

The concentration and temperature profiles are plotted at five locations along the tube circumference. These are labeled as 0°, 45°, 90°, 135° and 180° in the plots. Within each angular location, the profiles are plotted for thirteen axial locations on the tube. Each set of plot corresponds to a particular angular location, while each of the lines within the plot correspond to an axial location within the angular location. The axial distance are measured from the center of the tube or the point of droplet formation. Thus 0 mm denotes the tube center, while 12 mm denotes a point close to the edge of the tube shown in the figure.

As seen in Figure 4.24, the concentration is highest close to the surface of the tube and then decreases away from the surface, towards the liquid-vapor interface. This is because the lithium bromide solution at the interface absorbs water vapor from the vapor phase, causing a decrease in its concentration. Due to the poor mass diffusivity of water vapor in lithium bromide ($D_{AB} = 1.6 \times 10^{-9}$ m^2/s), most of the water vapor does not transport towards the inner regions of the film, but remains near the surface.

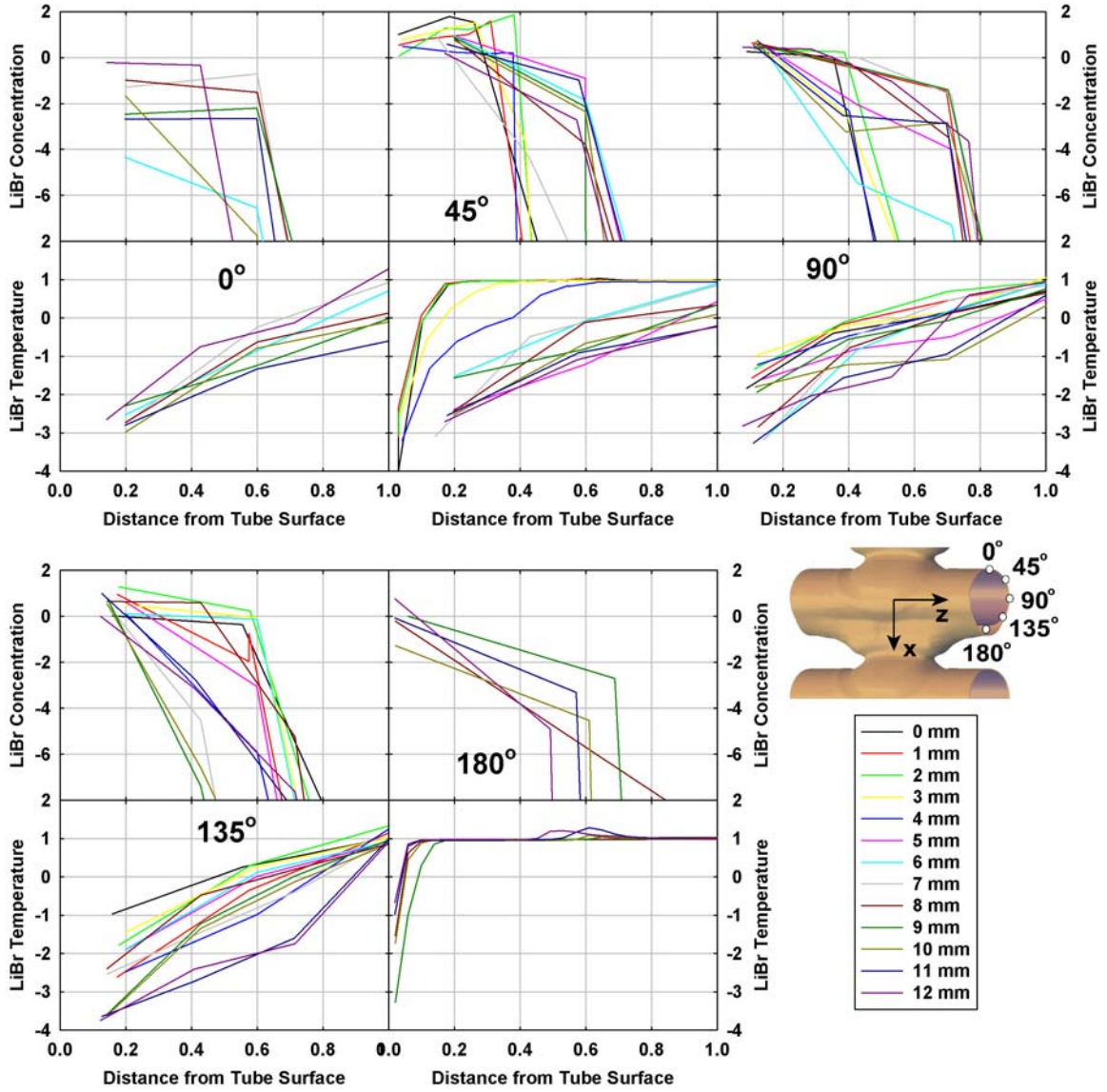

Figure 4.24: Concentration and temperature profiles for flow over a 6.35 mm diameter tube

Typically, the thickness of the lithium bromide solution film over the tube was very small (between 0.1 mm and 1.0 mm). Due to computational limitations there were usually very few grid cells (< 10) in the thin film region. Because of this limitation, the slopes and shapes of the profile plots may not be very accurate. For instance, in the concentration profiles at all of the angular locations, there is a variation in the distance from the tube at which the concentration starts decreasing to the interface concentration. This variation is not due to a difference in the actual profile, but due to difference in the locations of the very few available data points. Similarly the various points of sharp slope changes occur because there are very few data points in the film and the region between them is connected by straight lines.

It is also seen in Figure 4.24 that the temperature is lowest close to the surface of the tube and highest close to the liquid-vapor interface. The absorption that happens close to the liquid-vapor interface is an exothermic process, causing a rise in the temperature of the solution close to the surface. To compensate for this rise in temperature, the lithium bromide solution is cooled by a coolant flowing through the inside of the tube. Due to the cooling provided by this coolant, the lithium bromide solution close to the tube surface is at a lower temperature. The film thickness at 180° is higher than that at the other angular locations. As a result, the thermal boundary layer at the wall distinctly seen in the profile plot. In the wall thermal boundary layer region, the temperature rises sharply from the low temperature at the wall to the high free-stream solution temperature. Beyond the wall boundary layer, the temperature profile is relatively flat. This boundary layer and free-stream region is not seen at the other angular locations due to the small film thicknesses at those locations.

The lithium bromide solution possesses much better thermal transport properties ($k = 0.6$ W/mK than mass transport properties ($\mathrm{D_{AB}} = 1.6 \times 10^{-9}$ m^2/s). As a result the concentration gradients close to the interface are steeper than the temperature gradients. This is seen in the concentration and temperature profiles in Figure 4.24.

Due to the smaller diameter and tube spacing, and the higher film thickness, there is not a very pronounced droplet breakup and fall in the present case. After the first droplet hit the tube, the flow of the lithium bromide solution occurs through a steady liquid bridge between the two tubes. As a result there is no droplet impact and subsequent *wave generation* after the first droplet. Consequently the *mixing effect*, which mixes the concentration profiles on the film and present newer surfaces of the liquid for absorption, is absent in the present case. This is seen in the profiles in Figure 4.24, where there is no *flattening* of the concentration profiles, as was observed in the baseline case. The concentration profiles essentially stay unchanged throughout the course of the flow. As a result of this and the low mass diffusivity of water in lithium bromide, the potential for absorption gradually decreases with time. This was seen in the bulk concentration variation in Figure 4.22.

The Reynolds number for a film-wise flow around a tube is defined as $4u\delta/\nu$, where δ is the thickness of the film. The film thickness is different at different points on the tube and hence so is the Reynolds number. These local Reynolds numbers are integrated over the entire tube to calculate the average Reynolds number. Also, since the fluid velocity gradually increases with time, the Reynolds number also increases. Within the time interval computed, the average Reynolds number for this case was found to be always less than 470. The lithium bromide solution mass flux in this case was 0.011 kg/ms. The average heat transfer coefficient for this case was found to be 7024 W/m^2-K, while the average mass transfer coefficient was found to be 4.85×10^{-3} kg/m^2-s. The average Nusselt number (based on the tube diameter) for the flow was 74.3, while the average Sherwood number was 12.1. Compared to the baseline case, the heat transfer coefficient is much higher for the present case ($h = 1500$ W/m^2-K for baseline, while $h = 7024$ W/m^2-K for present case). This is expected considering the smaller tube size and higher flow velocities. However, the mass transfer coefficient is only marginally higher in the present case. ($h_m =$

4.67×10^{-3} kg/m^2-s for baseline, while $h_m = 4.85 \times 10^{-3}$ kg/m^2-s for present case). In spite of the smaller diameter and higher velocities, the mass transfer coefficient is lower than expected due to the large film thickness in the present case. The average film thickness in this case was 2.37 mm, while that in the baseline case was 0.74 mm. The mass transfer coefficient is more sensitive to film thickness than the heat transfer coefficient because the lithium bromide solution possesses much better thermal transport properties than mass transfer properties. The thermal conductivity of the solution is 0.6 W/mK, while the mass diffusivity is 1.6×10^{-9} m^2/s.

This concludes the discussion on the case with a different tube diameter and spacing. Due to the smaller spacing, it was seen that the flow occurs through a steady *liquid bridge* instead of discrete droplets. Due to the lack of discrete droplets and the impact of their fall, there is less of a *mixing effect* as was seen in the baseline case. The decreased mixing severely curtails absorption beyond the initial stages. The rate of concentration decrease at 0.12 s is 0.184 s^{-1}, while that at 0.25 s is 0.026 s^{-1}. Though the smaller tube provides high heat and mass transfer coefficients, overall it results in an *inferior* absorber, due to the difference in flow patterns. To take advantage of the reduction in size and increase in heat and mass transfer coefficients due to the smaller tubes, the flow regime needs to be changed to a drop-wise flow. This could be done by increasing the inter-tube distance so as to provide enough space for droplet breakup, and/or decrease the initial film thickness, thereby reducing the amount of fluid in the flow. Either or a combination of these two effects would restore the drop-wise flow and the resulting mixing and waves for the entire duration of the flow. This in combination with the higher heat and mass transfer coefficients and higher surface area per unit volume, could result in the design of an absorber much more efficient than the baseline case. However, it is to be noted that increasing the inter-tube distance decreases the amount of surface are per unit volume and increases the size of the absorber. Reducing the fluid flow rate could result in a need to add

Table 4.3: Operating conditions for the baseline case

Operating parameter	**Value**
Solution inlet concentration	65% by wt of LiBr
Solution inlet temperature	40.5℃
Sphere wall temperature	30℃
Sphere diameter	15.9 mm
Sphere pitch	15.9 mm
LiBr mass flux	0.0058 kg/ms

more tube banks to the absorber or increase the length of the tubes to achieve the target amount of absorption. These factors need to be considered while changing the geometry or flow rate to achieve a drop-wise flow.

4.4 Two dimensional baseline case

Having studied the effect of geometry on the absorption phenomenon, attention is now focused on the effect of the fluid inlet conditions. These include the inlet concentration, temperature, flow rate and the coolant temperature. In the following sections, these parameters are systematically varied and their effect on the local heat and mass transfer is closely analyzed. To reduce the computational effort, the parametric variation was conducted on a two dimensional grid. In order to be able to study the effect of the variation, the baseline case was first run on the two dimensional grid. The present section discusses the results of this baseline case on the two dimensional grid.

Table 4.3 shows the geometry and operating conditions for the baseline case. These conditions were selected based on the operating conditions of a typical lithium bromide absorber. The calculation was started by initially creating a thin lithium bromide film around the sphere and letting the solution in the film accumulate and fall in the form of a droplet. The concentration and temperature of the lithium bromide

solution in the film were the same as the inlet conditions specified in Table 4.3. The Reynolds number for a film-wise flow around a sphere is defined as $4u\delta/\nu$, where δ is the thickness of the film. The film thickness is different at different points on the tube and hence so is the Reynolds number. These local Reynolds numbers are integrated over the entire sphere to calculate the average Reynolds number. Also, since the fluid velocity gradually increases with time, the Reynolds number also increases. Within the time interval computed, the average Reynolds number for this case was found to always be less than 65.

4.4.1 Flow pattern

Figure 4.25 shows the fluid flow pattern and the droplet shape as it falls down the column of spheres. The droplet formation, growth and breakup follows a pattern very similar to the three dimensional case. The difference between the two cases lies in the effect of the impact of the droplet. In the three dimensional case, the impact of the droplet causes a generation of waves that propagate axially over the liquid film on the sphere. However, due to the two dimensional nature of the present simulation, it does not capture any of the effects in the axial direction, including the generation and propagation of waves and their effect on the local heat and mass transfer coefficients.

4.4.2 Concentration distribution

Figure 4.26 shows the local changes in the lithium bromide concentration as the solution falls down the column of spheres. As shown in the accompanying scale, the local concentrations are represented by varying colors, with red denoting the highest concentration at 65% and blue denoting the lowest concentration at 60%.

The nature of the concentration distribution is very similar to the distribution in the three dimensional case. Similar to the three dimensional case, the concentration

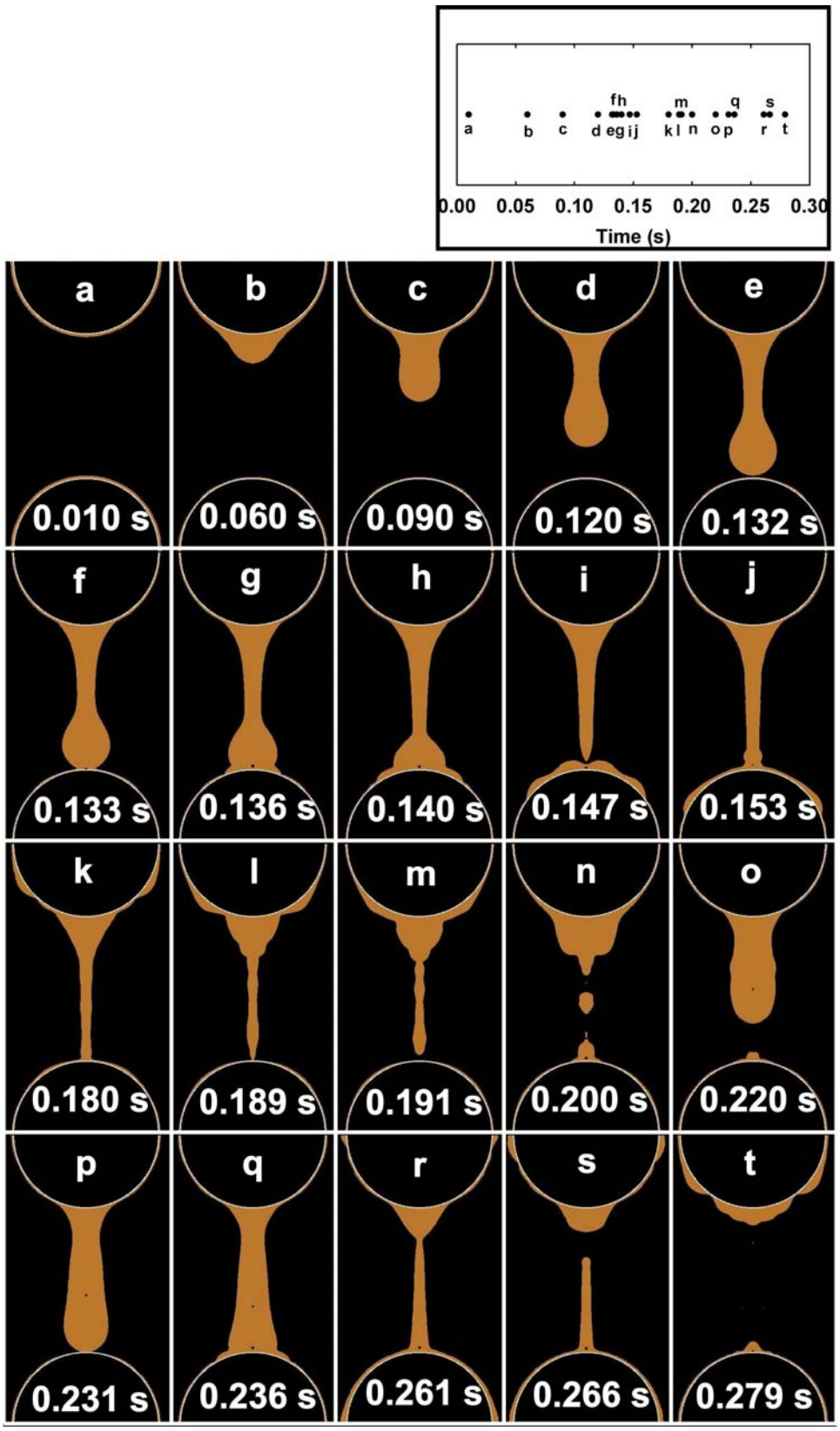

Figure 4.25: Droplet flow over a column of spheres

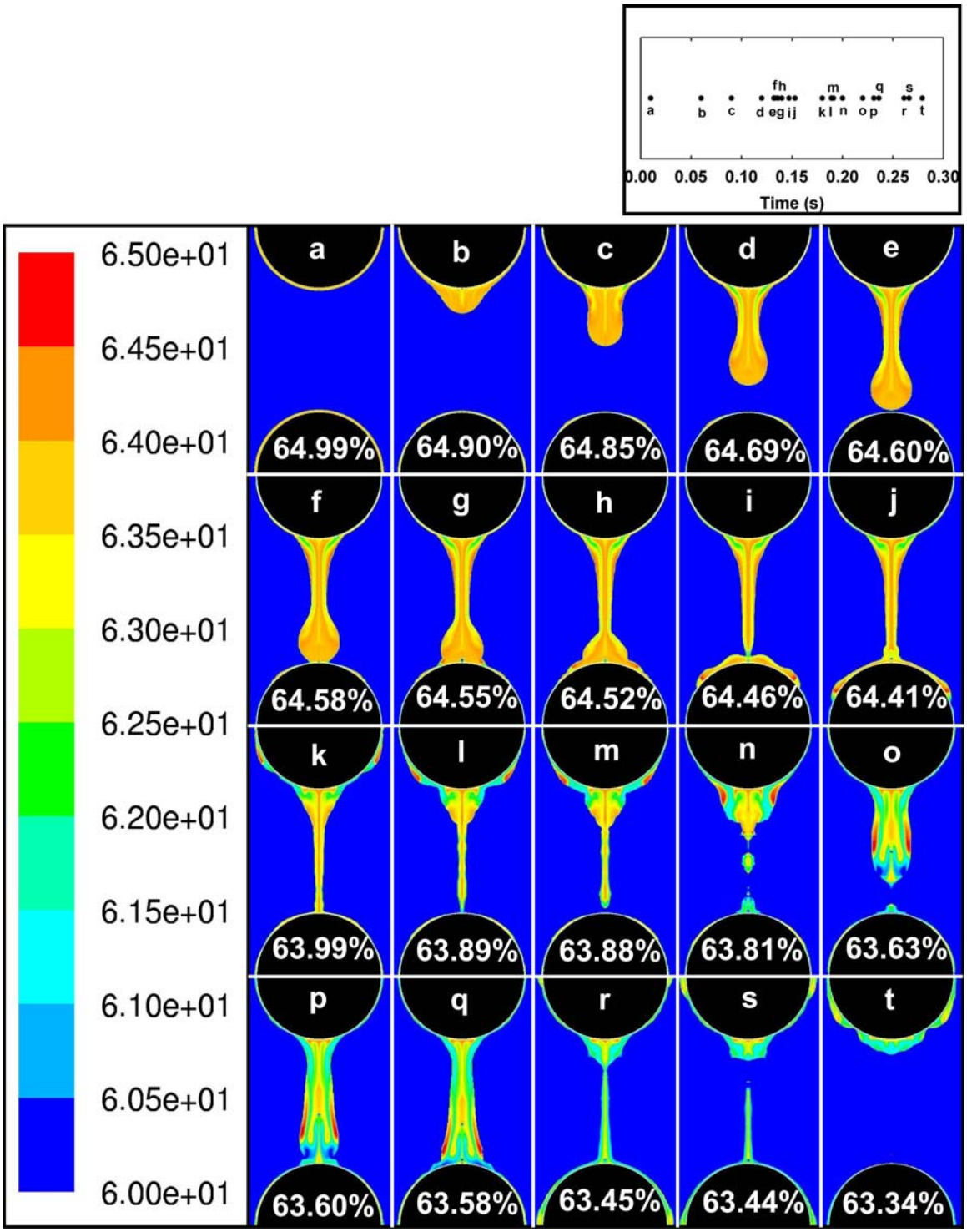

Figure 4.26: LiBr concentration distribution in a droplet falling over a column of spheres

is lowest at the liquid-vapor interface as the absorption process occurs there. Also, the absorption rates are higher at the interfaces in better thermal contact with the coolant as the coolant compensates for the rise in temperature of the solution due to absorption and sustains the process. This is seen in the frames with average concentrations of 64.69%, 64.60% and 64.58%, where most of the film over the sphere is green or blue in color, while most of the solution in the droplet is yellow or orange in color.

When the droplet falls on the sphere, the impact of the droplet mixes the lithium bromide solution in the film forming a more uniform concentration distribution in it. This is seen in Figure 4.26 in the frames with average concentrations of 64.60%, 64.58%, 64.55%, 64.52% and 64.46%. Before the droplet impacts the film (average concentration 64.60%), the surface of the film on the sphere is at a very low concentration (blue and green color), while the interior of the film is at a high concentration. However due to the low concentration layer on the surface, this high concentration interior cannot absorb any water vapor. When the droplet falls on the sphere, the impact of the fall mixes the fluid in the film, causing a more uniform concentration distribution in the film. This mixing causes a higher concentration at the surface of the film (orange, yellow and green colors) as seen in Figure 4.26 in the frames with average concentrations of 64.52% and 64.46%.

The difference between the concentration distributions in the present and the three dimensional cases is in the effect of the axial propagation of waves. In the three dimensional case, the wave generated during droplet impact propagates axially, mixes the concentration profiles on the film and increases the local velocities resulting in an increase in the local absorption rates. This effect of the wave is not seen in the concentration distribution in the present case.

4.4.3 Temperature distribution

Figure 4.27 shows the variation in the temperature of the lithium bromide solution as it falls over the column of spheres. The different temperatures are denoted by the variation in the colors, with red denoting the hottest temperature at 40.5 ℃ and blue denoting the coldest temperature at 30 ℃. Temperatures between these two extremes are denoted, in the order of decreasing temperatures by various shades of orange, yellow and green, respectively. Also, the average temperature of the lithium bromide solution at that time step is printed over the sphere in each frame.

The solution in the film over the sphere is usually low in temperature as it is cooled very effectively by the coolant inside the sphere. The solution in the droplet, being farther away from the coolant, is not cooled very effectively and hence is warmer in temperature. This is seen in Figure 4.27 where, most of the solution in the film over the sphere is marked in blue, while most of the solution in the droplet is marked in green or yellow.

Initially, the flow starts off with all the lithium bromide solution as a thin film over the sphere at a uniform temperature of 40.5 ℃. As the simulation proceeds, this film very quickly cools due to the coolant in the sphere at 30 ℃. As the droplet starts forming, the fluid in the droplet is at a warmer temperature than the film around the sphere. This is seen in Figure 4.27 in the frames with average temperatures 36.77 ℃, 36.12 ℃, 35.58 ℃ and 35.38 ℃.

When the droplet falls on the next sphere, as with the concentration distribution, the impact of the droplet causes a *mixing effect* of the temperature distribution. This is seen in Figure 4.27 in the frames with average temperatures 35.36 ℃, 35.30 ℃, 35.22 ℃, 35.03 ℃ and 34.87 ℃. Before the droplet impact, the lithium bromide solution in the film is cooled (marked in blue color), while the solution in the droplet is much warmer (marked in yellow and green colors). The warm temperature solution has a much lower potential for absorption of water vapor. When the droplet

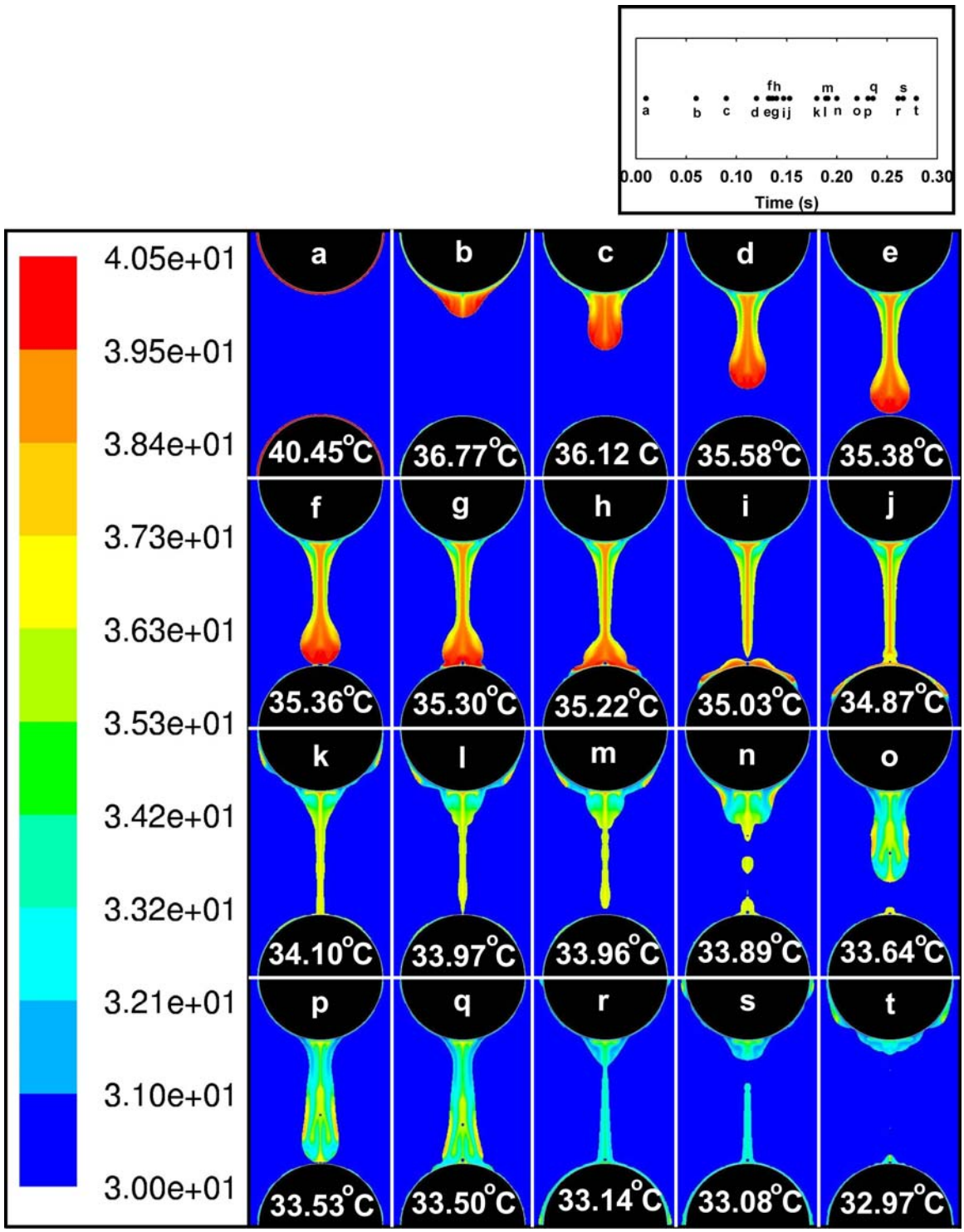

Figure 4.27: LiBr temperature distribution in a droplet falling over a column of spheres

impacts on the sphere, the fluid in the droplet region mixes with the fluid in the film forming a more even temperature distribution throughout the solution. This is noticeable in Figure 4.27 in the frames with average temperatures 34.10℃and 33.97℃, where almost the entire lithium bromide solution is close to the average temperature at that time step, and is marked in green. This *mixing effect* is very beneficial to the absorption phenomenon and is one of the biggest advantages of a drop-wise flow regime.

As explained earlier, the main difference between the present case and the three dimensional case is the absence of the axially propagating waves in this case.

4.4.4 Velocity distribution

Figure 4.28 shows the distribution of velocity in the lithium bromide solution. The velocity is represented by a series of arrows, where the direction of the arrow denote the direction of the velocity vector, while the length of the arrow is proportional to the magnitude of the velocity at that point.

The initial film was created by using a velocity inlet boundary condition at the sphere wall for a flow time of 0.01 s. This initial inlet velocity of the fluid is seen in the first frame in Figure 4.28 in the form of long radially outward arrows on the sphere wall. The film is gradually accelerated downwards due to gravity. Thus the average velocity of the fluid keeps increasing with time. This is seen in Figure 4.28 where the length of the arrows progressively increases with time.

When the droplet falls on the sphere, the impact of the fall causes the fluid to be dispersed in all directions in the form of waves. This is seen in Figure 4.28 at time steps 0.140 s, 0.147 s and 0.153 s, where, the fluid velocity at the point of impact is seen to the spread in all direction at high magnitudes. The formation and propagation of these waves have a significant impact on the heat and mass transfer processes.

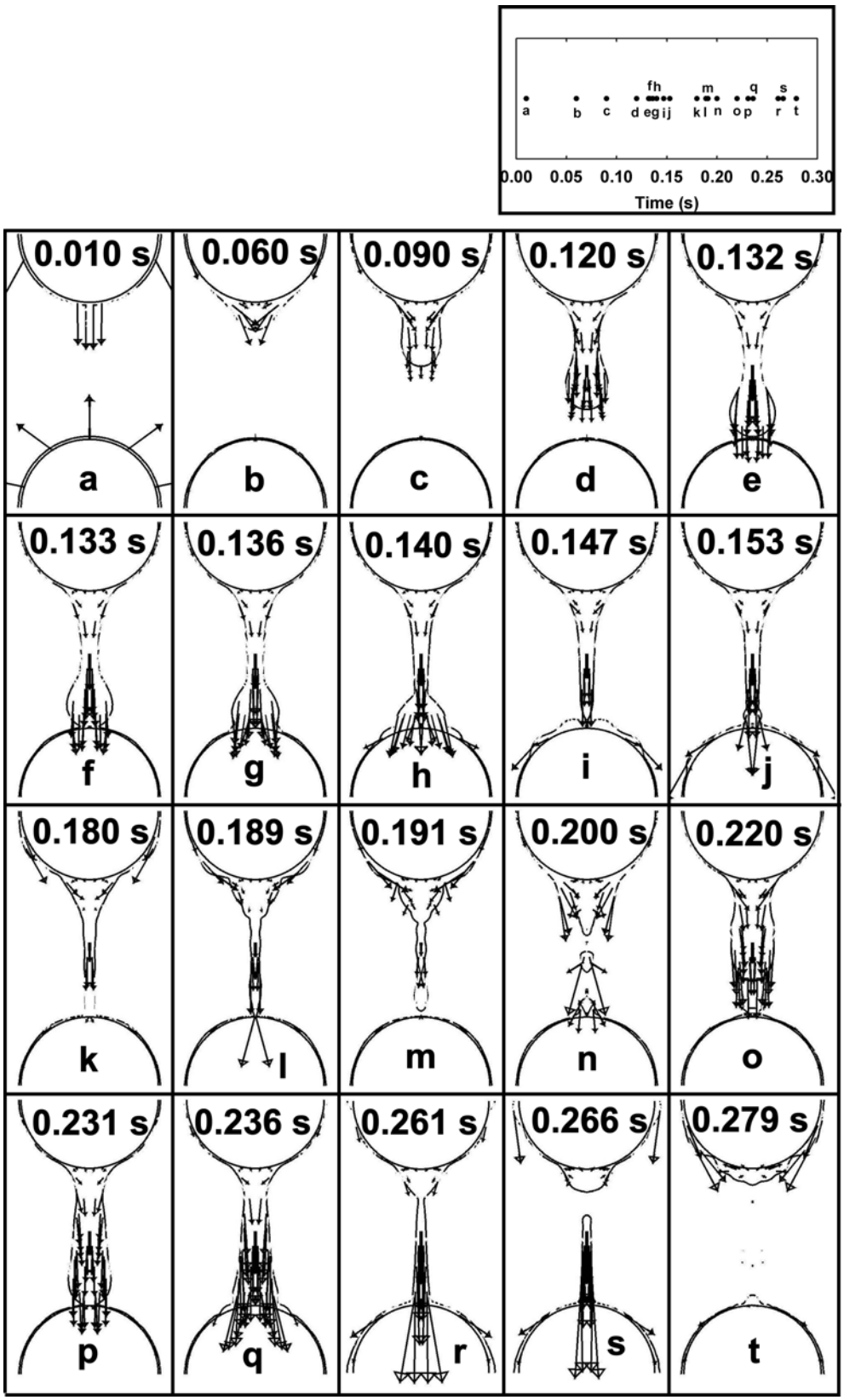

Figure 4.28: Velocity vectors in flow over a column of spheres

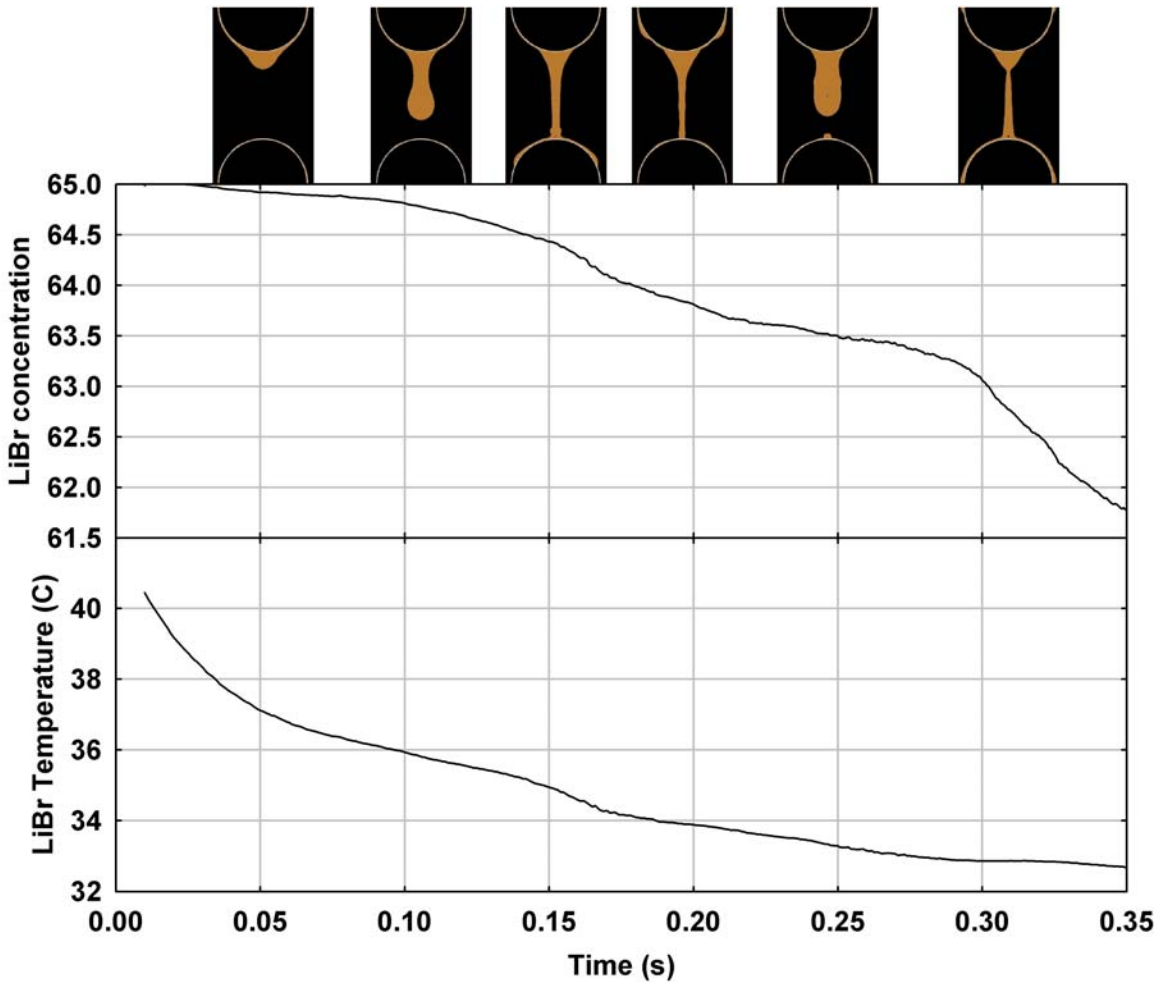

Figure 4.29: Temporal variation of bulk LiBr concentration and temperature

4.4.5 Bulk concentration and temperature variation

Figure 4.29 shows the temporal variation of the average concentration and temperature of the lithium bromide solution. The flow patterns at the respective times are shown above the plot.

Initially, the lithium bromide solution is present at a uniform concentration of 65%. As the droplet falls, it absorbs water vapor, causing a decrease in its concentration. The absorption is driven by the difference between the concentration of lithium bromide solution at the interface and the vapor pressure equilibrium concentration.

The equilibrium concentration decreases with decrease in the lithium bromide solution temperature.

Initially the lithium bromides solution is at a temperature of 40.5 ℃. At this temperature, the equilibrium concentration is 57.35%. Due to proximity to the coolant, the lithium bromide solution in the film rapidly cools to close to 30 ℃. This is seen in Figure 4.29 in the plot on temperature variation, where the temperature decreases at a rapid rate initially. At 30 ℃, the equilibrium concentration is 51.20%. Initially when the solution is warmer (40.5 ℃), the rate of the mass transfer process is relatively slow due the high equilibrium concentration, and hence low driving concentration difference. Thus, when the lithium bromide solution is at a temperature of 40.5 ℃ and a bulk concentration of 65%, the average driving concentration difference is 7.65%. However, as the temperature drops, the equilibrium concentration decreases and the large driving concentration difference results in a higher rate of mass transfer. At 0.05 s, when the temperature of solution in the film falls close to 30 ℃, and the bulk concentration is 64.92%, the average driving concentration difference is 13.72%. This is seen in Figure 4.29 in the plot of concentration change, where the concentration initially decreases slowly and then starts decreasing rapidly once the solution cools down.

After the initial sharp drop in temperature, the increased absorption and the accompanied heat generation causes a decrease in the rate of temperature drop. This decreased rate of cooling is also accompanied by a slight decrease in the rate of absorption. This is seen in Figure 4.29 from about 0.17 s to about 0.27 s, where both the concentration and temperature curves gradually level out after the sharp initial drops.

At about 0.27 s, the droplet hits the next sphere and forms a film around the second sphere. The impact of the droplet and the associated *waves* and *mixing effect* cause an increase in the heat and mass transfer coefficients. This leads to an increase

in the rate of cooling of the lithium bromide solution, as seen in Figure 4.29. The increased rate of cooling also causes an increase in the rate of absorption of water vapor, as seen from the plot on concentration change. Once the effect of the droplet impact phases out, the concentration and temperature curves level out once again, as seen in Figure 4.29 at about 0.30 s. When the next droplet hits the sphere, the rates of concentration and temperature changes increase and the entire cycle is repeated again.

4.4.6 Heat and Mass Transfer Coefficients

Figure 4.30 presents the local heat and mass transfer coefficients at various points on the sphere at times 0.201 s, 0.225 s, 0.240 s, 0.263 s and 0.280 s, respectively. The state of the flow at each time step is shown in the picture below the plot. The heat and mass transfer coefficients are calculated at ten locations on the sphere, with one being at the top of the sphere and ten being at the liquid interface aligned with the bottom of the sphere. These numbers are marked on the x-axis in the heat and mass transfer plots.

The local heat transfer coefficient at a point on the liquid-vapor interface is defined as the ratio of the normal local heat flux at that point and the difference between the local lithium bromide solution temperature at the interface and the bulk solution temperature. The local mass transfer coefficient at any point on the interface is defined as the ratio of the normal local mass flux at that point and the difference between the local interface concentration and the bulk lithium bromide solution concentration. The fluxes q''_n and $J_{i,n}$ are calculated in the direction normal to the liquid-vapor interface. The normal direction is calculated using the principle that the density gradient is maximum in the direction normal to the interface.

The solid line in Figure 4.30 presents the local heat and mass transfer coefficients

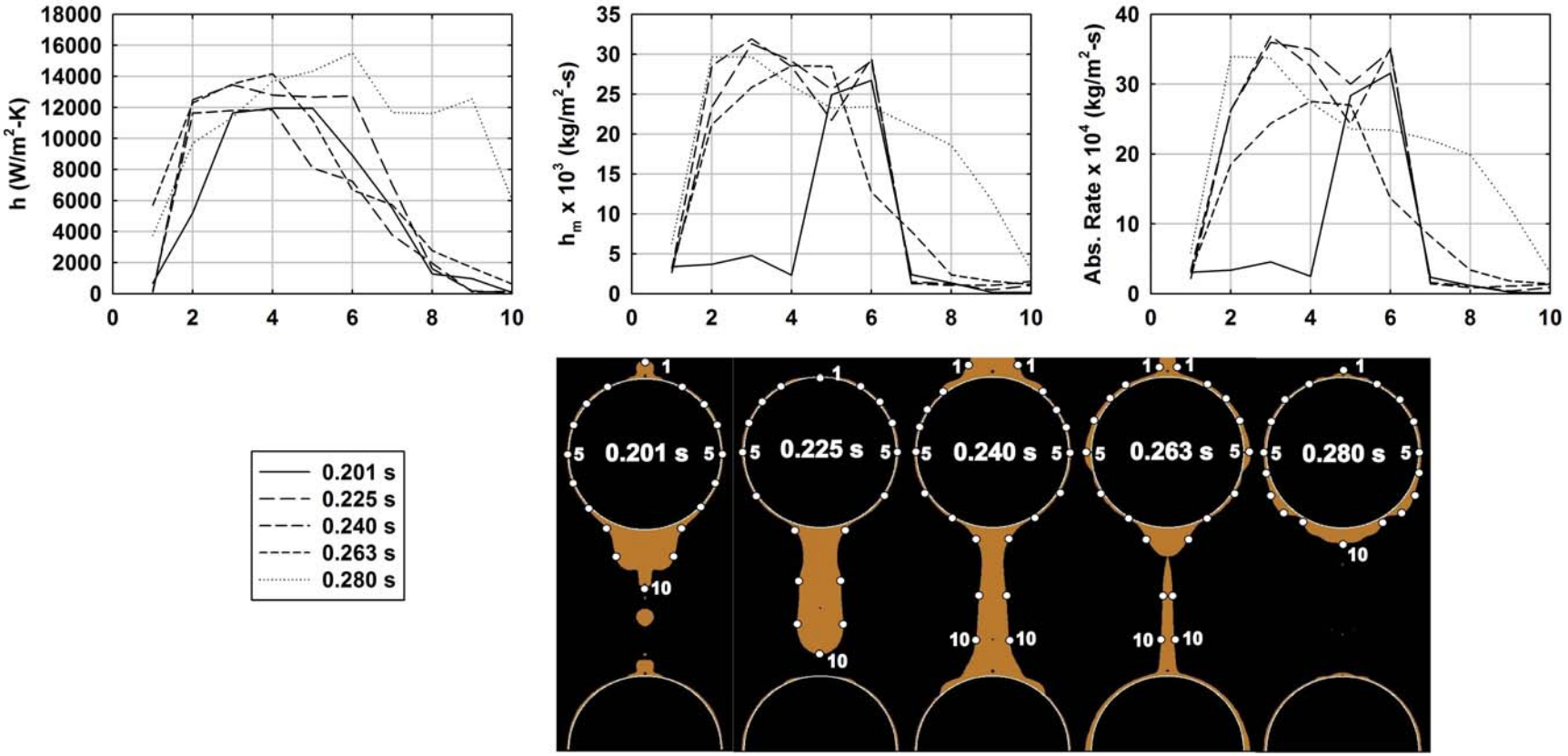

Figure 4.30: Local heat and mass transfer coefficients

at 0.201 s. As shown in the picture of the flow attached to the plot, at this time step, a droplet is being formed by drawing fluid away from the film over the sphere. A satellite droplet formed due to the detachment of the previous droplet is also in the process of falling down. The heat transfer coefficient is a function of the film thickness and fluid velocity. The film thickness is large at point 1 due to the remnants of liquid from the previous droplet. Also, the velocity of the fluid at point 1 is relatively low as the fluid momentarily stagnates at this point before being drawn away due to gravity. As a result, the heat transfer coefficient is quite low at 680 W/m^2-K at point 1. The film thickness gradually decreases from point 1 to 2 on to 3. The fluid velocities are also high in the thin film due to gravitational acceleration. Consequently the heat transfer coefficient also increases from 680 W/m^2-K at point 1, to 5209 W/m^2-K at point 2, to 11652 W/m^2-K at point 3. Beyond point 3, the film almost maintains the same thickness at points 4 and 5. As a result, the heat transfer coefficients at points 4 and 5 are about the same as that at points 3. The heat transfer coefficients at points 4 and 5 are 11947 W/m^2-K and 11953 W/m^2-K, respectively. Beyond point 5, the film thickness gradually increases from point 6 to point 10. The fluid velocity also decreases as the fluid starts accumulating in the droplet. Consequently the heat transfer coefficient gradually decreases from points 6 to 10. The heat transfer coefficients at points 6, 7, 8, 9 and 10 are, 8908 W/m^2-K, 5489 W/m^2-K, 1275 W/m^2-K, 969 W/m^2-K and 86 W/m^2-K, respectively.

Similar to the heat transfer coefficient, the mass transfer coefficient is also a function of the film thickness and fluid velocity. The mass transfer coefficient is low at points of large film thickness and relatively low velocity such as points 1 and 2. The mass transfer coefficients at points 1 and 2 are 3.40×10^{-3} kg/m^2-s and 3.68×10^{-3} kg/m^2-s, respectively. The mass transfer coefficient increases at points of low film thickness and high velocities, such as points 5 and 6. The mass transfer

coefficients at points 5 and 6 are, 24.9×10^{-3} kg/m^2-s and 26.7×10^{-3} kg/m^2-s, respectively. The vapor absorption rate also follows the same pattern as the mass transfer coefficient. The absorption rate is also high at points with low film thickness and high velocities, and low at points with large film thickness and low velocities. The absorption rate is a product of the mass transfer coefficient and the driving concentration difference, i.e. the difference between the interface equilibrium concentration and the bulk liquid concentration. The variation in the mass transfer coefficients was found to be more significant than the variation in the concentration differences and hence a much stronger factor in the determination of the local absorption rate. Absorption rates at large film thickness points such as 1 and 2 are 3.06×10^{-4} kg/m^2-s and 3.39×10^{-4} kg/m^2-s, respectively. Absorption rates at low film thickness points such as points 5 and 6 are 28.37×10^{-4} kg/m^2-s and 31.56×10^{-4} kg/m^2-s, respectively.

The long dashed line in Figure 4.30 presents the local heat and mass transfer coefficients at 0.225 s. At this time step the droplet has grown in size and is big enough to almost touch the next sphere. Once again, it is seen that the heat transfer coefficient is a strong function of the film thickness. The film thickness is high at point 1 and consequently the heat transfer coefficient is quite low at 114 W/m^2-K. The film thickness is very small at points 2, 3, 4, 5 and 6. The fluid velocity is also relatively high at these points as the fluid is being drawn downwards into the droplet. As a result, the heat transfer coefficients at these points are quite high. Beyond point 6, the heat transfer coefficients on the droplet are much lower than the heat transfer coefficients on the film. For example, the heat transfer coefficient at point 2 on the film is 12485 W/m^2-K, while that at point 9 on the droplet is 175 W/m^2-K.

The mass transfer coefficient is also low at point 1 due to a large film thickness. The film thickness is small and the local velocity is high at points 2 to 6, and consequently the mass transfer coefficient is high. Beyond point 6, mass transfer coefficients on the droplet are much lower than that on the film. For example, the mass transfer

coefficient at point 2 on the film is 23.4×10^{-3} kg/m^2-s, while that at point 9 on the droplet is 0.5×10^{-3} kg/m^2-s. The vapor absorption rate also follows a similar pattern as the mass transfer coefficient. It is high at points on the film, while low on points on the droplet. The absorption rate at point 2 on the film is 26.2×10^{-4} kg/m^2-s, while that at point 9 on the droplet is 0.4×10^{-4} kg/m^2-s.

The medium dashed line in Figure 4.30 presents the local heat and mass transfer coefficients at 0.240 s. At this time step the droplet has hit the next sphere, but has not detached from the previous sphere. The impact of the fall of the droplet causes a *wave* around the sphere, as seen in the picture in Figure 4.30. Unlike the previous time steps, at this time step the wave causes a significant variation in the local velocities and affects the local heat and mass transfer coefficients. Though the film thickness is not low at point 2, the heat transfer coefficient is high due to the presence of the wave. The wave increases the fluid velocity in the area and thus increases the local heat transfer coefficient. The heat transfer coefficient at point 2 is 11638 W/m^2-K. Similar to the droplet, the heat transfer coefficients on the liquid bridge are much lower than that on the film. For example, the heat transfer coefficient on the film at point 4 is 11828 W/m^2-K, while that at point 9 on the liquid bridge is 103 W/m^2-K.

The wave also increases the mass transfer coefficient at point 2. The mass transfer coefficient at point 2 is 28.5×10^{-3} kg/m^2-s. Also, the mass transfer coefficients on the film (e.g. 28.4×10^{-3} kg/m^2-s at point 4) are much higher than those on the liquid bridge (e.g. 1.03×10^{-3} kg/m^2-s at point 9). The vapor absorption rate also follows the same pattern as the mass transfer coefficient. The absorption rate is high at point 2 due to the rise in local velocities due to the wave. The absorption rate at point 2 is 26.26×10^{-4} kg/m^2-s. Also, the absorption rates on the film (e.g. 32.5×10^{-4} kg/m^2-s at point 4) are much higher than those on the liquid bridge (e.g. 1.09×10^{-4} kg/m^2-s at point 9).

The short dashed line in Figure 4.30 presents the local heat and mass transfer

coefficients at 0.263 s. At this time step the droplet has detached from the previous sphere and the broken liquid bridge is about to retract towards the two spheres. Also the wave that started due to droplet impact at the previous time step has propagated further down the sides of the sphere. The heat transfer coefficient at 1 is higher (5703 W/m^2-K) at this time step as compared to the previous times, due to the higher fluid velocity associated with the flow of the fluid from the impacted droplet, around the sphere. The heat transfer coefficients are high at points 2, 3, 4 and 5 due to high local velocities associated with the flow of the fluid from the impacted droplet over the sphere. The heat transfer coefficients at points 2, 3, 4 and 5 are, 12301 W/m^2-K, 13523 W/m^2-K, 14174 W/m^2-K and 11206 W/m^2-K, respectively. The wave associated with the droplet impact has not reached points on the film beyond point 5, and as a result the heat transfer coefficients are slightly lower at these points. The heat transfer coefficients at points 6 and 7 are, 6675 W/m^2-K and 5716 W/m^2-K, respectively. The heat transfer coefficient on the broken liquid bridge is lower than that on the film. For example the heat transfer coefficient at point 4 on the film is 14173 W/m^2-K, while that on the broken liquid bridge at point 9 is 1671 W/m^2-K. It is to be noted that though the heat transfer coefficient on the broken liquid bridge is lower than the film, it is significantly higher than that on the unbroken liquid bridge in the previous time step. The heat transfer coefficient at point 9 on the unbroken liquid bridge in the previous time step was 103 W/m^2-K. The increase in heat transfer coefficient is due to the increase in local velocities due to the quick *recoil* of the liquid bridge when it breaks.

The mass transfer coefficients are also high at points 2, 3, 4 and 5 due to the high local velocities associated with the propagation of the wave. The mass transfer coefficients at points 2, 3, 4, and 5 are 21.2×10^{-3} kg/m^2-s, 25.9×10^{-3} kg/m^2-s, 28.6×10^{-3} kg/m^2-s and 28.5×10^{-3} kg/m^2-s, respectively. Since the wave has not reached points beyond 5, the mass transfer coefficients are lower at points 6 and

7, 12.7×10^{-3} kg/m^2-s and 7.82×10^{-3} kg/m^2-s, respectively. The mass transfer coefficients at points 8, 9 and 10 on the broken liquid bridge are much lower than in the film, 2.35×10^{-3} kg/m^2-s, 1.58×10^{-3} kg/m^2-s and 1.17×10^{-3} kg/m^2-s, respectively. Unlike heat transfer coefficients, there is only a slight increase in the mass transfer coefficients on the broken liquid bridge, as compared to the unbroken bridge from the previous time step. The mass transfer coefficient at point 9 on the unbroken liquid bridge at the previous time step was 1.03×10^{-3} kg/m^2-s, as compared to 1.58×10^{-3} kg/m^2-s at point 9 at the present time step. Due to the very low mass diffusivity of water in the lithium bromide solution, the mass transfer coefficient is affected more significantly by a large film thickness than the heat transfer coefficient. Hence, in spite of the higher local velocities associated with bridge recoil, the mass transfer coefficients on the broken bridge are low.

The vapor absorption rate also follows the same pattern as the mass transfer coefficient. However as seen from Figure 4.30, the absorption rates on the film are a little lower than those at the previous time step. For example, at point 3 on the film, the absorption rate at the present time step is 24.4×10^{-4} kg/m^2-s, while that at the same point at the previous time step was 36.9×10^{-4} kg/m^2-s. This is because the fluid from the impacted droplet which flows around the sphere at this time step is at a higher temperature. This causes a temporary rise in the temperature of the film and consequently a decrease in the driving concentration difference.

The dotted line in Figure 4.30 presents the local heat and mass transfer coefficients at 0.280 s. At this time step the broken liquid bridge has retracted fully, the fluid from the impacted droplet has spread all around the sphere and all of the lithium bromide solution is present as a film around the sphere. This configuration of the fluid is particularly conducive to heat and mass transfer and the overall heat and mass transfer coefficients are the highest at this time step. The average heat and mass transfer coefficients at this time step are, 9223 W/m^2-K and 16.0×10^{-3} kg/m^2-s, respectively,

while those at the previous time step were, 7436 W/m^2-K and 10.7×10^{-3} kg/m^2-s. The average absorption rate at the present time step is 16.5×10^{-4} kg/m^2-s, while that at the previous time step was 10.2×10^{-4} kg/m^2-s. Within the time step, as with the previous time steps, the heat and mass transfer coefficients and the absorption rates depends strongly on the film thickness.

Overall, the heat transfer coefficient is seen to be strong function of the film thickness. Across all the time steps, the peak of the heat transfer coefficient is seen to occur at the regions of lowest film thickness. For the first four time steps, viz., 0.201 s, 0.225 s, 0.240 s and 0.263 s the solution exists both as a droplet and as a film, and the film thickness is lowest between points 3 and 6. Consequently for all of these time steps, the peak of heat transfer coefficient lies between points 3 and 6, and the heat transfer coefficient is lower at other points. At 0.280 s, the entire solution is present as a film around the sphere, and as a result the heat transfer coefficient is high for the entire region between points 2 and 9. Between points 2 and 9, the heat transfer coefficient varies with film thickness, as explained earlier. Except at 0.201 s and 0.280 s, the peak of the mass transfer coefficient and absorption rate was seen to lie between points 3 and 6. This is due to the film thickness being smaller at these points. At 0.201 s, the peak of the mass transfer coefficients and absorption rate lies in a narrower band of points 4 to 6, due to the remnants of the fallen droplet reducing the mass transfer coefficients at points 2 and 3. The additional film thickness of the remnants of the fallen droplet has a greater effect on the mass transfer coefficient than on the heat transfer coefficient because the mass transport properties of the lithium bromide solution are considerably worse than the heat transfer properties. At 0.280 s, due to a more evenly distributed film thickness, the mass transfer coefficient and absorption rate distribution are more uniform through all the points.

4.4.7 Film concentration and temperature profiles

Figure 4.31 presents the concentration and temperature profiles in the lithium bromide solution film on the sphere at times 0.201 s, 0.225 s, 0.240 s, 0.263 s and 0.280 s, respectively. The x-axis on the plots depicts the non-dimensional distance from the sphere surface, which is obtained by dividing the distance from the sphere by the film thickness at that point. The non-dimensional concentration at a point is obtained by dividing the difference in the concentration at that point and the bulk concentration, by the difference between the initial concentration and the bulk concentration. Similarly, the non-dimensional temperature at a point is obtained by dividing the difference in the temperature at that point and the bulk temperature, by the difference between the initial temperature and the bulk temperature.

The concentration and temperature profiles are plotted at five locations along the sphere circumference. These are labeled as 0°, 45°, 90°, 135° and 180° in the plots.

The leftmost plot in Figure 4.31 shows the concentration and temperature profiles at 0.201 s. At this time, the lithium bromide solution in the film has accumulated at a point to form a droplet and the droplet is growing in size. A satellite droplet formed during the breakup of the previous droplet is in the midst of its fall.

As seen in the concentration profiles at 0.201 s in Figure 4.31, the concentration is highest close to the surface of the sphere and then decreases away from the surface, towards the liquid-vapor interface. This is because the lithium bromide solution at the interface absorbs water vapor from the vapor phase, causing a decrease in its concentration. Due to the poor mass diffusivity of water vapor in lithium bromide ($D_{AB} = 1.6 \times 10^{-9}$ m^2/s), most of the water vapor does not transport towards the inner regions of the film, but remains near the surface.

It is also seen in Figure 4.31 that at 0.201 s, the temperature is lowest close to the surface of the sphere and highest close to the liquid-vapor interface due to the deposition of the heat of absorption at the interface and heat removal at the surface

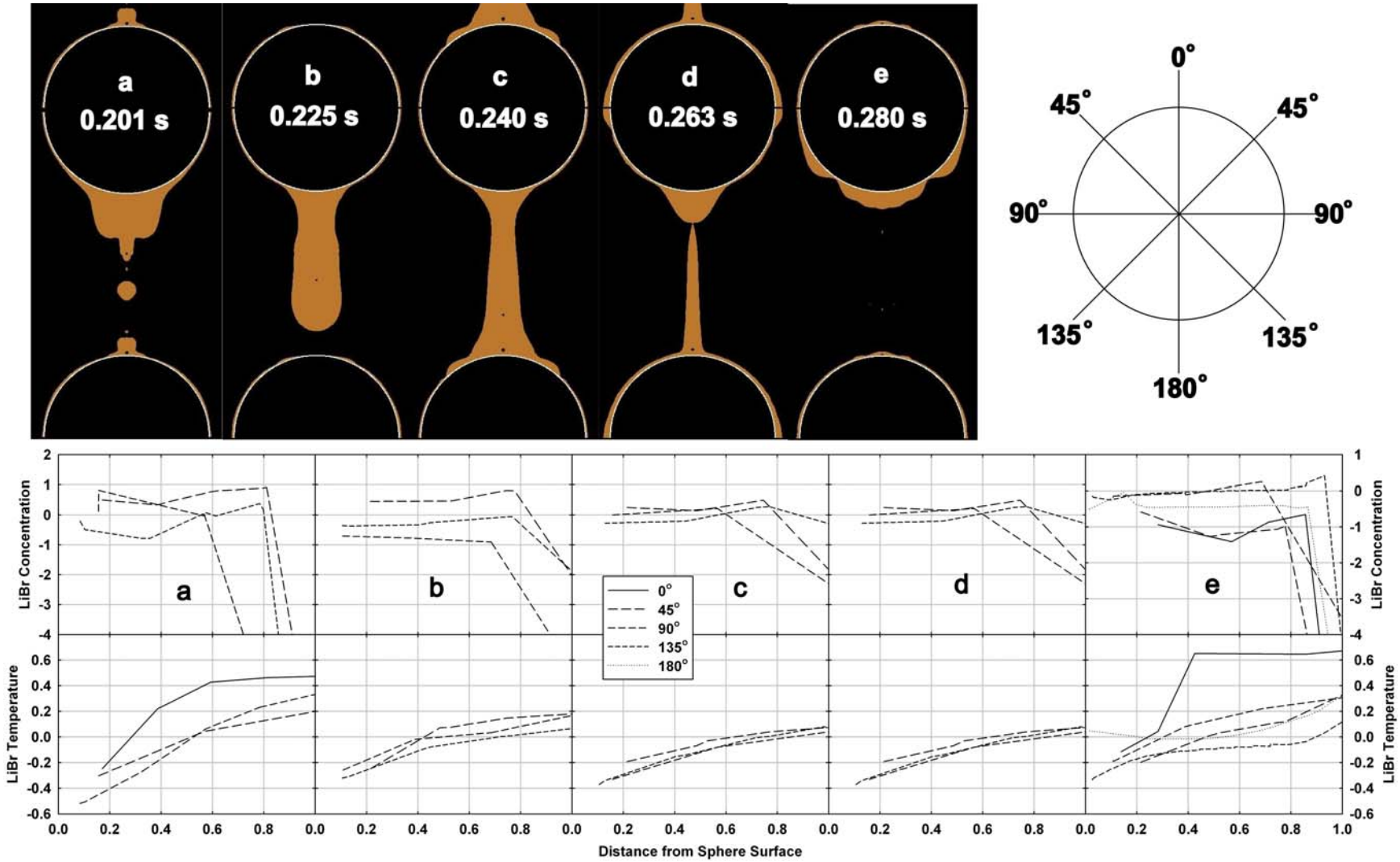

Figure 4.31: Concentration and temperature profiles on the film

of the sphere.

The lithium bromide solution possesses much better thermal transport properties ($k = 0.6$ W/mK) than mass transport properties ($D_{AB} = 1.6 \times 10^{-9}$ m^2/s). Thus, as seen in Figure 4.31, the concentration profiles have a steep gradient close to the interface, while the temperature profiles have a much shallower gradient.

The second plot in Figure 4.31 shows the concentration and temperature profiles at 0.225 s. At this time, the lithium bromide solution droplet has grown to such a size that it is close to hitting the next sphere. There is no significant change in the nature of the profiles at this time step. As with the concentration profiles in the previous time step, at 0.201 s the concentration is highest close to the surface of the sphere and then decreases away from the surface, towards the liquid-vapor interface. Also, similar to the previous time step, the temperature is lowest close to the surface of the sphere and highest close to the liquid-vapor interface.

The third plot in Figure 4.31 presents the concentration and temperature profiles at 0.240 s. At this time, the droplet has hit the lower sphere and a wave generated due to the impact of the droplet has just started propagating over the sphere. The impact of the droplet hitting the sphere mixes the solution in the film creating a more uniform concentration profile. This is seen in the concentration profiles at this time step, which are much flatter as compared to those at the previous time steps. The mixing effect of the droplet impact is also seen in the somewhat flatter temperature profiles, though less pronounced.

The fourth plot in Figure 4.31 shows the concentration and temperature profiles at 0.263 s. At this time step, the droplet has detached from the previous sphere and the wave generated due to the droplet impact has progressed around the sphere. The *mixing effect* is felt on the concentration profiles and as seen in Figure 4.31, the concentration profiles at this time step are flat, as the droplet impact and the subsequent

waves bring to the surface, the high concentration solution from underneath the surface. The *mixing effect* is also seen in the temperature profiles, where, the profiles are flatter as compared to those at the previous time steps.

The last set of plots in Figure 4.31 present the concentration and temperature profiles in the film at 0.280 s. At this time step, all of the lithium bromide solution is present as a film around the sphere. The wave generated due to the impact of the droplet has propagated around the sphere and dissipated away. It is seen that the concentration profiles have returned to their original sharp gradient seen before the droplet impact. This is because sufficient time has passed since the droplet impact and wave generation, and during this time the lithium bromide solution close to the interface has absorbed water vapor, causing a drop in its concentration. Due to poor mass transport properties, most of the absorbed water vapor stayed close to the liquid-vapor interface, causing sharp gradients.

The average Reynolds number for the case was always less than 65. The average heat transfer coefficient for this case was found to be 7452 W/m^2-K, while the average mass transfer coefficient was found to be 13.78×10^{-3} kg/m^2-s. The average Nusselt number (based on the sphere diameter) for the flow was 197.5, while the average Sherwood number was 86.0.

The average heat and mass transfer coefficients are higher in the two dimensional grid, as compared to the three dimensional case. The heat transfer coefficient in the present case is 7452 W/m^2-K, while that in the three dimensional case was 1500 W/m^2-K. Similarly, the mass transfer coefficient in the two dimensional case is 13.78×10^{-3} kg/m^2-s, while that in the three dimensional case is 4.67×10^{-3} kg/m^2-s. This difference in the heat and mass transfer coefficients is due to the difference in the nature of the two flows. In the three dimensional case, a significant portion of the momentum of the fluid is dissipated in the form of waves that propagate axially along the sphere. Due to these interactions, and the higher surface tension forces due

to higher fluid surface area, the lithium bromide solution traverses over the sphere at higher velocities as compared to the three dimensional case. In comparison, in the two dimensional case, due to the lack of axial waves and a large fluid surface area, the film velocities over the sphere are higher. These result in higher heat and mass transfer coefficients. However, besides the heat and mass transfer coefficients, the amount of absorption also depends on the concentration and temperature differences and the available surface area. The three dimensional geometry provides a much higher surface area in the film region where the heat and mass transfer coefficients are higher for a greater period of time. In the two dimensional geometry almost all of the lithium bromide solution is pulled in to form a big droplet, while in the three dimensional geometry, a significant portion of the solution is retained in the film during droplet formation. Thus, over the entire duration of the flow, the three dimensional geometry presents a significant portion of the lithium bromide solution as a film with high heat and mass transfer coefficients. In comparison, the solution in the two dimensional geometry alternates between being present almost entirely as a droplet and then almost entirely as a film. Also due to the mixing provided by the waves, the three dimensional geometry constantly exposes newer liquid surfaces for absorption, maintaining a higher concentration and temperature difference. Consequently, in spite of the higher heat and mass transfer coefficients, the amount of absorption is much higher in the three dimensional geometry. In a flow time of 0.35 s, the bulk lithium bromide solution concentration changes from 65% to 61.8% in the two dimensional case, while it changes from 65% to 58.6% in the three dimensional case. This is shown in Figure 4.32. The temperature change is lower in the three dimensional case due to the additional heat that must be removed with the increased amount of absorption. The temperature changes from 40.5℃ to 32.7℃ in the two dimensional case, while it changes from 40.5℃ to 33.5℃ in the three dimensional case.

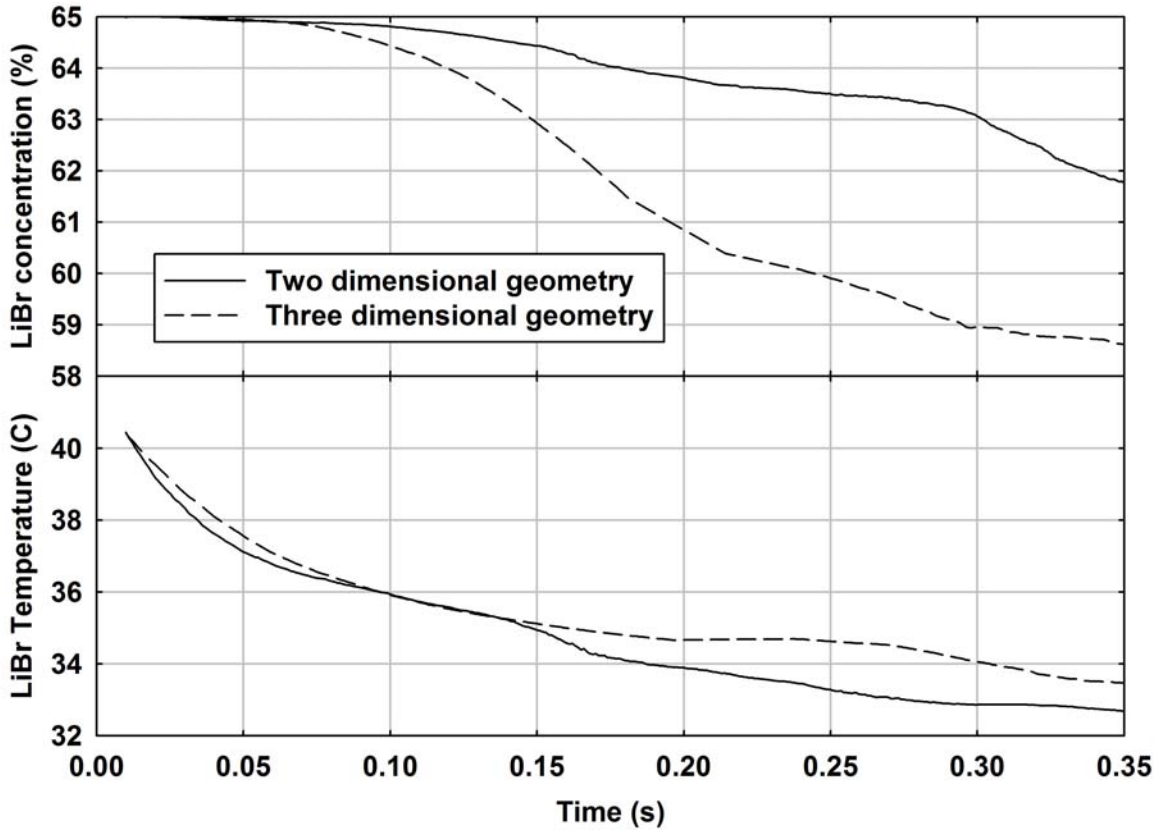

Figure 4.32: Comparison of results with the 2D and 3D grids

This concludes the discussion on the baseline case conducted on the two dimensional grid. As was seen from the results, though the nature of the results were the same in both the two and three dimensional grids, the three dimensional computations provided a much deeper insight into the axial propagation of the waves created due to droplet impact, and their effect on heat and mass transfer. There were also some differences in the results obtained with the two grids. However the two dimensional grid still captured most of the key elements of the flow such as, droplet formation, growth, fall and impact and its effect on the film (expect axial waves). It effectively tracked the influence of the various aspects of the flow on the heat and mass transfer processes. Also due to the difference in the size of the grids (19,740 for two dimensional grid and 1,185,870 for three dimensional grid), the three dimensional grid requires about 60 times as much time as the two dimensional grid to execute. Due to the required computational effort and the fact that the two dimensional grid accurately simulated most of the aspects of the flow, the parametric analyses were conducted on the two dimensional geometry.

4.5 Different inlet concentration

In this section, the inlet lithium bromide concentration is changed and its effect on the absorption phenomenon is investigated using a two dimensional grid. Thus, the inlet concentration is changed to 60% by weight of LiBr, from a baseline value of 65%. The operating conditions for this case are summarized in Table 4.4. The average Reynolds number in this case was always less than 65.

4.5.1 Flow pattern

Figure 4.33 shows the fluid flow pattern and the droplet shape as it falls down the column of spheres. As seen from the figure the flow pattern in this case is very similar

Table 4.4: Operating conditions for the different inlet concentration case

Operating parameter	**Baseline case**	**Present case**
Solution inlet concentration	*65% by wt of LiBr*	*60% by wt of LiBr*
Solution inlet temperature	40.5 ℃	40.5 ℃
Sphere wall temperature	30 ℃	30 ℃
Sphere diameter	15.9 mm	15.9 mm
Sphere pitch	15.9 mm	15.9 mm
LiBr mass flux	0.0058 kg/ms	0.0058 kg/ms

to the flow in the baseline case. Droplet formation occurs during 0.070 s and 0.100 s. Necking of the droplet is seen at 0.120 s and 0.134 s in Figure 4.33. Eventually, the droplet detaches from the sphere and falls off.

At a time of 0.138 s (Figure 4.33) the droplet reaches the next sphere before it detaches completely from the previous one. The impact of the droplet on the sphere causes a *ripple* or *wave* in the solution film on the sphere, which is seen at time steps 0.138 s and 0.145 s in Figure 4.33. The droplet detachment occurs at 0.183 s and satellite droplets are seen at 0.193 s and 0.196 s in Figure 4.33.

It is seen that the droplet flow patterns in the present case are very similar to the baseline case. This was expected since the flow patterns are governed primarily by the viscosity and surface tension of air and the lithium bromide solution, and these do not change appreciably for this change in concentration. For example, Kulankara and Herold [74] reported that the surface tension at 60% and 20 ℃ was 0.096 N/m, while that at 53% and 22 ℃ was 0.090 N/m. Also, Lee *et al.* [76] reported that the viscosity at 59.9% and 43 ℃ was 4.952×10^{-3} kg/m-s, while that at 65% and 60.4 ℃ was 5.680×10^{-3} kg/m-s.

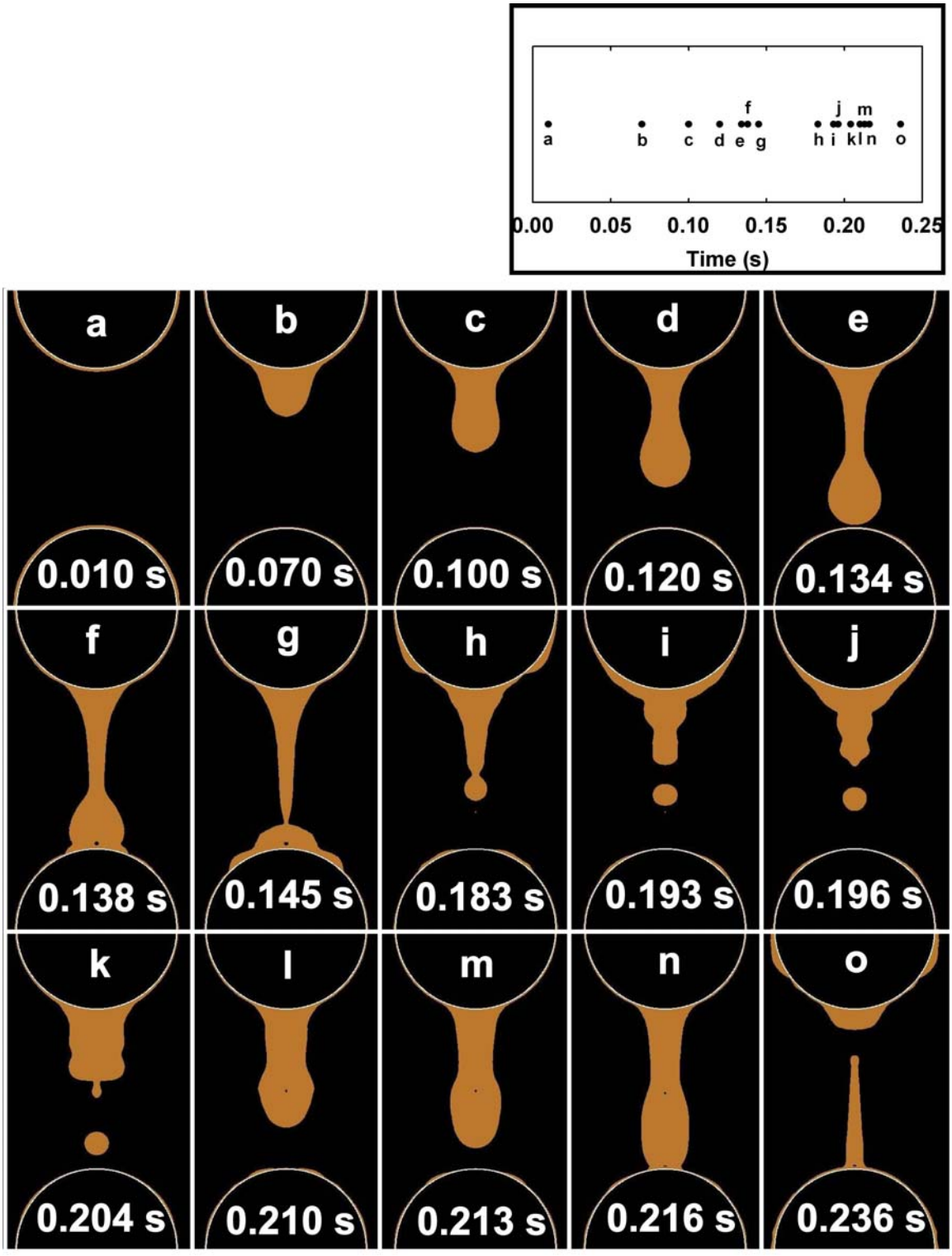

Figure 4.33: Droplet flow for an inlet concentration of 60%

4.5.2 Concentration distribution

Figure 4.34 shows the local changes in the lithium bromide concentration as it falls down the column of spheres. As shown in the accompanying scale, the local concentrations are represented by varying colors, with red denoting the highest concentration at 60% and blue denoting the lowest concentration at 55%.

Due to the different inlet concentration, the concentration distribution in the present case is significantly different than the baseline case. As the lithium bromide solution falls, it absorbs water vapor, causing a decrease in its concentration. The absorption process is driven by the difference between the concentration at the interface and the vapor pressure equilibrium concentration. Due to the lower inlet concentration, this concentration is much lower in the present case. As a result, the mass transfer and the resultant concentration change is lower in the present case as compared to the baseline case.

Similar to the baseline case, the concentration is lowest at the liquid-vapor interface due to absorption of vapor at the interface. Also the concentrations are typically lower in the film than on the droplet due to better thermal contact of the film with the coolant, as compared to the droplet. Due to the lower inlet concentration, the highest concentration in the present distribution plots is 60% as opposed to 65% in the baseline case. However, the lowest concentration, which is the interface equilibrium concentration, depends on the solution temperature and does not change significantly with change in the inlet concentration. Thus the concentration variation is limited to a 5% range in the present case, as compared to a 10% range in the baseline case.

4.5.3 Temperature distribution

Figure 4.35 shows the variation in the temperature of the lithium bromide solution as it falls through the spheres.

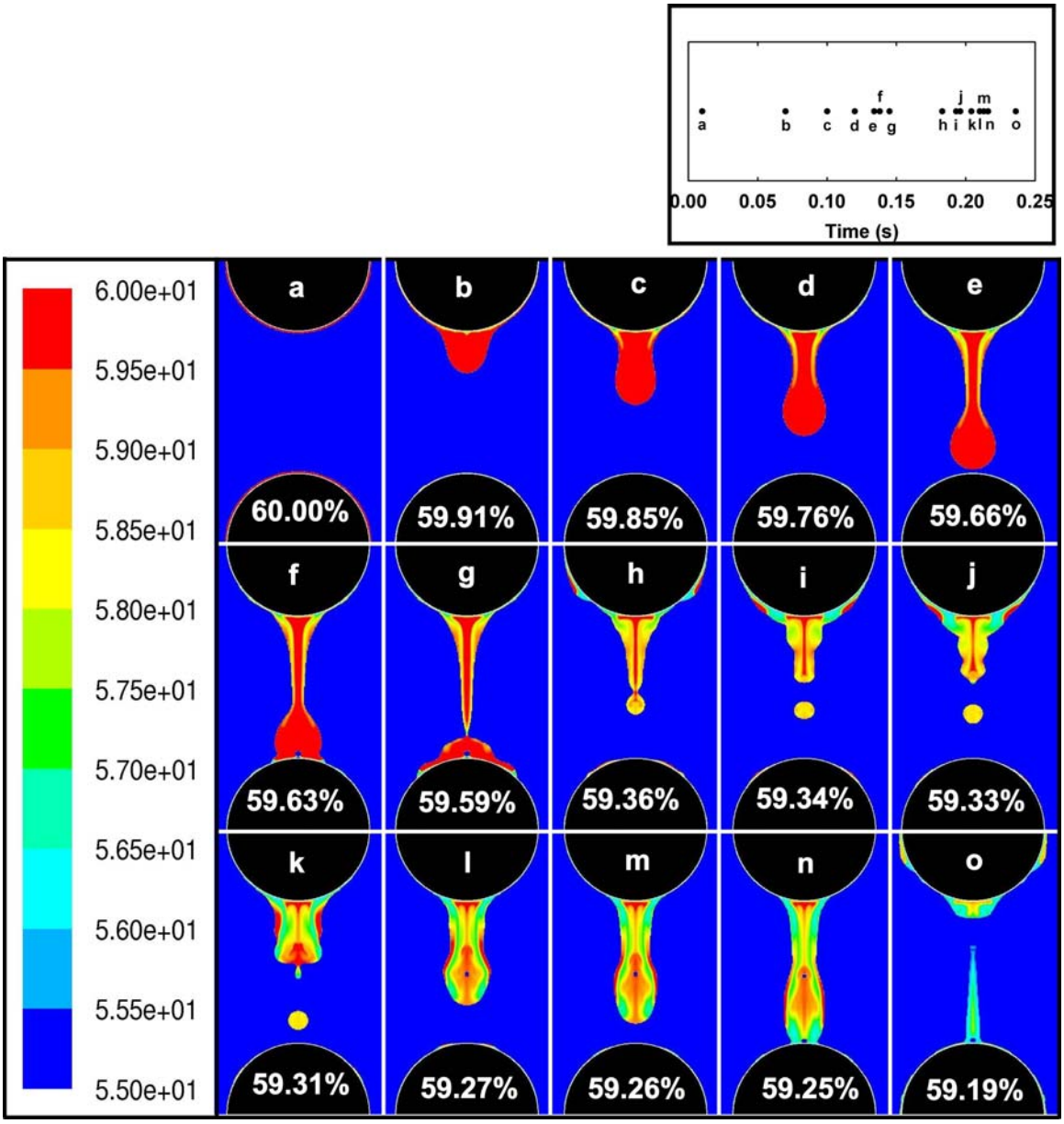

Figure 4.34: LiBr concentration distribution in a droplet for an inlet concentration of 60%

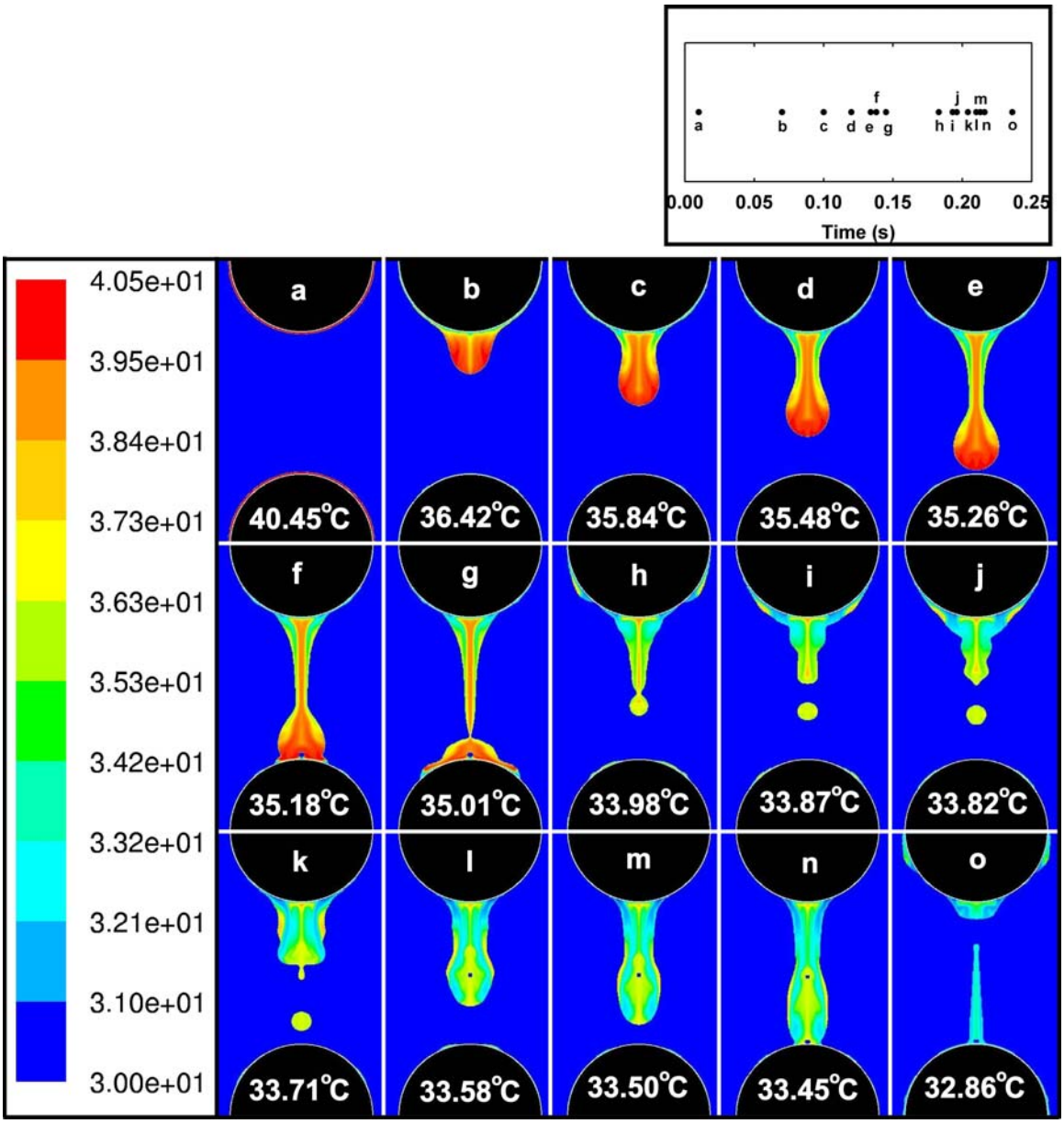

Figure 4.35: LiBr temperature distribution in a droplet for an inlet concentration of 60%

Since the total amount of vapor absorbed is lower in the present case as compared to the baseline case, the amount of heat generated is lower. As a result, the average temperature is slightly lower in the present case as compared to the baseline case. For example, at 0.30 s, the average temperature in the present case was 32.6℃, while it was 32.9℃ in the baseline case.

In spite of the difference in the average temperatures, the nature of the temperature variation is very similar in the present and baseline cases. Similar to the baseline case, the solution in the film over the sphere is usually low in temperature as it is cooled very effectively by the coolant inside the sphere. The solution in the droplet, being farther away from the coolant, is not cooled very effectively and hence is higher in temperature.

4.5.4 Velocity distribution

Figure 4.36 shows the distribution of velocity in the lithium bromide solution. As explained earlier, the flow patterns in the present case are very similar to the baseline case. Consequently, the velocity vectors in the present case are also very similar to the baseline case. This is because the flow velocities are governed primarily by the viscosity and surface tension of water vapor and the lithium bromide solution, and these do not change appreciably for this change in concentration.

4.5.5 Bulk concentration and temperature variation

Figure 4.37 shows the temporal variation of the average concentration *change* and temperature of the lithium bromide solution. The bulk change in concentration is plotted instead of the bulk concentration, to make it easier to compare the bulk variation with the baseline case. Since the initial concentration is 60% in the present case, and 65% in the baseline case, the plot of bulk concentration change offers better

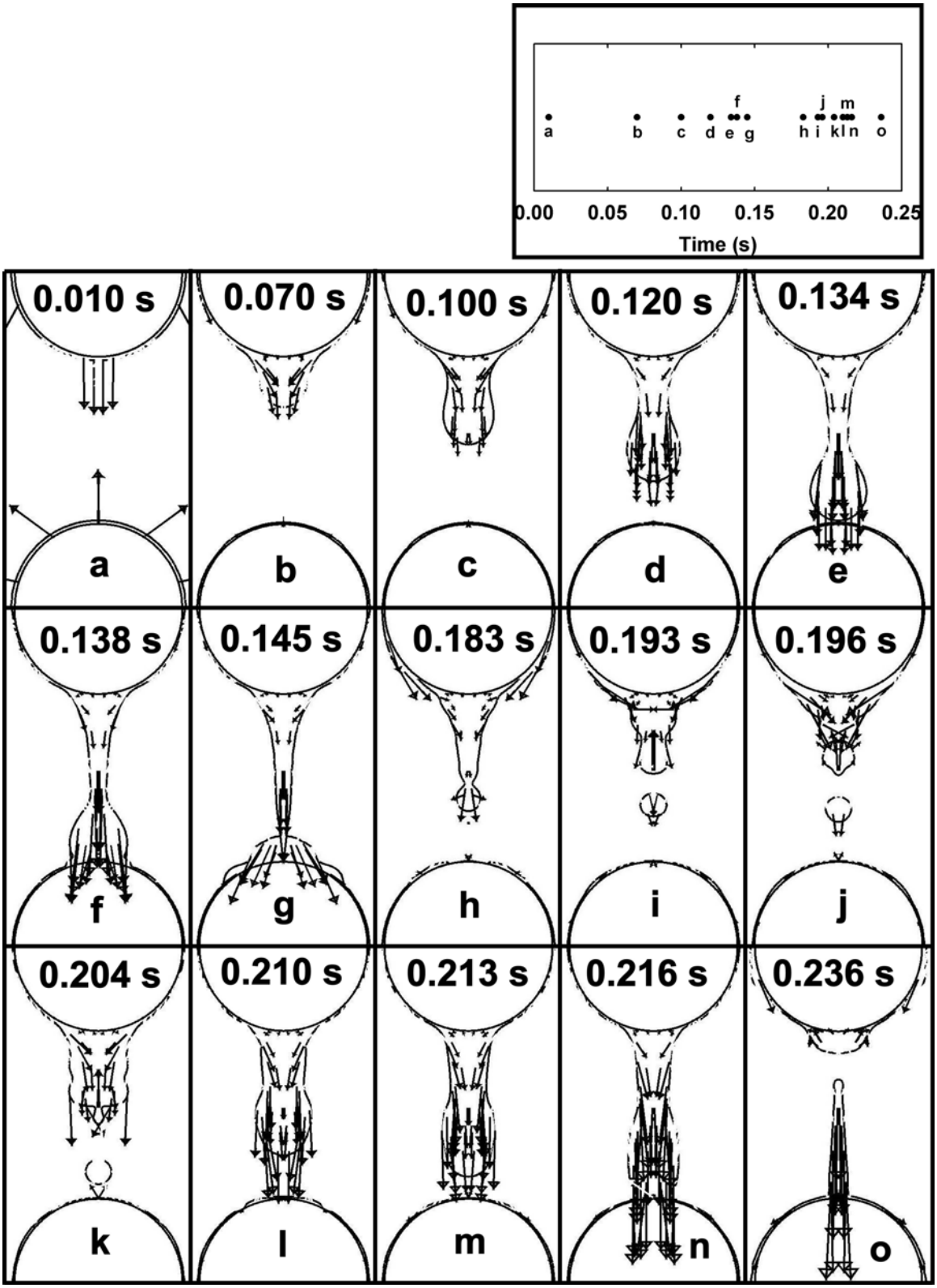

Figure 4.36: Velocity vectors for an inlet concentration of 60%

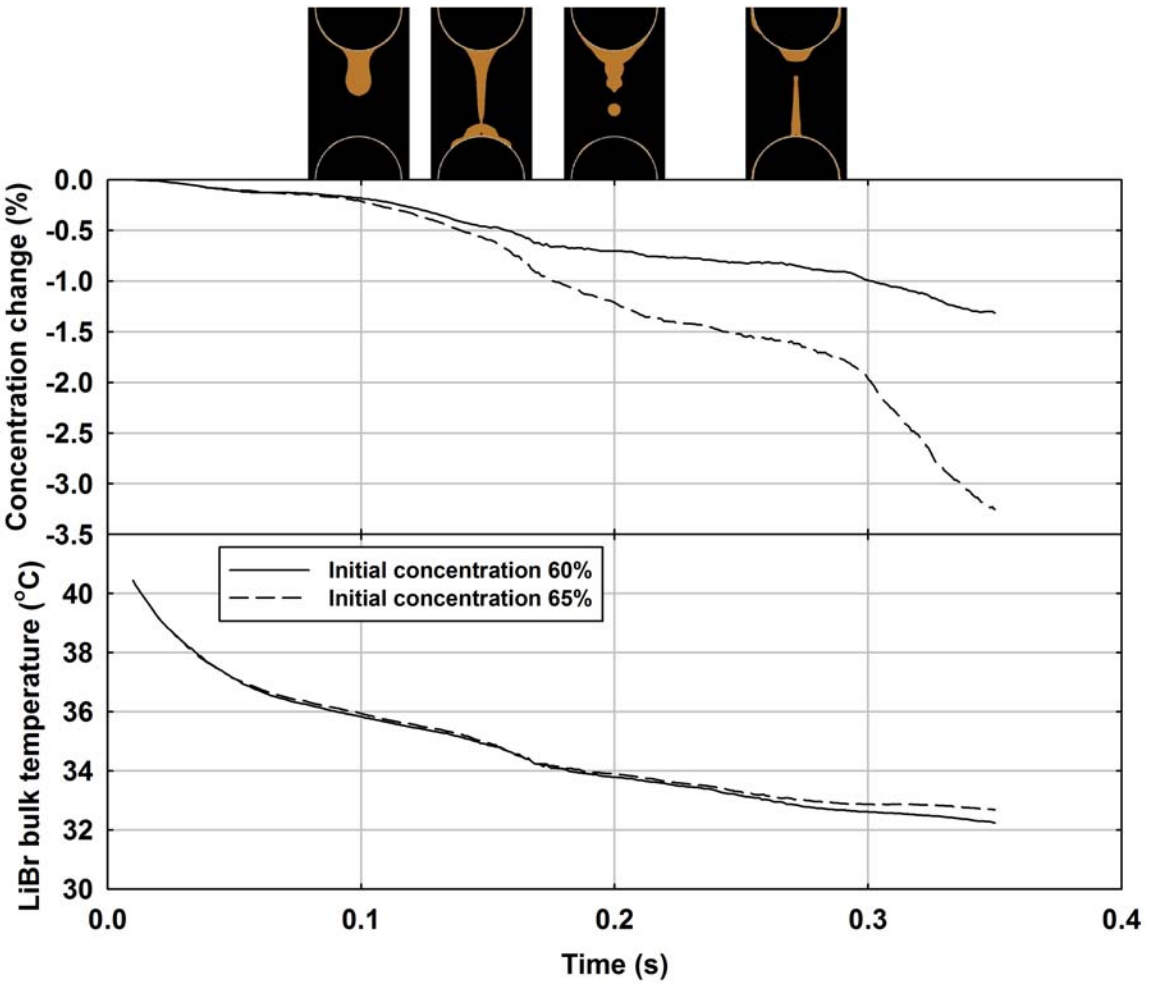

Figure 4.37: Temporal variation of bulk LiBr concentration and temperature for an inlet concentration of 60%

insights into the relative rates of concentration variation. The flow patterns at the respective times are shown above the plot.

Initially, the lithium bromide solution is present at a uniform concentration of 60%. As the droplet falls, it absorbs water vapor, causing a decrease in its concentration. The absorption is driven by the difference between the concentration of lithium bromide solution at the interface and the vapor pressure equilibrium concentration. Since the initial concentration is lower in the present case as compared to the baseline case, the driving concentration difference with the equilibrium concentration is also lower. As a result, the absorption rate in the present case is lower than in the

baseline case. This is seen in Figure 4.37, where the rate of concentration change is much lower in the present case, as compared to the baseline case. For example, at a time of 0.30 s, the concentration change in the present case is 0.99%, while that in the baseline case is 1.96%.

Due to the exothermic nature of the absorption process, the average temperature in the present case is slightly lower than the baseline case, due to decreased absorption. For example, at 0.30 s the average temperature in the present case was 32.6 ℃, while it was 32.9 ℃ in the baseline case. Though there is a significant difference in the amount of absorption, in both cases, the solution enters at the same temperature, and in subsequent time steps, the difference in the average temperatures is relatively small. This is due to the excellent thermal contact (i.e. high heat transfer coefficient) that the solution maintains with the coolant, resulting in the coolant side heat fluxes to be much higher than the heat generation due to absorption and thus being the dominant factor in determining the solution temperature.

4.5.6 Heat and mass transfer coefficients

Figure 4.38 presents the local heat and mass transfer coefficients and absorption rates at various points on the sphere at 0.285 s. The state of the flow at that time is shown in the picture below the plot.

The solid line in Figure 4.38 presents the local heat and mass transfer coefficients and absorption rates in the present case, while the dashed line presents the corresponding values for the baseline case. At this time step, all of the lithium bromide solution is present as a film around the sphere. It is seen that there is no significant difference in the heat and mass transfer coefficients between the present and baseline

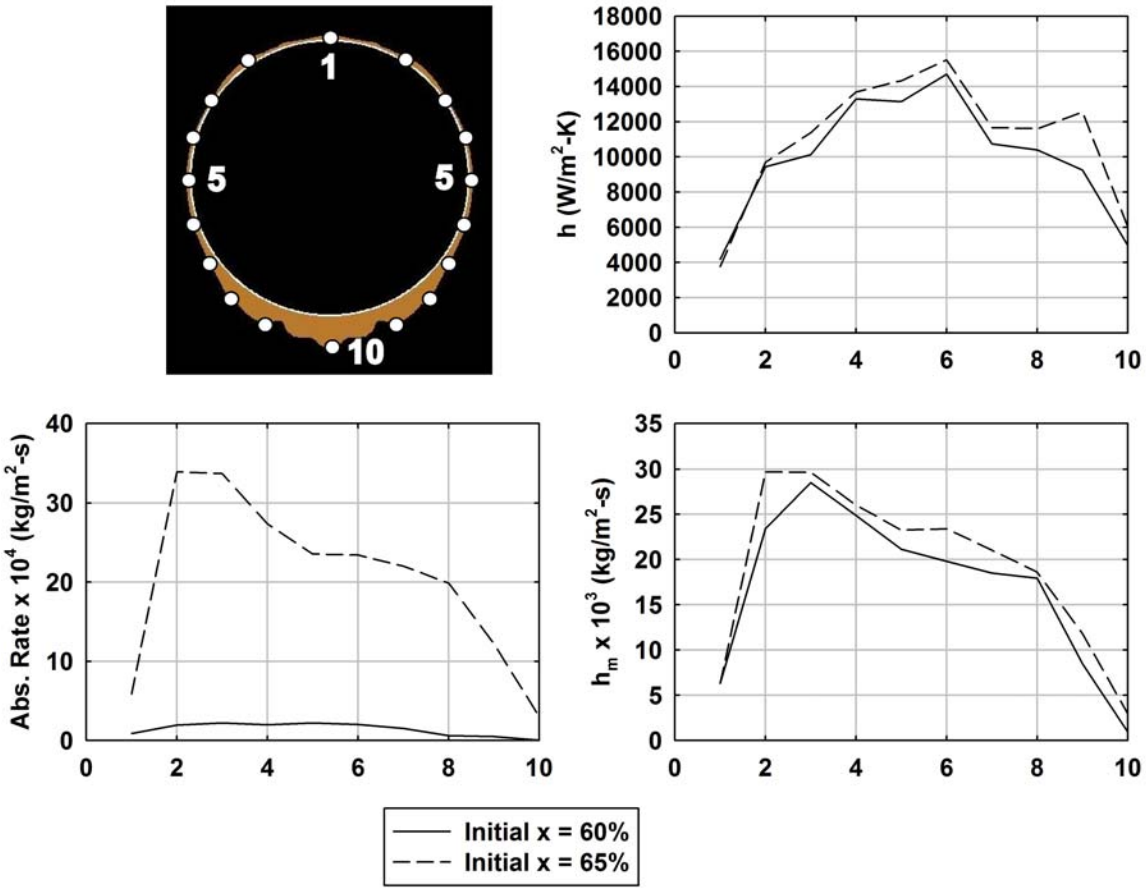

Figure 4.38: Local heat and mass transfer coefficients for an inlet concentration of 60%

cases. This is because the heat and mass transfer coefficients depend on the flow patterns, which are very similar in the two cases. For example, at point 4, the heat transfer coefficient in the present case is 13300 W/m^2-K, while that in the baseline case was 13696 W/m^2-K. Similarly, the mass transfer coefficient at point 4 in the present case is 24.9×10^{-3} kg/m^2-s, while that in the baseline case was 26.0×10^{-3} kg/m^2-s. The minor differences in the heat and mass transfer coefficients between the two cases can be attributed to differences in fluid properties and numerical resolution.

However, the absorption rate in the present case is much lower than that in the baseline case. At point 4, the absorption rate in the present case is 2.0×10^{-4} kg/m^2-s, while that in the baseline case was 27.4×10^{-4} kg/m^2-s. The absorption rate is lower in the present case because the concentration difference between the interface concentration and the vapor pressure equilibrium concentration is much lower in the present case, due to a lower initial concentration. For example, at the time step discussed, the bulk concentration in the present case is 59.1%, while that in the baseline case was 63.3%. At an interface temperature of 40°C, the equilibrium concentration is 57.1% and so the approximate driving concentration differences for the present and baseline cases are 2.0% and 6.2%, respectively. *It is to be noted that is calculation of the concentration difference is merely an estimate. The difference that actually drives the absorption process (both in the computations and in a real absorber) is the one between the interface equilibrium concentration and the concentration of the solution close to the interface.* Due to the poor mass transport characteristics of the lithium bromide solution, the concentration of the solution close to the interface is likely to be lower than the bulk concentration. Consequently, the concentration differences in the two cases are likely to be even more drastic than what the estimate indicates.

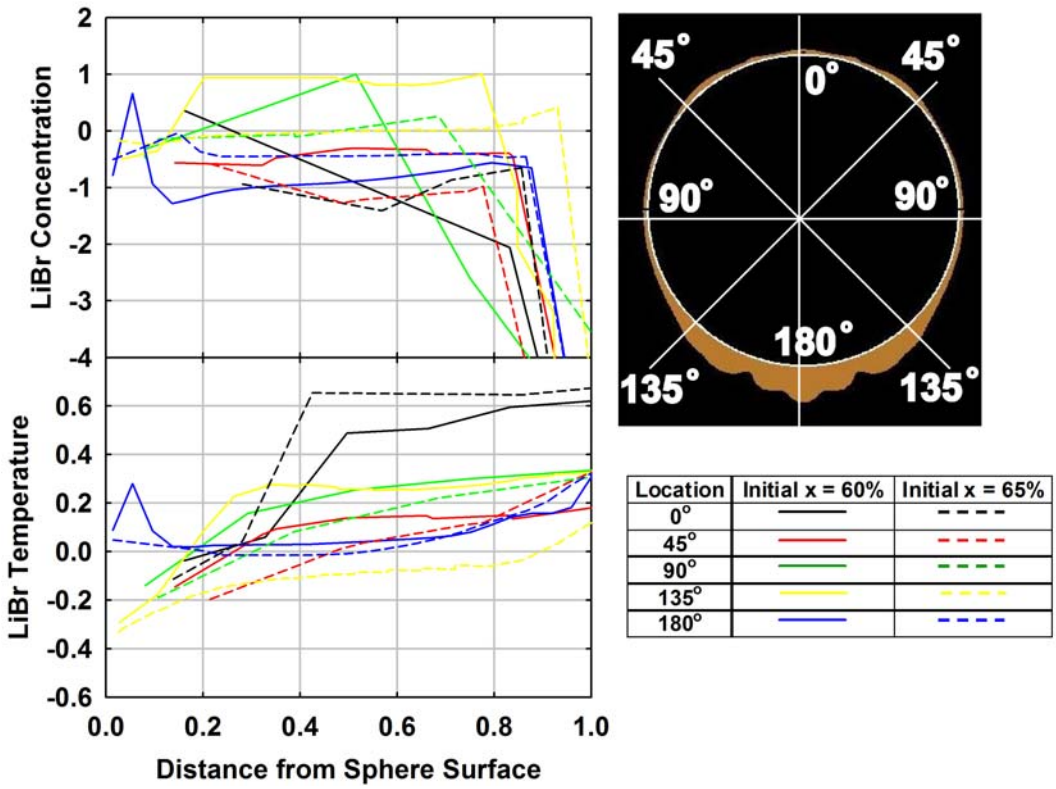

Figure 4.39: Concentration and temperature profiles for an inlet concentration of 60%

4.5.7 Film concentration and temperature profiles

Figure 4.39 presents the concentration and temperature profiles in the lithium bromide solution film on the sphere at 0.285 s. At this time, all of the lithium bromide solution is present in the form of a film around the sphere. The waves created due to droplet impact have propagated around the sphere and have dissipated away. For comparison the profiles for the baseline case are also plotted on the same graph and are shown in dashed lines. The concentration and temperature profiles are plotted at five locations along the sphere circumference. These are labeled as 0°, 45°, 90°, 135° and 180° in the plots.

As seen in Figure 4.39, the concentration and temperature profiles are very similar for the present and the baseline cases. This is in spite of the fact that the actual values of temperature and concentration are quite different in the two cases. This is because

the nature of the concentration and temperature profiles are mostly determined by the flow patterns, which are similar in the two cases. Similar to the baseline case, the concentration is highest close to the surface of the sphere and then decreases away from the surface, towards the liquid-vapor interface. Also, the temperature is lowest close to the surface of the sphere and highest close to the liquid-vapor interface.

The minor differences in the profiles in the two cases can be attributed to differences in fluid properties and numerical resolution. As mentioned earlier, due to the small thickness of the film, there are very few grid points (< 10) within the film for the profile plots. These low number of grid points cause the minor differences observed between the two sets of profile plots.

This concludes the discussion of the different inlet concentration case. It was seen that the different inlet concentration does not significantly affect the flow patterns or the heat and mass transfer coefficients or the nature of the concentration and temperature profiles. However due to a lower driving concentration difference, the absorption rate is much lower in the present case. The average Reynolds number for the case was always less than 65 which is the same as that for the baseline case. The average heat transfer coefficient for this case at 0.285 s was found to be 10030 W/m^2-K, while the average heat transfer coefficient for the baseline case at that time was 11023 W/m^2-K. The average mass transfer coefficient for this case was found to be 16.99×10^{-3} kg/m^2-s, while it was 19.26×10^{-3} kg/m^2-s for the baseline case. The average Nusselt number (based on the sphere diameter) for this case at 0.285 s was 265.8, while it was 292.1 for the baseline case. The average Sherwood number at 0.285 s was 106.0 for this case, while it was 120.2 for the baseline case. The average absorption flux in the present case at 0.285 s was 1.39×10^{-4} kg/m^2-s, while that in the baseline case was 20.51×10^{-4} kg/m^2-s. In the following section, the inlet temperature of the lithium bromide solution is varied and its effect on the local heat and mass transfer phenomenon is studied.

Table 4.5: Operating conditions for the 45℃ inlet temperature case

Operating parameter	**Baseline case**	**Present case**
Solution inlet concentration	65% by wt of LiBr	65% by wt of LiBr
Solution inlet temperature	*40.5℃*	*45.0℃*
Sphere wall temperature	30℃	30℃
Sphere diameter	15.9 mm	15.9 mm
Sphere pitch	15.9 mm	15.9 mm
LiBr mass flux	0.0058 kg/ms	0.0058 kg/ms

4.6 Different inlet temperature

In this section, the inlet lithium bromide temperature is changed and its effect on the absorption phenomenon is investigated using a two dimensional grid. The inlet temperature is changed to 45.0℃, from a baseline value of 40.5℃. The operating conditions for this case are summarized in Table 4.5. The average Reynolds number in this case was always less than 65.

4.6.1 Flow pattern

Figure 4.40 shows the fluid flow pattern and the droplet shape as it falls down the column of spheres. Droplet formation occurs between 0.070 s and 0.100 s. Necking of the droplet is seen at 0.120 s and 0.134 s in Figure 4.40. Eventually, the droplet detaches from the sphere and falls off.

At a time of 0.138 s (Figure 4.40) the droplet reaches the next sphere before it detaches completely from the previous one. The impact of the droplet on the sphere causes a *ripple* or *wave* in the solution film on the sphere, which is seen at time steps 0.138 s and 0.145 s in Figure 4.40. The droplet detachment occurs at 0.183 s and satellite droplets are seen at 0.193 s and 0.196 s in Figure 4.40.

It is seen that the droplet flow patterns in the present case are very similar to the

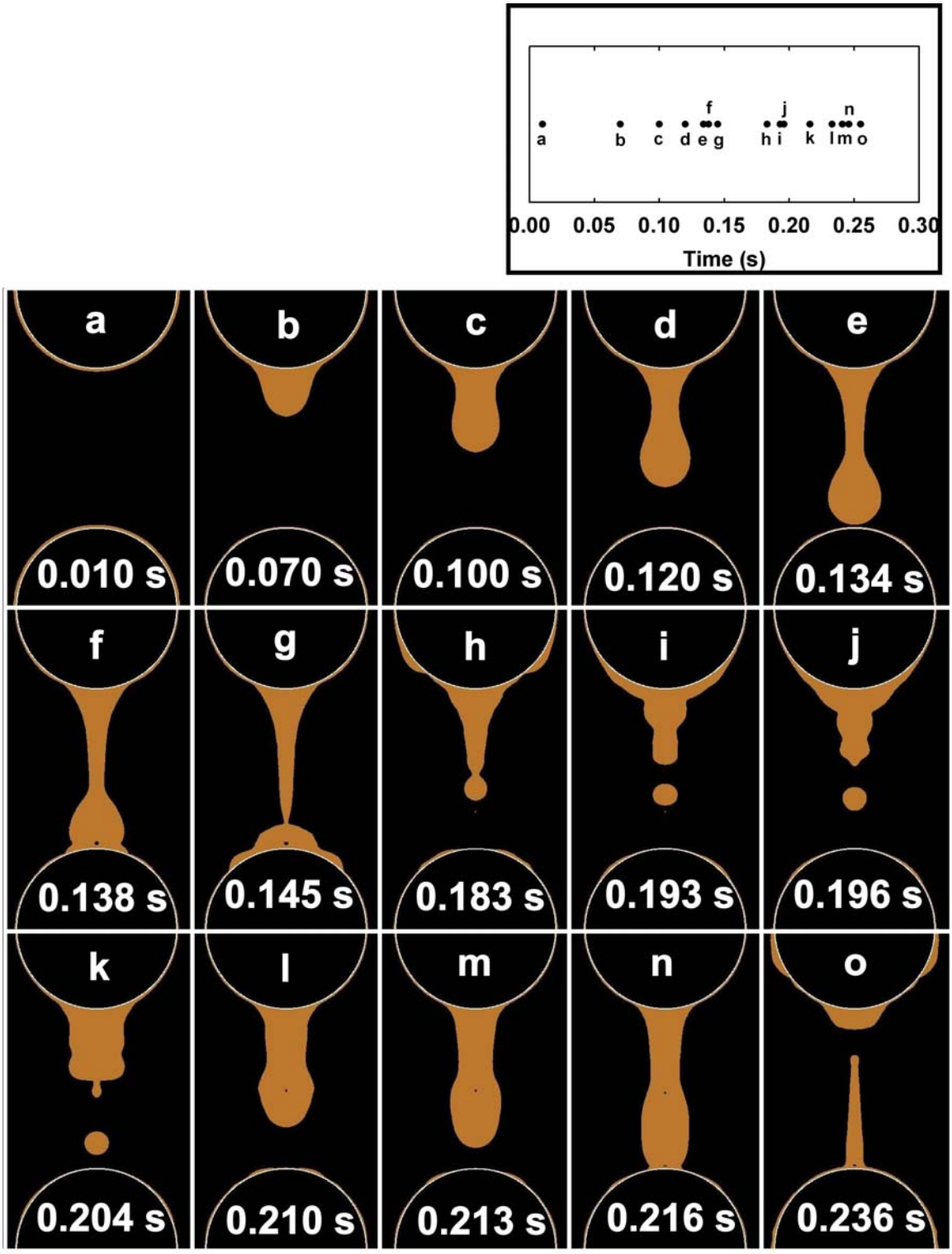

Figure 4.40: Droplet flow for an inlet temperature of 45℃

baseline case. This was expected, since the flow patterns are governed primarily by the viscosity and surface tension of air and the lithium bromide solution, and these do not change appreciably for this change in temperature [74, 76].

4.6.2 Concentration distribution

Figure 4.41 shows the local changes in the lithium bromide concentration as it falls down the column of spheres. The average concentration of the lithium bromide solution at each of the time steps is also printed over the sphere.

Due to the different inlet temperature, the concentration distribution in the present case is significantly different from that in the baseline case. The absorption process is driven by the difference between the concentration at the interface and the vapor pressure equilibrium concentration. The vapor pressure equilibrium concentration is a strong function of the lithium bromide solution temperature. This was shown in Figure 4.7. The equilibrium concentration at 40.5 °C is 57.4%, while the equilibrium concentration at 45.0 °C is 59.6%. Due to the higher equilibrium concentration, the driving concentration difference is much lower in the present case. As a result, the mass transfer and the resultant concentration change are lower in the present case as compared to the baseline case.

Similar to the baseline case, the concentration is lowest at the liquid-vapor interface due to absorption of vapor at the interface. Also the concentrations are typically lower in the film than on the droplet due to better thermal contact of the film with the coolant, as compared to the droplet. Similar to the baseline case, the highest concentration in the present distribution plots is 65%. However, the lowest concentration, which is the interface equilibrium concentration, depends on the solution temperature and is higher in the present case as compared to the baseline case. The lowest average concentration in the present case is 64.19%, while it was 63.34% in the baseline case.

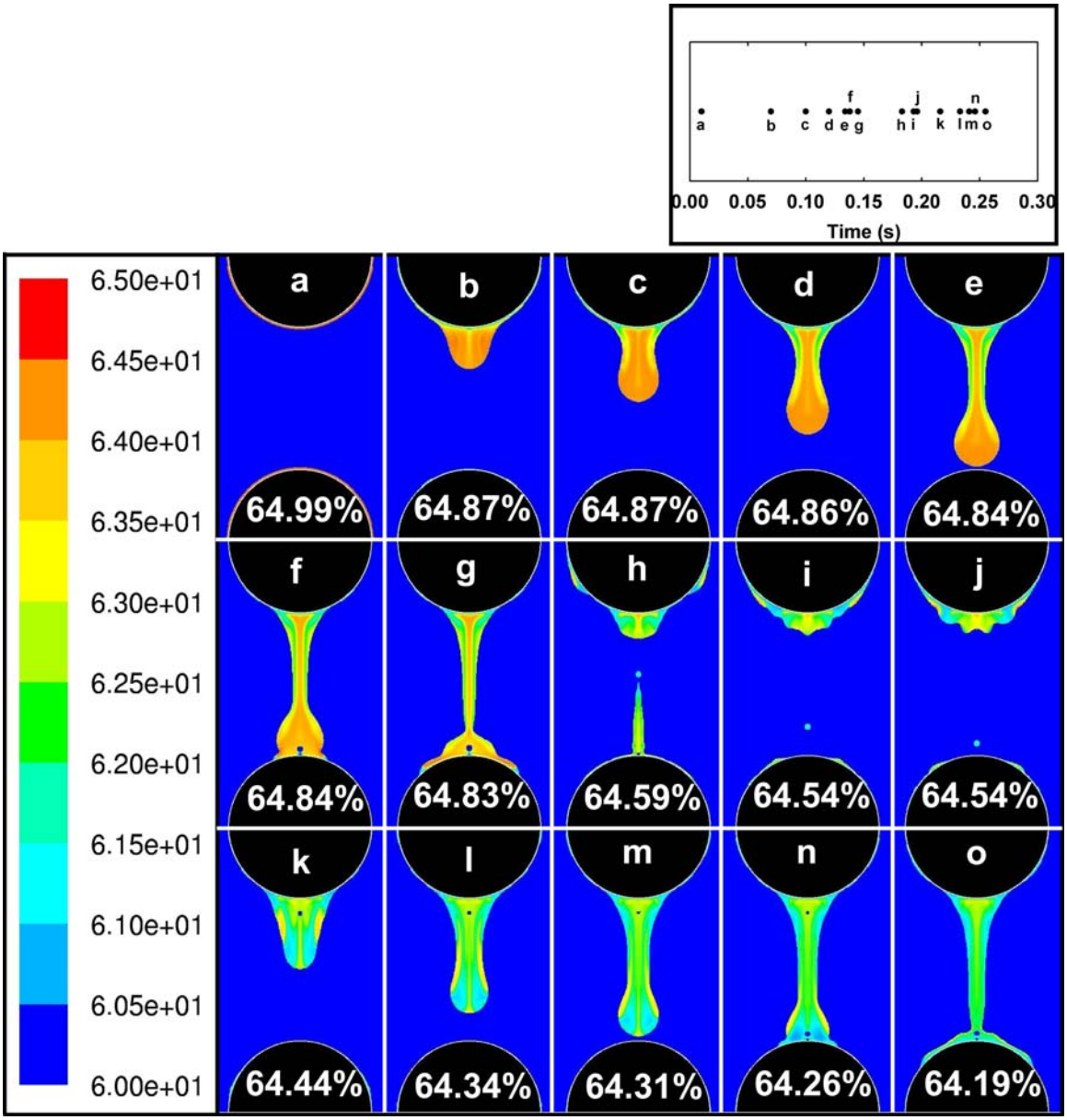

Figure 4.41: LiBr concentration distribution in a droplet for an inlet temperature of 45 ℃

4.6.3 Temperature distribution

Figure 4.42 shows the variation in the temperature of the lithium bromide solution as it falls through the spheres. The average temperature of the lithium bromide solution at that time step is printed over the sphere in each frame.

Due to the higher initial temperature, the solution temperatures in the present case are significantly higher from those in the baseline case. This is especially true for the initial time steps. In the later time steps, the solution cools significantly due to the coolant. Due to the higher temperature difference between the solution and the coolant in the present case (45 ℃ solution and 30 ℃ coolant), the rate of cooling is higher than the baseline case. Hence as the flow progresses, the average solution temperature gradually approaches the baseline values. For example, initially the average temperature in the present case is 45.0 ℃, while that in the baseline case was 40.5 ℃, while at 0.30 s the average temperature in the present case is 33.8 ℃, while it was 32.9 ℃ in the baseline case.

In spite of the difference in the average temperatures, the nature of the temperature variation is very similar in the present and baseline cases. Similar to the baseline case, the solution in the film over the sphere is usually low in temperature as it is cooled very effectively by the coolant inside the sphere. The solution in the droplet, being farther away from the coolant, is not cooled very effectively and hence is warmer in temperature.

4.6.4 Velocity distribution

Figure 4.43 shows the distribution of velocity in the lithium bromide solution. As explained earlier, the flow patterns in the present case are very similar to the baseline case. Consequently, the velocity vectors in the present case are also very similar to

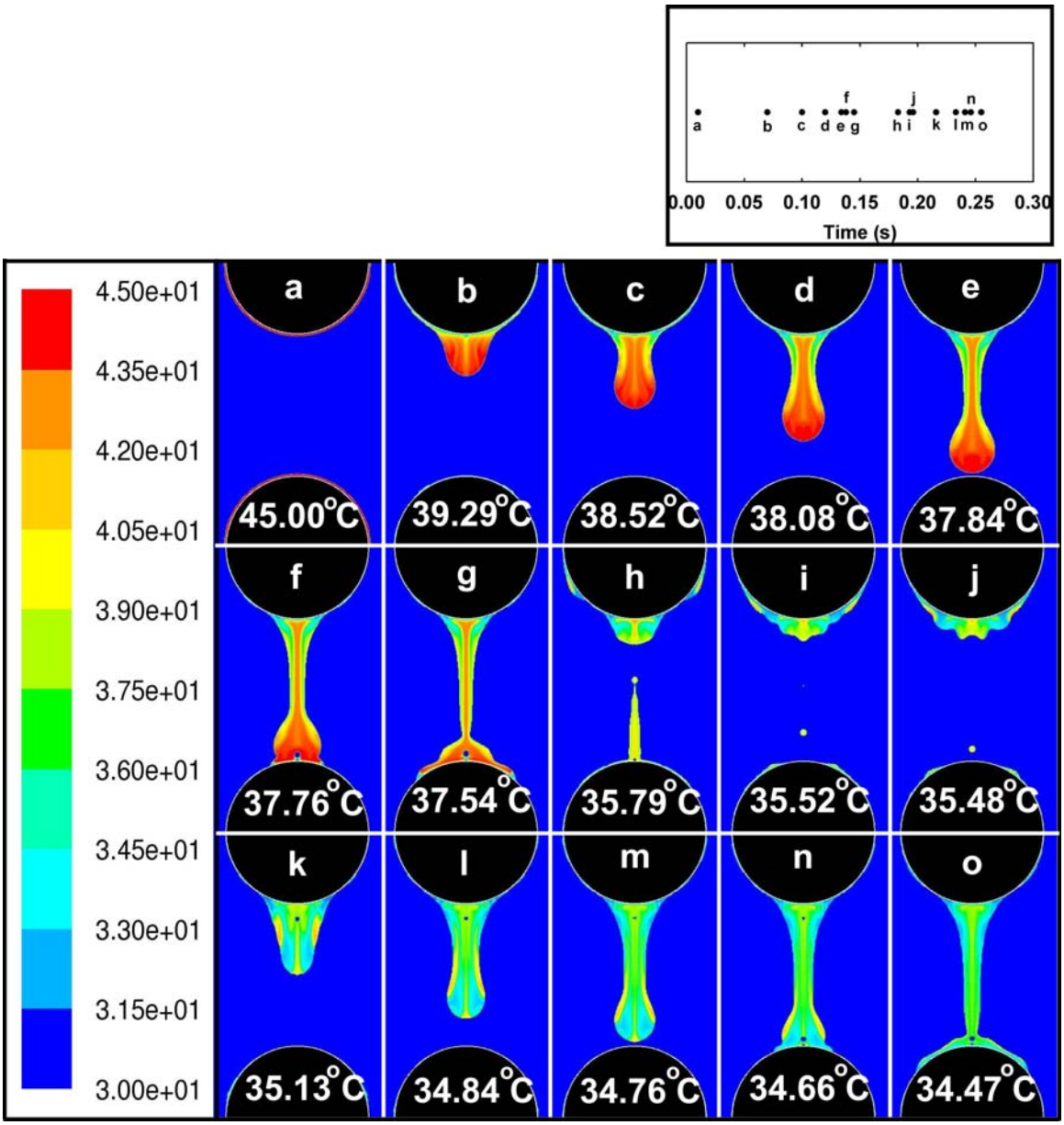

Figure 4.42: LiBr temperature distribution in a droplet for an inlet temperature of 45 ℃

the baseline case. This is because the flow velocities are governed primarily by the viscosity and surface tension of water vapor and the lithium bromide solution, and these do not change appreciably for this change in solution temperature [74, 76].

4.6.5 Bulk concentration and temperature variation

Figure 4.44 shows the temporal variation of the average concentration change and temperature of the lithium bromide solution. The bulk concentration and temperature variation for the baseline case is also shown for the sake of comparison. The variation for the present case is represented by a solid line, while that for the baseline case is shown by a dashed line. The flow patterns at the respective times are shown above the plot.

Due to the higher initial lithium bromide temperature and the corresponding difference with the coolant temperature, the rate of temperature decrease is higher in the present case. This is seen in the bulk temperature variation Figure 4.44, where the solid line corresponding to the present case decreases faster than the dashed line corresponding to the baseline case.

The higher lithium bromide solution temperature also corresponds to higher interface equilibrium concentration and thus a lower concentration difference for mass transfer. The equilibrium concentration at 45.0 ℃ is 59.6%, while that at 40.5 ℃ is 57.4%. Due to this lower concentration difference, the rate of concentration decrease is lower in the present case. This is seen in the bulk concentration variation in Figure 4.44, where the solid line corresponding to the present case decreases slower than the dashed line corresponding to the baseline case.

Besides the difference in the rate of concentration and temperature changes, the nature of the bulk temperature and concentration variations are very similar in the present and the baseline cases. This is because the flow patterns, which depend on

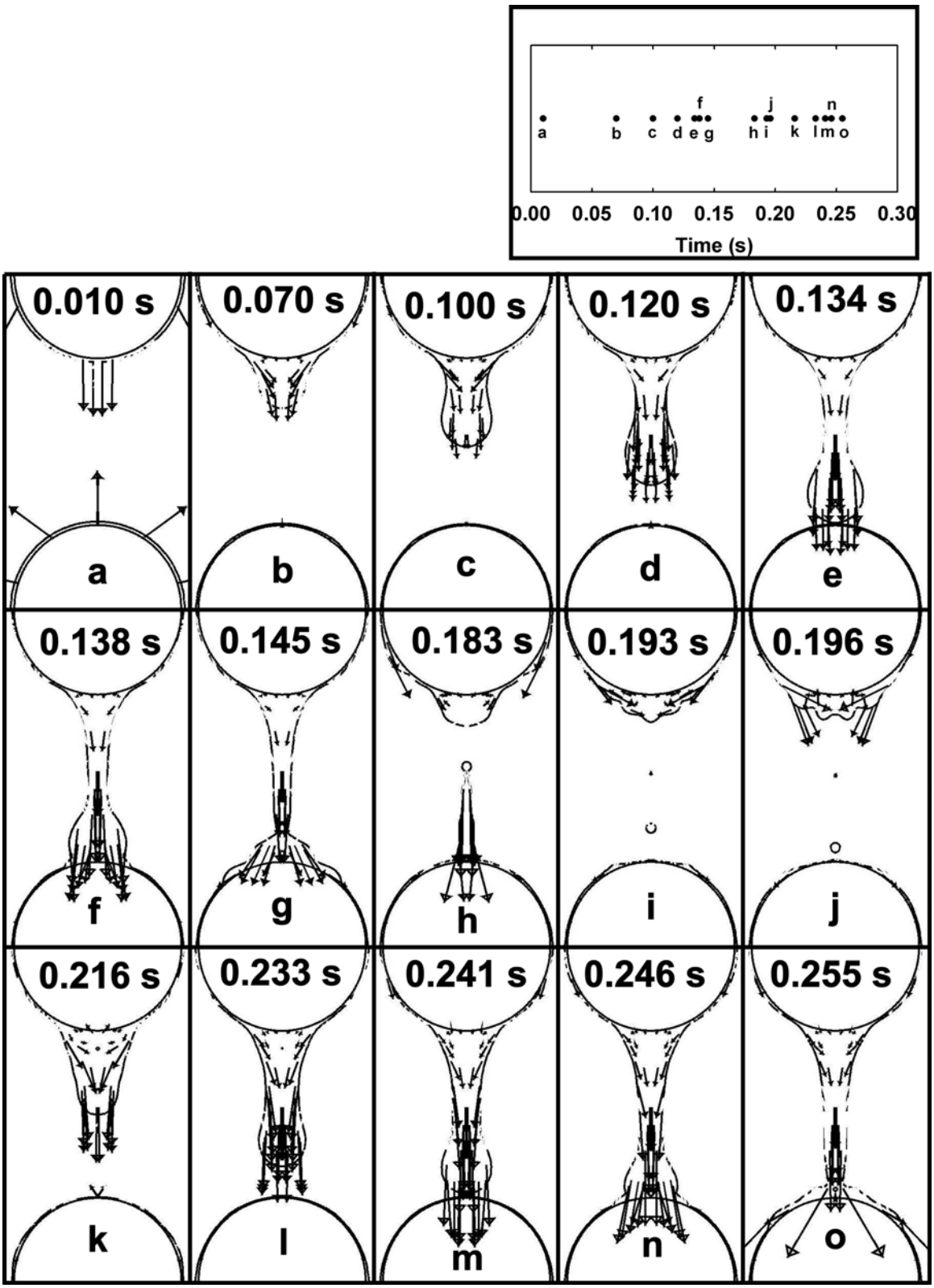

Figure 4.43: Velocity vectors for an inlet temperature of 45 ℃

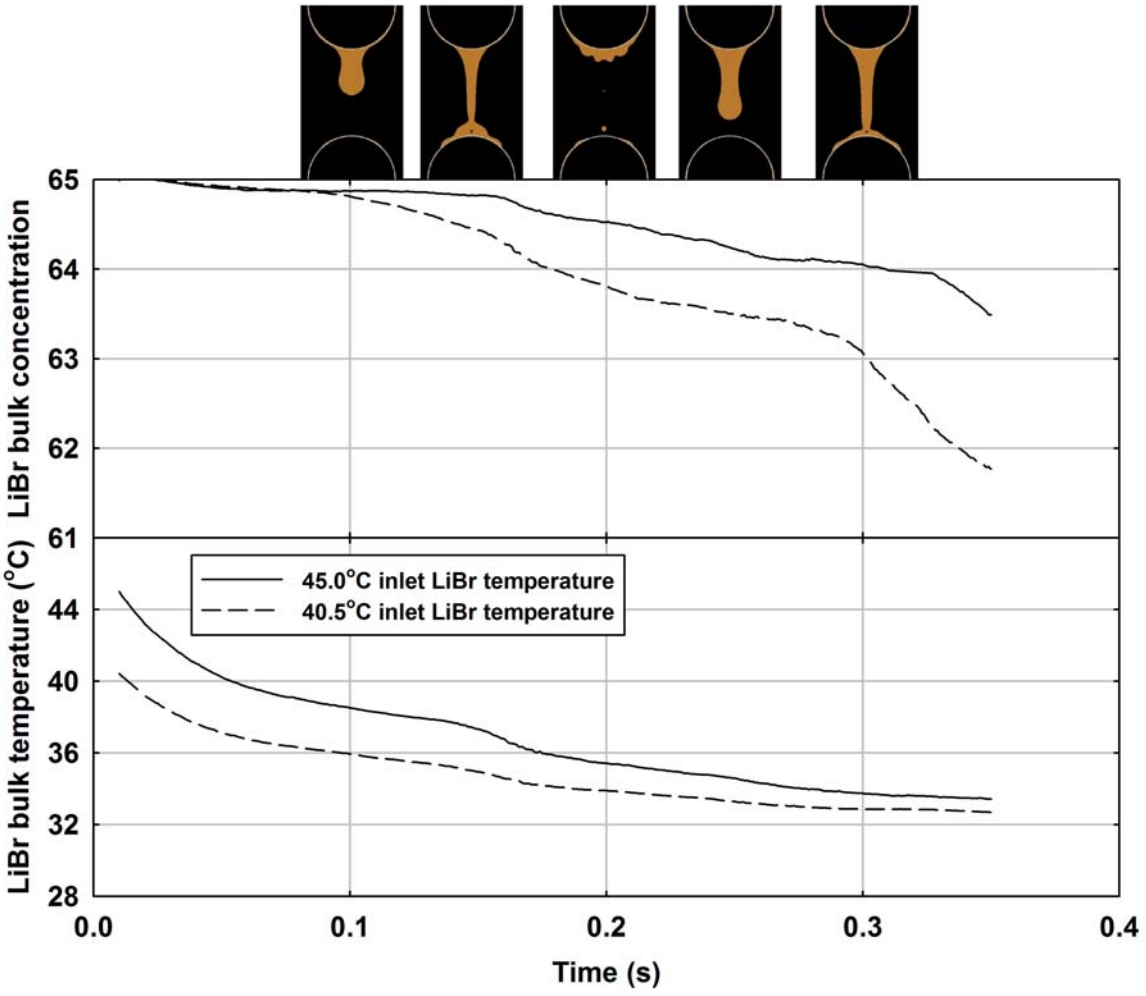

Figure 4.44: Temporal variation of bulk LiBr concentration and temperature for an inlet temperature of 45℃

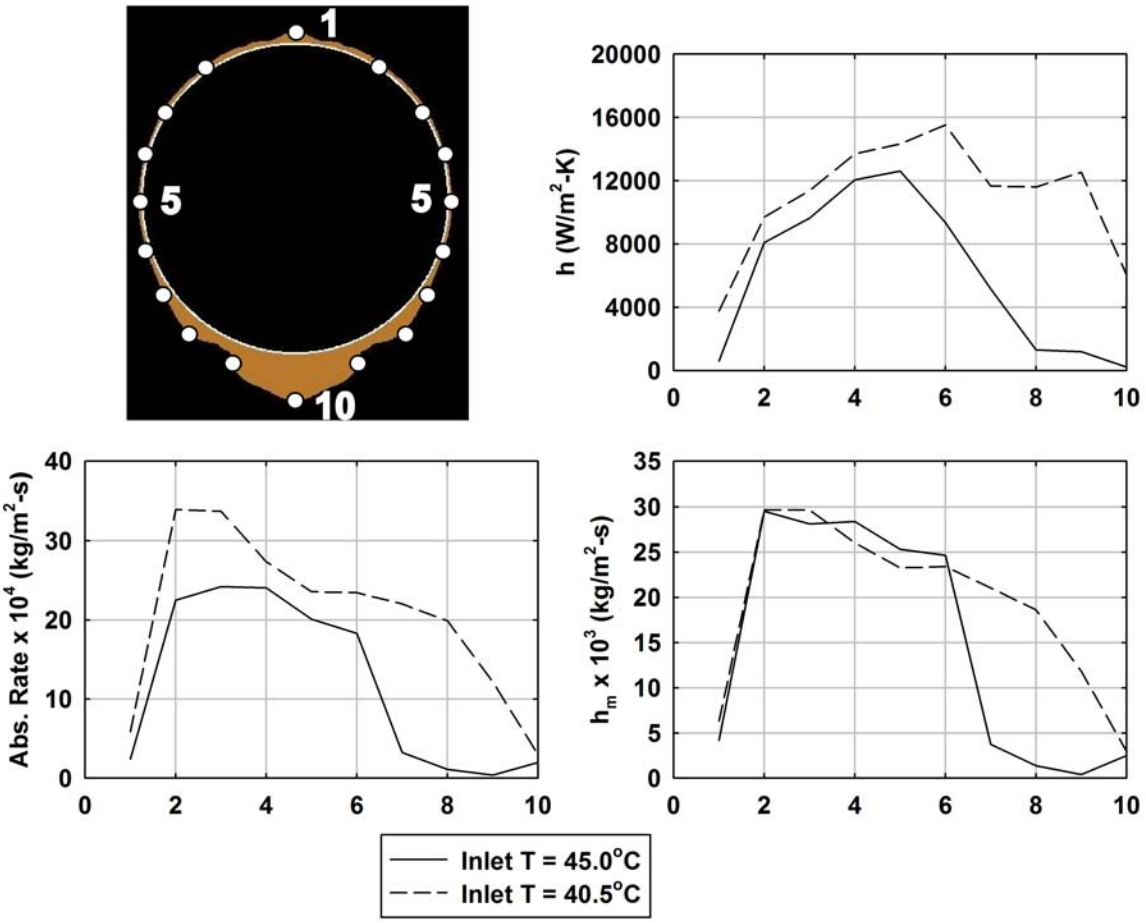

Figure 4.45: Local heat and mass transfer coefficients for an inlet temperature of 45 ℃

the viscous and surface tension forces, are very similar in the two cases.

4.6.6 Heat and mass transfer coefficients

Figure 4.45 presents the local heat and mass transfer coefficients and absorption rates at various points on the sphere at 0.191 s. The state of the flow at that time is shown in the picture below the plot. For the sake of comparison, the results from the baseline case are also plotted on the same graph.

The solid line in Figure 4.45 presents the local heat and mass transfer coefficients and absorption rates in the present case, while the dashed line presents the corresponding values for the baseline case. It is seen that the absorption rates in the

present case are lower than those in the baseline case. Due to the higher inlet temperature temperature, the interface equilibrium concentrations are higher in the present case, resulting in a lower driving concentration difference. The inlet temperature in the present case is 45.0 ℃, at which the equilibrium concentration is 59.6%, while the inlet temperature in the baseline case is 40.5 ℃, at which the equilibrium concentration is 57.4%. So initially, when the bulk lithium bromide concentration is 65.0% in both cases, the driving concentration difference is 5.4% for the present case, while it is 7.6% for the baseline case. The absorption rate in the present case at point 3 is 24.23×10^{-4} kg/m^2-s, while that for the baseline case is 33.73×10^{-4} kg/m^2-s. Similarly the absorption rate in the present case at point 7 is 3.24×10^{-4} kg/m^2-s, while that for the baseline case is 22.03×10^{-4} kg/m^2-s. A difference in the mass transfer coefficients also contributes to the lower absorption rate in the present case at point 7. The mass transfer coefficient in the present case at point 7 is 3.75×10^{-3} kg/m^2-s, while that in the baseline case is 21.00×10^{-3} kg/m^2-s.

Since the flow patterns are similar in the present and the baseline cases, it was expected that the heat and mass transfer coefficients would be the same in the two cases. However, it is seen that there are some differences in the heat and mass transfer coefficient values at certain points. The differences are particularly prominent near the bottom of the tube. For example at point 8, the heat transfer coefficient in the present case is 1303 W/m^2-K, while that in the baseline case is 11666 W/m^2-K. Similarly the mass transfer coefficient in the present case at point 8 is 1.4×10^{-3} kg/m^2-s, while that in the baseline case is 18.6×10^{-3} kg/m^2-s. This difference in the heat and mass transfer coefficients occurs because even though the flow patterns in the two cases are very similar, there is a slight difference in the film thicknesses near the bottom in the two cases. At the bottom of the sphere, the film thickness in the present case is 2.59 mm, while that in the baseline case is 1.79 mm. The higher film thickness in the present case causes the lower heat and mass transfer coefficients in

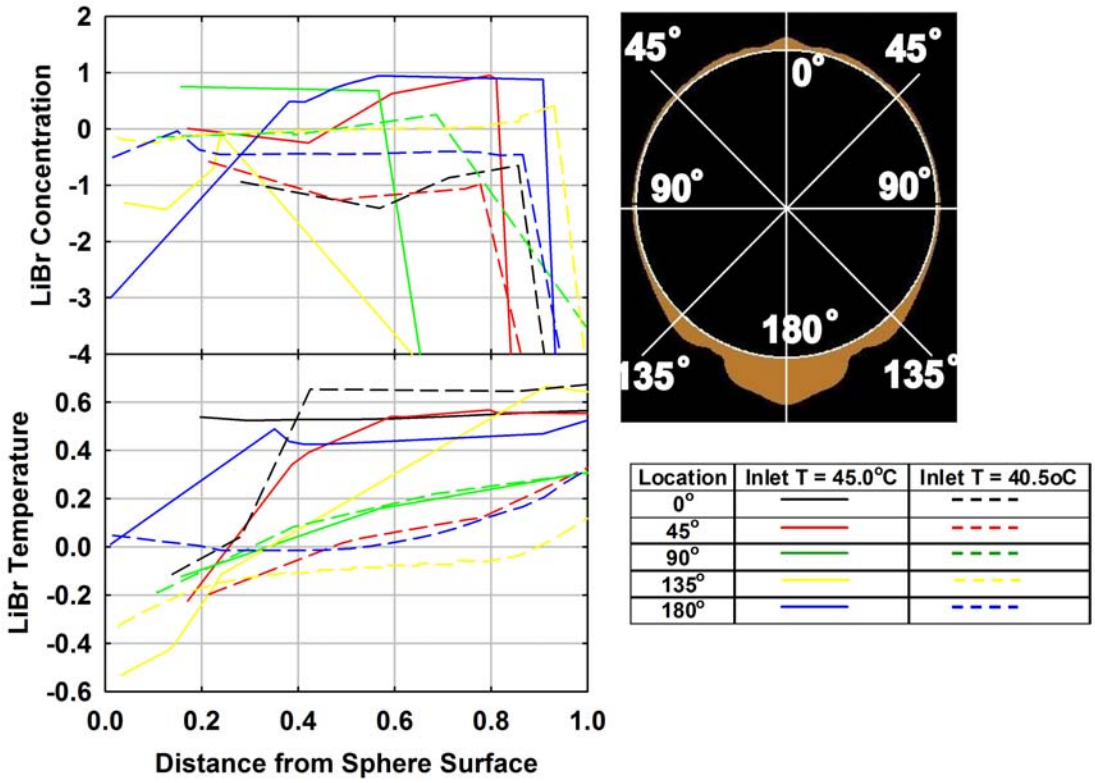

Figure 4.46: Concentration and temperature profiles for an inlet temperature of 45 °C

the regions near the bottom.

4.6.7 Film concentration and temperature profiles

Figure 4.46 presents the concentration and temperature profiles in the lithium bromide solution film on the sphere at 0.191 s. At this time, all of the lithium bromide solution is present in the form of a film around the sphere. The waves created due to droplet impact have propagated around the sphere and have dissipated away. For comparison the profiles for the baseline case are also plotted on the same graph and are shown in dashed lines.

As seen in Figure 4.46, the concentration and temperature profiles are very similar for the present and the baseline cases. This is in spite of the fact that the actual value of temperature and concentration are quite different in the two cases. This is because

the nature of the concentration and temperature profiles are mostly determined by the flow patterns, which are similar in the two cases. Similar to the baseline case, the concentration is highest close to the surface of the sphere and then decreases as away from the surface, towards the liquid-vapor interface. Also, the temperature is lowest close to the surface of the sphere and highest close to the liquid-vapor interface.

The minor differences in the profiles in the two cases can be attributed to differences in fluid properties and numerical resolution. As mentioned earlier, due to the low thickness of the film, there are very few grid points (< 10) within the film for the profile plots. These low number of grid points cause the minor differences observed between the two sets of profile plots. Also as mentioned earlier, there are slight differences in the film thicknesses at some locations in the two cases. For, example at 180°, the film thickness in the present case is 1.79 mm, while that in the baseline case was 2.59 mm. These differences in film thickness also contribute to the differences in the concentration and temperature profiles.

This concludes the discussion on the different inlet temperature case. It was seen that the different inlet temperature does not significantly affect the flow patterns or the heat and mass transfer coefficients or the nature of the concentration and temperature profiles. However the higher temperature causes a higher equilibrium concentration, which results in a lower driving concentration difference. This causes the absorption rate in the present case to be lower than in the baseline case. The average Reynolds number for the case was always less than 65, which is the same as that in the baseline case. The average heat transfer coefficient for this case at 0.191 s was found to be 6023 W/m^2-K, while that for the baseline case was 11023 W/m^2-K. The average mass transfer coefficient for this case was found to be 14.83×10^{-3} kg/m^2-s, while that for the baseline case was 19.26×10^{-3} kg/m^2-s. The average Nusselt number (based on the sphere diameter) for this case at 0.191 s was 159.6, while that for the baseline case was 265.8. The average Sherwood number for this case was

Table 4.6: Operating conditions for the case with a 0.30 mm thick initial film

Operating parameter	**Baseline case**	**Present case**
Solution inlet concentration	65% by wt of LiBr	65% by wt of LiBr
Solution inlet temperature	40.5 ℃	40.5 ℃
Sphere wall temperature	30 ℃	30 ℃
Sphere diameter	15.9 mm	15.9 mm
Sphere pitch	15.9 mm	15.9 mm
Initial film thickness	*0.35 mm*	*0.30 mm*
LiBr mass flux	*0.0058 kg/ms*	*0.0042 kg/ms*

92.6, while that for the baseline case was 106.0. The average absorption flux for the present case at 0.191 s was 11.83×10^{-4} kg/m^2-s, while that for the baseline case was 20.51×10^{-4} kg/m^2-s. In the following section, the lithium bromide solution flow rate is varied to study its effect on the local heat and mass transfer phenomena.

4.7 Different flow rate

In this section, the lithium bromide flow rate is changed and its effect on the absorption phenomenon is investigated on a two dimensional grid. In the baseline case, the flow is started with a uniform 0.35 mm lithium bromide solution film around the sphere. In this case, the initial solution film thickness is reduced to 0.30 mm, which results in a lower flow rate. The operating conditions for this case are summarized in Table 4.6. The average Reynolds number in this case was always less than 49.

4.7.1 Flow pattern

Figure 4.47 shows the fluid flow pattern and the droplet shape as it falls down the column of spheres. Due to the different flow rate, the flow patterns in the present case are different from those in the baseline case. Though the nature of the flow remains the same, the flow velocities are lower and droplet formation, breakup and fall takes

a lot longer than the baseline case. For example, in the baseline case, the first droplet hits the next sphere at 0.133 s, while in the present case, the first droplet hits the next sphere at 0.208 s.

4.7.2 Concentration distribution

Figure 4.48 shows the local changes in the lithium bromide concentration as it falls down the column of spheres. The average concentration of the lithium bromide solution at each of the time steps is also printed over the sphere.

Due to the different flow rate, the concentration distribution in the present case is significantly different than in the baseline case. The different flow rate results in lower local fluid velocities, which result in lower local mass transfer coefficients. As a result, the mass transfer and the resultant concentration change is lower in the present case as compared to the baseline case. For example, after a time of 0.25 s, the average concentration in the present case is 64.06%, while that in the baseline case was 63.50%. Similar to the baseline case, the concentration is lowest at the liquid-vapor interface due to absorption of vapor at the interface. Also the concentrations are typically lower in the film than on the droplet due to better thermal contact of the film with the coolant, as compared to the droplet. Though the initial thickness is lower in this case, the film thickness during the flow is not very different from the baseline case. This is because in the sphere geometry, almost all of the fluid in the initial film is absorbed into the droplet. So, due to the lower initial film thickness, the droplet size is lower that the baseline case. For most of the flow the film thicknesses in both the cases are extremely small.

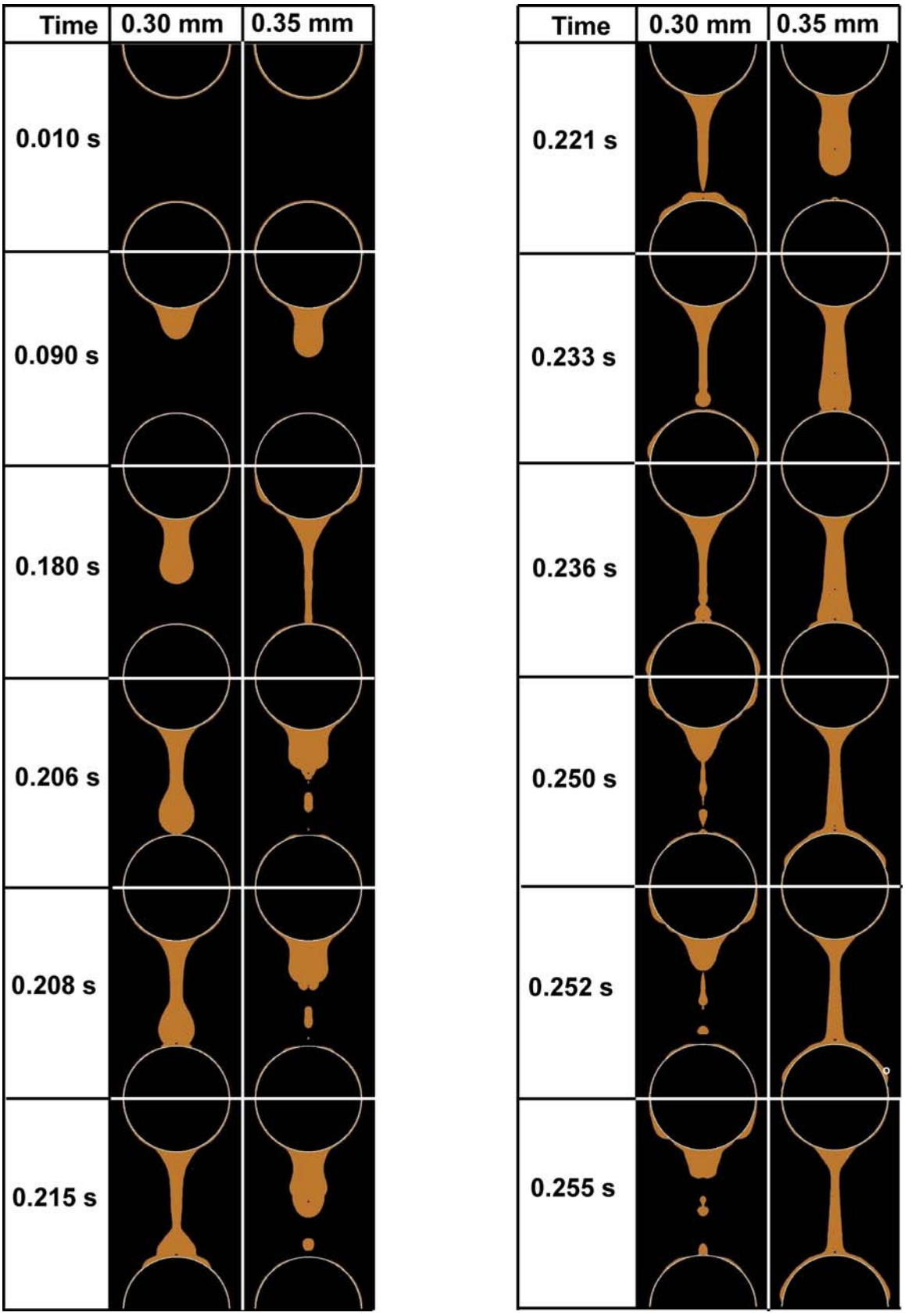

Figure 4.47: Droplet flow for a 0.30 mm thick initial film

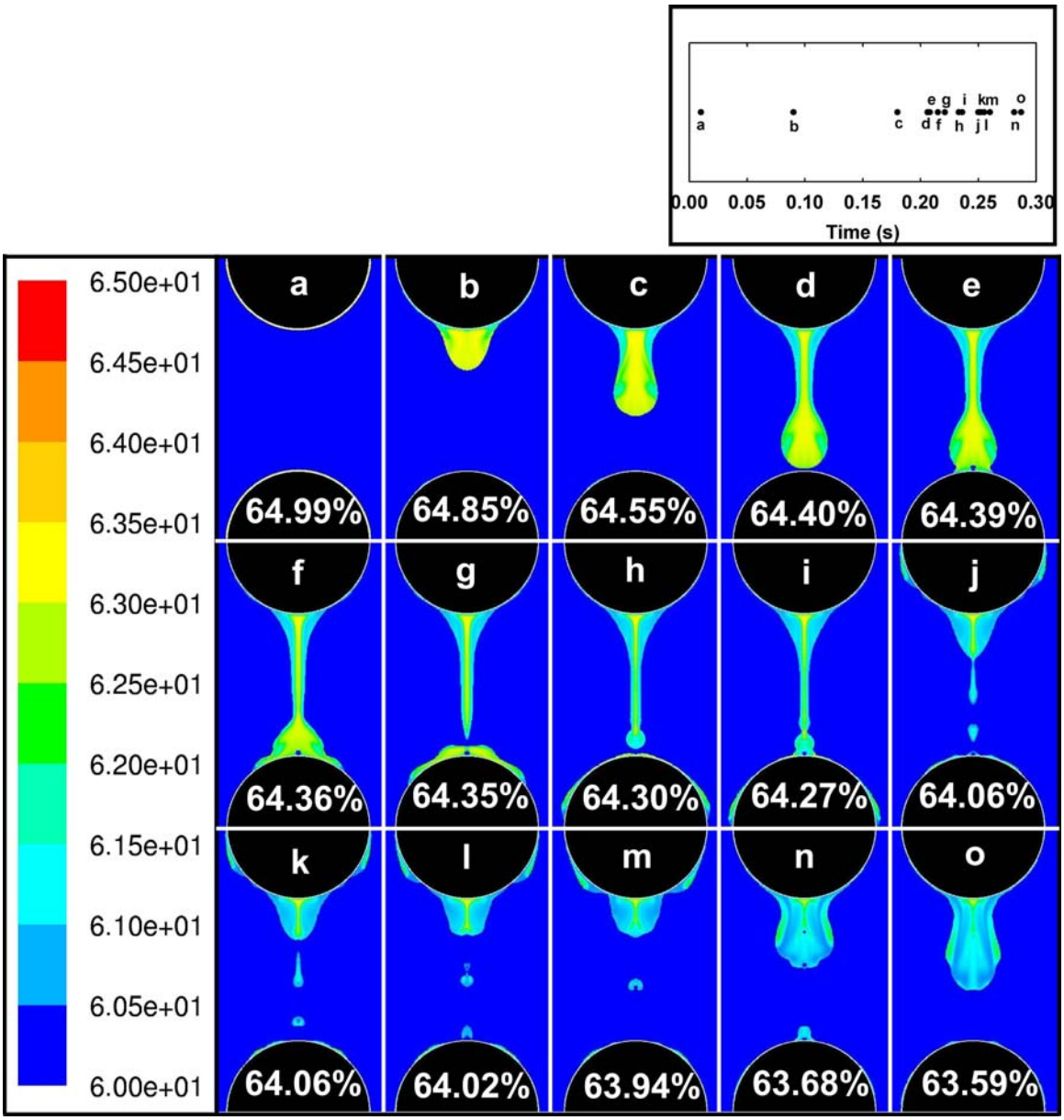

Figure 4.48: LiBr concentration distribution in a droplet for a 0.30 mm thick initial film

4.7.3 Temperature distribution

Figure 4.49 shows the variation in the temperature of the lithium bromide solution as it falls through the spheres. The average temperature of the lithium bromide solution at that time step is printed over the sphere in each frame.

Due to the different flow rate, the temperature distribution in the present case is significantly different from that in the baseline case. The lower flow rate results in lower local fluid velocities, which results in lower heat transfer coefficients. Also as seen in the previous section, due to lower mass transfer coefficients, the amount of vapor absorbed is lower in the present case. This results in lower amount of heat generation at the interface during the absorption process. Consequently, the average temperatures in the present case are slightly lower than those in the baseline case. For example, after 0.25 s, the average temperature in the present case is 32.83 ℃, while that in the baseline case is 33.29 ℃.

In spite of the difference in the average temperatures, the nature of the temperature variation is very similar in the present and baseline cases. Similar to the baseline case, the solution in the film over the sphere is usually low in temperature as it is cooled very effectively by the coolant inside the sphere. The solution in the droplet, being farther away from the coolant, is not cooled very effectively and hence is warmer in temperature.

4.7.4 Velocity distribution

Figure 4.50 shows the distribution of velocity in the lithium bromide solution. The velocity is represented by a series of arrows, where the direction of the arrows denote the direction of the velocity vector, while the length of the arrow is proportional to the magnitude of the velocity at that point. Due to the lower flow rate, the local velocities in the present case are smaller. Consequently the velocity vectors in the

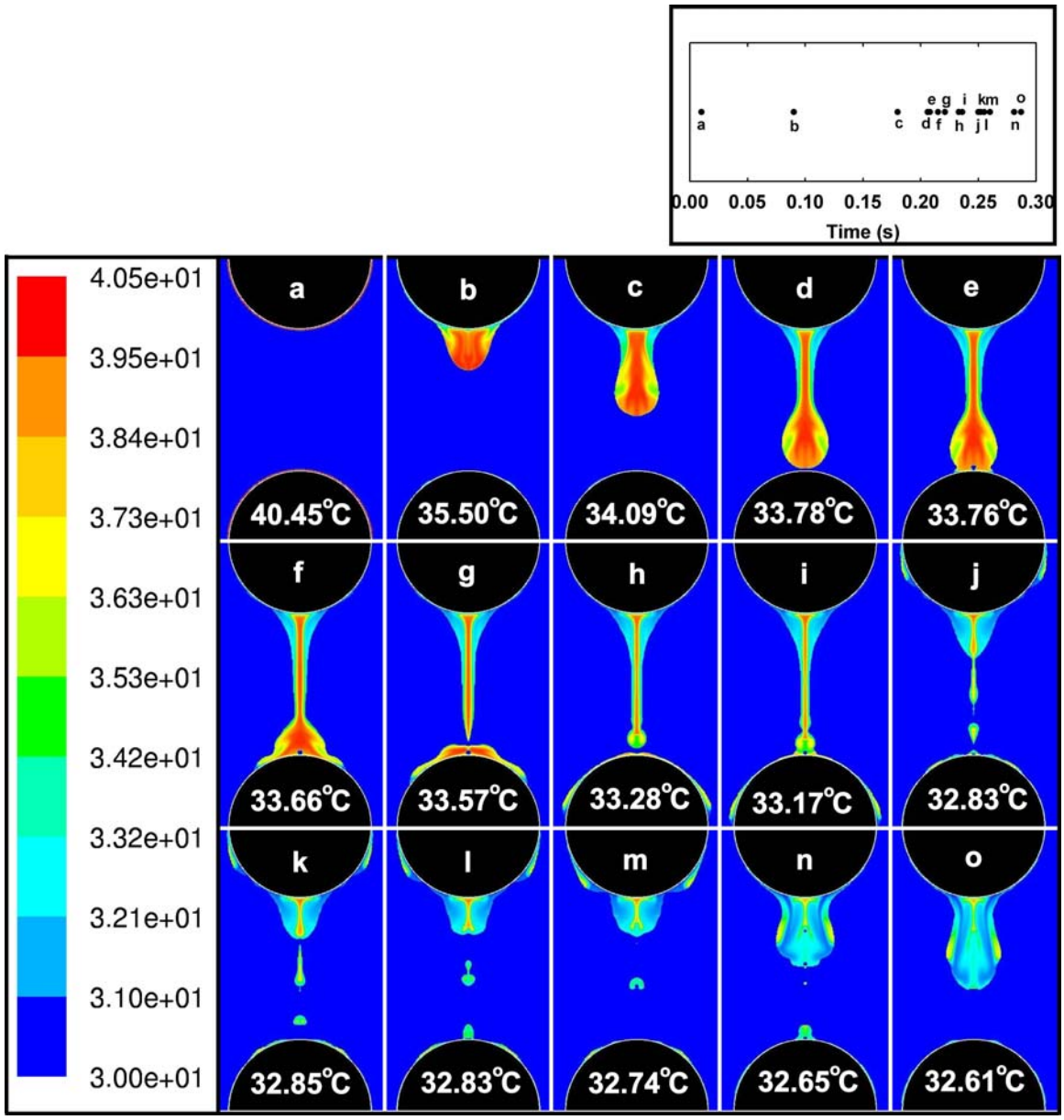

Figure 4.49: LiBr temperature distribution in a droplet for a 0.30 mm thick initial film

present case are shorter than those in the baseline case. In the baseline case, the first droplet hits the next sphere at 0.133 s, while in the present case, the first droplet hits the next sphere at 0.208 s. Though the actual velocities are lower, the nature of the velocity distribution is similar in the present and baseline cases.

4.7.5 Bulk concentration and temperature variation

Figure 4.51 shows the temporal variation of the average concentration change and temperature of the lithium bromide solution. The bulk concentration and temperature variation for the baseline case is also shown for the sake of comparison. The variation for the present case is represented by a solid line, while that for the baseline case is shown by a dashed line. The flow patterns at the respective times are shown above the plot.

Due to the lower flow rate, the mass transfer coefficients are lower in the present case. As a result, the rate of absorption and consequently the rate of bulk concentration decrease are lower in the present case. For example, after a time of 0.25 s, the average concentration in the present case is 64.06%, while that in the baseline case was 63.50%. Also, due to the lower amount of absorption, the amount of heating due to absorption is lower in the present case. Consequently, the average temperatures in the present case are slightly lower than those in the baseline case. For example, after 0.25 s, the average temperature in the present case is 32.83 ℃, while that in the baseline case is 33.29 ℃.

Due to the lower flow rate, the droplet formation and fall take a longer than the baseline case. Consequently, though the nature of the bulk concentration and temperature variation in the present case is similar to the baseline case, the plots are *out of phase*. For example in the present case, the droplet hits the next sphere at about 0.21 s and that causes the mixing effect, which increase the absorption rate.

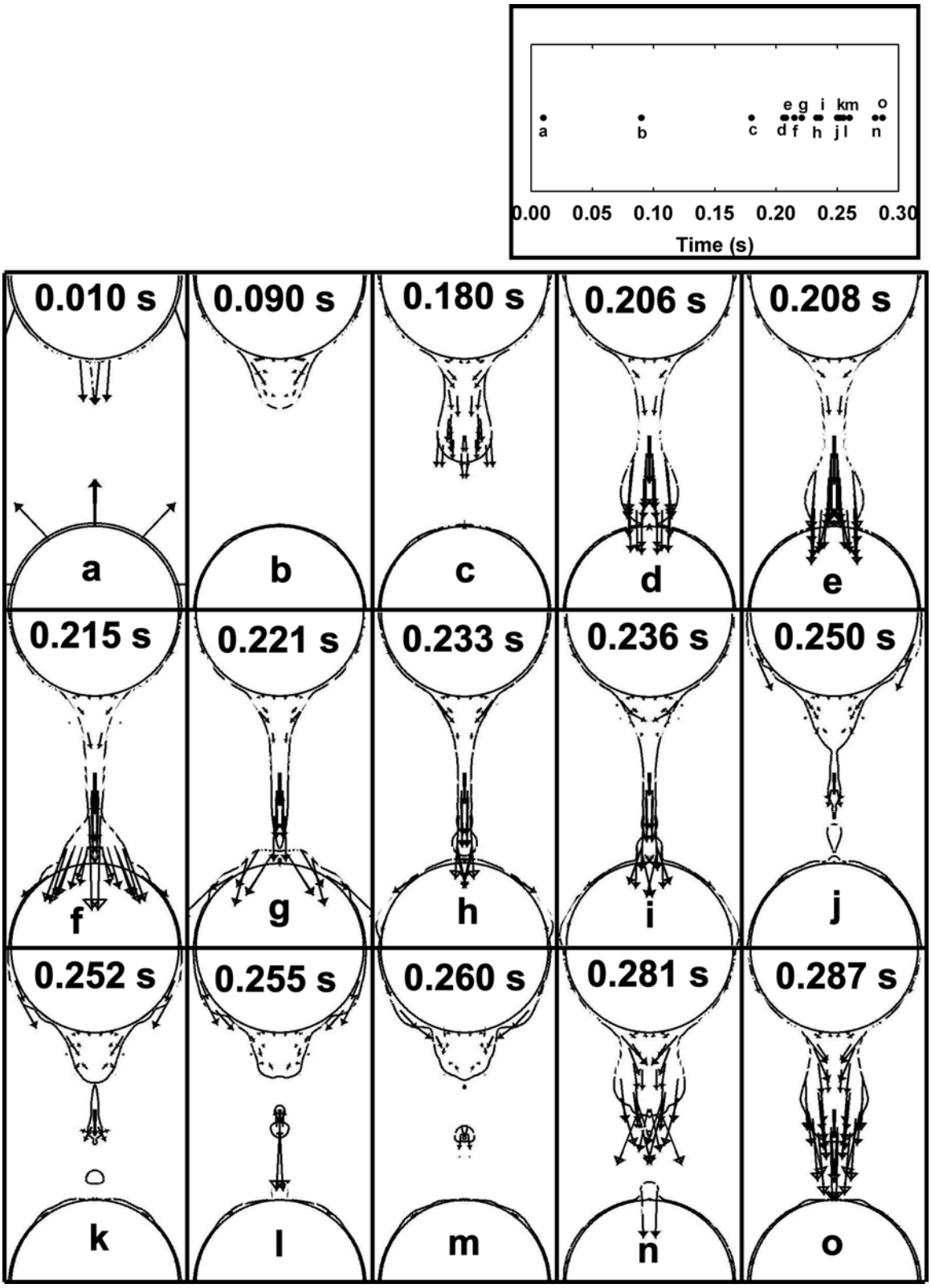

Figure 4.50: Velocity vectors for a 0.30 mm thick initial film

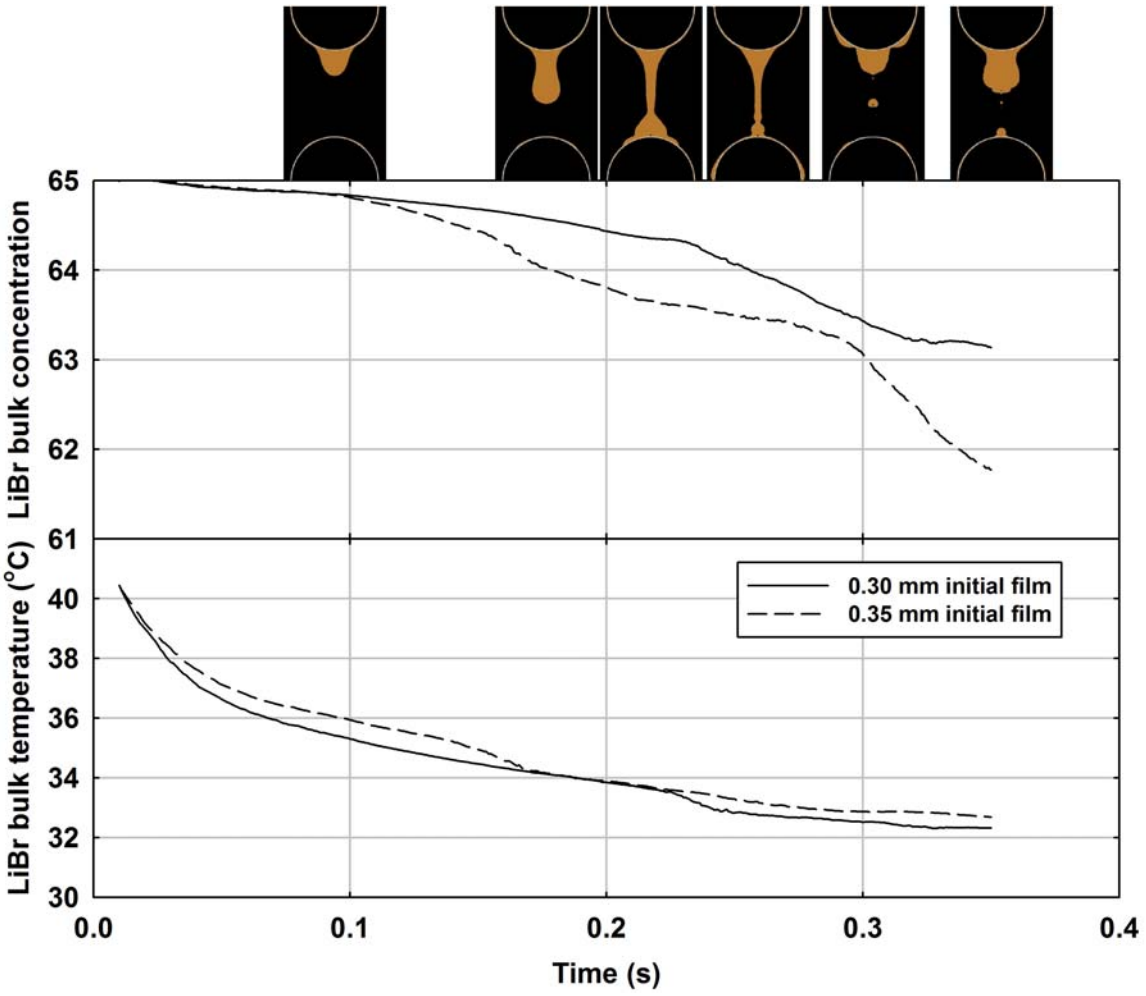

Figure 4.51: Temporal variation of bulk LiBr concentration and temperature for a 0.30 mm thick initial film

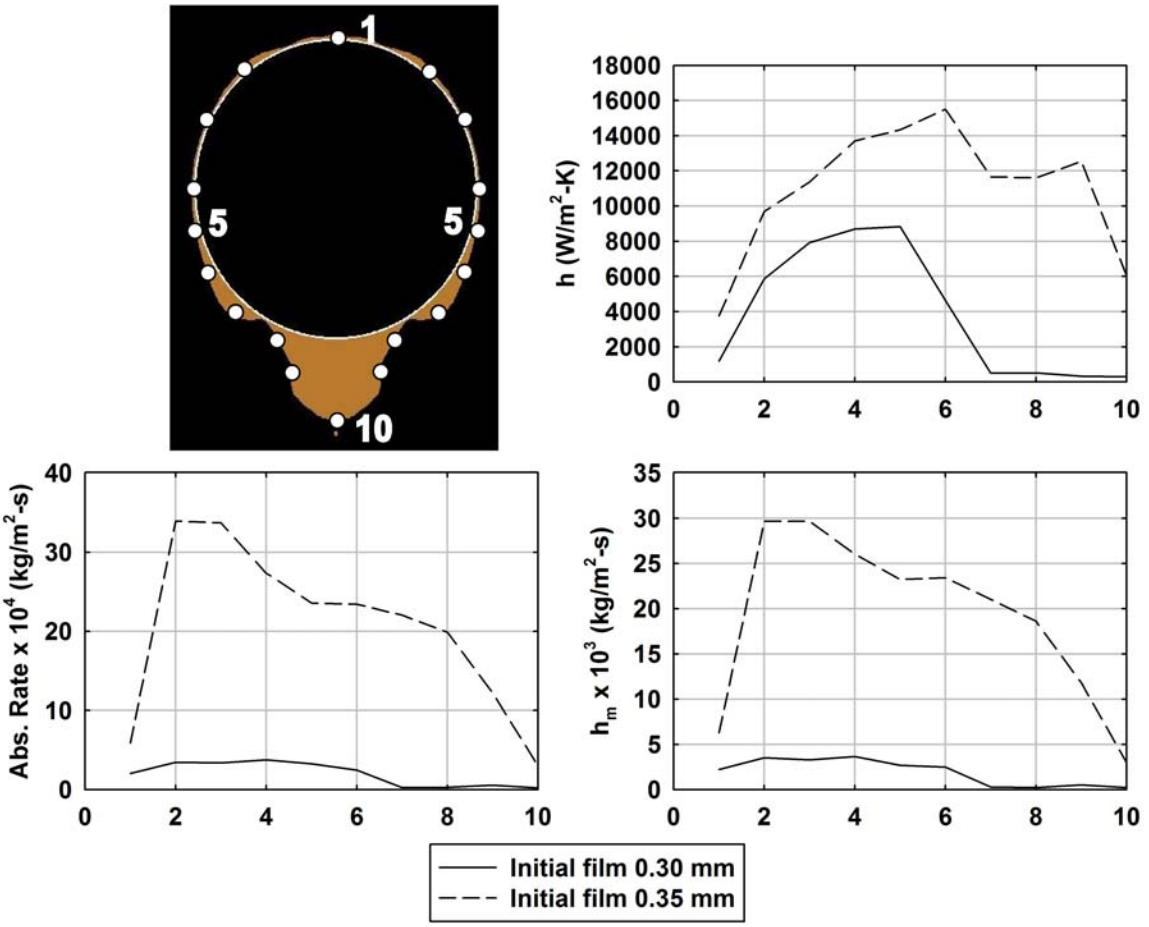

Figure 4.52: Local heat and mass transfer coefficients for a 0.30 mm thick initial film

The corresponding increase in absorption rate due to droplet impact is seen in the baseline case at about 0.14 s.

4.7.6 Heat and mass transfer coefficients

Figure 4.52 presents the local heat and mass transfer coefficients and absorption rates at various points on the sphere at 0.258 s. The state of the flow at that time is shown in the picture below the plot. For the sake of comparison, the results from the baseline case are also plotted on the same graph.

The solid line in Figure 4.52 presents the local heat and mass transfer coefficients

and absorption rates in the present case, while the dashed line presents the corresponding values for the baseline case. As shown in the picture of the flow attached to the plot, at this time step all of the lithium bromide solution is present as a film around the sphere. It is seen that the heat and mass transfer coefficients for the present case are much lower than the baseline case. This is because the lower flow rate results in lower local velocities, which in turn lead to the lower local heat and mass transfer coefficients. The average velocity of the lithium bromide solution in the present case is 0.12 m/s, while that in the baseline case is 0.14 m/s. For example, at point 4, the heat transfer coefficient in the present case is 8705 W/m^2-K, while that in the baseline case was 13696 W/m^2-K. Similarly, the mass transfer coefficient in the present case at point 4 is 3.7×10^{-3} kg/m^2-s, while that in the baseline case was 26.0×10^{-3} kg/m^2-s. It is seen that the change in velocity has a bigger effect on the mass transfer coefficient than the heat transfer coefficient. This is because the thermal transport characteristics (k=0.6 W/m-K) of the lithium bromide solution are much better than the mass transport characteristics ($D_{AB} = 1.6 \times 10^{-9}$ m^2/s). Though the reduction in flow velocity affects the convective thermal transport, the diffusion thermal transport terms being high enough can overcome some of the thermal transport losses due to low velocity. However, as the diffusion terms for mass transport are also low due to a low D_{AB}, the reduction in convective mass transport due to reduction in velocity cannot be overcome, and the lower velocity drastically affects the mass transfer coefficient. The absorption rate in the present case is also lower than that in the baseline case, due to the lower mass transfer coefficients. At point 4, the absorption rate in the present case is 3.7×10^{-4} kg/m^2-s, while that in the baseline case was 27.4×10^{-4} kg/m^2-s.

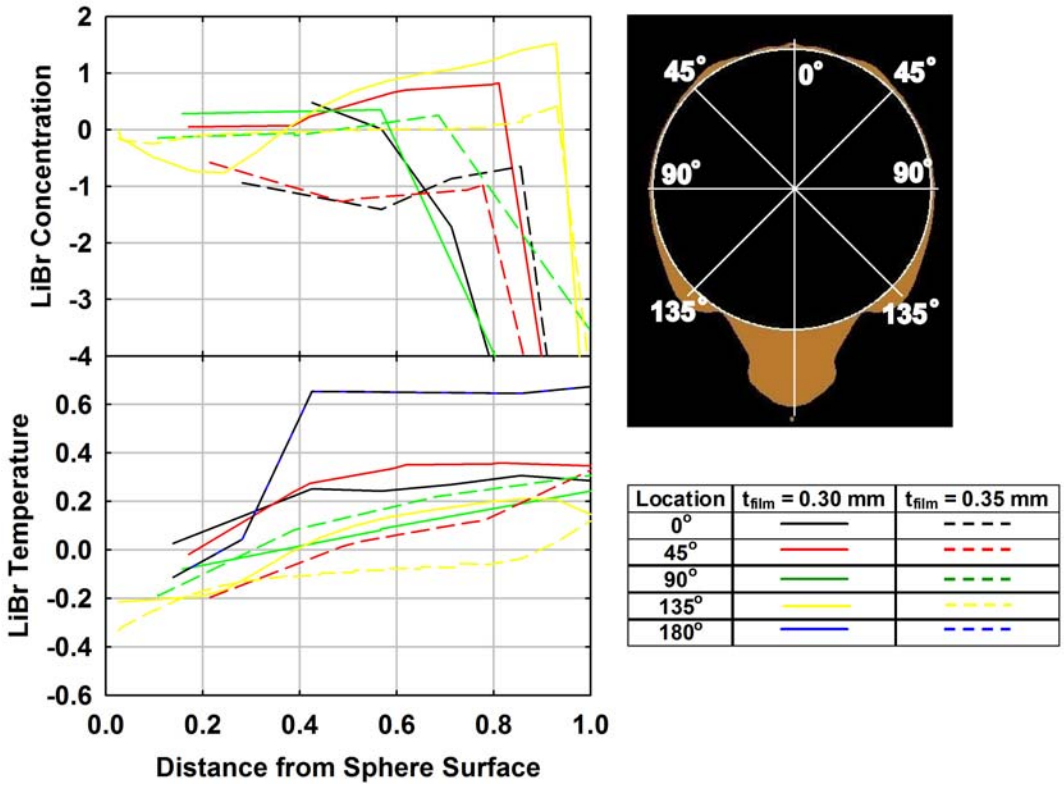

Figure 4.53: Concentration and temperature profiles for a 0.30 mm thick initial film

4.7.7 Film concentration and temperature profiles

Figure 4.53 presents the concentration and temperature profiles in the lithium bromide solution film on the sphere at 0.258 s. At this time all of the lithium bromide solution is present in the form of a film around the sphere. The waves created due to droplet impact have propagated around the sphere and have dissipated away. For comparison the profiles for the baseline case are also plotted on the same graph and are shown in dashed lines.

As seen in Figure 4.53, the concentration and temperature profiles are very similar for the present and the baseline cases. This is in spite of the fact that the actual value of temperature and concentration are quite different in the two cases. This is because the nature of the concentration and temperature profiles are mostly determined by the flow patterns, which are similar in the two cases, albeit a little out of phase. Similar

to the baseline case, the concentration is highest close to the surface of the sphere and then decreases as away from the surface, towards the liquid-vapor interface. Also, the temperature is lowest close to the surface of the sphere and highest close to the liquid-vapor interface.

This concludes the discussion of the different flow rate case. It was seen that the different flow rate does not significantly affect the nature of the flow, but the velocity field is significantly altered. Due to lower velocities, the droplet formation, detachment and fall occurs at a slower pace as compared to the baseline case. Consequently the mixing due to droplet impact occurs at a later time as compared to the baseline case. Also, the heat and mass transfer coefficients and absorption rates are significantly lower due to lower fluid velocities. The nature of the concentration and temperature profiles remain unchanged . The average Reynolds number for the case was always less than 49, while that for the baseline case was always less than 65. The average heat transfer coefficient for this case at 0.258 s was found to be 3880 W/m^2-K, while that for the baseline case was 11023 W/m^2-K. The average mass transfer coefficient for this case was found to be 1.92×10^{-3} kg/m^2-s, while that for the baseline case was 19.26×10^{-3} kg/m^2-s. The average Nusselt number (based on the sphere diameter) for this case at 0.258 s was 102.8, while that for the baseline case was 292.1. The average Sherwood number in this case was 12.0, while that in the baseline case was 120.2. The average absorption flux in the present case was 1.97×10^{-4} kg/m^2-s, while that for the baseline case was 20.51×10^{-4} kg/m^2-s. In the following section the coolant temperature is varied and its effect on the local heat and mass transfer phenomena is studied.

Table 4.7: Operating conditions for the 35 ℃ coolant temperature case

Operating parameter	Baseline case	Present case
Solution inlet concentration	65% by wt of LiBr	65% by wt of LiBr
Solution inlet temperature	40.5 ℃	40.5 ℃
Sphere wall temperature	*30 ℃*	*35 ℃*
Sphere diameter	15.9 mm	15.9 mm
Sphere pitch	15.9 mm	15.9 mm
LiBr mass flux	0.0058 kg/ms	0.0058 kg/ms

4.8 Different coolant temperature

In this section, the coolant is changed and its effect on the absorption phenomenon is studied on a two dimensional grid. The coolant temperature is changed to 35.0 ℃, from a baseline value of 30.0 ℃. The operating conditions for the present case are summarized in Table 4.7. The average Reynolds number in this case was always less than 65.

4.8.1 Flow pattern

Figure 4.54 shows the fluid flow pattern and the droplet shape as it falls down the column of spheres. Droplet formation occurs between 0.070 s and 0.100 s. Necking of the droplet is seen at 0.120 s and 0.134 s in Figure 4.40. Eventually, the droplet detaches from the sphere and falls off.

At a time of 0.138 s (Figure 4.40) the droplet reaches the next sphere before it detaches completely from the previous one. The impact of the droplet on the sphere causes a *ripple* or *wave* in the solution film on the sphere, which is seen at time steps 0.138 s and 0.145 s in Figure 4.40. The droplet detachment occurs at 0.183 s and satellite droplets are seen at 0.193 s and 0.196 s in Figure 4.40.

It is seen that the droplet flow patterns in the present case are very similar to those in the baseline case. This was expected since the flow patterns are governed

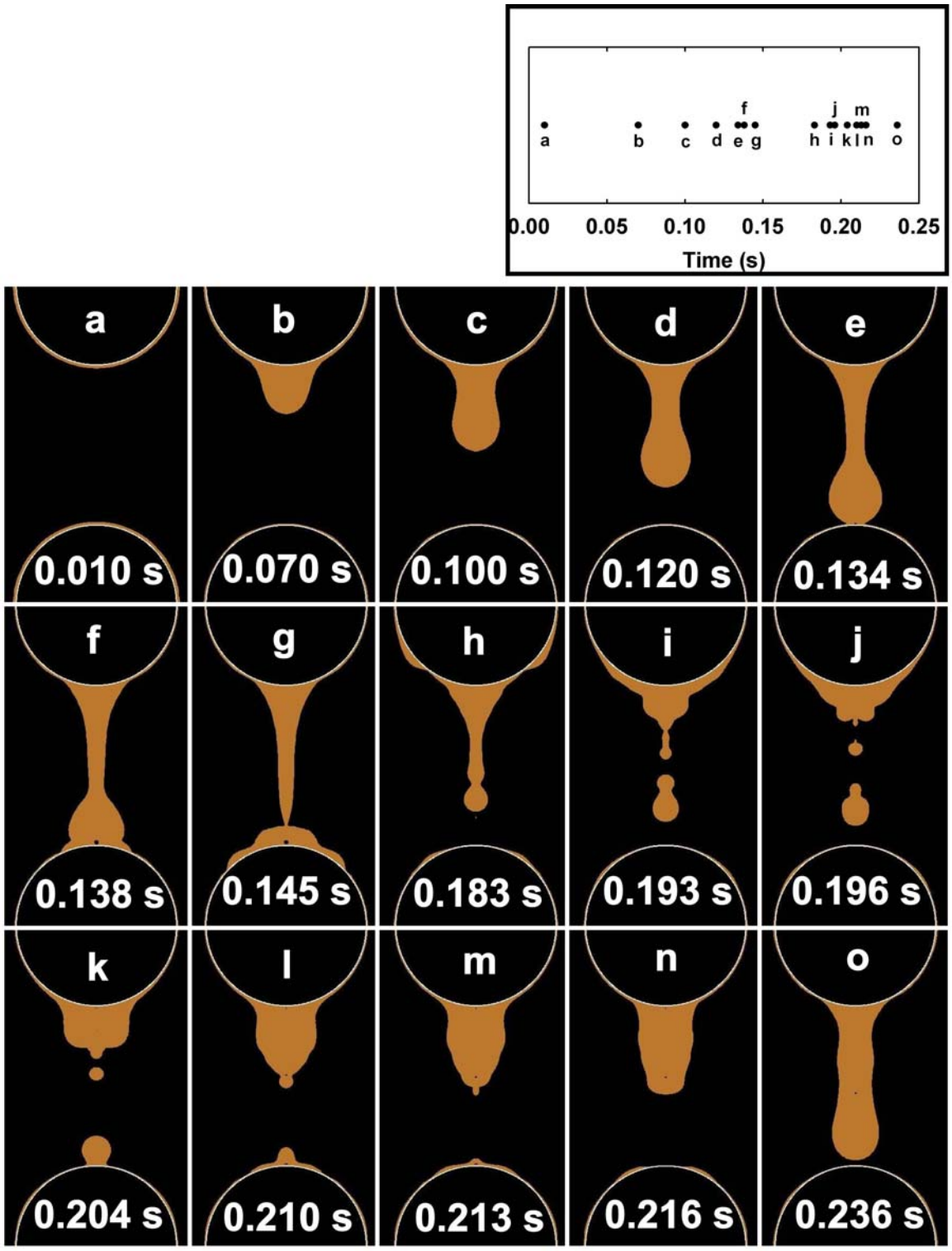

Figure 4.54: Droplet flow for a 35℃ coolant temperature

primarily by the viscosity and surface tension of water vapor and the lithium bromide solution, and these do not change appreciably for this change in temperature [74, 76].

4.8.2 Concentration distribution

Figure 4.55 shows the local changes in the lithium bromide concentration as it falls down the column of spheres. The average concentration of the lithium bromide solution at each of the time steps is also printed over the sphere.

Due to the different coolant temperature, the concentration distribution in the present case is significantly different from that in the baseline case. Due to the higher coolant temperature, the solution temperature is higher in the present case as compared to the baseline case. The absorption process is driven by the difference between the concentration at the interface and the vapor pressure equilibrium concentration. The vapor pressure equilibrium concentration is a strong function of the lithium bromide solution temperature. The equilibrium concentration at 30°C is 51.2%, while the equilibrium concentration at 35°C is 54.3%. Due to the higher equilibrium concentration, the driving concentration difference is much lower in the present case. As a result, the mass transfer and the resultant concentration change is lower in the present case as compared to the baseline case.

Similar to the baseline case, the concentration is lowest at the liquid-vapor interface due to absorption of vapor at the interface. Also the concentrations are typically lower in the film than on the droplet due to better thermal contact of the film with the coolant, as compared to the droplet. Similar to the baseline case, the highest concentration in the present distribution plots is 65%. However, the lowest concentration, which is the interface equilibrium concentration, depends on the solution temperature and is higher in the present case as compared to the baseline case. The lowest average concentration in the present case is 63.84%, while it was 63.34% in the baseline case.

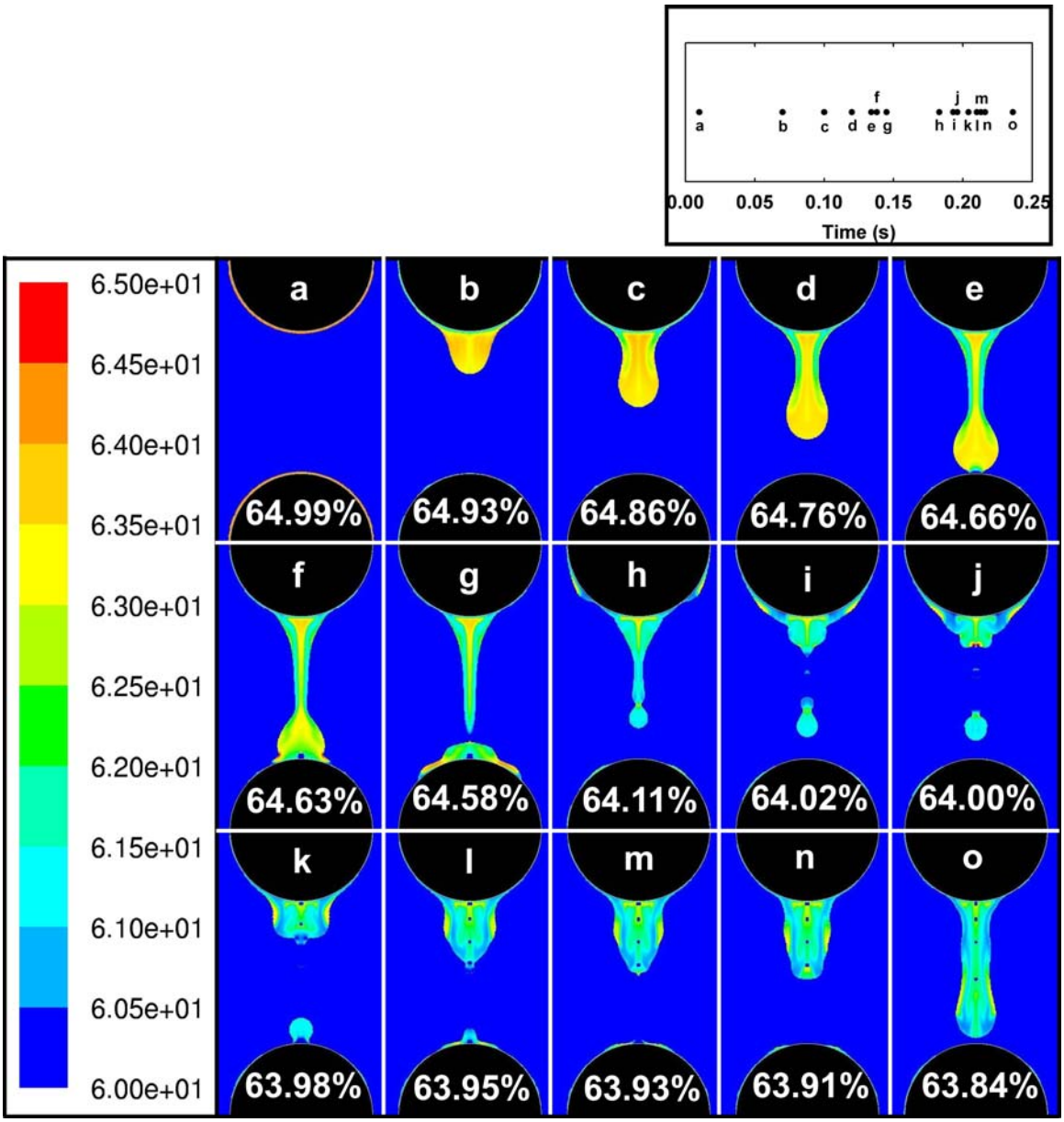

Figure 4.55: LiBr concentration distribution in a droplet for a 30℃ coolant temperature

4.8.3 Temperature distribution

Figure 4.56 shows the variation in the temperature of the lithium bromide solution as it falls through the spheres. The average temperature of the lithium bromide solution at that time step is printed over the sphere in each frame.

Due to the different coolant temperature, the temperature distribution in the present case is significantly different from that in the baseline case. Due to the higher coolant temperature, the solution temperatures are higher in the present case. For example, at 0.25 s, the average temperature in the present case is 36.7 ℃, while it was 33.3 ℃ in the baseline case. The coolant temperature places a limit on the lowest possible temperature to which the lithium bromide solution can be cooled. Hence the lowest temperature in the scale in Figure 4.56 is 35 ℃ in the present case, while it was 30 ℃ in the corresponding plot for the baseline case.

In spite of the difference in the average temperatures, the nature of the temperature variation is very similar in in the present and baseline cases. Similar to the baseline case, the solution in the film over the sphere is usually low in temperature as it is cooled very effectively by the coolant inside the sphere. The solution in the droplet, being farther away from the coolant, is not cooled very effectively and hence is warmer in temperature.

4.8.4 Velocity distribution

Figure 4.57 shows the distribution of velocity in the lithium bromide solution. As explained earlier, the flow patterns in the present case are very similar to the baseline case. Consequently, the velocity vectors in the present case are also very similar to the baseline case. This is because the flow velocities are governed primarily by the viscosity and surface tension of water vapor and the lithium bromide solution, and

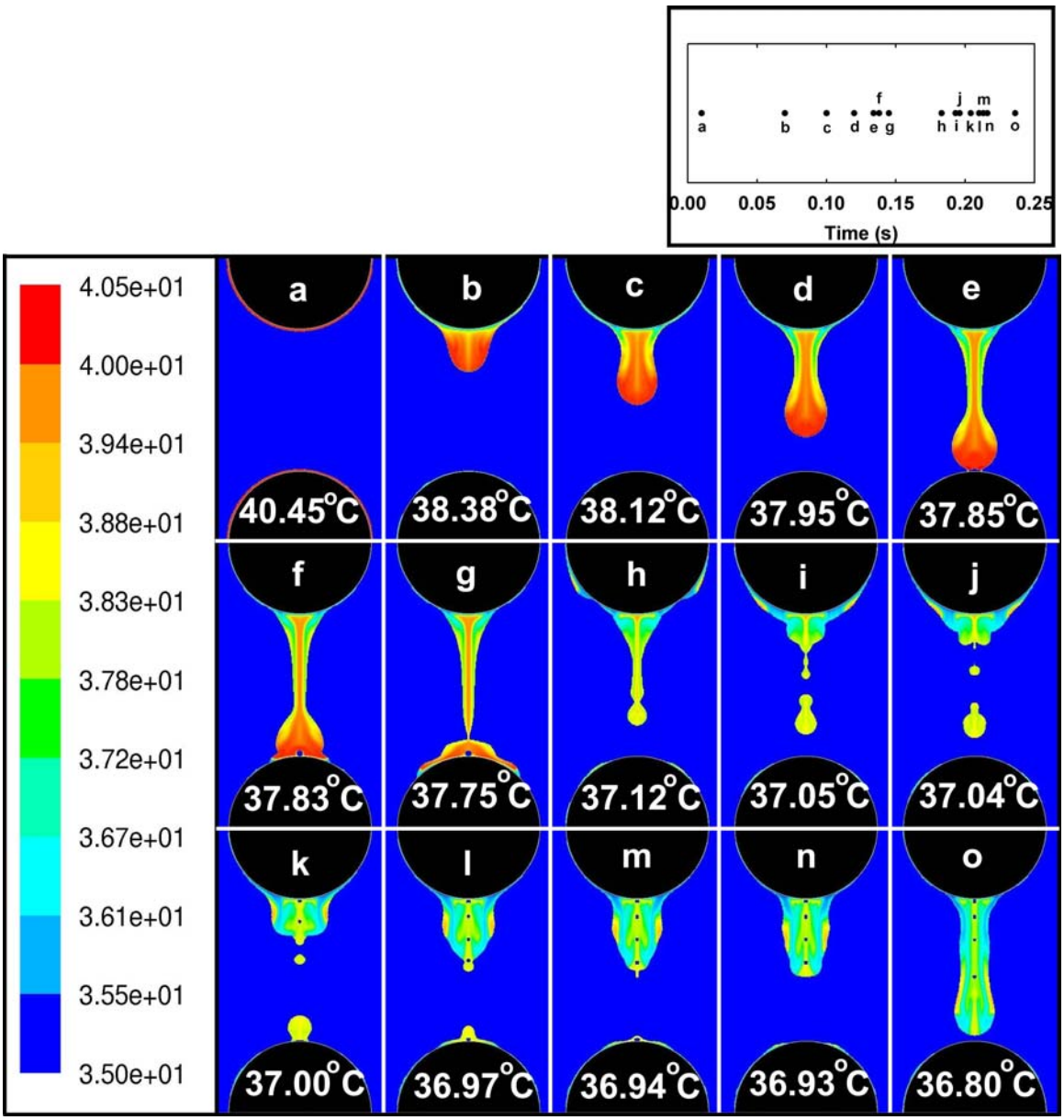

Figure 4.56: LiBr temperature distribution in a droplet for a 30℃ coolant temperature

these do not change appreciably for this change in solution temperature [74, 76].

4.8.5 Bulk concentration and temperature variation

Figure 4.58 shows the temporal variation of the average concentration change and temperature of the lithium bromide solution. The bulk concentration and temperature variations for the baseline case are also shown for the sake of comparison. The variation for the present case is represented by a solid line, while that for the baseline case is shown by a dashed line. The flow patterns at the respective times are shown above the plot.

Due to the higher coolant temperature and the corresponding lower temperature difference with the lithium bromide solution, the rate of temperature decrease is lower in the present case as compared to the baseline case. This is seen in the bulk temperature variation Figure 4.58, where the solid line corresponding to the present case decreases faster than the dashed line corresponding to the baseline case.

The higher lithium bromide solution temperature also corresponds to higher interface equilibrium concentration and thus a lower concentration difference for mass transfer. The equilibrium concentration at 30℃ is 51.2%, while the equilibrium concentration at 35℃ is 54.3%. Due to this lower concentration difference, the rate of concentration decrease is lower in the present case. This is seen in the bulk concentration variation in Figure 4.58, where the solid line corresponding to the present case decreases slower than the dashed line corresponding to the baseline case.

Besides the difference in the rate of concentration and temperature changes, the nature of the bulk temperature and concentration variations are very similar in the present and the baseline cases. This is because the flow patterns, which depend on the viscous and surface tension forces, are very similar in the two cases.

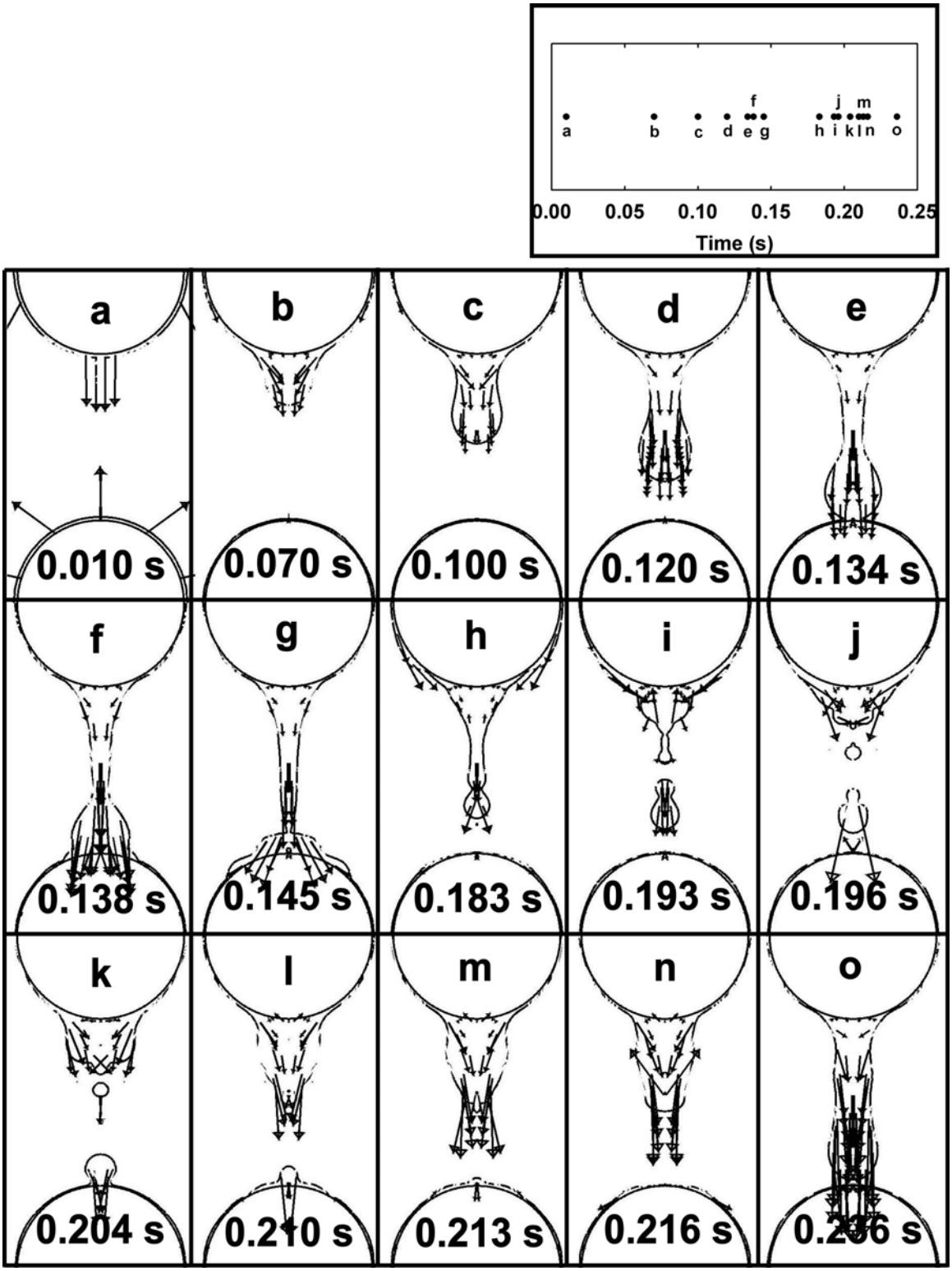

Figure 4.57: Velocity vectors for a 30°C coolant temperature

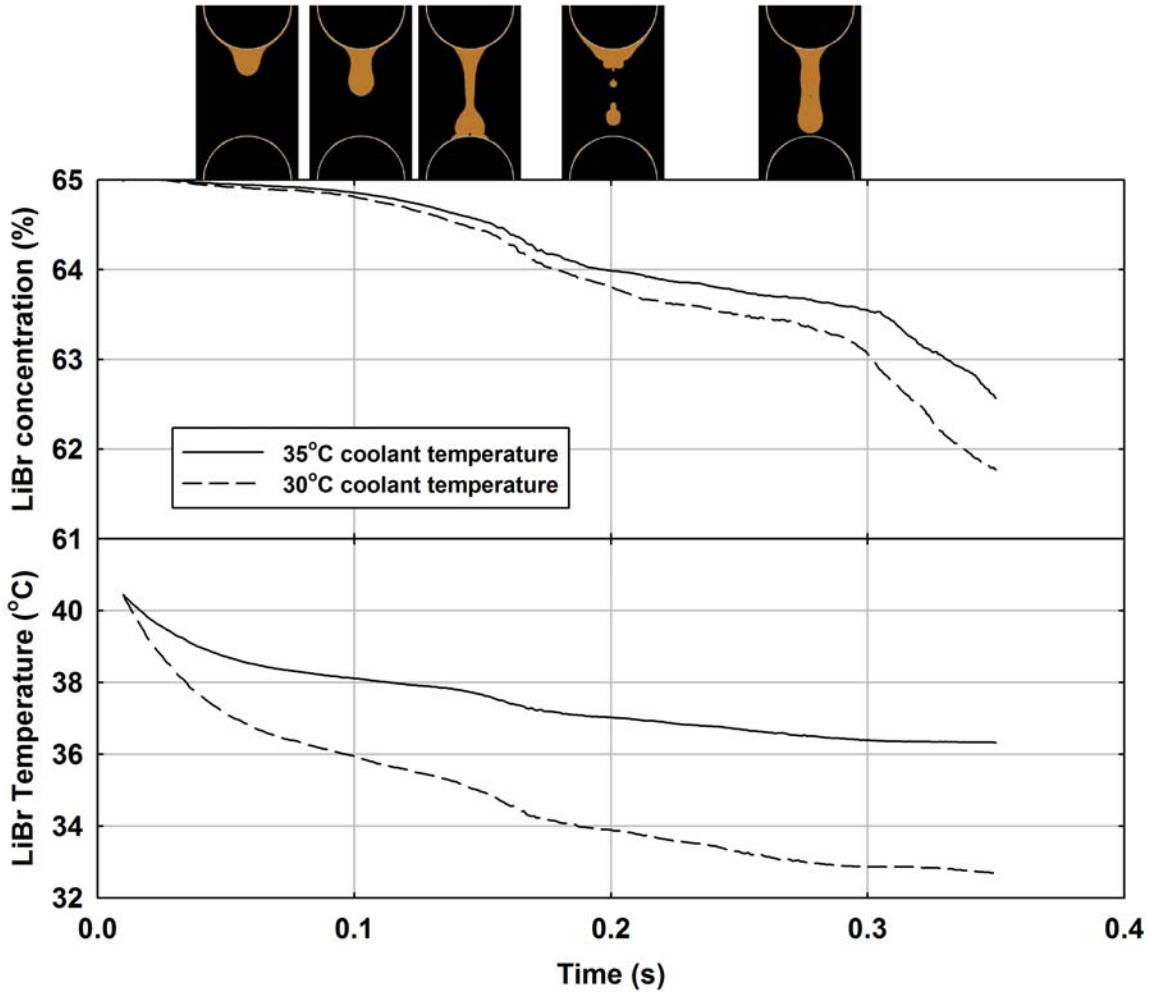

Figure 4.58: Temporal variation of bulk LiBr concentration and temperature for a 30 ℃ coolant temperature

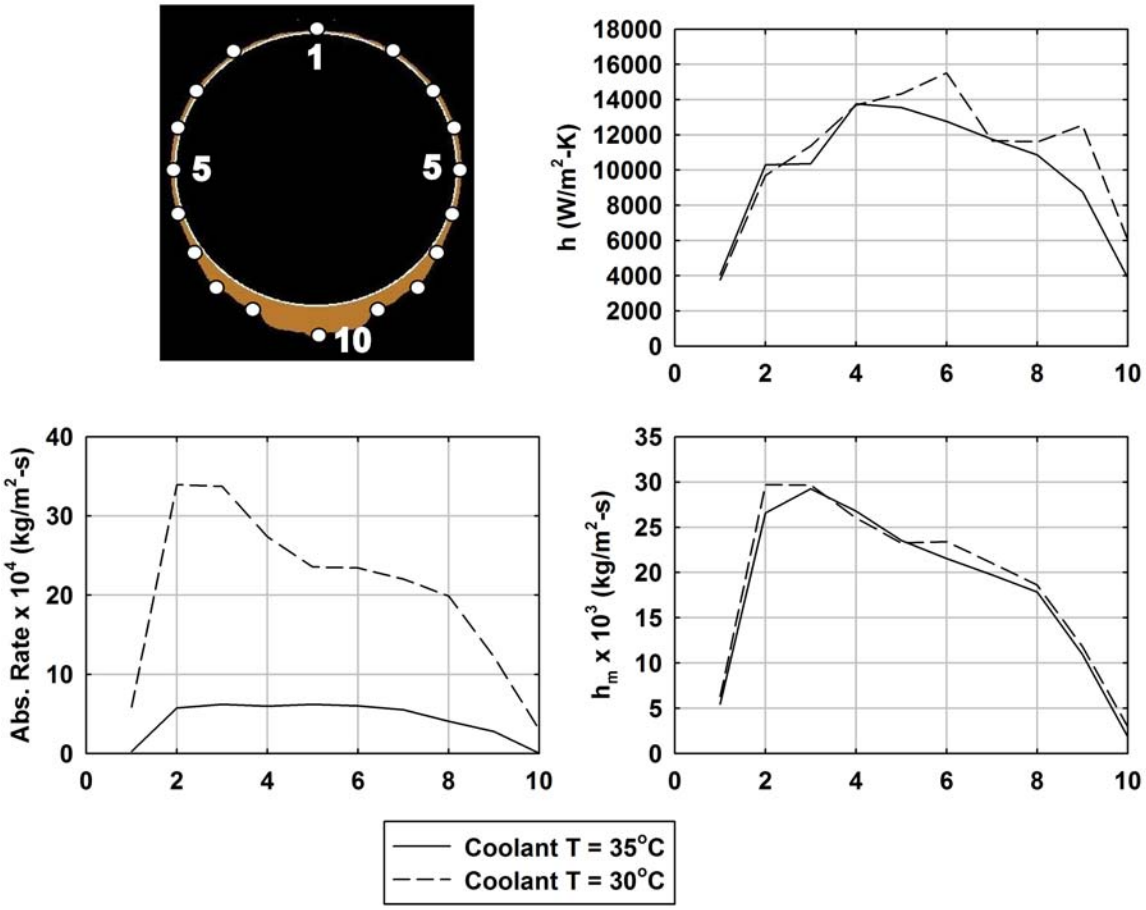

Figure 4.59: Local heat and mass transfer coefficients for a 30℃ coolant temperature

4.8.6 Heat and mass transfer coefficients

Figure 4.59 presents the local heat and mass transfer coefficients and absorption rates at various points on the sphere at 0.295 s. The state of the flow at that time is shown in the picture below the plot. For the sake of comparison, the results from the baseline case are also plotted on the same graph.

The solid line in Figure 4.59 presents the local heat and mass transfer coefficients and absorption rates in the present case, while the dashed line presents the corresponding values for the baseline case. The absorption rate in the present case is lower than that in the baseline case. This because the concentration difference between the interface concentration and the vapor pressure equilibrium concentration

is lower in the present case, due to a higher coolant temperature. At the time step discussed the bulk concentration and temperature in the present case are 63.6% and 36.4℃, respectively, while that in the baseline case are 63.2% and 32.9℃, respectively. If the interface temperature is assumed to be close to the bulk temperature, the equilibrium concentrations for the present and baseline cases are 55.1% and 53.1, respectively. This corresponds to concentration differences of 8.5% and 10.1% for the present and baseline cases. For example at point 5, the absorption rate in the present case is 6.20×10^{-4} kg/m^2-s, while that in the baseline case is 23.6×10^{-4} kg/m^2-s.

It is seen that there is not much difference in the heat and mass transfer coefficients between the present and baseline cases. This is because the heat and mass transfer coefficients depend on the flow patterns, which are very similar in the two cases. For example at point 4, the heat transfer coefficient in the present case is 13757 W/m^2-K, while that is the baseline case is 13696 W/m^2-K. Similarly, the mass transfer coefficient at point 4 in the present case is 26.8×10^{-3} kg/m^2-s, while that in the baseline case is 26.0×10^{-4} kg/m^2-s. There are some minor differences in the heat and mass transfer coefficients in the two cases. For example, at point 6 the heat transfer coefficient in the present case is 12764 W/m^2-K, while that in the baseline case is 15516 W/m^2-K. These differences in the heat and mass transfer coefficient values can be attributed to fluid property differences and numerical resolution.

4.8.7 Film concentration and temperature profiles

Figure 4.60 presents the concentration and temperature profiles in the lithium bromide solution film on the sphere at 0.295 s. At this time all of the lithium bromide solution is present in the form of a film around the sphere. The waves created due to droplet impact have propagated around the sphere and have dissipated away. For comparison the profiles for the baseline case are also plotted on the same graph and

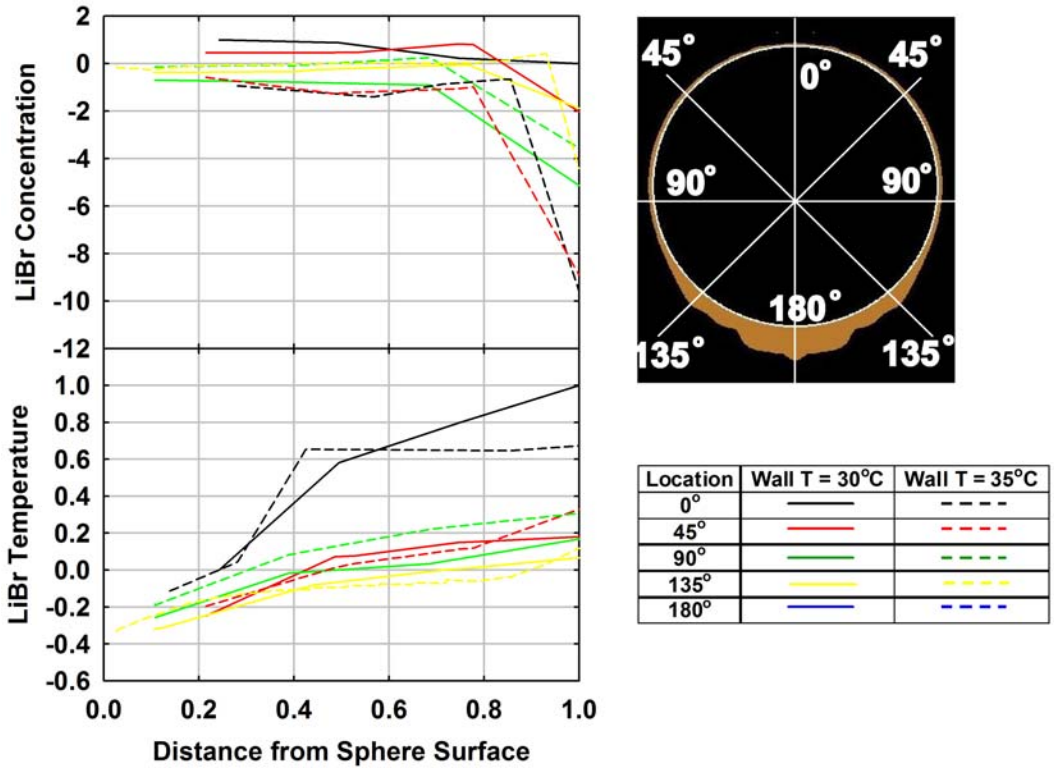

Figure 4.60: Concentration and temperature profiles for a 30 °C coolant temperature

are shown in dashed lines.

As seen in Figure 4.60, the concentration and temperature profiles are very similar for the present and the baseline cases. This is in spite of the fact that the actual value of temperature and concentration are quite different in the two cases. This is because the nature of the concentration and temperature profiles are mostly determined by the flow patterns, which are similar in the two cases. Similar to the baseline case, the concentration is highest close to the surface of the sphere and then decreases as away from the surface, towards the liquid-vapor interface. Also, the temperature is lowest close to the surface of the sphere and highest close to the liquid-vapor interface.

The minor differences in the profiles in the two cases can be attributed to differences in fluid properties and numerical resolution. As mentioned earlier, due to the low thickness of the film, there are very few grid points (< 10) within the film for the profile plots. These low number of grid points cause the minor differences observed

between the two sets of profile plots.

This concludes the discussion on the different coolant temperature case. It was seen that the different coolant temperature does not significantly affect the flow patterns or the heat and mass transfer coefficients or the nature of the concentration and temperature profiles. However the higher temperature causes a higher equilibrium concentration, which results in a lower driving concentration difference. This causes the absorption rate in the present case to be lower than the baseline case. The average Reynolds number for the case was always less than 65, which is the same as the baseline case. The average heat transfer coefficient for this case at 0.295 s was found to be 10004 W/m^2-K, while it was 11023 W/m^2-K for the baseline case. The average mass transfer coefficient for this case was found to be 18.35×10^{-3} kg/m^2-s, while is was 19.26×10^{-3} kg/m^2-s for the baseline case. The average Nusselt number (based on the sphere diameter) for this case at 0.295 s was 265.1, while that for the baseline case was 265.8. The average Sherwood number for this case was 114.5, while that for the baseline case was 106.0. The average absorption flux for the present case at 0.295 s was 4.29×10^{-4} kg/m^2-s, while that for the baseline case was 20.51×10^{-4} kg/m^2-s. In the following section the effect of grid size on the computational results will be explored.

4.9 Effect of grid size

After having studied the effect of the variation of various operating parameters, the effect of the choice of grid on the results is documented . All of the two dimensional computations were conducted on a grid with a minimum size of 0.08 mm. This grid was seen in Figure 3.4. The same computations are now conducted on a coarser grid with minimum size 0.1 mm and a finer grid with minimum size 0.064 mm. The results from these computations are seen in Figures 4.61, 4.62 and 4.63.

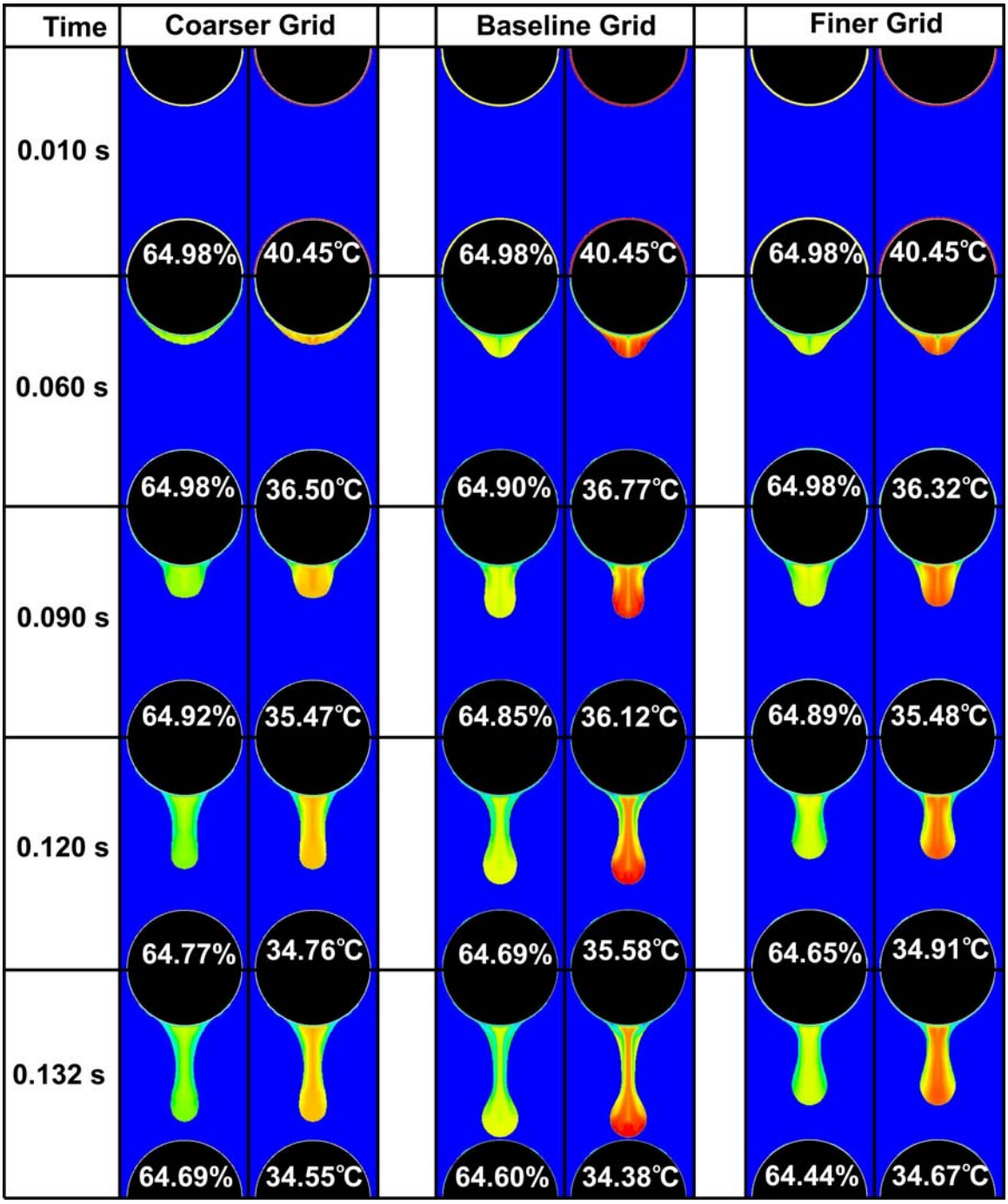

Figure 4.61: Comparison of concentration and temperature distributions with three grids

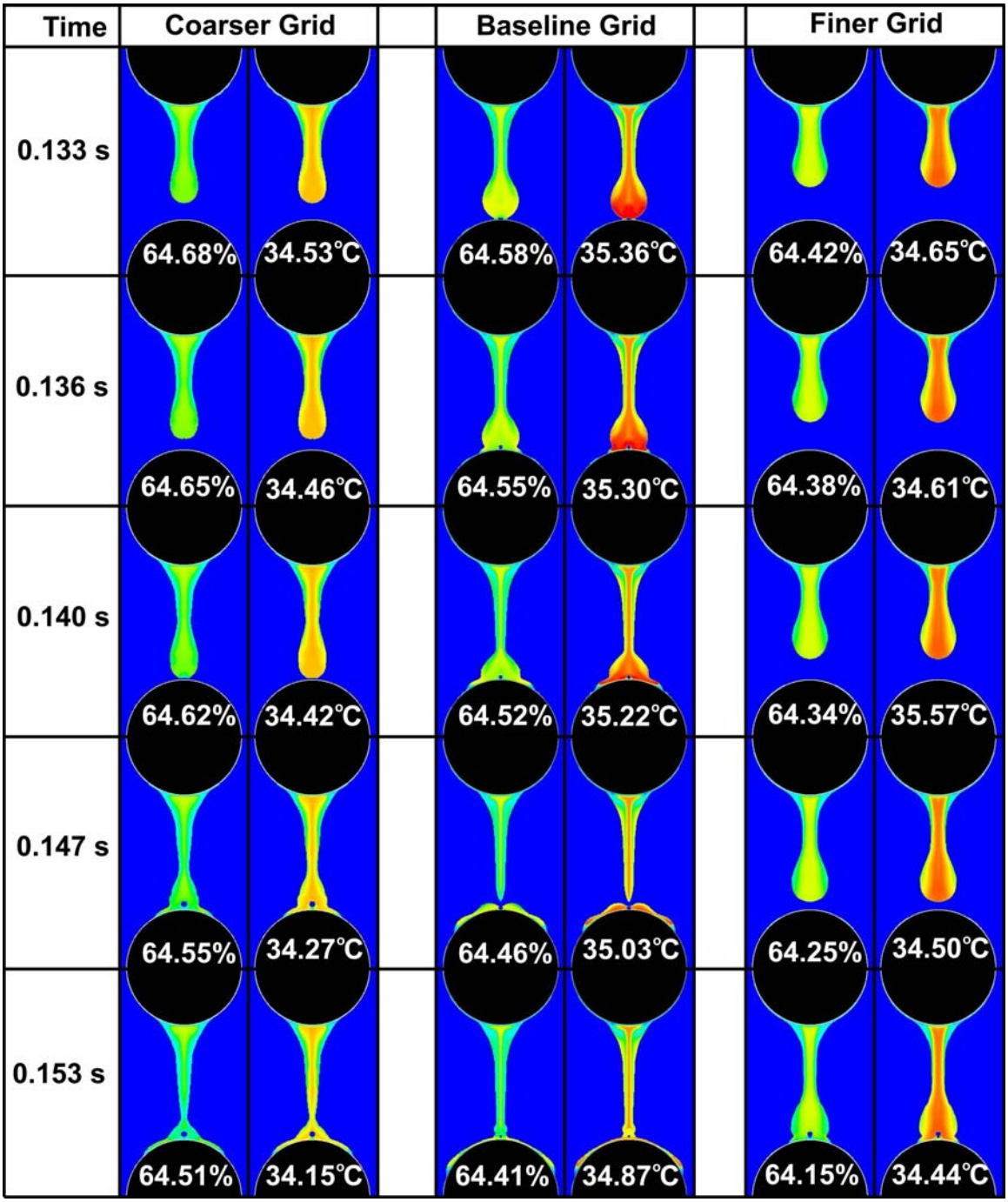

Figure 4.62: Comparison of concentration and temperature distributions with three grids (continued)

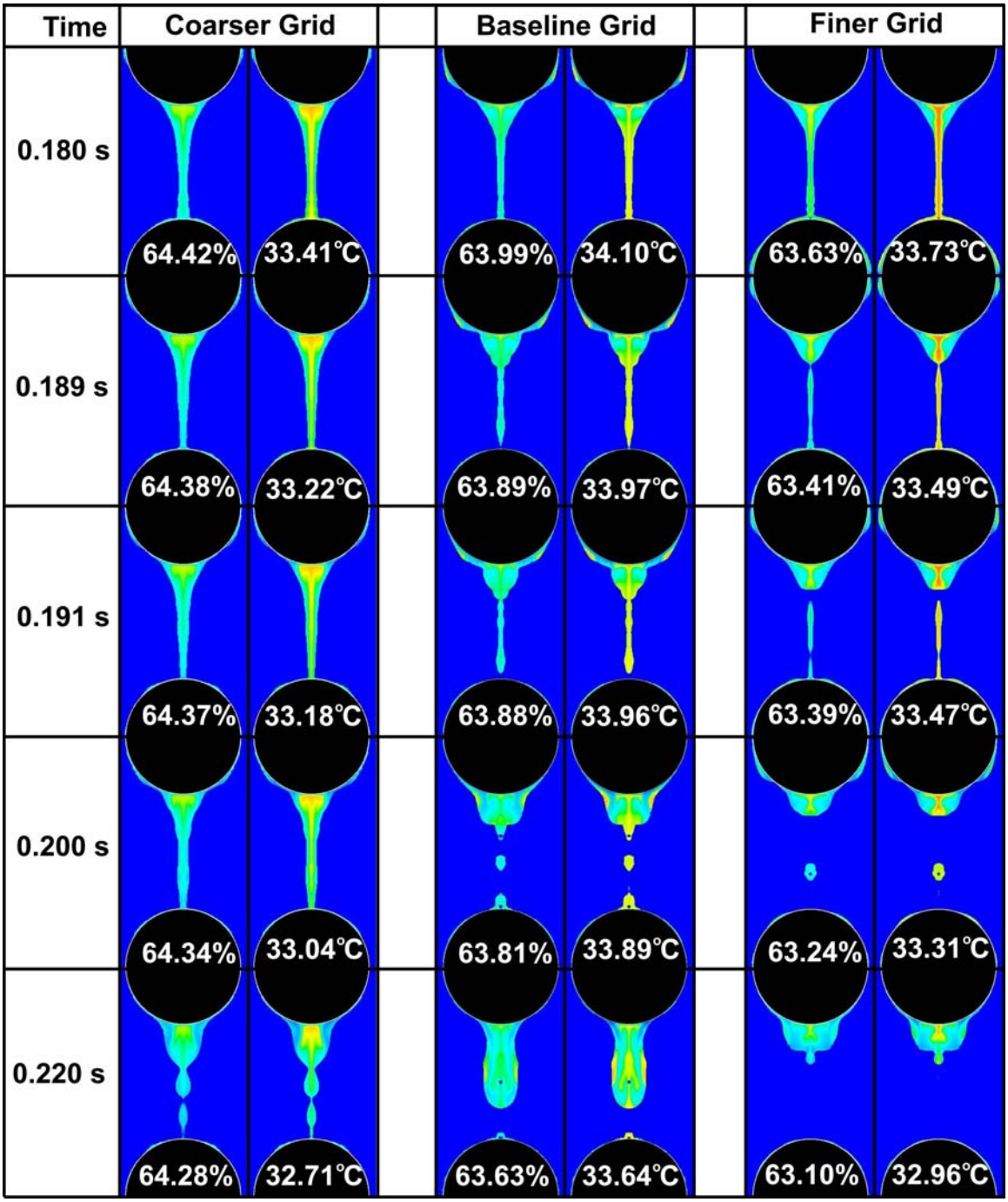

Figure 4.63: Comparison of concentration and temperature distributions with three grids (continued)

Figures 4.61, 4.62 and 4.63 show the local changes in the lithium bromide concentration and temperature for the three grids. The local concentrations and temperatures are represented by varying colors, with red denoting the highest concentration and temperature at 65% and 40.5℃, respectively, and blue denoting the lowest concentration and temperature at 60% and 30℃, respectively. Concentrations and temperatures in between these limits are denoted in a decreasing order by different shades orange, yellow and green respectively. The average concentrations and temperatures of the lithium bromide solution at each of the time steps is also printed over the tube.

As seen from the figures, there is some difference in the speed of fall of the droplet with the three grids. The droplet seems to fall fastest with the baseline grid, while it seems to fall slowest with the finer grid. For example, the first droplet hits the next tube at 0.133 s with the baseline grid, 0.140 s with the coarser grid and at 0.153 s with the finer grid. Due to the difference in the rate of fall, there is also some difference in the bulk concentration and temperature variations. For example, after 0.120 s, the average concentration with the baseline grid is 64.69%, while the concentration with the coarser and finer grids are, 64.77% and 64.65%, respectively. Similarly, at 0.120 s, the average temperature with the baseline grid is 35.58℃, while the temperatures with the coarser and finer grids are, 34.76℃ and 34.91℃, respectively. The bulk concentration and temperature variations for the three grids are shown in Figure 4.64. Through 0.30 s, the average absorption rate in the baseline, coarser and finer grids are, 2.86×10^{-5} kg/s, 1.70×10^{-5} kg/s and 3.57×10^{-5} kg/s, respectively. Also, the average heat load in the baseline, coarser and finer grids through 0.30 s are 21.2 W, 24.1 W and 23.3 W, respectively.

Though the speed of the fall of the droplet and the average concentration and temperature variations for the three grids are a little different, the internal distributions of the concentration and temperature are very similar. For all the three grids,

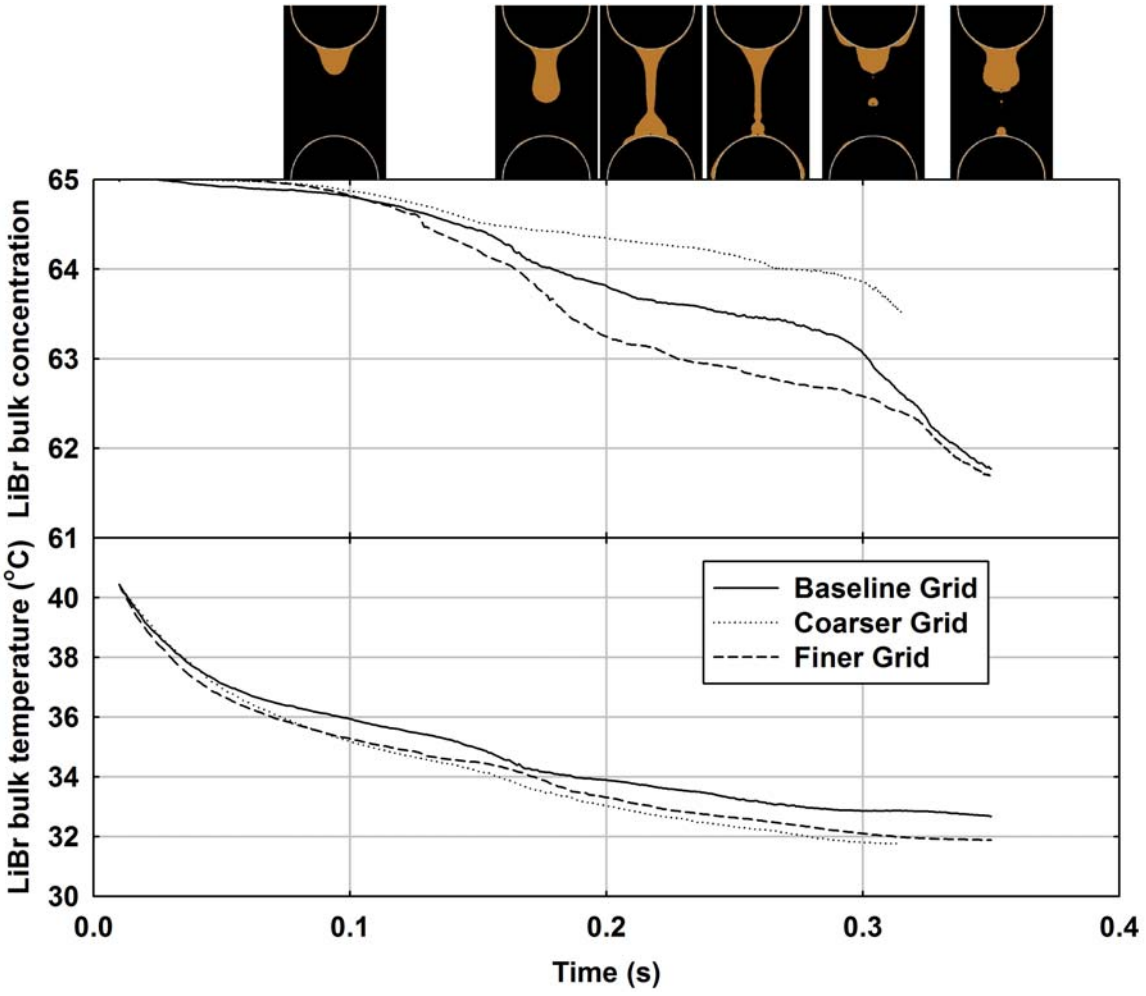

Figure 4.64: Comparison of bulk concentration and temperature variations with three grids

the concentration is the lowest at the liquid-vapor interface, since the vapor absorption happens there. Also the vapor absorption rates are higher in the interfaces close to the tube, as compared to interfaces on the droplet, which are far away from the coolant in the tube. Similarly the temperature distribution is also very similar for the three grids. The temperatures are high at the interface, where the exothermic absorption process happens, and are low at regions close to the coolant tube, which provides cooling to the solution.

The *mixing effect* due to the impact of the droplet on the tube is seen in all the three grids, albeit at slightly different times. The droplet impacts next tube in the baseline, coarser and finer grids at, 0.133 s, 0.140 s and 0.153 s, respectively. On impact, in all the three grids, the droplet mixes the lithium bromide solution in the film forming a more uniform concentration distribution in it. This exposes newer surfaces of the lithium bromide solution for absorption, and greatly improves the absorber performance.

The reason for the difference in the droplet speeds in the three grids is that the *interface tracking* algorithm deployed in the computations, uses a *grid sensitive* time step choosing scheme. The time step is chosen in accordance with Equation 4.9.

$$\delta t_{vof} < CFL \times \frac{\delta x_i}{|u_{i,j}|} \tag{4.9}$$

Such a choice of time step ensures that the droplet interface does not traverse more than one grid cell within a time step. This is an important condition that needs to be satisfied for the sake of stability of the algorithm. To ensure that this condition is never violated, the code automatically modifies the time step for the volume of fluid calculation if it is greater than the maximum allowed value. This automatic modification of the time step, makes the droplet speed computed by the algorithm dependent on the size of the grid.

It is to be noted that though the speed of fall of droplet in the three grids were different, the flow patterns and concentration and temperature distributions were

exactly the same. The results from the three grids were merely a little *off phase* from each other. In spite of the lack of absolute grid independence, since all of the parametric variation of the operating conditions were conducted on the baseline grid, the obtained results are still indicative of the primary absorption phenomena and the actual effect of the change of the absorber conditions. The present results would need to be compared to experiments to ascertain the actual speed of fall of the droplet.

4.10 Comparison of results with literature

The previous section presented a detailed description of the results from the various computations conducted. The present section compares these results with prior work conducted in the area and enunciates the novel contributions of this work to the literature.

Vliet [77] conducted an experimental study of absorption in water-lithium bromide falling films on horizontal tubes. The study was conducted for flow over two geometries, viz., 0.766 in (19.46 mm) diameter, 5 tubes/column, 80/20 cupro-nickel; and 1.660 in diameter (42.16 mm), 3 tubes/column, 90/10 cupro-nickel tubes. The solution and refrigerant were circulated to the absorber using variable flow gear pumps. LiOH (0.2% by weight) was used as an inhibitor, while the surfactant octyl alcohol was used as an additive.

Vliet [77] presented the film Nusselt number and film Reynolds number values for the various test cases. Based on the cases tested, he found that the Nusselt number varied with Reynolds number as,

$$\frac{Nu_f}{Nu_{fo}} = \left[\frac{Re_f}{Re_{fo}}\right]^{0.46} \tag{4.10}$$

He also found that the Nusselt number increased with increase in tube size as,

$$\frac{Nu_{fd}}{Nu_{fo}} = \left[\frac{d}{d_o}\right]^{-0.2} \tag{4.11}$$

where, d_o is the reference tube diameter of 0.766 in (19.46 mm). It is to be noted that the tube diameter scaling is based on data from the two tube diameters that Vliet [77] tested; and hence extrapolation to the present case may not be strictly justified. This Reynolds number and the tube diameter scaling is applied here to all of the test results from Vliet [77] to compare them with the results for the Reynolds number and tube diameter used in the present study. The Reynolds number and tube diameter for the baseline case in the present case are 110 and 15.9 mm, respectively. In order to compare results from the present study with the results from Vliet [77], the Nusselt number in the present case is converted from a diameter based value of 39.8 to a film thickness based value of 1.85. This value is compared to the scaled results by Vliet [77], and the percentage error is calculated for each test result. The results from this comparison are presented in Table 4.8. It is to be noted that the temperature difference between the interface and the coolant was used by Vliet [77] in the calculation of heat transfer coefficient and Nusselt number, while the temperature difference between the interface and the bulk solution was used in the present study. In the absence of detailed information on the coolant temperatures and the tube-side resistances used in their study, this could cause some discrepancies in the comparison of the results.

It is seen that the Nusselt number predicted by the scaled results from Vliet [77] are of the same order of magnitude as those from the present study. The difference between the two results varies between 5% and 48%. The higher Nusselt number in the study by Vliet [77] can be attributed to the use of surfactant octyl alcohol, which enhances heat and mass transfer, and to the other differences in the definition of temperature difference for the evaluation of heat transfer coefficients, and the scaling of their relationship beyond the range of its applicability.

Nakoryakov *et al.* [7] experimentally measured the heat and mass transfer coefficients during absorption over vertical falling films for various flow rates, concentration

Table 4.8: Comparison of present results with Vliet [77]

	$\mathbf{Re_f}$	$\mathbf{Nu_f}$	$\mathbf{Nu_{scaled}}$	% difference
Vliet [77]	22.5	1.00	2.16	15
	23.2	1.39	2.96	38
	45.4	1.56	2.43	24
	45.0	1.72	2.70	32
	19.7	1.15	2.65	30
	32.6	1.85	3.36	45
	29.1	1.45	2.78	34
	81.3	2.40	2.87	36
	70.5	1.61	2.06	11
	68.8	1.62	2.10	12
	66.7	1.48	1.94	5
	56.6	2.43	3.43	46
	49.2	2.36	3.55	48
	50.0	2.16	3.23	43
	55.4	2.42	3.46	47
	40.0	1.83	3.04	39
	37.6	1.33	2.28	19
	30.2	1.57	2.97	38
	22.2	1.34	2.92	37
	20.0	0.88	2.00	8
	72.8	2.01	2.52	27
	64.6	2.08	2.77	33
	58.5	1.93	2.69	31
	59.4	1.96	2.71	32
	55.8	1.78	2.53	27
Present study	110.0	1.85	–	–

and temperatures. Their results are summarized in Table 4.9. They observed heat transfer coefficients between 1600 W/m^2-K and 5300 W/m^2-K and mass transfer coefficients between 95.5×10^{-3} kg/m^2-s and 286.6×10^{-3} kg/m^2-s. In comparison, the average heat and mass transfer coefficients for the baseline three dimensional case were 1500 W/m^2-K and 4.67×10^{-3} kg/m^2-s, respectively. The local film mass flow rate in the present work (0.125 kg/m-s) is about 50% lower than the lowest flow rate used in the work by Nakoryakov *et al.* [7] (0.226 kg/m-s). The heat transfer coefficient the present work is only slightly lower than those observed by Nakoryakov *et al.* [7], and that can be attributed to the lower flow rate. However the mass transfer coefficient in the present work is an order of magnitude lower. The primary reason for this difference is that Nakoryakov *et al.* [7] do not account for the *mixing* provided by waves in the falling film. These waves mix the concentration profiles, sustain a high concentration difference for mass transfer and enhance absorption. Nakoryakov *et al.* [7] don't account for mixing, but instead attribute the high absorption rate to increased mass transfer coefficients. Thus the mass transfer coefficients calculated by Nakoryakov *et al.* [7] could be erroneously high. Besides, Nakoryakov *et al.* [7] conducted their study on steady falling films, while the flow in the present study contains droplets falling over a bank of tubes. The differences in the flow patterns also lead to differences in the heat and mass transfer coefficients.

Andberg and Vliet [42] presented results from the absorption of water vapor into a lithium bromide liquid film, flowing downward on a vertical flat plate. Their operating conditions are summarized in Table 4.10. It is seen that the pressure, temperature and concentration conditions are very similar in the two studies. However the mass flow rate used by Andberg and Vliet [42] is much higher and the study was conducted on a much larger geometry as compared to the present study. They plotted the heat and mass fluxes and the bulk concentration and temperature variation as a function of the downstream distance. At the interface, they observed vapor absorption mass

Table 4.9: Summary of results from Nakoryakov *et al.* [7]

	Flow rate $\mathbf{kg/m \cdot s}$	**P** **kPa**	$\mathbf{T_{wall}}$ **°C**	$\mathbf{T_{in}}$ **°C**	$\mathbf{Y_{in}}$ **%**	**h** $\mathbf{W/m^2K}$	$\mathbf{h_m}$ $\mathbf{kg/m^2s}$
Nakoryakov *et al.* [7]	0.226	0.95	24.0	24.2	59.04	2000	108.3×10^{-3}
	0.344	0.96	24.0	41.8	60.47	2400	119.4×10^{-3}
	0.344	0.96	24.0	24.0	60.35	2600	111.4×10^{-3}
	0.344	0.96	24.0	33.0	60.34	1900	119.4×10^{-3}
	0.272	0.97	24.1	35.6	60.20	1800	95.5×10^{-3}
	0.381	0.98	24.1	35.8	60.08	2000	133.7×10^{-3}
	0.552	0.97	24.1	35.6	60.09	3100	184.7×10^{-3}
	0.381	1.41	24.1	39.0	60.02	2000	111.4×10^{-3}
	0.381	2.03	24.1	42.2	60.08	2000	132.1×10^{-3}
	0.726	1.97	24.6	32.0	59.65	3500	219.7×10^{-3}
	0.225	0.95	27.5	40.0	59.40	4800	114.6×10^{-3}
	0.306	0.93	24.0	32.4	58.60	2400	106.7×10^{-3}
	0.318	0.93	24.0	32.0	59.52	2400	130.5×10^{-3}
	0.318	0.93	24.0	32.0	59.50	2200	95.5×10^{-3}
	0.318	0.93	24.2	24.2	59.00	2200	108.3×10^{-3}
	0.318	0.93	23.0	32.0	60.05	1600	95.5×10^{-3}
	0.318	0.92	29.0	29.0	60.06	2700	116.2×10^{-3}
	0.548	0.93	24.6	34.0	58.67	2400	132.1×10^{-3}
	0.828	0.93	24.1	34.2	58.70	2900	159.2×10^{-3}
	0.560	1.33	23.9	38.4	58.80	2700	184.7×10^{-3}
	0.827	1.33	23.9	38.5	58.75	2100	162.4×10^{-3}
	0.570	0.93	15.1	30.3	59.51	2300	167.2×10^{-3}
	1.539	0.93	15.0	29.8	59.20	4700	286.6×10^{-3}
	0.726	0.92	24.2	24.2	59.20	3300	143.3×10^{-3}
	0.318	1.97	23.8	24.0	59.25	2400	121.0×10^{-3}
	0.713	1.99	24.2	24.0	59.25	5300	237.2×10^{-3}
Baseline 3D	0.125	1.00	30.0	40.5	65.00	1500	4.67×10^{-3}

Table 4.10: Operating conditions used by Andberg and Vliet [42]

Operating parameter	**Andberg and Vliet [42]**	**Present study**
Pressure (kPa)	0.9348	1.0
Wall temperature (°C)	35	30
Inlet concentration (%)	60	65
Inlet temperature (°C)	44.44	40.5
LiBr mass flow rate (kg/s)	0.01	8.6×10^{-5}

fluxes of about 2×10^{-3} kg/m^2-s initially, which rises to about 3×10^{-3} kg/m^2-s at 0.5 mm, when the effect of the coolant reaches the interface, and then decreases with a power law dependence as the driving concentration goes down. In comparison, the average vapor absorption mass flux in the present study for the three dimensional baseline case was found to be 0.594×10^{-3} kg/m^2-s. The absorption fluxes are much lower due to the lower flow rate and because some of the solution is present in the form of a droplet. Due to the constant film flow with no mixing in the study by Andberg and Vliet [42], the mass fluxes decreased drastically beyond 0.1 mm. However, due to the mixing associated with droplet impact and waves, the mass fluxes observed in the present study were fairly uniform throughout the duration of the flow.

Brauner [26] presented an analytical model for the absorption of vapor onto a falling liquid film. She plotted Nusselt and Sherwood numbers as functions of downstream distance (with the downstream distance as the characteristic length). She observed a Sherwood number of 12.0 for an inlet concentration of 70%, and a Sherwood number of 7.8 for a 50% inlet concentration. The Nusselt number was found to be independent of the inlet concentration and was found to be 2.8 for both the inlet concentrations. In comparison, in the present study, an average Nusselt number of 39.8 and an average Sherwood number of 29.2 was observed. The higher Nusselt and Sherwood numbers in the present study can be attributed to the different geometry (horizontal tubes), and the heat and mass transfer enhancements provided by the

waves generated during droplet impact.

Patnaik and Perez-Blanco [17] studied absorption in wavy films falling over a vertical tube. They presented a numerical model that solved the heat and mass transfer equations for the flow. They used the thickness of the film as characteristic length for the calculation of the Reynolds, Nusselt and Sherwood numbers. They observed that the Nusselt number increased linearly with increase in Reynolds number for up to a Reynolds number of 300. Also, they found that the Sherwood number increased linearly with Reynolds number up to a Reynolds number of 200. For the Reynolds number in the three dimensional baseline case in the present study ($Re = 110$), Patnaik and Perez-Blanco [17] found the Nusselt number to be 0.7 and the Sherwood number to be 80. In comparison the Nusselt and Sherwood numbers in the present case were found to be 39.8 and 29.2 respectively. The difference in the results can be attributed to the different geometry (vertical tube as opposed to horizontal tube) used in the study by Patnaik and Perez-Blanco [17].

Patnaik *et al.* [18] also developed a simpler analytical model for the design of vertical tube absorbers. Using this model, they plotted the bulk concentration and temperature, and heat and mass transfer rates as functions of the flow length. The flow conditions used in the study are summarized in Table 4.11. For a solution flow rate of 0.01 kg/s and a coolant flow rate of 0.025 kg/s, they observed that the absorption rate increased linearly with flow distance. The absorption rate increased with distance because the coolant flowed in the direction counter to the solution flow direction. As the solution flowed further it came in contact with coolant at lower temperatures, thus increasing its absorption potential. The bulk concentration decreased from an inlet value to 60.0% to 59.2% over the course of the flow. In comparison, the bulk concentration decreases from 65.0% to 58.6% over a flow time of 0.36 s in the present study. The concentration change is higher in the present case because of the much lower lithium bromide solution mass flow rate.

Table 4.11: Operating conditions used by Patnaik *et al.* [18]

Operating parameter	**Patnaik *et al.* [18]**	**Present study**
Pressure (kPa)	1.2	1.0
Coolant temperature (°C)	29.44 (inlet)	30
Inlet concentration (%)	60	65
Inlet temperature (°C)	saturated	40.5
Tube outer diameter (mm)	19.05	15.9
LiBr flow rate (kg/s)	0.01	8.6×10^{-5}

Conlisk and Mao [49] presented an analytical solution for the absorption in a film of lithium bromide solution falling over a horizontal tube. The operating conditions used in their study are summarized in Table 4.12. They found that the heat transfer coefficient was maximum at the top of the tube and decreased gradually towards the bottom. This was in agreement with results found in the present study, where in the absence of any waves, the heat transfer coefficients were an inverse function of the film thickness, which was lowest on top and highest at the bottom of the tube. The average heat transfer coefficient on the tube at time $t = 0$ was 7000 W/m^2-K. In comparison, in the present case, the average heat transfer coefficient for the three dimensional baseline case was 1500 W/m^2-K. The heat transfer coefficient is lower in the present study because it is averaged over the entire flow domain, i.e. the film and the droplet regions, while Conlisk and Mao [49] only consider a film-wise flow in their work. The heat transfer coefficient averaged only over the film region for the baseline case at 0.264 s was 3123 W/m^2-K. Over the course of their solution, the bulk lithium bromide solution concentration decreased from 62.61% to 61.90%, while the temperature increased slightly from 46.9 °C to 47.3 °C. In comparison, in the three dimensional baseline case in the present study, over a flow time of 0.36 s, the bulk concentration decreased from 65.0% to 58.6%, while the bulk temperature decreased from 40.5 °C to 33.4 °C. The bulk concentration and temperature change is higher in the present case due to the lower lithium bromide solution flow rate.

Table 4.12: Operating conditions used by Conlisk and Mao [49]

Operating parameter	**Conlisk and Mao [49]**	**Present study**
Pressure (kPa)	1.31	1.0
Reynolds number	40	110
Inlet concentration (%)	62.61	65.00
Inlet temperature (℃)	46.9	40.5
LiBr mass flow rate (kg/s)	0.12	8.6×10^{-5}

Min and Choi [50] numerically modeled vapor absorption by a lithium bromide solution film falling over a horizontal tube. They conducted their modeling on a two dimensional grid for a flow with a Reynolds number of 16.7. The used the film thickness as the characteristic length for the Reynolds number calculation, and the tube radius as the characteristic length for the calculation of the Nusselt and Sherwood numbers. They found that the Nusselt and Sherwood numbers were fairly uniform over various angular positions on the tube. They observed an average Nusselt number of 50 and an average Sherwood number of 100. In comparison, the Nusselt and Sherwood numbers in the three dimensional baseline case in the present study were 39.8 and 29.2, respectively. It is seen that while the Nusselt numbers agree within 20%, the Sherwood numbers in the present study are significantly different than the ones observed by Min and Choi [50]. The differences between the results can attributed to the different Reynolds numbers of the two flows (110 for present study) and the difference in the geometries. Drop-wise flow with a low heat and mass transfer coefficient, which is an integral part of the flow in the present study, reduces the average Nusselt and Sherwood numbers. Also the droplet impact and waves play a crucial role in the heat and mass transfer. Due to the mass transport properties of the lithium bromide solution being worse than the thermal transport properties, the mixing due to the droplet impact and waves affects mass transfer more than heat transfer. That would explain the larger discrepancy in the Sherwood number as

Table 4.13: Operating conditions used by Kirby and Perez-Blanco [51]

Operating parameter	**Kirby and Perez-Blanco [51]**	**Present study**
Pressure (kPa)	0.87	1.0
Reynolds number	25	110
Inlet concentration (%)	62.00	65.00
Inlet temperature (℃)	48.0	40.5
Coolant temperature (℃)	28.0	30.0
LiBr mass flow rate (kg/s)	0.01	8.6×10^{-5}

compared to the Nusselt number in the two studies.

Kirby and Perez-Blanco [51] conducted a segmental analysis on a horizontal tube water/lithium bromide absorber. The operating conditions used by them are summarized in Table 4.13. For a solution mass flow rate of 0.01 kg/s, they observed a concentration change from 62.0% to 60.4%. They also observed a solution temperature change from 48.0℃ to 37.0℃. This change occurred during the fall of the solution over six tubes. In comparison, in the present case, for a solution flow rate of 8.6×10^{-5} kg/s, the solution concentration changes from 65.0% to 58.6%, and the temperature changes from 40.5℃ to 33.4℃. The concentration and temperature changes are higher in the present case due to the low flow rates.

Jeong and Garimella [54] studied the absorption of water vapor into a lithium bromide solution over horizontal tubes, with particular emphasis on the flow mechanisms. The operating conditions used in their study are summarized in Table 4.14. They observed mass transfer coefficients of 11.46×10^{-3} kg/m^2-s on the film and 12.74×10^{-3} kg/m^2-s on the droplet during formation. In comparison, in the present case the mass transfer coefficient on the film at 0.264 s, was found to be 10.30×10^{-3} kg/m^2-s, while that on the droplet was found to be 5.94×10^{-3} kg/m^2-s. Jeong and Garimella [54] observed a higher mass transfer coefficient on the droplet, while the mass transfer coefficient was found to be higher on the film in the present case. The lithium bromide solution mass flux is lower in the present case, and this

Table 4.14: Operating conditions used by Jeong and Garimella [54]

Operating parameter	**Jeong and Garimella [54]**	**Present study**
Tube diameter	15.9 mm	15.9 mm
Tube pitch	5.12 mm	15.9 mm
Inlet concentration (%)	62.00	65.00
Coolant temperature (°C)	32.0	30.0
LiBr mass flux (kg/m-s)	0.024	0.0086

could account for the lower overall mass transfer coefficients.

Jeong and Garimella [55] also studied the effect of change in tube size and arrangement on absorber performance. One of the geometries used by them is compared to the smaller tube used in the present work. The operating conditions are compared in Table 4.15. The tube diameter and pitch are the same in the two studies. However, the mass flux used by Jeong and Garimella [55] is much higher. They observed absorption mass fluxes between 3×10^{-3} kg/m^2-s and 1.8×10^{-3} kg/m^2-s over five tube passes with eight rows of tubes in each pass. In comparison, an average absorption mass flux in the present study was found to be 0.4×10^{-3} kg/m^2-s. The absorption mass flux in lower in the present case due to the lower solution flow rate. In the course of flow over all the rows and passes of tube, Jeong and Garimella [55] found the temperature of the lithium bromide solution to decrease from 48 °C to 36 °C. In comparison, in the present case, over the course of passage over three tubes, the bulk temperature of the lithium bromide solution changes from 40.5 °C to 35.1 °C. The difference in the temperatures can be attributed to the difference in the coolant temperatures, the flow rate and the number of tubes considered in the study.

This concludes the section on the comparison of results from the present study with those from the literature. The following section presents the comparison of the present results with a simple penetration theory based model.

Table 4.15: Operating conditions used by Jeong and Garimella [55]

Operating parameter	**Jeong and Garimella [55]**	**Present study (smaller tube)**
Tube diameter	6.35 mm	6.35 mm
Tube pitch	5.12 mm	5.12 mm
Inlet concentration (%)	62.00	65.00
Coolant temperature (°C)	32.0	30.0
LiBr mass flux (kg/m-s)	0.02	0.011

4.11 Comparison with a penetration theory model

The bulk characteristics of the absorption process can be captured with a one dimensional penetration theory based model to obtain an order of magnitude estimate. In this model, it is assumed that all of the absorption happens on the film and that the droplet does not contribute to the absorption process. This is a reasonable assumption since it was calculated that for the baseline case, the droplet accounted for about 4.4% of the total absorption. Also, the convective terms in the species equation are ignored, and the mass transfer is assumed to be purely diffusive. With these assumptions, the species equation simplifies to,

$$\frac{\partial Y_i}{\partial t} = D_{AB} \frac{\partial^2 Y_i}{\partial x^2} \tag{4.12}$$

Applying the penetration theory to this equation, the average absorption mass flux over a residence time θ can be calculated by,

$$J_{i,avg} = \frac{1}{\theta} \int_0^{\theta} -D_{AB} \left[\frac{\partial Y_i}{\partial x} \right]_{interface} dt \tag{4.13}$$

The residence time θ was calculated based on the relative volumes of the film and droplet, as this would the approximate residence time of a fluid particle on the film. Over a flow time of 0.30 s, the residence time was approximated to be equal to 0.15 s.

The spatial derivative in Equation 4.13 was approximated as a difference between the bulk and equilibrium concentrations, divided by 10% of the film thickness. Based

on an inspection of the concentration profiles obtained in this study, the absorbed water vapor was assumed to penetrate to only 10% of the film thickness.

$$\left[\frac{\partial Y_i}{\partial x}\right]_{interface} = \frac{Y_{i,bulk} - Y_{i,eq}}{0.1\delta_{film}} \tag{4.14}$$

The calculated value the absorption mass flux was multiplied by the surface area and time step size, to obtain the mass of water vapor absorbed. Having calculated the mass of water vapor absorbed, a simple mass balance was carried out to find the change in concentration of the lithium bromide solution. Also, an energy balance accounting for the heat of absorption and the heat transferred from the coolant, was carried out to find the change in the lithium bromide temperature. With a time step size of 0.003 s, this procedure was repeated to track the bulk concentration and temperature variations up to a flow time of 0.30 s. The results from this analysis are presented in Figure 4.65.

It is seen from Figure 4.65 that while the bulk temperature profiles are in good agreement in the two analyses, the concentration variation is underpredicted by the penetration theory. This can be attributed to neglecting the convective terms in the species equation, and the lack of any mixing in the penetration model. As the thermal diffusive properties of the lithium bromide solution are much better than the mass diffusive properties, the above mentioned effects have a bigger impact on mass transfer. Also, the absorption rate was found to be almost constant with the penetration model, while in the three dimensional baseline study, the absorption rate gradually increased after a very low initial value. This increase can be attributed to the increase in the fluid velocity from the initial stationary value in the baseline case. As velocity does not feature in the penetration model, the variation in absorption rate due to velocity increase is not seen. As was discussed earlier, the mixing effect and film waviness are extremely beneficial to absorption, and their absence in the penetration model is probably the chief reason for the underprediction of absorption in the penetration model.

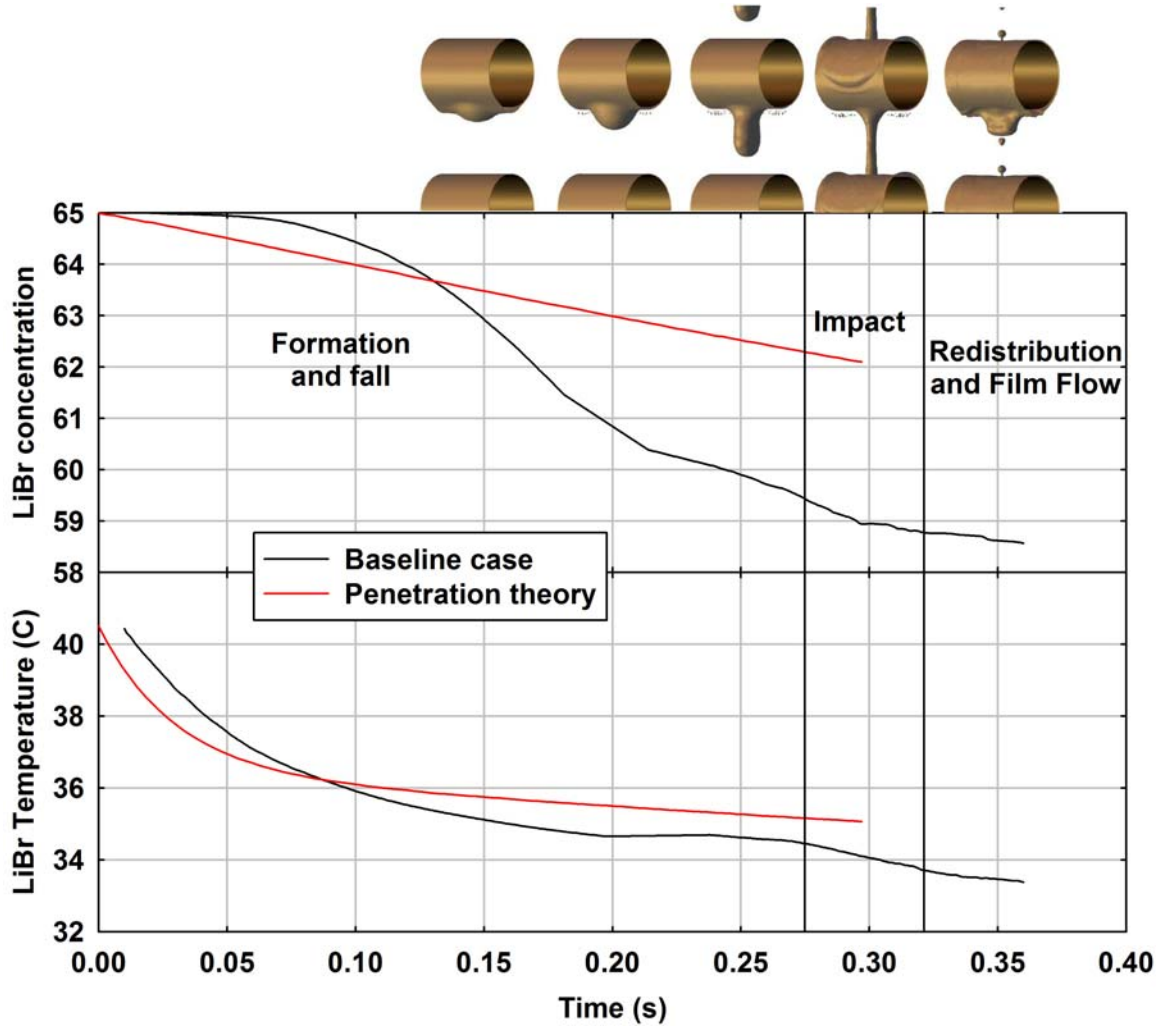

Figure 4.65: Comparison of bulk concentration and temperature variations with results from a penetration theory model

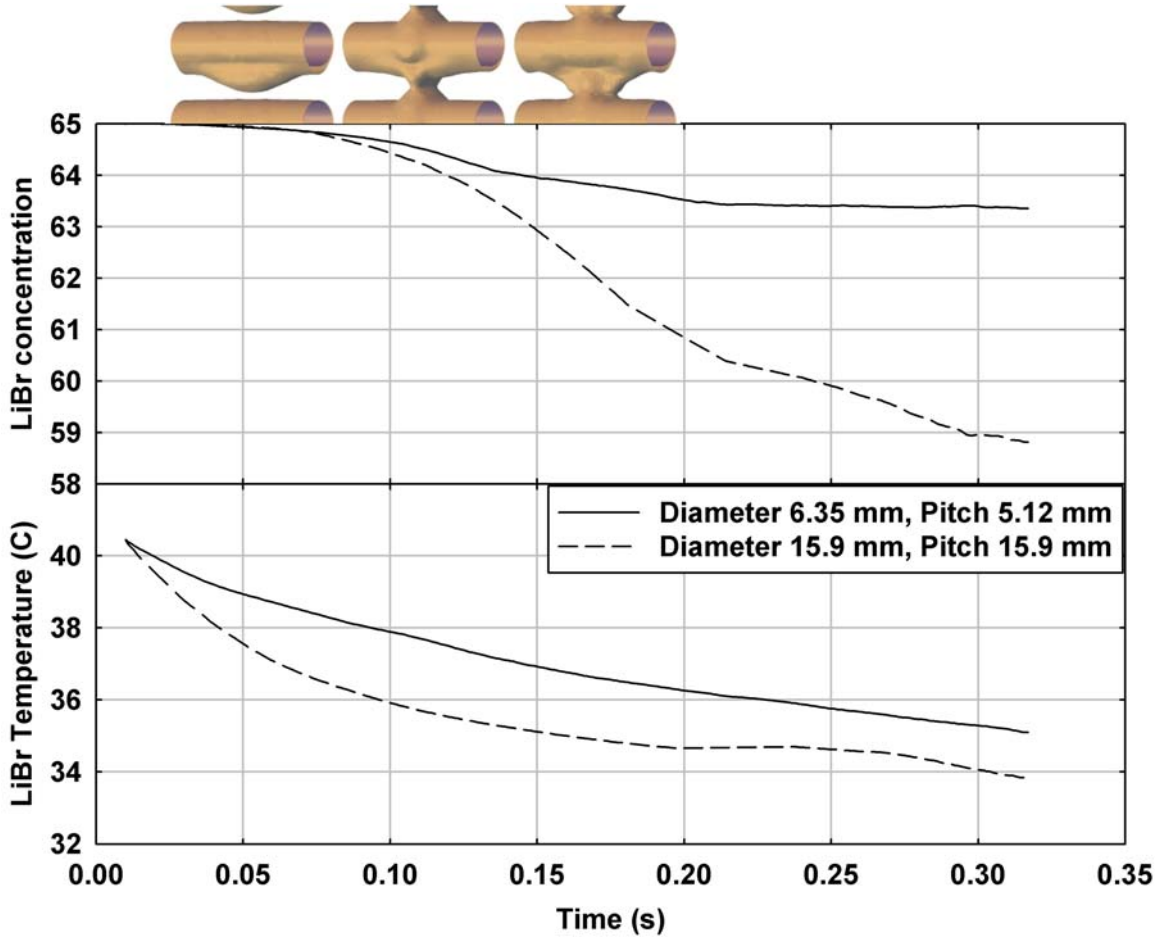

Figure 4.66: Summary of bulk concentration and temperature variations for the 3D cases

This concludes the section on the comparison of results from the present study with those from a penetration theory model. The following section summarizes all the results from the study and highlights its salient features.

4.12 Summary of results

Having discussed in detail, the results from the various computations, in this section the salient points from the results are summarized to provide guidance for absorber design. Figures 4.66, 4.67 and 4.68 summarize the bulk concentration and temperature changes in all the cases.

The first case studied was the baseline three dimensional case, with an inlet lithium bromide solution concentration of 65% and temperature of 40.5℃. It was seen that the vapor absorption rates were highest when the solution was present in the form of a thin film. Due to poor mass transport properties, the *mixing effect* of the droplet impact was required to mix the concentration profiles and expose newer regions of the lithium bromide solution to the vapor. The impact of the droplet generated waves, which propagated axially along the tube. These waves *mixed* the concentration profiles and increased heat and mass transfer coefficients, by increasing the local fluid velocities. The average Reynolds number for the case was always less than 110. The average heat transfer coefficient for this case was found to be 1500 W/m^2-K, while the average mass transfer coefficient was found to be 4.67×10^{-3} kg/m^2-s. The average Nusselt number for the flow was 39.8, while the average Sherwood number was 29.2. The average absorption flux on the film was 6.65×10^{-4} kg/m^2-s, while that on the droplet was 1.78×10^{-4} kg/m^2-s. The droplet accounted for 4.4% of the total absorption in the lithium bromide solution.

The tube geometry was changed for the next case. The tube diameter and spacing were changed to 6.35 mm and 5.12 mm, respectively, from their baseline values of 15.9 mm, each. Due to the smaller tube spacing, there was no explicit droplet formation, breakup and fall in this case. The flow occurred through a steady *liquid bridge* connecting the two tubes. Due to the lack of droplet impact, the mixing effect was absent in this case. This severely affected the absorption process beyond the initial stages. The lithium bromide solution film formed a low-concentration barrier at the interface that prevented any further vapor absorption, and failed to diffuse to the inner regions of the film due to its poor mass transport properties. This is seen in Figure 4.66, where the solid line corresponding to this case shows that the absorption initially starts off well, but drops off drastically once the steady liquid bridge has been formed. In contrast, the larger diameter case concentration continues to

decrease steeply beyond this time, signifying continued large absorption rates. The average Reynolds number for this case was always less than 470. The average heat transfer coefficient for this case was found to be 7024 W/m^2-K, while the average mass transfer coefficient was found to be 4.85×10^{-3} kg/m^2-s. The average Nusselt number for the flow was 74.3, while the average Sherwood number was 12.1. Even though the heat and mass transfer coefficients are higher for this case, the overall absorption rates are lower because of lower driving concentration differences due to the absence of mixing.

The remainder on the parametric analysis was carried out on a two dimensional grid. The two dimensional grid being smaller requires much less computational time than the three dimensional grid. Though the nature of the results were the same in both the two and three dimensional grids, there were some differences in the results. The three dimensional computations provided much deeper insights into the contributions of the axial propagation of the waves created due to droplet impact, and their effect on heat and mass transfer. However the two dimensional grid still captured most of the key elements of the flow such as, droplet formation, growth, fall and impact and its effect on the film (expect axial waves). It effectively tracked the impact of the various aspects of the flow on the heat and mass transfer processes. The average Reynolds number for two dimensional the case was always less than 65. The average heat transfer coefficient for this case was found to be 7452 W/m^2-K, while the average mass transfer coefficient was found to be 13.78×10^{-3} kg/m^2-s. The average Nusselt number for the flow was 197.5, while the average Sherwood number was 86.0. The average absorption mass flux on the film was 18.72×10^{-4} kg/m^2-s, while that on the droplet was 1.15×10^{-4} kg/m^2-s. The average absorption heat flux on the film was 4650 W/m^2, while that on the droplet was 286 W/m^2.

Figure 4.67 provides a comparison of the bulk concentration and temperature

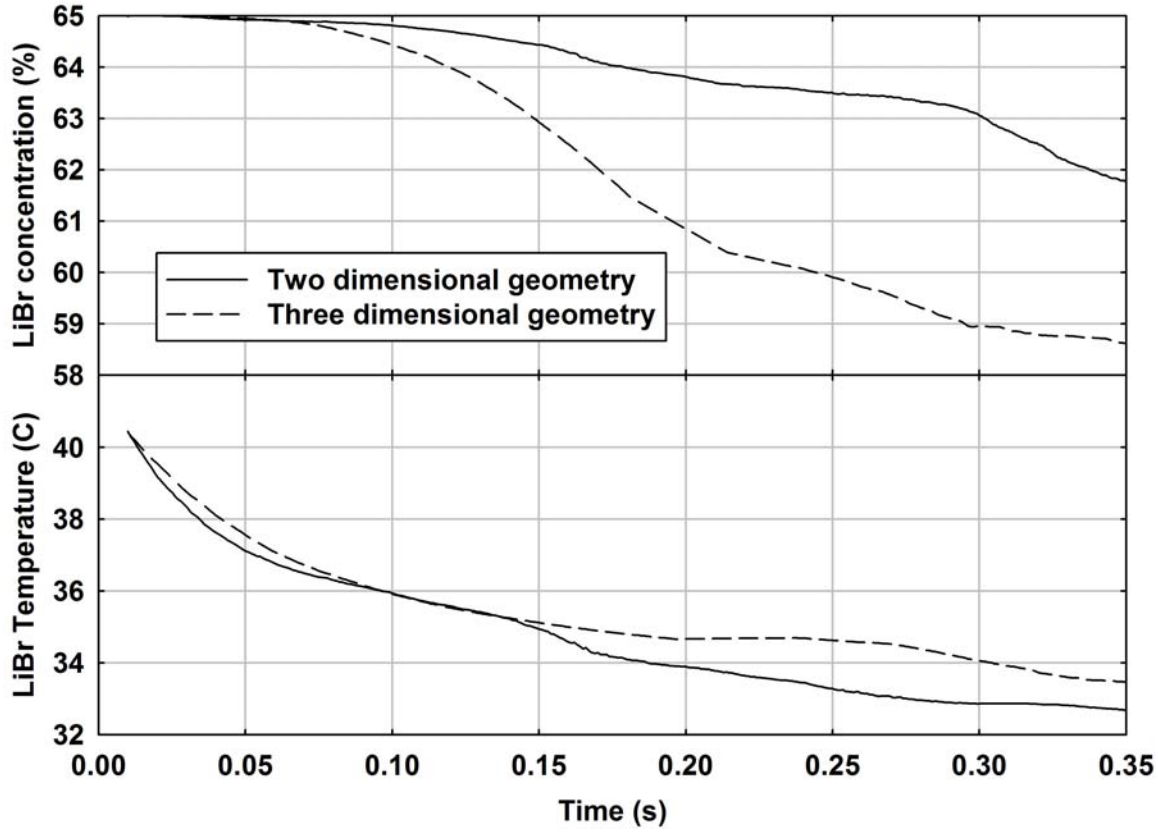

Figure 4.67: Comparison of the bulk concentration and temperature variations for the 2D and 3D cases

variations with the two dimensional and three dimensional grids. The three dimensional geometry provides a much higher surface area, especially in the film region where the heat and mass transfer coefficients are higher. Also due to the mixing provided by the waves, the three dimensional geometry constantly exposes newer liquid surfaces for absorption, maintaining a higher concentration and temperature difference. Consequently, in spite of the higher heat and mass transfer coefficients in the two dimensional geometry, the amount of absorption is much higher in the three dimensional geometry. The average absorption mass flux in the three dimensional geometry is lower, 5.94×10^{-4} kg/m^2-s, while that in the two dimensional geometry is 14.85×10^{-4} kg/m^2-s, but the larger surface area in the three dimensional case yields higher absorption rates. The temperature change is lower in the three dimensional case due to the increased amount of absorption in this case.

As a first in a series of parametric variations, the lithium bromide inlet concentration was reduced to 60%, from its baseline value of 65%. The bulk variations from this case are indicated by the red line in Figure 4.68. Due to a lower difference between the lithium bromide solution concentration and the equilibrium concentration, the absorption rates are lower in this case. However, as seen from the plot, the absorption rate remains fairly steady and does not drop off like it did in the three dimensional different geometry case. The average Reynolds number for the case was always less than 65. The average heat transfer coefficient for this case at 0.285 s was found to be 10030 W/m^2-K, while the average mass transfer coefficient was found to be 16.99×10^{-3} kg/m^2-s. The average Nusselt number for the flow at 0.285 s was 265.8, while the average Sherwood number was 106.0.

Next, the tube inlet temperature was increased to 45.0 ℃, from a baseline value of 40.5 ℃. The bulk concentration and temperature variation for this case are presented in Figure 4.68 with a green line. The higher temperature increases the equilibrium concentration and thus reduces the driving concentration difference. As a result,

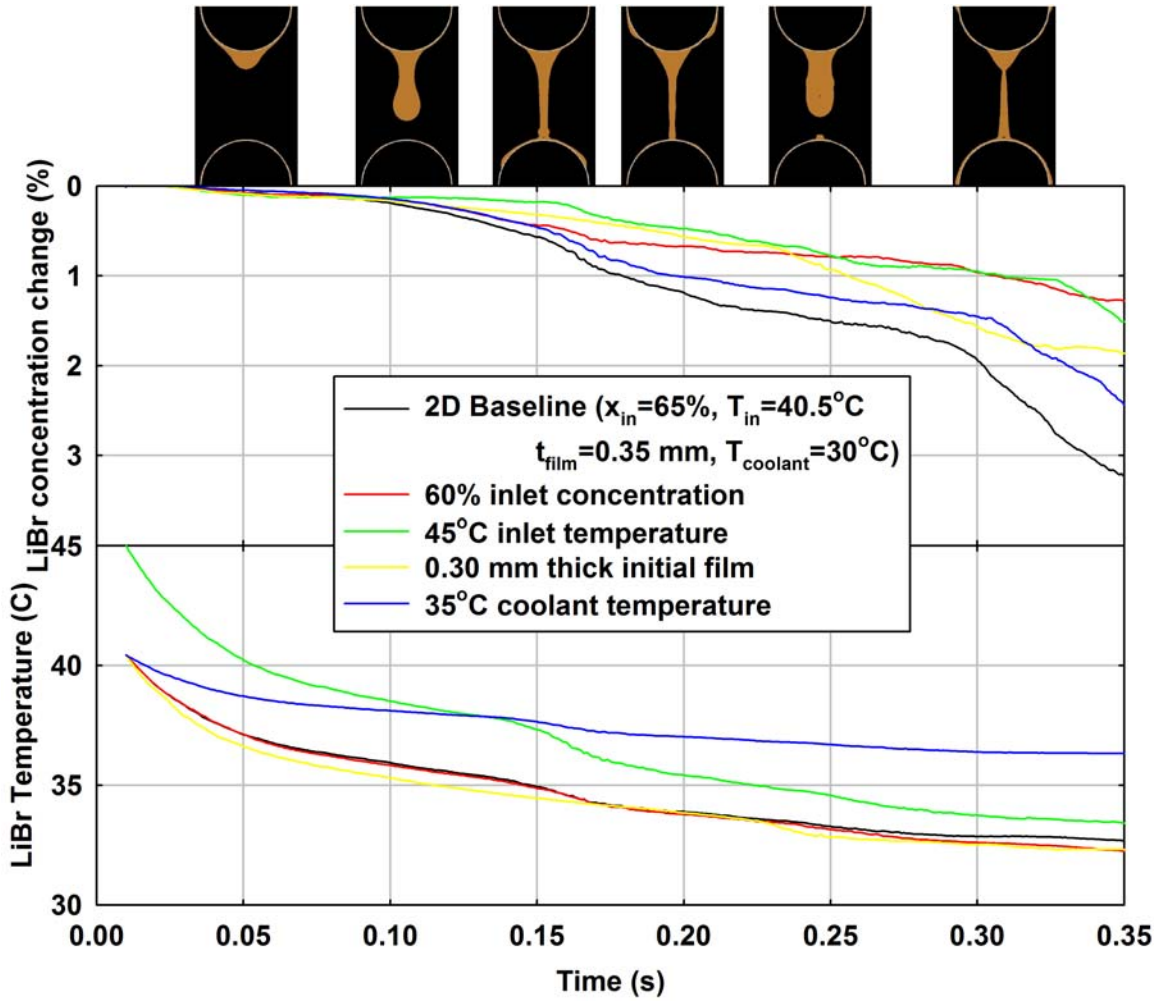

Figure 4.68: Summary of bulk concentration and temperature variations for the 2D cases

the absorption rates are lower than the baseline case. As with the different inlet concentration case, the absorption rates for this case are fairly steady. The amount of absorption in this case is very close to that in the different concentration case. The average Reynolds number for the case was always less than 65. The average heat transfer coefficient for this case at 0.191 s was found to be 6023 W/m^2-K, while the average mass transfer coefficient was found to be 14.83×10^{-3} kg/m^2-s. The average Nusselt number for the flow at 0.191 s was 159.6, while the average Sherwood number was 92.6.

After varying the inlet lithium bromide temperature, the solution flow rate was varied. This was achieved by reducing the initial lithium bromide solution film thickness at the start of the computation to 0.30 mm, from its baseline value of 0.35 mm. The results from this computation are denoted by the yellow line in Figure 4.68. The lower flow rate results in lower heat and mass transfer coefficients and causes a decrease in the amount of vapor absorbed. However, the decrease in absorption seems to be lower than the decrease in the previous three cases. The absorption mass flux decreased from 20.51×10^{-4} kg/m^2-s in the baseline case to 1.97×10^{-4} kg/m^2-s in this case. The absorption heat flux decreased from from 5095 W/m^2 in the baseline case to 489 W/m^2. The actual quantity of change in absorption is also a function of the degree of change in the operating conditions. In this case the flow rate was changed by a value small enough that the flow patterns were not significantly altered, and so the performance penalty was low. If the flow rates were altered to an extent that the flow patterns were indeed altered (like in the 3D different geometry case), the results are likely to be more drastic. The average Reynolds number for the case was always less than 49. The average heat transfer coefficient for this case at 0.258 s was found to be 3880 W/m^2-K, while the average mass transfer coefficient was found to be 1.92×10^{-3} kg/m^2-s. The average Nusselt number (based on the sphere diameter) for the flow at 0.258 s was 102.8, while the average Sherwood number was 12.0.

Lastly, the coolant temperature was increased to 35℃, from its baseline value of 30℃. The bulk concentration and temperature variations for this case are shown in blue in Figure 4.68. The higher coolant temperature increases the lithium bromide solution temperature, which in turn increases the equilibrium concentration. This decreases the driving concentration difference and thus decreases absorption. However as seen from Figure 4.68, the change in coolant temperature causes the least decrease in the amount of absorption among all the cases. The heat transfer coefficients in the thin film are quite high and the 5℃ increase in coolant temperature, still leaves enough temperature difference between the coolant and solution for effective cooling of the lithium bromide solution. The vapor pressure equilibrium concentration at 30℃ is 51.2%, while that at 35℃ is 54.3%. Thus, the coolant temperature decreases the maximum driving concentration difference from 13.8% to 10.7%. Since this is a relatively small drop in the concentration difference, the decrease in absorption due to this change is relatively low. However if the coolant temperature were raised to close to the solution temperature, absorption is likely to be severely affected. The average Reynolds number for the case was always less than 65. The average heat transfer coefficient for this case at 0.295 s was found to be 10004 W/m^2-K, while the average mass transfer coefficient was found to be 18.35×10^{-3} kg/m^2-s. The average Nusselt number (based on the sphere diameter) for the flow at 0.295 s was 265.1, while the average Sherwood number was 114.5. The average absorption mass flux on the film was 3.07×10^{-4} kg/m^2-s, while that on the droplet was 0.34×10^{-4} kg/m^2-s. The average absorption heat flux on the film was 762 W/m^2, while that on the droplet was 84 W/m^2.

Table 4.16 summarizes the heat and mass transfer results from all the computations conducted on the two dimensional geometry. It is seen that the flow patterns have the biggest impact on the absorption process. The drop-wise mode of flow

Table 4.16: Summary of the parametric analyses

Case	**h**	$\mathbf{h_m}$ $\times\mathbf{10^3}$	$\mathbf{\dot{m}_{abs}}$ $\times\mathbf{10^4}$	$\mathbf{q_{abs}}$ $\times\mathbf{10^4}$	**Nu**	**Sh**	$\mathbf{\Delta x}$[a]	$\mathbf{\Delta T}$[a]
Baseline 2D	11023	19.26	20.51	5095	292.1	120.2	1.94	7.64
$x_{in} = 60\%$	10030	16.99	1.39	345	265.8	106.0	0.96	7.88
$T_{in} = 45\,℃$	6023	14.83	11.83	2939	159.6	92.6	0.95	11.25
$t_{film} = 0.30\ mm$	3880	1.92	1.97	489	102.8	12.0	1.57	7.98
$T_{coolant} = 35\,℃$	10004	18.35	4.29	1066	265.1	114.5	1.45	4.11

[a] Bulk concentration and temperature changes after 0.30 s

ensures the mixing of the concentration profiles and sustains absorption. In the absence of mixing the absorption decreases drastically after the initial stages. The heat transfer coefficients in the film are generally quite high and so minor a change in the coolant temperature does not have a very big effect. The change in flow rate affects the heat and mass transfer coefficients but for small changes its effect is also relatively small. The changes in inlet concentration and temperature directly affect the driving concentration difference and hence affect absorption. However even in those cases, for moderate changes, the absorption rate remains fairly steady, albeit a little different from the baseline case.

This concludes the present chapter on the computational results. The next chapter presents conclusions from this dissertation and highlights the salient points from this work. It will also offer suggestions for further work on this theme.

CHAPTER V

CONCLUSIONS AND RECOMMENDATIONS

5.1 Conclusions

Vapor absorption systems act as an advantageous replacement for conventional vapor compression systems for certain refrigeration and air-conditioning applications. They use heat as their primary source of energy and provide opportunities to innovatively use waste heat or solar energy to drive these systems. The absorber is the most crucial component of the vapor absorption system and has the largest impact on system performance. Absorber design requires a keen understanding of the underlying heat and mass transfer phenomena.

A review of the major absorption models in the literature was conducted. The models in the literature neglected some of the crucial aspects of the solution flow in horizontal tube absorbers. They assumed the flow to occur in the form of uniform films around the tube. A few of the models like the ones by Patnaik *et al.* [16–20] and Barrdahl [21,22] accounted for the effect of waves on the film. Even these models only considered the increase in heat and mass transfer coefficients due to the waves and ignored the mixing of the film concentration and temperature profiles due to the wave. Besides none of the models accounted for droplet formation, growth, breakup, fall, its impact on the tube and the formation of satellite droplets. These aspects of the flow have a significant impact of the absorption process. The present work endeavored to fill this gap in the literature by studying the absorption heat and mass transfer under real-life absorber flow conditions.

Numerically modeling the interface heat and mass transfer presents significant challenges, due to the discontinuous nature of the governing equations and the sharp

gradients at the interface. The model presented in this study overcame these challenges and successfully simulated the absorption heat and mass transfer phenomenon under flow conditions close to the actual flow in a horizontal tube absorber. It accounted for finer nuances of the flow such as the fluid mixing due to droplet impact and the axial propagation of waves on the film over the tube.

The lithium bromide solution concentration at the interface is determined by the vapor pressure equilibrium condition, while the absorption mass transfer process is governed by the species transport equation. Due to the low mass diffusivity of water in lithium bromide, the concentration gradients close to the liquid-vapor are very sharp. The severe numerical difficulties encountered due to these sharp gradients were overcome by defining a fictitious concentration field in the vapor phase, and defining the concentration as a continuous function in the entire computational domain.

The vapor absorption process being exothermic also produces sharp thermal gradients near the liquid-vapor interface. This heat of absorption is included in the governing energy equation as an energy source term. The energy source term is a Gauss' theorem-based volumetric formulation of the interface heat fluxes and depends on the concentration gradients in the direction normal to the interface. The normal direction was computed using the principle that the density gradients are maximum in the direction normal to the interface.

Indigenous codes were developed for solving the species and energy equations and overcome the numerical challenges in their modeling. Codes were also developed to track the direction and shape of the interface, implement the various interface and boundary conditions, and track and conserve the overall mass and energy of the system. These codes were executed synchronously with a Gauss Seidel based numerical solver in the commercial CFD package Fluent [63].

The baseline line case was computed on an elaborate three dimensional grid with 1,185,870 grid cells. The average Reynolds number in the case was always less than

110. The local surface heat and mass transfer coefficients and film concentration and temperature profiles were plotted for various locations on the tube. The average heat transfer coefficient for this case was found to be 1500 W/m^2-K, while the average mass transfer coefficient was found to be 4.67×10^{-3} kg/m^2-s. The average Nusselt number for the flow was 39.8, while the average Sherwood number was 29.2. The *mixing effect* due to the impact of droplet fall was seen to play an important role in the absorption process. The impact of the droplet mixed the film concentration profiles, making newer surfaces of the solution film available for vapor absorption. This effect was crucial due to the extremely poor mass transport characteristics of the lithium bromide solution. The average absorption flux on the film was 6.65×10^{-4} kg/m^2-s, while that on the droplet was 1.78×10^{-4} kg/m^2-s. The droplet accounted for 4.4% of the total absorption in the lithium bromide solution. The results from this case were compared with experimental results by Vliet [77]. The scaled Nusselt number values from the experimental work were between 5 and 48% higher than the results from the present study. This discrepancy may be attributed to the use of octyl alcohol as a surfactant in the studies by Vliet [77], while no surfactants were used in the present study. Also, the extrapolation of the correlations from that study to the present case, which is outside the range of geometries studied by him, as well as different bases for temperature differences used for the calculation of heat transfer coefficients, lead to these differences.

A case with a tube diameter and spacing of 6.35 mm and 5.12 mm, respectively, was also investigated. Due to the smaller tube spacing, there was no explicit droplet formation, breakup and fall in this case. The flow occurred through a steady *liquid bridge* connecting the two tubes. Due to the lack of droplet impact, the mixing effect was absent in this case. This severely affected the absorption process beyond the initial stages. The lithium bromide solution film formed a low-concentration barrier at the interface that prevented any further vapor absorption, and failed to

diffuse to the inner regions of the film due to its poor mass transport properties. The average Reynolds number for this case was always less than 470. The average heat transfer coefficient for this case was found to be 7024 W/m^2-K, while the average mass transfer coefficient was found to be 4.85×10^{-3} kg/m^2-s. The average Nusselt number for the flow was 74.3, while the average Sherwood number was 12.1. The average vapor absorption flux decreased from 5.94×10^{-4} kg/m^2-s for the baseline case, to 2.44×10^{-4} kg/m^2-s in this case. The average absorption heat flux decreased from 1475 W/m^2 in the baseline case to 606 W/m^2 in this case.

The remainder of the parametric analyses were carried out on a two dimensional grid. Though the nature of the results were the same in both the two and three dimensional grids, there were some differences in the results. The three dimensional computations provided a much deeper insight into the axial propagation of the waves created due to droplet impact, and their effect on heat and mass transfer. However the two dimensional grid still captured most of the key elements of the flow such as, droplet formation, growth, fall and impact and its effect on the film (expect axial waves). It effectively tracked the impact of the various aspects of the flow on the heat and mass transfer processes. The average Reynolds number for two dimensional baseline case was always less than 65. The average heat transfer coefficient for this case was found to be 7452 W/m^2-K, while the average mass transfer coefficient was found to be 13.78×10^{-3} kg/m^2-s. The average Nusselt number for the flow was 197.5, while the average Sherwood number was 86.0. The average absorption mass flux in the present case was found to be 14.85×10^{-4} kg/m^2-s and the average heat flux due to absorption was found to be 3689 W/m^2.

A decrease in the lithium bromide inlet concentration from 65% to 60% led to a smaller difference between the lithium bromide solution concentration and the equilibrium concentration, which resulted in lower absorption rates. An increase in the tube inlet temperature from 40.5 ℃ to 45.0 ℃ increased the equilibrium concentration

from 57.4% at 40.5 ℃ to 59.6% at 45.0 ℃ and thus reduced the initial driving concentration difference between the interface and bulk fluid from 7.6% to 5.4%, resulting in lower absorption rates.

A decrease in the solution flow rate was simulated by reducing the initial lithium bromide solution film thickness at the start of the computation to 0.30 mm, from its baseline value of 0.35 mm. The lower flow rate resulted in lower heat and mass transfer coefficients and caused a decrease in the amount of vapor absorbed. However, the decrease in absorption was found to be lower than the decrease due to the change in inlet concentration and temperature. This was because the flow rate was changed by a value small enough that the flow patterns were not significantly altered, and so the performance penalty was low. The average Reynolds number for the case was always less than 49.

Lastly, the coolant temperature was increased to 35 ℃, from its baseline value of 30 ℃. The higher coolant temperature, increased the lithium bromide solution temperature, which in turn increased the equilibrium concentration. This decreased the driving concentration difference, which in turn decreased absorption. The change in coolant temperature caused the least decrease in the amount of absorption among all the cases. The heat transfer coefficients in the thin film were quite high and the 5 ℃ increase in coolant temperature, still left enough temperature difference between the coolant and solution for effective cooling of the lithium bromide solution. Also the drop in the maximum driving concentration difference due to the coolant temperature change was quite small (decreased from 13.8% to 10.7%). Due to these factors, the decrease in absorption due to this change was relatively low.

A change in the flow pattern was seen to have the biggest impact on the absorption process. When the lithium bromide solution ceased to flow in the form of droplets, the absorption rate was severely affected due to the lack of the *mixing effect* associated with the impact of the droplet on its fall. Change in the inlet lithium bromide solution

concentration or temperature affected the concentration difference that drove the mass transfer. Hence these changes had the next most significant impact on the absorption process. The change in the solution flow rate without change in flow patterns did not significantly alter the absorption rate. Lastly due to the high film heat transfer coefficients and relatively small drop in driving concentration difference, moderate changes in the coolant temperature did not have a severe affect of the absorption rate.

The results from the present study provide insights into the local heat and mass transfer phenomena that occur during vapor absorption. The results from this study can be used to guide absorber design, by obtaining a deeper, physics-based understanding of the parameters affecting the absorption process.

5.2 Recommendations for future work

The present work represents a pilot work in the numerical study of the vapor absorption process taking the actual absorber flow conditions into consideration. There is tremendous potential and need for further work in this area. This section presents a few avenues for extending this study.

5.2.1 Advancement of numerical algorithms for two-phase heat and mass transfer

The model presented in this study addressed the heat and mass transfer phenomena at the interface. However it was subject to severe stability constraints. The time step for the computations had to be set very low ($\sim 10^{-6}$ s) to ensure convergence of the solution. The algorithm was also found to be extremely resource intensive and required about four months to solve the problem on the three dimensional grid, on a Sun Fire V40z server with eight 64 bit AMD Opteron processors and 16 GB RAM.

Also, the results were found to differ slightly with changes in the grid size. There is opportunity for improving on the algorithm used here and overcoming these deficiencies with the use of innovative mathematical techniques.

5.2.2 Inter droplet interaction

The formation and fall of a single droplet and its effect on heat and mass transfer was modeled in the present study. In an actual absorber, multiple droplets fall from the tube and the waves generated by the impact of these droplets interfere with each other and modify the heat and mass transfer characteristics not only in the inter-tube region, but also in the film characteristics on the tube surface. The nature of this interference depends on the distance between the droplets, their relative size and velocities and the phase lag between them. This multi-droplet interaction needs to be studied by modeling multiple droplets on a bigger grid. The main difficulty in such a computation is its time and resource requirement. However, with advancements in the algorithm as outline the previous paragraph, it might be possible to achieve this.

5.2.3 Use of different working fluid pairs

A similar study needs to be conducted for the other popular refrigerant-absorbent combination, viz. ammonia-water. As mentioned in the first chapter, due to the lower freezing point of ammonia as compared to water, ammonia-water systems can be used to run refrigeration and heat pump cycles at much lower evaporator temperatures than water-lithium bromide systems. The heat and mass transfer modeling of ammonia-water absorbers present an additional challenge in that the refrigerant and absorbent are present as a mixture in both the solid and the liquid phases, as opposed to a pure refrigerant vapor in the present study. This further complicates the interface mass transfer phenomena and must be accounted for.

5.2.4 Effect of surfactants

Surfactants such as octyl alcohol are frequently used with water-lithium bromide systems to improve their mass transfer characteristics. These surfactants induce *Marangoni convection* at the interface and mix the liquid at the interface with the bulk liquid. This increases the driving concentration difference and significantly benefits absorption. Surfactants present a significant modeling challenge and they introduce several new aspects into an already complicated interface phenomenon. But due to the potential for significant performance improvements, the effect of surfactants need to be modeled and their effects studied in detail.

5.2.5 Use of structured surfaces

Tubes with structured and enhanced surfaces improve the interface heat and mass transfer by tripping the boundary layers at the interface and inducing local mixing in the flow. It however significantly increases the complexity of the geometry and would likely need a finer grid than the one used for smooth tubes. But there is scope for performance enhancements due to their use and their effects should be studied in greater detail.

5.2.6 Experimental verification

Experimental verification of the results from this work poses tremendous challenges. The focus of this work is the local level heat and mass transfer variations, which are very difficult to measure experimentally. Innovations in such local measurements would considerably improve the ability to validate the results from the present study. In the interim, experimental validation using measurements at the bulk level should

be conducted and would complement this study very well.

APPENDIX A

BENCHMARK COMPARISON

The numerical model developed in this study was first tested on simple problems with known results, to test the validity of the model. Besides validation, benchmark problems being smaller also help in quicker model development, as they reduce the time lag between the writing and testing of preliminary versions of the code.

In this study, the model was benchmarked using the problem of a liquid droplet freely falling on a sphere. This problem has been well studied, and Ranz and Marshall [78] have proposed the following solution:

$$Nu_D = 2 + 0.6Re_D^{1/2}Pr^{1/3} \tag{A.1}$$

The average Reynolds number based on film thickness was always less that 65 for this flow. This corresponds to a Reynolds number of 3040 based on diameter. For this Reynolds number, the average Nusselt number calculated using Equation A.1 was 82.7. In comparison, the average Nusselt number computed by the model in the present study was 102.0. This corresponds to an error of 19%, which is within the acceptable error limits of most correlations.

REFERENCES

[1] Lemmon, E., McLinden, M., and Huber, M., "Reference fluid thermodynamic and transport properties," *National institute of standards and technology*, 2002.

[2] Herold, K., Radermacher, R., and Klein, S., *Absorption chillers and heat pumps*. CRC Press, 1996.

[3] Mahmoud, I., Ishida, K., and Monde, M., "Analysis of ammonia vapor absorption into ammonia water mixtures: mass diffusion flux," *Heat Mass Transfer*, vol. 41, pp. 875–889, 2005.

[4] Grigor'eva, N. and Nakoryakov, V., "Exact solution of combined heat- and mass-transfer problem during film absorption," *Journal of Engineering Physics*, vol. 33, no. 5, pp. 1349 – 53, 1977.

[5] Nakoryakov, V. Y. and Grigor'yeva, N. I., "Combined heat and mass transfer in film absorption.," *Heat Transfer - Soviet Research*, vol. 12, no. 3, pp. 111 – 117, 1980.

[6] Nakoryakov, V. and Grigoryeva, N., "Heat and mass transfer in film absorption," *Russian Journal of Engineering Thermophysics*, vol. 2, no. 1, pp. 1 – 16, 1992.

[7] Nakoryakov, V. Y., Bufetov, N. S., and Grigor'yeva, N. I., "Heat and mass transfer in film absorption.," *Fluid Mechanics - Soviet Research*, vol. 11, no. 3, pp. 97 – 115, 1982.

[8] Nakoryakov, V. E. and Grigor'eva, N. I., "Calculation of heat and mass transfer in nonisothermal absorption on the initial portion of a downflowing film.," *Theoretical Foundations of Chemical Engineering (English Translation of Teoreticheskie Osnovy Khimicheskoi Tekhnologii)*, vol. 14, no. 4, pp. 305 – 309, 1980.

[9] Nakoryakov, V. and Grigor'eva, N., "Combined heat and mass transfer during absorption in drops and films," *Journal of Engineering Physics*, vol. 32, no. 3, pp. 243 – 7, 1977.

[10] Nakoryakov, V. E., Grigor'eva, N. I., and Potaturkina, L. V., "Analysis of exact solutions to heat and mass transfer problems for absorption with films or streams," *Theoretical Foundations of Chemical Engineering*, vol. 31, no. 2, pp. 119 –, 1997.

[11] Nakoryakov, V., Burdukov, A., Bufetov, N., Grigor'yeva, N., and Dorokhov, A., "Coefficients of heat and mass transfer in falling wavy liquid films," *Heat Transfer - Soviet Research*, vol. 14, no. 3, pp. 6 – 11, 1982.

[12] Kholpanov, L. P., Malyusov, V. A., and Zhavoronkov, N. M., "Hydrodynamics and heat- and mass-transfer in a liquid film in the presence of a gas stream or of surface tension.," *Theoretical Foundations of Chemical Engineering (English Translation of Teoreticheskie Osnovy Khimicheskoi Tekhnologii)*, vol. 16, no. 3, pp. 201 – 207, 1982.

[13] Grossman, G., "Simultaneous heat and mass transfer in film absorption under laminar flow," *International Journal of Heat and Mass Transfer*, vol. 26, no. 3, pp. 357 – 71, 1983.

[14] Grossman, G., "Analysis of interdiffusion in film absorption," *International Journal of Heat and Mass Transfer*, vol. 30, no. 1, pp. 205 – 8, 1987.

[15] Grossman, G., "Heat and mass transfer in film absorption," in *Handbook of Heat and Mass Transfer*, vol. 2, ch. 6, pp. 211–57, Gulf publishing, Houston, 1986.

[16] Patnaik, V. and Perez-Blanco, H., "Roll waves in falling films: An approximate treatment of the velocity field," *International Journal of Heat and Fluid Flow*, vol. 17, no. 1, pp. 63 – 70, 1996.

[17] Patnaik, V. and Perez-Blanco, H., "A study of absorption enhancement by wavy film flows," *International Journal of Heat and Fluid Flow*, vol. 17, no. 1, pp. 71 – 77, 1996.

[18] Patnaik, V., Perez-Blanco, H., and Ryan, W., "A simple analytical model for the design of vertical tube absorbers," *ASHRAE Transactions*, vol. 99, no. 2, pp. 69 – 80, 1993.

[19] Patnaik, V. and Perez-Blanco, H., "A counterflow heat-exchanger analysis for the design of falling-film absorbers," in *Proceedings of the International Absorption Heat Pump Conference*, pp. 209 – 216, 1994.

[20] Patnaik, V., Miller, W. A., and Perez-Blanco, H., "An empirical methodology for the design of vertical-tube absorbers," *ASHRAE Transactions*, vol. 100, no. 2, pp. 185–196, 1994.

[21] Barrdahl, R., "On the stability of falling films - Periodic, finite-amplitude waves.," *AIChE Journal*, vol. 32, no. 5, pp. 789 – 797, 1986.

[22] Barrdahl, R., "Mass transfer in falling films: Influence of finite amplitude waves," *AIChE Journal*, vol. 34, no. 3, pp. 493 – 8, 1988.

[23] Kawae, N., Shigechi, T., Kanemaru, K., and Yamada, T., "Water vapor evaporation into laminar film flow of a lithium bromide-water solution (influence of variable properties and inlet film thickness on absorption mass transfer rate)," *Heat Transfer - Japanese Research*, vol. 18, no. 3, pp. 58 – 70, 1989.

[24] Brauner, N., Maron, D. M., and Meyerson, H., "Effect of absorbate concentration level in hygroscopic condensation.," *International Communications in Heat and Mass Transfer*, vol. 15, no. 3, pp. 269 – 279, 1988.

[25] Brauner, N., Maron, D. M., and Meyerson, H., "Coupled heat condensation and mass absorption with comparable concentrations of absorbate and absorbent," *International Journal of Heat And Mass Transfer*, vol. 32, pp. 1897–1906, Oct. 1989.

[26] Brauner, N., "Nonisothermal vapor absorption into falling film," *International Journal of Heat And Mass Transfer*, vol. 34, pp. 767–784, Mar. 1991.

[27] van der Wekken, B. J. C. and Wassenaar, R. H., "Simultaneous heat and mass-transfer accompanying absorption in laminar-flow over a cooled wall," *International Journal of Refrigeration-Revue Internationale Du Froid*, vol. 11, pp. 70–77, Mar. 1988.

[28] Habib, H. and Wood, B., "Simultaneous heat and mass transfer for a falling film absorber. The two phase flow problem," *Proceedings of the 12th Annual International Solar Energy Conference*, pp. 61 – 67, 1990.

[29] Yang, R. and Wood, B. D., "A numerical modeling of an absorption process on a liquid falling film," *Solar Energy*, vol. 48, no. 3, pp. 195–198, 1992.

[30] Hajji, A. and Worek, W. M., "Transient heat and mass-transfer in film absorption of finite depth with nonhomogeneous boundary-conditions," *International Journal of Heat and Mass Transfer*, vol. 35, pp. 2101–2108, Sept. 1992.

[31] Hajji, A. and Lavan, Z., "Effect of film depth and interfacial convection on transient heat and mass transfer in film absorption," *Proceedings of teh International Heat Transfer Conference*, pp. 347–352, 1990.

[32] Ramadane, A., Aoufoussi, Z., and Le Goff, H., "Experimental investigation and modeling of gas-liquid absorption with a high thermal effect," *Institution of Chemical Engineers Symposium Series*, vol. 1, no. 128, pp. 451–459, 1992.

[33] Conlisk, A. T., "Falling film absorption on a cylindrical tube," *AICHE Journal*, vol. 38, pp. 1716–1728, Nov. 1992.

[34] Conlisk, A., "Use of boundary layer techniques in the design of a falling film absorber," *Proceedings of the International Absorption Heat Pump Conference*, pp. 163 – 170, 1994.

[35] Conlisk, A. T., "Semi-analytical design of a falling film absorber," *Journal of Heat Transfer*, vol. 116, pp. 1055–1058, Nov. 1994.

[36] Conlisk, A. T., "Structure of falling film heat and mass-transfer on a fluted tube," *AICHE Journal*, vol. 40, pp. 756–766, May 1994.

[37] Conlisk, A. T., "Analytical solutions for the heat and mass-transfer in a falling film absorber," *Chemical Engineering Science*, vol. 50, pp. 651–660, Feb. 1995.

[38] Conlisk, A. T., "Effect of coolant flow conditions on the performance of an absorber," *ASHRAE Transactions*, vol. 101, no. 2, pp. 73 – 80, 1995.

[39] Ibrahim, G. A. and Vinnicombe, G. A., "A hybrid method to analyze the performance of falling film absorbers," *International Journal of Heat and Mass Transfer*, vol. 36, pp. 1383–1390, Mar. 1993.

[40] Jernqvist, A. and Kockum, H., "Simulation of falling film absorbers and generators," in *Proceedings of the International Ab-Sorption Heat Pump Conference*, vol. 1, pp. 311 – 8, 1996.

[41] Andberg, J. W. and Vliet, G. C., "Design guidelines for water-lithium bromide absorbers.," *ASHRAE Transactions*, vol. 89, no. 1B, pp. 220 – 232, 1983.

[42] Andberg, J. W. and Vliet, G. C., "Nonisothermal absorption of gases into falling liquid films.," *Proceedings of the ASME - JSME Thermal Engineering Joint Conference*, vol. 2, pp. 423 – 431, 1983.

[43] Andberg, J., *Absorption of vapors into liquid films falling over cooled horizontal tubes*. PhD thesis, University of Texas, Austin, 1986.

[44] Andberg, J. and Vliet, G., "A simplified model for absorption of vapors into liquid films flowing over cooled horizontal tubes," *ASHRAE Transactions*, vol. 93, no. 2, pp. 2454 – 63, 1987.

[45] Andberg, J. W. and Vliet, G. C., "Absorption of vapors into liquid films flowing over cooled horizontal tubes.," *Proceedings of the ASME - JSME Thermal Engineering Joint Conference*, vol. 2, pp. 533 – 541, 1987.

[46] Choudhury, S., Nishiguchi, A., Hisajima, D., Fukushima, T., Ohuchi, T., and Sakaguchi, S., "Absorption of vapors into liquid films flowing over cooled horizontal tubes," *ASHRAE Transactions*, vol. 99, no. 2, pp. 81 – 89, 1993.

[47] Lu, Z., Li, D., Li, S., and Yu-Chi, B., "A semi-empirical model of the falling film absorption outside horizontal tubes," in *Proceedings of the International Ab-Sorption Heat Pump Conference*, vol. 2, pp. 473–80, 1996.

[48] Winterton, R., "Where did the Dittus and Boelter equation come from?," *International Journal of Heat and Mass Transfer*, vol. 41, no. 4-5, pp. 809 – 10, 1998.

[49] Conlisk, A. T. and Mao, J., "Nonisothermal absorption on a horizontal cylindrical tube .1. the film flow," *Chemical Engineering Science*, vol. 51, pp. 1275–1285, Apr. 1996.

[50] Min, J. and Choi, D., "Analysis of the absorption process on a horizontal tube using Navier-Stokes equations with surface-tension effects," *International Journal of Heat and Mass Transfer*, vol. 42, no. 24, pp. 4567 – 4578, 1999.

[51] Kirby, M. J. and Perez-Blanco, H., "A design model for horizontal tube water/lithium bromide absorbers," in *ASME Heat Pump and Refrigeration Systems Design, Analysis and Applications*, vol. 32, pp. 1 – 10, 1994.

[52] Sultana, P., Wijeysundera, N., Ho, J., and Yap, C., "Modeling of horizontal tube-bundle absorbers of absorption cooling systems," *International Journal of Refrigeration*, vol. 30, no. 4, pp. 709 – 23, 2007.

[53] Wijeysundera, N., Sultana, P., Ho, J., and Yap, C., "Simplified models for inter-tube absorption in horizontal-tube-bundle absorbers," in *Proceedings of the 22nd IIR International Congress of Refrigeration*, 2007.

[54] Jeong, S. and Garimella, S., "Falling-film and droplet mode heat and mass transfer in a horizontal tube LiBr/water absorber," *International Journal of Heat and Mass Transfer*, vol. 45, no. 7, pp. 1445 – 58, 2002.

[55] Jeong, S. and Garimella, S., "Optimal design of compact horizontal tube LiBr/water absorbers," *HVAC and R Research*, vol. 11, no. 1, pp. 27 – 44, 2005.

[56] Killion, J. and Garimella, S., "A critical review of models of coupled heat and mass transfer in falling-film absorption," *International Journal of Refrigeration*, vol. 24, no. 8, pp. 755 – 797, 2001.

[57] Killion, J. and Garimella, S., "A review of experimental investigations of absorption of water vapor in liquid films falling over horizontal tubes," *HVAC and R Research*, vol. 9, no. 2, pp. 111 – 136, 2003.

[58] Killion, J. D. and Garimella, S., "Gravity-driven flow of liquid films and droplets in horizontal tube banks," *International Journal of Refrigeration*, vol. 26, no. 5, pp. 516 – 526, 2003.

[59] Killion, J. and Garimella, S., "Pendant droplet motion for absorption on horizontal tube banks," *International Journal of Heat and Mass Transfer*, vol. 47, no. 19-20, pp. 4403 – 14, 2004.

[60] Killion, J. D., "An investigation of droplets and films falling over horizontal tubes," Master's thesis, Iowa State University, 2003.

[61] Killion, J. D. and Garimella, S., "Simulation of pendant droplets and falling films in horizontal tube absorbers," *Journal of Heat Transfer*, vol. 126, no. 6, pp. 1003 – 1013, 2004.

[62] Yuan, Z. and Herold, K. E., "Thermodynamic properties of aqueous lithium bromide using a multiproperty free energy correlation," *HVAC and R Research*, vol. 11, no. 3, pp. 377 – 393, 2005.

[63] Fluent Inc., "Fluent 6.2.16," 2005.

[64] Hirt, C. and Nichols, B., "Volume of fluid (VOF) method for the dynamics of free boundaries," *Journal of Computational Physics*, vol. 39, no. 1, pp. 201 – 25, 1981.

[65] Issa, R., "Solution of the implicitly discretised fluid flow equations by operator-splitting," *Journal of Computational Physics*, vol. 62, no. 1, pp. 40 – 65, 1986.

[66] Youngs, D., "Time-dependent multi-material flow with large fluid distortion," in *Numerical Methods for Fluid Dynamics* (Morton, K. and Baines, M., eds.), Academic Press, 1982.

[67] Brackbill, J., Kothe, D., and Zemach, C., "A continuum method for modeling surface tension," *Journal of Computational Physics*, vol. 100, no. 2, pp. 335 – 54, 1992.

[68] Fluent Inc., *Fluent 6.2 User's Guide*, 2005.

[69] Holmes, D. and Connell, S., "Soultion of the 2D Navier-Stokes equations on unstructured adaptive grids," in *Proceedings of the 9th AIAA Computational Fluid Dynamics Conference*, June 1989.

[70] Rauch, R., Batira, J., and Yang, N., "Spatial adaptation procedures on unstructured meshes for accurate unsteady aerodynamic flow computations," Tech. Rep. AIAA-91-1106, AIAA, 1991.

[71] Rhie, C. and Chow, W., "Numerical study of the turbulent flow past an airfoil with trailing edge separation," *AIAA Journal*, vol. 21, no. 11, pp. 1525 – 32, 1983.

[72] Patankar, S. and Spalding, D., "A calculation procedure for heat, mass and momentum transfer in three-dimensional parabolic flows," *International Journal of Heat and Mass Transfer*, vol. 15, no. 10, pp. 1787 – 806, 1972.

[73] Patankar, S. V., *Numerical heat transfer and fluid flow.* Hemisphere Pub. Corp., Washington D.C., 1980.

[74] Kulankara, S. and Herold, K., "Surface tension of aqueous lithium bromide with heat/mass transfer enhancement additives: the effect of additive vapor transport," *International Journal of Refrigeration*, vol. 25, pp. 383–389, 2002.

[75] Ziegler, B. and Trepp, C., "Equation of state for ammonia-water mixtures.," *International Journal of Refrigeration*, vol. 7, no. 2, pp. 101 – 106, 1984.

[76] Lee, R., DiGuilio, R., Jeter, S., and Teja, A., "Properties of lithium bromide-water solutions at high temperatures and concentrations - II: Density and viscosity," *ASHRAE Transactions*, vol. 96, no. 1, pp. 709–714, 1990.

[77] Vliet, G. C., "Absorption heat and mass transfer in falling water-lithium bromide films on horizontal tubes," Tech. Rep. Project 405-RP, ASHRAE, 1989.

[78] Ranz, W. and Marshall, W. *Chem. Eng. Prog.*, vol. 48, p. 141, 1952.